SSEF
SCHWEIZERISCHES GEMMOLOGISCHES INSTITUT
SWISS GEMMOLOGICAL INSTITUTE
INSTITUT SUISSE DE GEMMOLOGIE

Gem-A
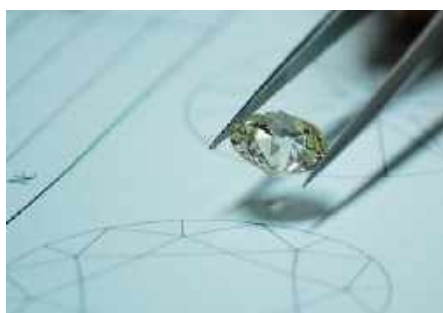THE GEMMOLOGICAL ASSOCIATION
OF GREAT BRITAIN

SSEF ✚

SCHWEIZERISCHES GEMMOLOGISCHES INSTITUT
SWISS GEMMOLOGICAL INSTITUTE
INSTITUT SUISSE DE GEMMOLOGIE

ORIGIN DETERMINATION · TREATMENT DETECTION

DIAMOND GRADING · PEARL TESTING

EDUCATION · RESEARCH

THE SCIENCE OF GEMSTONE TESTING™

COLUMNS

Cover photo: *An article on pp. 262–280 of this issue describes the characteristics of chrysocolla chalcedony from Taiwan, Indonesia and USA. This pendant/brooch designed by Paula Crevoshay and Glenn Lehrer, called 'Georgia's Dream', features a 53.57 ct piece of chrysocolla chalcedony from Arizona, USA, that was carved by Lehrer, and is accompanied by another chrysocolla chalcedony (top, 3.59 ct pear shape) along with 52 blue zircons, 37 blue apatites, 43 tsavorites and 93 diamonds. Photo by Orasa Weldon.*

ARTICLES

240
Photo by M. H. Smith

307
Photo by Z. Song

Gem-A
THE GEMMOLOGICAL ASSOCIATION OF GREAT BRITAIN

SSEF
SCHWEIZERISCHES GEMMOLOGISCHES INSTITUT
SWISS GEMMOLOGICAL INSTITUTE
INSTITUT SUISSE DE GEMMOLOGIE

AGL
AMERICAN GEMOLOGICAL LABORATORIES

The Journal of Gemmology

COVERED BY THE FOLLOWING ABSTRACTING AND INDEXING SERVICES:

Clarivate Analytics' (formerly Thomson Reuters/ISI) Science Citation Index Expanded (in the Web of Science), *Journal Citation Reports (Science Edition)* and *Current Contents (Physical, Chemical and Earth Sciences)*; Elsevier's Scopus; Australian Research Council's Excellence in Research for Australia (ERA) Journal List; China National Knowledge Infrastructure (CNKI Scholar); EBSCO's Academic Search Ultimate; ProQuest (Cambridge Scientific Abstracts); GeoRef; CrossRef; Chemical Abstracts (CA Plus); Mineralogical Abstracts; Index Copernicus ICI Journals Master List; Gale Academic OneFile; British Library Document Supply Service; and Copyright Clearance Center's RightFind application.

Science Citation Index Expanded
Web of Science

CONTENT SUBMISSION

The Editor-in-Chief is glad to consider original articles, news items, conference reports, announcements and calendar entries on subjects of gemmological interest for publication in *The Journal of Gemmology*. A guide to the various sections and the preparation of manuscripts is given at https://gem-a.com/membership/journal-of-gemmology/submissions, or contact the Editor-in-Chief.

SUBSCRIPTIONS

Gem-A members receive *The Journal* as part of their membership package, full details of which are given at https://gem-a.com/membership. Laboratories, libraries, museums and similar institutions may become direct subscribers to *The Journal*; download the form from *The Journal*'s home page.

ADVERTISING

Enquiries about advertising in *The Journal* should be directed to advertising@gem-a.com.
For more information, see https://gem-a.com/membership/media-pack-2020.

COPYRIGHT AND REPRINT PERMISSION

For full details of copyright and reprint permission contact the Editor-in-Chief. *The Journal of Gemmology* is published quarterly by Gem-A, The Gemmological Association of Great Britain. Any opinions expressed in *The Journal* are understood to be the views of the contributors and not necessarily of the publisher.

DESIGN & PRODUCTION

Zest Design, London. www.zest-uk.com

PRINTER

DG3 Group (Holdings) Ltd, London. www.dg3.com

FSC Mixed Sources
Product group from well-managed forests and other controlled sources
www.fsc.org Cert no. TT-COC-002454
© 1996 Forest Stewardship Council

What's New

NEWS AND PUBLICATIONS

Illustrious Opals Series

The first of four planned issues highlighting opal was released August 2020 from Beckett Media, the publisher of *Rock & Gem* magazine. It can be freely downloaded from www.rockngem. com/IllustriousOpals_series.pdf and includes articles on cutting, carving, terminology and colouration, as well as information on events and auctions and a showcase of opal specimens from the issue's sponsors.

Mintabie Opal Resource Evaluation Report

In January 2020, the Government of South Australia released the 2nd edition of its report *Mintabie Opal Resource Evaluation: Current Value of Opal Resources and Projected Value of Undiscovered Resources*, which reviews the potential of the area's remaining opal resources and includes a detailed geospatial analysis conducted in 2018. The report also discusses the current decline in production and proposes prospecting methods to help make new discoveries. Visit https://sarigbasis.pir.sa.gov. au/WebtopEw/ws/samref/sarig1/wci/Record?r=0&m=1&w=catno=2041901.

The Impact of COVID-19 on African Communities Affected by Diamond Mining

In June 2020, the Kimberley Process Civil Society Coalition released this report at www.kpcivilsociety. org/report/the-impact-of-covid-19-on-african-communities-affected-by-diamond-mining. It is accompanied by a 6 July webinar. The topics include the geography and nature of selected diamond mining areas in seven African countries, the health impact of COVID-19 and its effect on diamond mining, trading and socioeconomics, as well as support programs, regulations and human rights issues. The report ends with policy recom-mendations to support the affected communities.

A Rough Cut Trade: Africa's Coloured-Gemstone Flows to Asia

In July 2020, the Global Initiative Against Trans-national Organized Crime released a report on the multi-billion-dollar international gem trade linking African suppliers with traders in Asia. The information is based on interviews with traders, gemmologists and government representatives, as well as other ongoing research. The 56-page report proposes that the informal nature of the trade in rough gem materials contributes to the potential for illicit activities and makes it difficult to improve conditions in mining communities. Recommendations are provided. Download the report at https://globalinitiative.net/africa-asia-gemstones-trade.
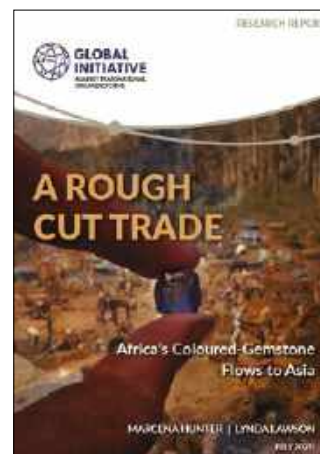
TRAFFIC Reports on Illicit Ivory Trade and Ivory Identification

TRAFFIC International is a UK-based charity organisation dedicated to global wildlife conservation and trade. In July 2020, it released a 76-page report titled *Trading Faces: A Snapshot of the Online Ivory Trade in Indonesia, Thailand and Viet Nam in 2016 with an Update in 2019*, which investigates the online trade in elephant ivory that continues to take place in these three countries. Download the report at www.traffic.org/site/assets/files/12981/three-country-ivory-report.pdf. This was followed in August 2020 by the fourth edition of *Identification Guide for Ivory and Ivory Substitutes*, which provides characteristic features of elephant, mammoth, walrus, whale, narwhal, hippopotamus and warthog ivories, along with natural and manufactured ivory substitutes, as well as modern methods of laboratory identification. This guide is available at www.traffic.org/site/assets/files/13065/identification-guide-for-ivory.pdf.
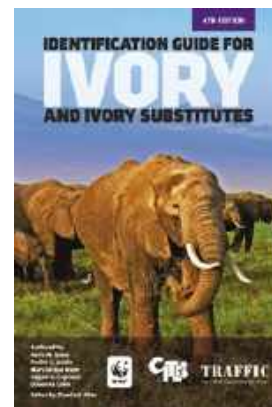
OTHER RESOURCES

Crystal Models and Software

Holland-based Smorf Crystal Models, which offers crystallographically accurate plastic models of mineral crystals, is now providing free crystal-drawing software (Dexter, on the Windows platform) at www.smorf.nl/index.php#news. It enables the user to create a crystal drawing for essentially any mineral. The website also includes a link to purchase the company's pre-made plastic crystal models that are produced by 3D printing.
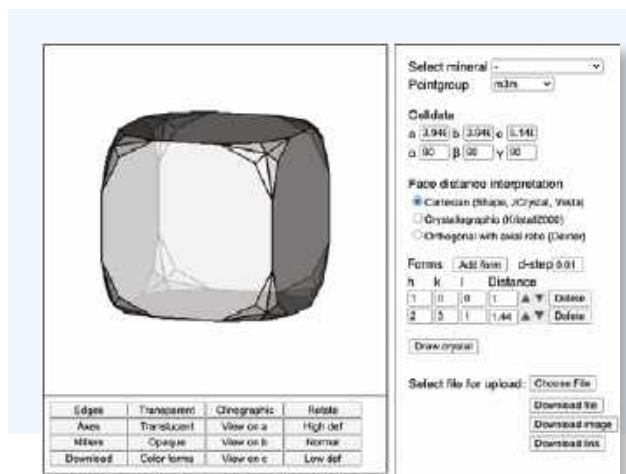
RJC Due Diligence Member Toolkit

The Responsible Jewellery Council (RJC) released this new contribution to its Code of Practices in August 2020. The toolkit includes a 46-page booklet, which describes the goals and methods for RJC members to 'exercise due diligence over their supply chains' according to the Organization for Economic Cooperation and Development or other RJC-recognised frameworks. Templates described in the booklet are provided in a separate download, with Word files the user can edit to include company-specific information before signing and endorsing each document. This is a requirement for RJC members, but others in the trade will likely find the information valuable. Download the booklet and tools at www.responsiblejewellery.com/support/cop-2019-walkthrough/provision-07.

Webinars and Other Online Resources for Gemmological Education

Various educational and gem industry organisations are providing webinars and archived video content of interest to gemmologists during the ongoing quarantines associated with the COVID-19 pandemic. The following add to the list of such resources provided in the previous issue of *The Journal*.

- The **Accredited Gemologists Association** offers webinars on pink diamonds from the Argyle mine in Australia, ruby treatments and current market conditions. Visit www.gotostage.com/channel/06607e7c75d5433eb5f81a1c669a85c3 to register and watch these webinars.

- **Christie's Collecting Guides** are an ongoing feature of this auction house's website. The online articles cover various subjects, often focusing on collecting items from specific jewellers and artists, as well as on more general topics such as ancient engraved gems, Art Deco jewellery and tips for collecting ancient jewellery. Visit www.christies.com/features?FeatureTypeID=10&CategoryID=8&T=F&LID=1.

Collecting guide: Graff diamonds

- **'The Divers of Sewa'**, a film by Dr Laurent Cartier, was released online in August 2020 at https://vimeo.com/444162165. The nine-minute video—which Dr Cartier premiered at the November 2019 Gem-A Conference—shows how artisanal divers search for diamonds in gravels beneath the Sewa River in Sierra Leone.

- The **Far East Gem Institute** has a variety of fee-based 'On Demand Learning' webinars and other educational resources as videos and PDFs at https://fareastgem.institute/learn. Topics include heat treatment of corundum, amber from Myanmar, diamonds from Kalimantan (Indonesia) and more.

- Podcasts from **Gemology Worldwide** cover topics such as 'Value with Richard Drucker', 'Emeralds with Jeffery Bergman', 'Trade Shows with Doug Hucker' and many more. Visit http://gemologyworldwide.com for a full listing.

- **Home Gemmology**, from Rui Galopim de Carvalho, now has webinars archived at www.youtube.com/channel/UCfQJ4Jnf9LtZCTFB9RIaAuQ, which include topics such as Brazilian diamonds, Lalique jewellery, natural pearls, amethyst and coloured diamonds. The Home Gemmology Blog at www.ruigalopim.com/blog hosts a variety of online articles that have addressed topics such as historic Portuguese jewels, coral, pearls and more.

- **JewelleryAdvisor Pro**, from former Gem-A tutor Julia Griffith, hosts pre-recorded webinars on diamond formation, rare gems, the world's most expensive gems, and more at www.jewelleryadvisor.com/on-demand-webinars.

- **Jewelry Connoisseur**, a website from Rapaport USA, offers podcasts on period jewellery including 'The Enduring Appeal of Art Deco', 'Educating Estate Jewelry Collectors', 'Defining the Cartier Style' and 'Victorian Jewelry'. Visit http://jewelryconnoisseur.net/the-jewelry-connoisseur-podcast.

- **Jewellery Outlook**, an online trade magazine, offers webinars on a range of gem and jewellery marketing topics, such as the impact of COVID-19 on trade shows, digital advances in gem and jewellery trade practices, and more. Visit https://jewelleryoutlook.com/category/webinar-lists.

- **Les Enluminures**, a Paris-based art and antique gallery, offers videos and podcasts on various subjects of interest to gemmologists, such as historical jewellery pieces and interviews with experts such as Diana Scarisbrick, Beatriz Chadour-Sampson and Benjamin Zucker. Visit www.lesenluminures.com/video.

- **Martin Rapaport Webinars** has a YouTube channel with numerous webinars from diamond expert Martin Rapaport. They vary from brief 'editorials' to detailed 'State of the Diamond Industry' reports dealing with the effects of the virus pandemic. To view the full list, visit www.youtube.com/playlist?list=PLy2qi24iNJAT3MyYEp2bcPCDA09a7QhGF.

- **Mineral Talks Live** is a series of mineral-related webinars produced by the Mineralogical & Geological Museum at Harvard University, the Society of Mineral Museum Professionals and BlueCap Productions.

Episodes feature museum curators, mineral dealers and other prominent members of the mineralogical community. The webinars are archived on the BlueCap Productions YouTube channel at www.youtube.com/playlist?list=PLYUSEUgiTprl9Vh7ZLXu8x_hHp0dN_TDJ, which also hosts playlists containing video reports from past mineral shows and presentations given at Dallas Mineral Collecting Symposia at www.youtube.com/c/bluecapproductions/playlists.

- The **Museo del Gioiello Vicenza** website hosts webinars from their 'Tuesdays at the Jewellery Museum' series. Some of them are presented in English, such as 'Symbolism in High Jewellery' and 'The Future of Jewellery'. Visit www.museodelgioiello.it/en/webinar.

- In addition to hosting webinars on their YouTube channel as mentioned in the previous issue, the **Responsible Jewellery Council** has made various webinars available on their website at www.responsiblejewellery.com/hub/news-and-events, including 'Responsible Sourcing of Gold and Diamonds in a Post-COVID-19 World', 'Gold Jewellery Industry in the Pandemic – Now and Future', business leadership discussions and other global jewellery topics.

- The annual **Rochester Mineralogical Symposium** was held online on 25 April 2020, and videos of the presentations are available at www.youtube.com/playlist?list=PL4AllrO7xkRd_rartqBETPUBxfAGwTx6f. The 13 talks cover apatite chemistry and inclusions, optically anomalous crystals, what's new in minerals and more. Abstracts from the e-symposium are also available at www.rasny.org/minsymp/47th RMS Program Notes.pdf.

- The **Symposium on the Effects of Covid-19 on ASMs [Artisanal and Small-Scale Miners] in the Gemstone Supply Chain** was held online 13–14 May 2020 and hosted by the Responsible Jewelry Transformative (producer of the Chicago Responsible Jewelry Conference). Day one covered grassroots initiatives to help small-scale gem miners, while day two moved to global projects. Videos highlighting these discussions from each day are available at https://the-symposium-on-artisanal-small-scale-gemstone-mi.heysummit.com.

Gem Notes

COLOURED STONES

Amazonite in Quartz from Bahia, Brazil

Gem-quality amazonite feldspar is well known from Brazil, particularly from pegmatites of the Early Prote-rozoic Itiúba alkaline massif in Bahia State (Couto 2000). During the February 2020 gem shows in Tucson, Arizona, USA, Leonardo Silva Souto (Gems in Gems, Teófilo Otoni, Minas Gerais, Brazil) had some new production of amazonite from Bahia that was notable for occurring together with transparent to translucent quartz (Figure 1). It was sold in Tucson as 'Paraíba amazonite' in reference to its bright blue to greenish blue colouration. It lacked the white, grid-like mottling that is usually associated with this feldspar variety.

The rough material first entered the market at the August 2019 Feira Internacional de Pedras Preciosas (FIPP) show in Teófilo Otoni, and the initial production consisted of about 400 kg of broken pieces. Since then, approximately 1,000 kg more amazonite has been mined, and approximately 20,000 carats of tablets and cabochons have been polished in sizes ranging up to about 32 × 26 mm. The material is reportedly not treated in any way, and displays various patterns and proportions of amazonite and quartz, as well as brown to black staining in some stones. A considerable portion of the material has been cut as bicoloured gems displaying a sharp demarcation between the amazonite and quartz (again, see Figure 1).

Figure 1: This polished tablet (8 × 6 mm) consists of amazonite and quartz from Bahia, Brazil. Photo by Vicky Rodríguez Garrido.

This material provides an alternative to the more expensive matrix specimens of Paraíba tourmaline with albite and/or quartz that have been polished for gem use.

Brendan M. Laurs FGA

Reference

Couto, P. 2000. *Gemologic Map of the State of Bahia—Explanatory Text*. CPRM – Serviço Geológico do Brasil, Salvador, Bahia, Brazil, 76 pp.

Blue Apatite in Jasper from Brazil

Gem-quality blue to greenish blue apatite from Bahia State in Brazil has been known since approximately 1990 and was mentioned by Koivula *et al.* (1993) as occurring in heavily etched crystals in association with jasper. During the February 2020 Tucson gem shows, Marco Campos Venuti (Gems in Gems, Seville, Spain) had some specimens of blue apatite in jasper that were produced fairly recently from an undisclosed locality, probably in Minas Gerais State. He first encountered the rough material in 2018, but it was of rather low quality, consisting of small (about 5 mm) opaque blue dots in jasper. Later, during the August 2019 FIPP show in Teófilo Otoni, Brazil, he obtained about 300 kg of much better-quality material containing larger-sized gem-quality apatite crystals that were up to 20–25 cm long and 10 cm wide. The apatite was often transparent and sometimes occurred in well-formed crystals within the jasper (e.g. Figure 2).

The jasper matrix is yellow-orange with dark spots, and appears similar to so-called Cheetah jasper from

Figure 2: Viewed in transmitted light, this slab shows well-formed crystals of apatite in a jasper matrix. Photo courtesy of Marco Campos Venuti.

Figure 3: The polished tablet of apatite in jasper weighs 2.13 ct and measures 11 × 8 mm. Photo by Vicky Rodríguez Garrido.

Brazil that has been cut into spheres, pyramids and other *objets d'art*. However, this is the first time that Campos Venuti is aware of apatite being associated with such material. So far he has cut about 300 cabochons and polished tablets/slabs ranging up to approximately 50 × 20 cm. Since the apatite is rather dark, the stones need to be cut thin enough for light to readily pass through them. The contrast between the blue apatite and orange jasper is rather striking (e.g. Figure 3), and it is unusual for this colour combination to occur in gem materials. The blue colour of the apatite is natural and the gems are reportedly not treated in any way. A few of the cabochons cut from this apatite show distinct chatoyancy.

Campos Venuti continues to experiment with the best way to process the rough material, which is challenging to work with since the apatite tends to detach from the jasper matrix. Smaller pieces of transparent apatite of 1–2 cm appear to be best faceted into gemstones, while specimens containing larger crystals of apatite will probably be cut and polished as slabs.

Brendan M. Laurs FGA

Reference

Koivula, J.I, Kammerling, R.C. & Fritsch, E. (eds) 1993. Gem News: Apatite from Brazil and Madagascar. *Gems & Gemology*, **29**(1), 53–54.

Aquamarine Crystal with 'Enhydro' Inclusion from Brazil

The most common hosts for large fluid inclusions with movable gas bubbles—known as 'enhydros'—are quartz crystals and agate/chalcedony. Enhydros have also been documented in other materials such as emerald, tanzanite and gypsum (Johnson & Koivula 1999 and references therein). Perhaps the first mention of such inclusions in beryl was documented by Kesler *et al.* (2013, p. 398):

> In the 13th century…Albertus Magnus, a German medieval scholar and Archbishop of Cologne, wrote a book on lapidary ('de mineralibus') with a note on fluid inclusions in beryl, that states 'Beryl is a shining and transparent gemstone of pale color. The most precious kind is the one, in which you see water moving when you turn him' (translation from German provided by Albert Gilg).

During the February 2020 Tucson gem shows, Steve Ulatowski (New Era Gems, Grass Valley, California, USA) showed this author a remarkable aquamarine crystal from Brazil with an elongate enhydro inclusion (Figure 4). The specimen consisted of a transparent pale bluish green hexagonal prism that was terminated on one end and broken on the other end. It measured approximately 89 × 17 mm, and along its centre was a channel oriented parallel to the *c*-axis that was about 56 mm long and 3 mm wide that contained a movable gas bubble. As the crystal was rotated perpendicular to its length away from a horizontal orientation, the bubble slowly travelled the length of the channel, much like the behaviour of the bubble in a builder's level. The channel started at a growth disturbance located about 31 mm from the broken end of the crystal and extended to within nearly 2 mm

Figure 4: This aquamarine crystal contains an elongate growth channel oriented parallel to the *c*-axis that has a movable gas bubble (here, positioned about halfway along its length). The crystal measures approximately 89 × 17 mm, and the growth channel is about 56 mm long and 3 mm wide. Photo by B. M. Laurs.

of its termination; the channel narrowed slightly along its length. A tiny dimple on the flat termination of the crystal was present adjacent to where the growth channel ended, perhaps manifesting a dislocation associated with the formation of the channel (Figure 5).

Elongate two-phase (liquid and gas) fluid inclusions oriented parallel to the *c*-axis are quite common in beryl from granitic pegmatites (e.g. Cameron *et al.* 1951). The formation of these inclusions in such beryl crystals was described in detail by Sunagawa and Urano (2000) and Sunagawa (2005), who attributed them to a growth-dissolution-regrowth process that was due to local fluctuations in the supply and composition of the late-stage pegmatitic fluids. When foreign mineral grains are trapped on the growing crystal as inclusions, tube-like fluid inclusions are formed behind the particles, and dislocations in the crystal are generated from where the inclusion is enclosed. The resulting tube-like two-phase inclusions and associated dislocations are formed in the direction of the *c*-axis, 'and spiral growth proceeds from the outcrop of these dislocations on the {0001} face' (Sunagawa 2005, p. 242).

In the present crystal, it is interesting to note that the growth channel hosting the fluid inclusion nearly intersected the termination, and had it not been sealed by the final stages of the crystal's growth, then the fluid

Figure 5: (**a**) The growth channel hosting the bubble ends within about 2 mm of the aquamarine crystal's termination. (**b**) In reflected light, a tiny dimple is visible as a dark spot on the flat termination of the crystal, and is located adjacent to where the growth channel ends. Photos by B. M. Laurs.

would have leaked out, leaving a hollow channel. It is rare for such large enhydros to be encountered in beryl, particularly with such a long distance along which the bubble can travel.

Brendan M. Laurs FGA

References

Cameron, E.N., Rowe, R.B. & Weis, P.L. 1953. Fluid inclusions in beryl and quartz from pegmatites of the Middletown District, Connecticut [part 2]. *American Mineralogist*, **38**(3–4), 218–262.

Johnson, M.L. & Koivula, J.I. (eds) 1999. Gem News: An "enhydro" emerald from Colombia. *Gems & Gemology*, **35**(1), 49.

Kesler, S.E., Bodnar, R.J. & Mernagh, T.P. 2013. Role of fluid and melt inclusion studies in geologic research. *Geofluids*, **13**(4), 398–404, https://doi.org/10.1111/gfl.12055.

Sunagawa, I. 2005. *Crystals: Growth, Morphology and Perfection*. Cambridge University Press, New York, New York, USA, 295 pp.

Sunagawa, I. & Urano, A. 2000. Beryl crystals from pegmatites: Morphology and mechanism of crystal growth. *Journal of Gemmology*, **26**(1), 521–533, https://doi.org/10.15506/jog.1999.26.8.521.

Catapleiite from Mont Saint-Hilaire, Québec, Canada

Catapleiite is a hydrated zirconosilicate (ideally $Na_2Zr[Si_3O_9] \cdot 2H_2O$) that forms a solid-solution series with calciocatapleiite ($CaZr[Si_3O_9] \cdot 2H_2O$) and is a dimorph of gaidonnayite. It is monoclinic (while calciocatapleiite and gaidonnayite are orthorhombic), but the crystals typically show a tabular to platy pseudo-hexagonal morphology. Individual crystals range from millimetre size up to 5 cm, and they often form rosettes that can attain maximum dimensions of 15 cm (Wight 1992, 2011). Catapleiite occurs in a wide range of colours: colourless to beige, or tan to pale grey, and rarely light yellow, pale orange, pink and pale blue (Wight 1992), but in gem quality it seems only to be colourless. Although found worldwide, the scarcity of facetable material makes it a rare collector's stone. The best and largest specimens of catapleiite were mined from Mont Saint-Hilaire, La Vallée-du-Richelieu, Montérégie, Québec, Canada, which has been famous for producing a variety of rare minerals since the 1960s (Pendlebury 1964; Wight 1992, 1996). The largest known faceted catapleiite weighs 2.48 ct (Wight 2011).

The 0.43 ct catapleiite gemstone described here (Figure 6) was reportedly mined at Mont Saint-Hilaire in 2012 or earlier, and was recently characterised by the author in order to add more gemmological data to the literature. It showed the following properties: colour—colourless (appearing silvery white); lustre—dull but somewhat pearly; diaphaneity—transparent; RI—1.591–1.629; birefringence—0.038; optic character—biaxial positive; hydrostatic SG—2.77; magnetism—no reaction to an N52 (neodymium) magnet; Chelsea Colour Filter reaction—none; and fluorescence—inert to long- and short-wave UV radiation. These data are consistent with those reported previously for catapleiite (Wight 1992, 1996; O'Donoghue 2006), and are distinct from the properties of calciocatapleiite and gaidonnayite.

Microscopic examination revealed irregular veils, partially healed fissures and unevenly distributed highly reflective growth channels (Figure 7a, b). Also observed were negative crystals and a few bubble-like inclusions that could correspond to the 'bubbles' mentioned by Pendlebury (1964). Observations were obstructed somewhat by apparent growth features. Strain-like patterns of interference colours were visible throughout the stone when viewed between crossed polarisers (Figure 7c), and it remained uniformly bright when rotated in the polariscope. According to Chen and Chao (1973), catapleiite crystals from Mont Saint-Hilaire are invariably polysynthetically twinned, which may explain these optical features.

A visible-near infrared (Vis-NIR) spectrum was collected from the stone but, as expected for most colourless gem materials, it did not show any absorption features.

Figure 6: This 0.43 ct catapleiite (6.3 × 4.3 × 2.8 mm) is from a locality that is famous for producing rare minerals: Mont Saint-Hilaire, Québec, Canada. Photo by T. Cathelineau.
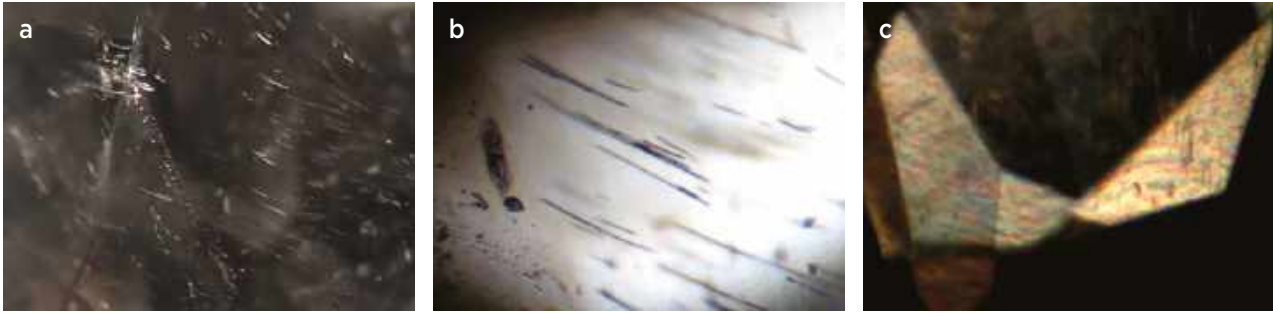
Figure 7: Microscopic examination of the catapleiite reveals (**a**) veils, partially healed fissures and unevenly distributed highly reflective growth channels; (**b**) growth channels; and (**c**) strain-like patterns of interference colours. Photomicrographs by T. Cathelineau, using (a) reflected light, (b) darkfield illumination and (c) crossed polarisers; image widths (a) 2 mm, (b) 0.6 mm and (c) 3 mm.

Infrared reflectance spectra were collected from several spots on the stone's table and pavilion facets, and all showed essentially the same pattern (Figure 8). The material's identification was confirmed by checking the pattern against the log(1/T) transformation of Russian and Norwegian catapleiite spectra (Chukanov 2014: samples TiSi69, TiSi149, TiSi208 and TiSi240). A spectrum for calciocatapleiite from Russia was slightly different (Chukanov 2014: sample TiSi76). The bands in the range of 1100–900 cm^{-1} are due to Si-O stretching vibrations and the band at 1650 cm^{-1} is attributed to non-degenerate H-O-H deformation vibrations (Aksenov *et al.* 2016).

The stone's photoluminescence (PL) spectra were collected using 254, 375 and 405 nm excitations to look for bluish white luminescence due to TiO_6 complexes (as mentioned by Gaft *et al.* 2015) and green luminescence due to UO_2^{2+} (http://fluomin.org/uk/fiche.php?id=278), but without success. For the 405 nm excitation, a very faint and broad asymmetric background from 400 to 700 nm (with a maximum at about 450 nm) was observed on which a narrow band, broadened at its base, was superimposed at 472 nm. This corresponded to the 3500 cm^{-1} Raman band (see RRUFF R060208 broad scan), which is associated with OH by analogy to IR bands (Aksenov *et al.* 2016).

Thierry Cathelineau
(thierry.cathelineau@spec4gem.info)
Paris, France
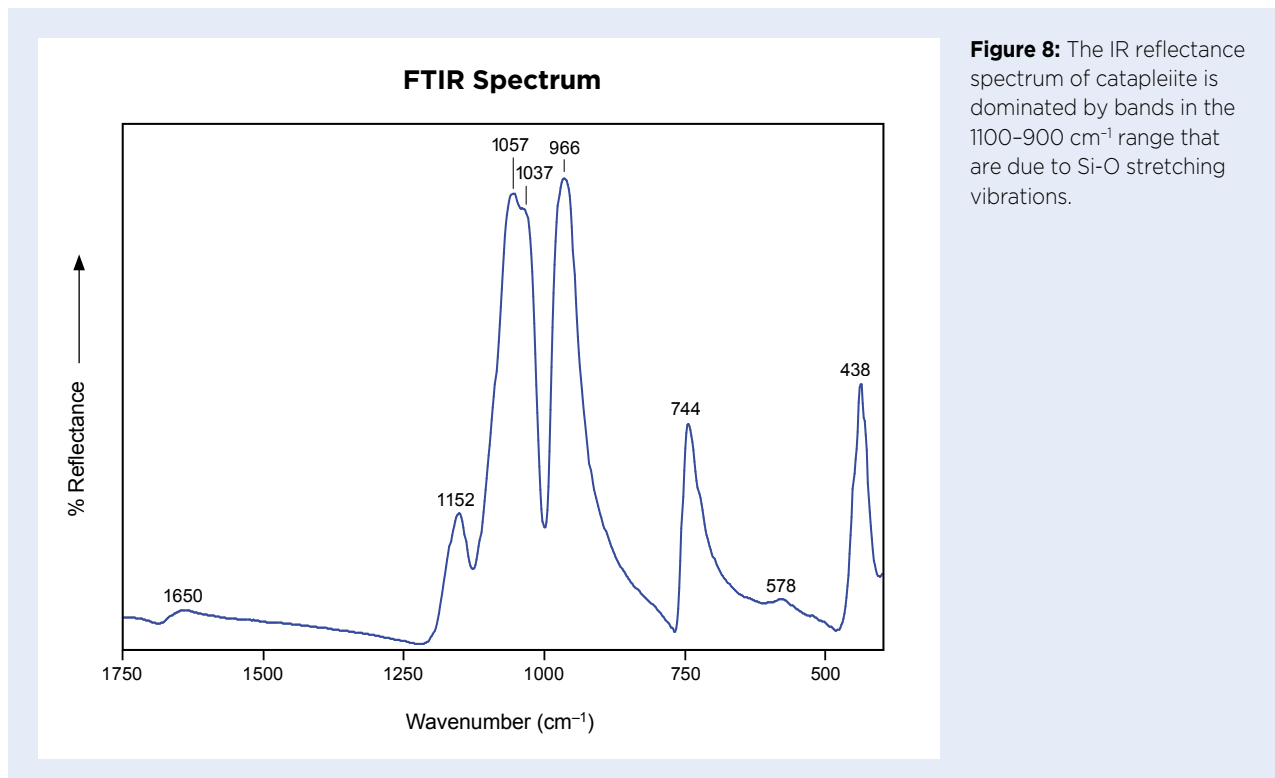
Figure 8: The IR reflectance spectrum of catapleiite is dominated by bands in the 1100–900 cm^{-1} range that are due to Si-O stretching vibrations.

FTIR Spectrum

References

Aksenov, S.M., Portnov, A.M., Chukanov, N.V., Rastsvetaeva, R.K., Nelyubina, Y.V., Kononkova, N.N. & Akimenko, M.I. 2016. Ordering of calcium and vacancies in calcium catapleiite CaZr[Si_3O_9] • $2H_2O$. *Crystallography Reports*, **61**(3), 376–382, https://doi.org/10.1134/s1063774516030020.

Chen, T.T. & Chao, G.Y. 1973. Twinning in catapleiite. *Geological Society of America Abstracts with Programs*, Dallas, Texas, USA, 573–574.

Chukanov, N.V. 2014. *Infrared Spectra of Mineral Species*. Springer, Dordrecht, Germany, 1,726 pp., https://doi.org/10.1007/978-94-007-7128-4.

Gaft, M., Reisfeld, R. & Panczer, G. 2015. *Modern Luminescence Spectroscopy of Minerals and Materials*, 2nd edn. Springer, Cham, Switzerland, 625 pp., https://doi.org/10.1007/978-3-319-24765-6.

O'Donoghue, M. (ed) 2006. *Gems*, 6th edn. Butterworth-Heinemann, Oxford, 873 pp.

Pendlebury, G.B. 1964. Catapleiite from St. Hilaire Mountain, Quebec. *Canadian Mineralogist*, **8**(1), 120–121.

Wight, W. 1992. Check-list for rare gemstones – Catapleiite. *Canadian Gemmologist*, **13**(2), 46–49.

Wight, W. 1996. The gems of Mont Saint-Hilaire, Quebec, Canada. *Journal of Gemmology*, **25**(1), 24–44, https://doi.org/10.15506/JoG.1996.25.1.24.

Wight, W. 2011. Rare gemstones from Mont Saint-Hilaire, Québec, Canada. *32nd International Gemmological Conference*, Interlaken, Switzerland, 13–17 July, 123–128.

Chrysocolla Chalcedony from the Democratic Republic of Congo

The Democratic Republic of Congo (DRC) hosts some important copper deposits, which occasionally produce rough material that is polished into gemstones (e.g. Zwaan 2015).

During the February 2020 Tucson gem shows, this author was informed about a new find of attractive chrysocolla chalcedony from DRC by Boukoubongui Tchagole (Idar-Oberstein, Germany). The material was found in November 2019 and only a few pieces were available. It showed bright greenish blue colouration and good transparency (Figure 9).

Gem silica from DRC was briefly mentioned by Currier (2002), and the pieces seen recently in Tucson demonstrate the potential for high-quality chrysocolla chalcedony to be produced from DRC in the future.

Brendan M. Laurs FGA

References

Currier, R.H. 2002. Into the heart of darkness: Searching for minerals in the Democratic Republic of the Congo. *Mineralogical Record*, **33**(6), 473–487.

Zwaan, J.C. 2015. Gem Notes: Stabilized shattuckite and bisbeeite from the Democratic Republic of Congo. *Journal of Gemmology*, **34**(8), 663–666.

Figure 9: These samples of chrysocolla chalcedony are from a new find in DRC. The sawn piece of rough weighs 311 g and the cabochon is about 19 ct. Photo by B. M. Laurs.

Pink Diaspore from Afghanistan

Gem-quality diaspore is known mainly from Muğla Province in Turkey, and typically appears near-colourless to brownish green in daylight and lavender to pinkish yellow/brown in incandescent light (e.g. Duroc-Danner 1987; Hatipoglu & Chamberlain 2011). Since July 2018, some fine crystal specimens of Turkish diaspore have been produced that displayed attractive purple colouration (Southwood 2020; Wilson & Moore 2020). Pink to purple diaspore is also known from Myanmar (Shen & Lu 2018) and from the Ural Mountains in Russia (Spiridonov *et al.* 2006), but neither locality has produced material of facetable size/quality.

In mid-March 2020, one of the authors (MHS) learned about a new find of gem-quality pink diaspore from Afghanistan. According to his Afghan supplier, the mining area is located in 'Kama Goshta' near Jalalabad, which apparently corresponds to the Kama and/or Goshta Districts in Nangarhar Province of eastern Afghanistan. Author MHS initially obtained a single piece of rough weighing 2 g and a faceted stone that recut to 23.36 ct. He also saw a 146 g parcel of rough material containing pieces ranging from about 1 to 10 g (approximately 2.5 g on average) that was suitable for cutting stones of 1–10 ct (Figure 10). In May 2020 he obtained a 70 g parcel of rough (0.6–12 g pieces), which he had faceted into 35 stones ranging from 0.50 to 10.91 ct (e.g. Figure 11a). The cutting yield was very low due to the presence of cleavage fractures in the rough material. In addition, he acquired a faceted stone that recut to 46.97 ct (Figure 11b). This is the largest gemstone he is aware of from

Figure 10: This parcel of rough pink diaspore is from a new find in Afghanistan. The stones range from about 1 to 10 g and the entire parcel weighs 146 g. Photo by M. H. Smith.

this deposit. Since that time, he has purchased several other gems weighing over 20 ct from the same supplier.

All the rough material seen by author MHS has been of similar colour, and the slight variations seen in the faceted stones were likely due to the various cutting orientations and the material's very strong pleochroism. The cut stones ranged from slightly brownish light pink to slightly brownish light purple. Viewed in different light sources there was no colour change, but a subtle colour shift was seen in which larger stones (>10 ct) appeared more pinkish in warm light and purplish pink in cool light. The following gemmological properties were collected by author MHS on two faceted stones weighing
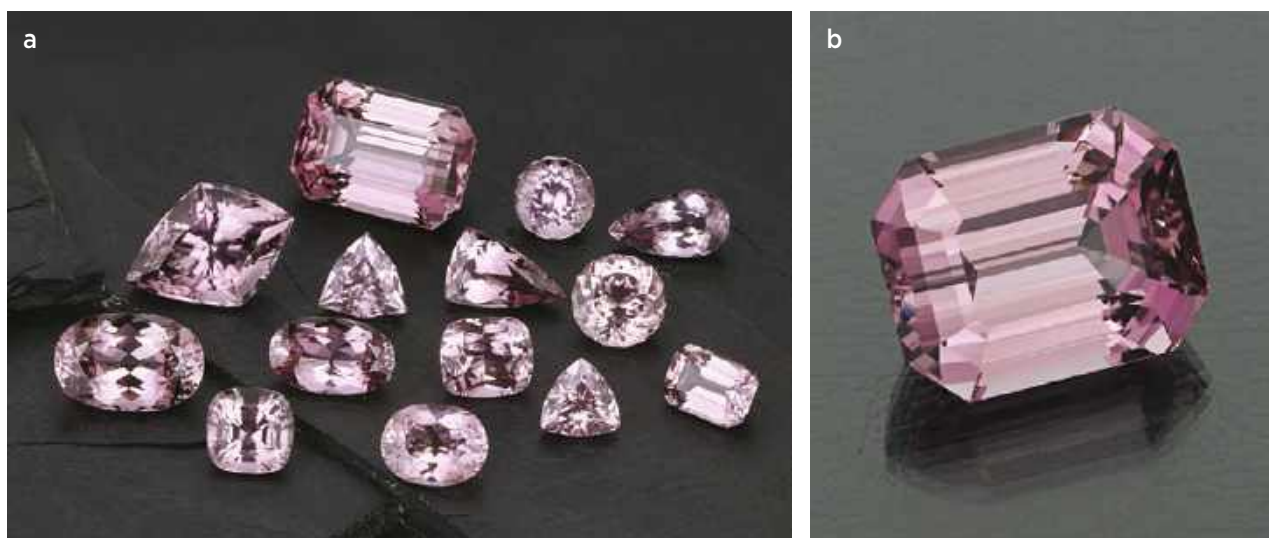
Figure 11: Pink Afghan diaspore has been faceted into attractive gemstones, and those shown here weigh (**a**) 2.05–23.36 ct and (**b**) 46.97 ct. The largest gem is now in the collection of Herb and Monika Obodda (Warwick, Rhode Island, USA). Photos by M. H. Smith.
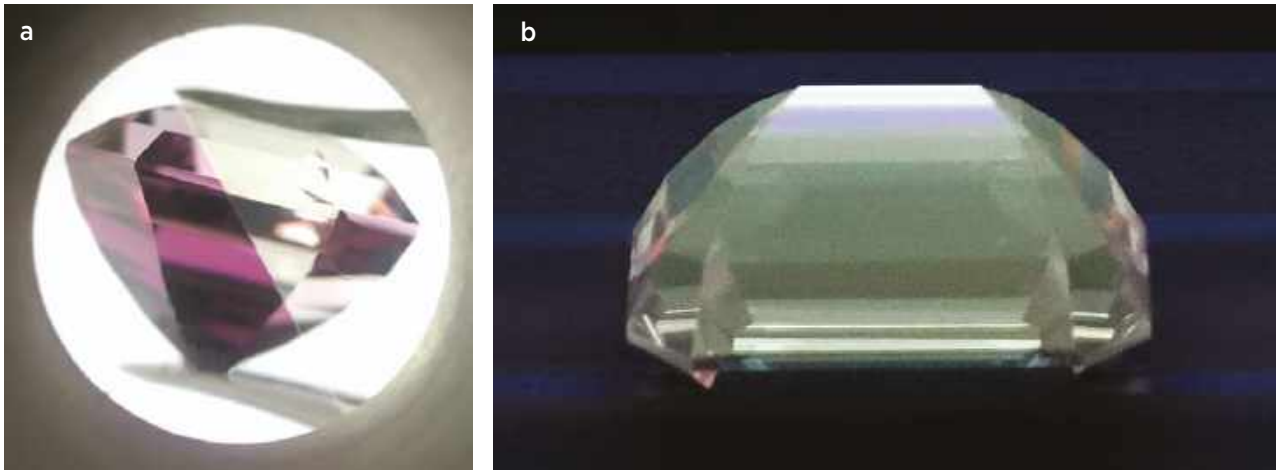
Figure 12: The Afghan diaspore shows (**a**) strong pleochroism and (**b**) weak chalky yellowish green fluorescence to short-wave UV radiation. Photos by M. H. Smith (a, 13.45 ct) and GIT (b, 23.36 ct).

13.45 and 23.36 ct: Pleochroism—very strong, in light yellow and dark purplish pink (Figure 12a); RI—n_α = 1.699–1.700, n_β = 1.720–1.721 and n_γ = 1.748–1.749; birefringence—0.049–0.050; optic character—generally B+; and hydrostatic SG—3.39–3.40.

The 23.36 ct stone was also examined at The Gem and Jewelry Institute of Thailand (GIT) in Bangkok, where the UV fluorescence was documented as inert to long-wave UV and weak chalky yellowish green under short-wave UV radiation (Figure 12b). In addition, the stone appeared reddish when viewed with the Chelsea Colour Filter.

Chemical analysis by energy-dispersive X-ray fluorescence (EDXRF) spectroscopy using an EDAX Eagle III instrument showed traces of Ti, Fe, Ga, V and Cr. Polarised ultraviolet-visible (UV-Vis) absorption spectra were collected with a PerkinElmer Lambda 1050 spectrophotometer in two polarisation directions (purplish pink and near-colourless; Figure 13), and showed features at 398 nm (Fe^{3+}), 450 nm (Fe^{3+}) and 480 nm, as well as broad bands centred at about 400 and 550 nm (V^{3+} and Cr^{3+}; cf. Shen & Lu 2018). A transmission window above about 650 nm is responsible for the overall purplish pink colour of the stone. The
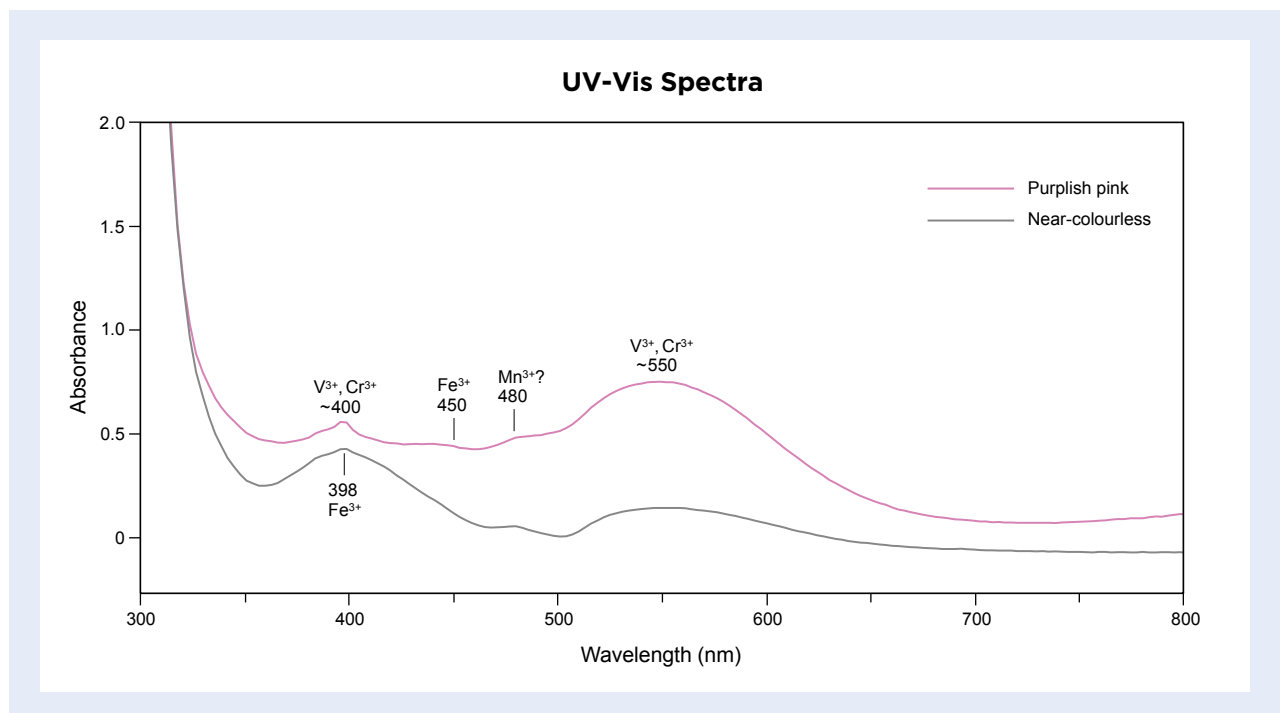
Figure 13: UV-Vis spectroscopy of the 23.36 ct diaspore reveals absorption features at about 398, 450 and 480 nm, as well as broad bands centred at about 400 and 550 nm. A transmission window above about 650 nm is responsible for the purplish pink colour of this diaspore. The path length of the beam was approximately 11 mm.

480 nm feature was not well defined in the spectra, but is probably related to Mn^{3+} (cf. GRR 73 at http://minerals.caltech.edu/FILES/Visible/diaspore/Index.html), which is a strong chromophore and could therefore influence the spectrum when present in very small amounts that are below the detection limit of EDXRF spectroscopy. The spectral features were more pronounced in the purplish pink direction, corresponding to the strong pleochroism, and indicate that the colouration of this pink diaspore is due to a combination of Fe^{3+}, V^{3+}, Cr^{3+} and probably Mn^{3+}.

The supplier of the Afghan diaspore indicated that there continues to be minor production of small- to medium-sized gems but that rough material suitable for cutting clean larger stones (20+ ct) is rare.

Mark H. Smith (mark@thailanka.com)
Thai Lanka Trading Ltd Part.
Bangkok, Thailand

Thanapong Lhuaamporn
GIT Gem Testing Laboratory
Bangkok, Thailand

Brendan M. Laurs FGA

References

Duroc-Danner, J.M. 1987. Diaspore, a rare faceted gem. *Journal of Gemmology*, **20**(6), 371–375, https://doi.org/10.15506/jog.1987.20.6.371.

Hatipoglu, M. & Chamberlain, S.C. 2011. A gem diaspore occurrence near Pinarcik, Mugla, Turkey, *Rocks & Minerals*, **86**(3), 242–249, https://doi.org/10.1080/00357529.2011.568304.

Shen, C. & Lu, R. 2018. The color origin of gem diaspore: Correlation to corundum. *Gems & Gemology*, **54**(4), 394–403, https://doi.org/10.5741/gems.54.2.394.

Southwood, M. 2020. Connoisseur's Choice: Diaspore, Muğla Province, Turkey. *Rocks & Minerals*, **95**(2), 145–153, https://doi.org/10.1080/00357529.2020.1689336.

Spiridonov, E.M., Alferova, M.S. & Fattykhov, T.G. 2006. Gem minerals from the Saranovskoye chromite deposit, western Urals. *Journal of Gemmology*, **30**(1–2), 91–102, https://doi.org/10.15506/jog.2006.30.1.91.

Wilson, W.E. & Moore, T.P. 2020. The diaspore mines near Pinarcik in the Ilbir Mountains, Muğla [*sic*] Province, Turkey. *Mineralogical Record*, **51**(4), 541–554.

Pink Fluorite from Inner Mongolia

The Huanggang mining complex is located approximately 30 km west of Linxi town, near the city of Chifeng in Inner Mongolia, China. This large Fe-Sn polymetallic ore deposit was discovered in 1959 and is exploited by several major mines (Lavinsky & Chen 2012; Mei *et al*. 2014).

During the February 2020 Tucson gem shows, Dr Robert Lavinsky (The Arkenstone, Richardson, Texas, USA) had pink fluorite from Huanggang mine no. 5 as mineral specimens and faceted stones (e.g. Figures 14 and 15). This is the first time that pink fluorite had been produced from this locality since an initial find in the latter part of 2010 that yielded translucent octahedral crystals up to 13 cm. At that time, many of the fluorites were broken off their matrix before the miners knew their value as mineral specimens. In addition, some of the fluorite was damaged by thermal shock due to temperature changes when they were taken out of the cold mines or even while being handled with bare hands (Lavinsky & Chen 2012).

Figure 14: This fluorite crystal cluster was recently produced from Huanggang mine no. 5 in Inner Mongolia. The specimen measures 10 cm across. Courtesy of The Arkenstone; photo by Beth Van Allen.
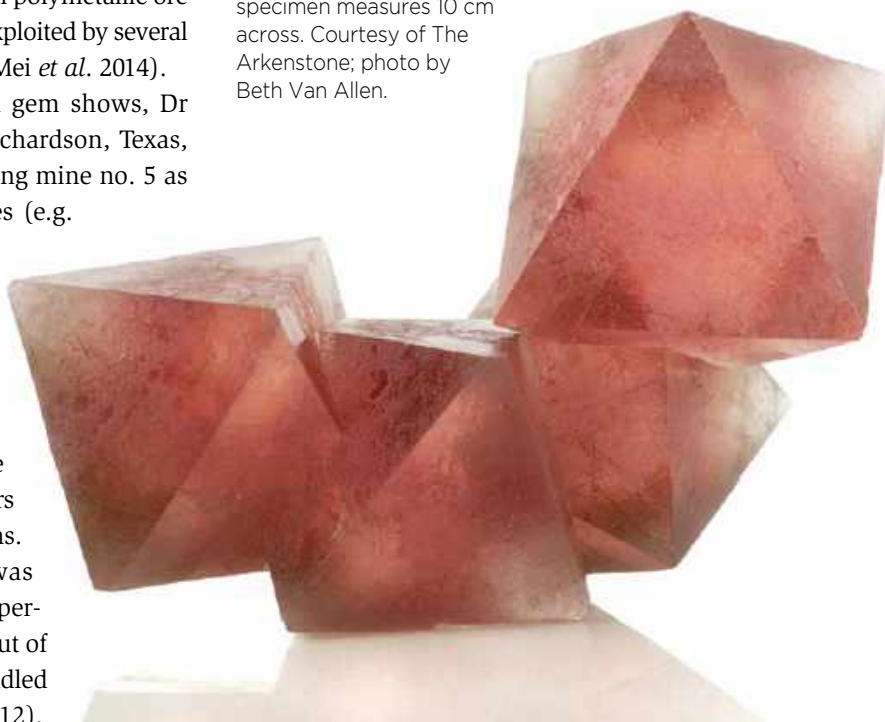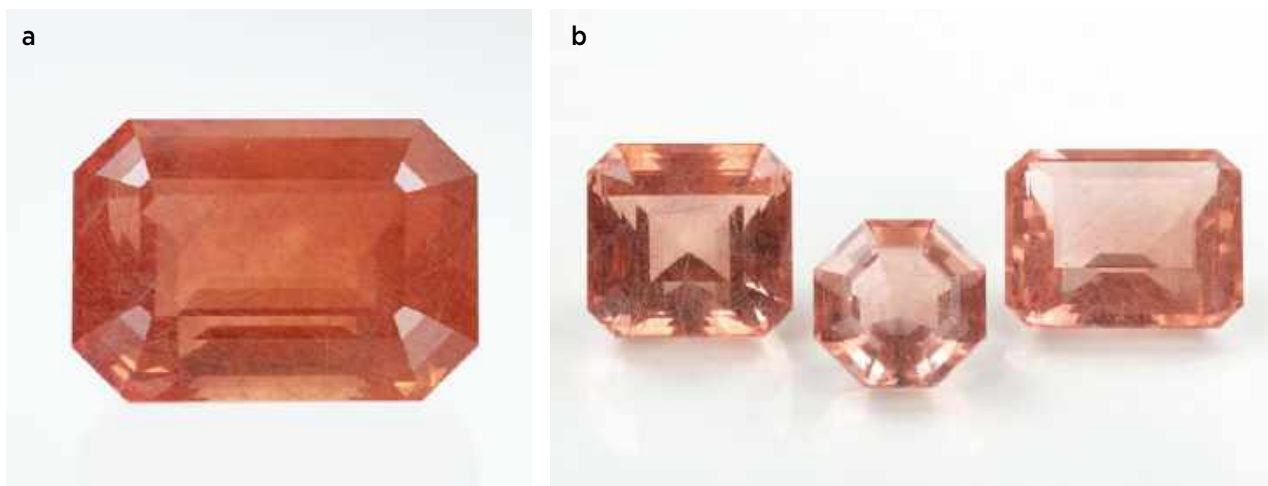
Figure 15: (**a**) Weighing approximately 271 ct, this is probably the largest fine gemstone that was cut from the fluorite produced recently in Inner Mongolia (now in the Robert Lavinsky collection). (**b**) These fluorites are representative of more typical sizes cut from this find, and from left to right they weigh approximately 55, 24 and 46 ct; courtesy of The Arkenstone, and now in the collections of Gail and Jim Spann (Rockwall, Texas, USA) and The Smithsonian Institution (Washington DC, USA). Photos by Beth Van Allen.

The Huanggang fluorite that Lavinsky displayed in Tucson came from a large pocket that was mined—this time more carefully—from the edge of a skarn on 26–29 August 2019. Thousands of loose single octahedral crystals were associated with aggregates of pale grey-green byssolite and byssolite-included quartz. Also recovered were some crystal clusters (again, see Figure 14) and a few dozen large fluorite crystals (up to 16 cm). About 100 good-quality matrix specimens were produced, and approximately 5 kg of gem rough were obtained (mostly from broken crystals).

A total of about 100–150 gemstones have been faceted in China from this fluorite. Good-quality stones can range up to about 270 ct, but most are in the 25–50 ct range (e.g. Figure 15). The larger cut stones typically appear orangey pink while the smaller ones show less of an orangey tinge. Nearly all of them contain long straight or curved needles of byssolite. The fluorite is inert to long- and short-wave UV radiation.

In addition to the fluorite described here, gem-quality colourless scheelite (Williams *et al.* 2014) and quartz containing interesting patterns of dark inclusions (Laurs

2016) have also been produced from the Huanggang mines. As mining continues, it seems likely that additional interesting gem and mineral discoveries will take place there in the future.

Brendan M. Laurs FGA

References

Laurs, B.M. 2016. Gem Notes: Quartz slabs from Inner Mongolia. *Journal of Gemmology*, **35**(1), 15–16.

Lavinsky, R. & Chen, X. 2012. Visiting the Huanggang mines. *Mineralogical Record*, **43**(5), 571–581.

Mei, W., Lü, X., Cao, X., Liu, Z., Zhao, Y., Ai, Z., Tang, R. & Abfaua, M.M. 2014. Ore genesis and hydrothermal evolution of the Huanggang skarn iron-tin polymetallic deposit, southern Great Xing'an Range: Evidence from fluid inclusions and isotope analyses. *Ore Geology Reviews*, **64**, 239–252, https://doi.org/10.1016/j.oregeorev.2014.07.015.

Williams, C., Williams, B. & Laurs, B.M. 2014. Gem Notes: Scheelite from Inner Mongolia. *Journal of Gemmology*, **34**(3), 202–203.

Natrolite from Java, Indonesia

Natrolite is a zeolite mineral that commonly forms radiating fibrous aggregates. It rarely occurs in facetable crystals, but creative gem cutters have polished the compact masses into cabochons to show their interesting radial textures (e.g. Laurs & Renfro 2017).

During the February 2020 Tucson gem shows, Joel Ivey (www.IndoAgate.com, Bangkok, Thailand) informed this author about natrolite cabochons from a new source in Indonesia—Nusa Kambangan Island, Cilacap Regency, Central Java. The natrolite-bearing area is located near

Figure 16: These cabochons of natrolite from Java, Indonesia, display radiating patterns. Photo by Yusef Sulaeman (Mineral and Art, Sukabumi, West Java, Indonesia).

a high-security prison, and Ivey's supplier indicated that the material is gathered by local villagers as well as prisoners. The mining is done with hand tools to a maximum depth of 3–5 m.

More than 2 tonnes of rough material have been sold to various cutting operations, and an additional 150 kg of rough has been stockpiled, in pieces up to approximately 80 mm. Several Indonesian workshops are cutting free-form cabochons (typically 15–40 mm) from this new material for sale through social media websites.

The identity of the Indonesian material as natrolite was confirmed by a report issued by a German gemmological laboratory. The cabochons are mottled white to pale pink or orangey pink, and take a good polish (Figure 16). Their colouration is different from the polished natrolite aggregates from Portugal that were documented by Laurs and Renfro (2017), which were mostly white with some yellow and black patterned staining.

Brendan M. Laurs FGA

Reference

Laurs, B.M. & Renfro, N.D. 2017. Gem Notes: Natrolite from Portugal. *Journal of Gemmology*, **35**(7), 578–579.

A Second Opal from Indonesia with an Insect Inclusion

In January 2019, media reports circulated about the discovery of a fossilised insect that was contained in opal rather than amber (e.g. Solly 2019). The specimen was subsequently described in the gemmological literature (Smith & Renfro 2019) and eventually studied in detail by Chauviré *et al.* (2020). The 5 mm insect was enclosed in mottled brown opal, showing local areas of play-of-colour, which came from the well-known opal deposits in West Java, Indonesia. Chauviré *et al.* (2020) identified the fossil as a probable exuvia (cast-off outer skin) of a cicada nymph, and indicated that it provides the first record of an animal fossil preserved in opal formed by weathering (although other instances have been documented in opal from hydrothermal settings).

During the February 2020 Tucson gem shows, Dr Robert Lavinsky showed this author another opal specimen that contained an entombed insect (Figure 17). The specimen was originally purchased on the resale jewellery market in Indonesia in December 2019 and reportedly came from the same mining area as the other insect-bearing opal specimen mentioned above. The piece measured 40.9 × 14.1 × 11.3 mm and weighed 23.05 ct, and consisted of white translucent to colourless transparent opal displaying small areas of play-of-colour. Dr Lavinsky was told by entomological experts that the insect was a bee. The lack of visible wings suggests to the present author that it could be the pupa of a solitary bee species (cf. www.livescience.com/44724-leafcutter-bee-fossils-la-brea.html).

A brief description of the specimen can be found on an auction website (https://fineart.ha.com/itm/nature-and-science/fossilized-bee-in-jelly-opal-pliocene-miocene-genteng-formation-java-indonesiaandlt-/p/5434-12001.s?ic4), which postulates that the bee could have been entrapped in amber that was then converted to opal over time. However, this scenario seems unlikely according to the very recent age of opal formation in the Javanese deposits (i.e. Late Pliocene through Holocene; Ansori 2010). Rather, the model proposed by Chauviré *et al.* (2020) appears equally applicable to the present specimen, in which the ground-dwelling insect was surrounded by silica-rich fluids, which subsequently turned into a gel and finally into opal.

Indonesia's play-of-colour opal deposits are situated in the Lebak Regency of Banten Province in West Java, where they are hosted by the Genteng Formation, which

Figure 17: This opal specimen (40.9 × 14.1 × 11.3 mm) contains what appears to be a fossilised bee. Courtesy of The Arkenstone; photo by Arjuna Irsutti.

consists of a layered volcanic series of pumice tuff, tuffaceous sandstone and claystone that has been weathered into a paleosol (Einfalt 2007; Tay *et al*. 2009; Ansori 2010). Opal formed from fluids circulating through porous volcanoclastic rocks (particularly pumiceous volcanic glass) during the weathering process. Opal mineralisation took place where the circulating silica-rich fluids were trapped by less permeable clay-rich layers, particularly in cavities that may have originated from the degradation of plant remains (Ansori 2010). According to geologist Joel Ivey (www.IndoAgate.com, Bangkok, Thailand), the opal mining area in Banten Province is also known to produce opalised snail shells, limb casts and logs. In some other West Java locations, the fossilised wood is associated with copper-bearing blue opal (Laurs 2018) and also pink opal.

Brendan M. Laurs FGA

References

Ansori, C. 2010. Model mineralisasi pembentukan opal Banten [Mineralisation model of Banten opal formation]. *Jurnal Geologi Indonesia*, **5**(3), 151–170, https://doi.org/10.17014/ijog.v5i3.100 (in Indonesian with English abstract).

Chauviré, B., Houadria, M., Donini, A., Berger, B.T., Rondeau, B., Kritsky, G. & Lhuissier, P. 2020. Arthropod entombment in weathering-formed opal: New horizons for recording life in rocks. *Scientific Reports*, **10**, article 10575 (9 pp.), https://doi.org/10.1038/s41598-020-67412-9.

Einfalt, H.C. 2007. Some observations on the composition and origin of opals from Java. *Journal of Gemmology*, **30**(7), 383–398, https://doi.org/10.15506/jog.2007.30.7.383.

Laurs, B.M. 2018. Gem Notes: Copper-bearing opal from West Java, Indonesia. *Journal of Gemmology*, **36**(1), 10–11.

Smith, T. & Renfro, N. 2019. *G&G* Micro-World: Fossil insect in opal. *Gems & Gemology*, **55**(1), 113–114.

Solly, M. 2019. Gemologist finds insect entombed in opal rather than amber. *Smithsonian Magazine*, www.smithsonianmag.com/smart-news/gemologist-identifies-insect-entombed-opal-rather-amber-180971336, 24 January, accessed 14 August 2020.

Tay T.S., Mok P.S., Liew S.P., Paramita, M., Arps, C.E.S., Atichat W., Fritsch, E., Kang W.W. & Wijaya, K. 2009. Precious opal from Java: Gemmological properties, micro- and nano-structures. *Australian Gemmologist*, **23**, 513–528.

Bicoloured Phenakite from Russia

Phenakite is a beryllium silicate (Be_2SiO_4) with a Mohs hardness of 7½–8 that is not commonly encountered as a gemstone. An important source of gem-quality material is the well-known emerald mining area at Malyshevo in the central Ural Mountains of Russia, where phenakite crystals up to 13 cm in dimension occur in schist associated with beryl and chrysoberyl/alexandrite (Cook 2009).

Phenakite from Malyshevo is generally colourless or yellow-brown. In March 2020, gem dealer Dudley Blauwet (Dudley Blauwet Gems, Louisville, Colorado, USA) received a large parcel of mostly colourless Malyshevo phenakite that his supplier had cut from rough material which was recovered by local people searching the old mine tailings for alexandrite. Surprisingly, one of the stones (weighing 14.77 ct) was distinctly bicoloured in

Figure 18: This phenakite from Malyshevo, Russia, is distinctly bicoloured. The stone weighs 14.77 ct and measures 17.1 × 12.5 mm. Photo by Aria Agarwal/Dudley Blauwet Gems.

colourless and yellow-brown (Figure 18). In Blauwet's experience, only about 5% of the Russian phenakite shows the yellow-brown colouration, and this is the first time he had encountered a distinctly bicoloured stone after dealing in about 1,000 carats of faceted stones.

The bleaching of phenakite's colour upon exposure to UV radiation or high temperature indicates that it is associated with electron-hole centres, and Nikolaev *et al.* (2018) attributed the yellow-brown colouration to the paramagnetic complex $[PO_4]^{4-}$. This centre induces yellow-brown colouration in phenakite due to its strong absorption in the UV region of the spectrum, which gradually decreases through the visible range. In the phenakite described here, the $[PO_4]^{4-}$ radical was evidently present in sufficient amounts to cause yellow-brown colour in only half of the stone.

Brendan M. Laurs FGA

References

Cook, R.B. 2009. Connoisseur's Choice: Phenakite, Mount Antero, Chaffee County, Colorado. *Rocks & Minerals*, **84**(4), 338–344, https://doi.org/10.3200/RMIN.84.4.338-344.

Nikolaev, A.G., Nizamutdinov, N.M. & Popov, M.P. 2018. Gem News International: Color origin of phenakites from the Ural emerald mines. *Gems & Gemology*, **54**(1), 101–102.

Rhodonite from Southern Iran

Rhodonite is a calcium-manganese silicate ($CaMn_3Mn[Si_5O_{15}]$) that is found in metamorphosed manganese ore deposits and some hydrothermal ore veins (Bauer 1990). In most of Iran's Mn mines (e.g. south of Mashhad and in northern Kurdistan), rhodonite can be found in small quantities associated with other Mn-bearing minerals. However, until now there has been no report of gem-quality rhodonite occurring in significant quantities. In the summer of 2016, a vein of rhodonite was found associated with the Mn ore occurrence in the Fannuj (or Fanoj) ophiolite complex in southern Iran, and here we describe the occurrence and properties of this material.

An ophiolite is a remnant of oceanic lithosphere that has been tectonically emplaced onto continental margins during plate tectonic movements. The Fannuj ophiolite complex contains various ultramafic and mafic rocks, sometimes with thin radiolarite units (Sepidbar *et al.* 2020). The Mn ore typically occurs in the sedimentary sequence adjacent to the radiolarite units in the upper levels of the ophiolite, and is accompanied by rhodonite veins. These veins are often thin (less than 20 cm wide) and may attain lengths up to 10 m. Most of the rhodonite has been eroded and is collected from nearby secondary deposits. Pieces of rhodonite weighing up to 50 kg have been found.

The gem potential of most of the rhodonite appears rather low, and slicing it is helpful for evaluating its colour quality and ability to take a good polish (Figure 19). So far 200 kg of the rhodonite have been processed

Figure 19: This rhodonite from southern Iran has been sliced into two pieces (5 × 12 cm each) to reveal the quality of the material. Photo by B. Rahinzadeh.

Figure 20: Iranian rhodonite has been fashioned into cabochons of various shapes (here, 1.2–3.0 cm wide). Photo by Behnam Zaheri.

Figure 21: This pendant features a 25 ct pear-shaped Iranian rhodonite cabochon that is surrounded by enamel designs. Photo by Farid Forqani.

into several hundred carvings and polished stones (e.g. Figure 20). Some of the rhodonite is being incorporated into various Iranian crafts, together with precious metals, tapestry or enamel (e.g. Figure 21).

The gemmological properties of six polished samples of the rhodonite were obtained at the Gemmological Centre of Shahid Beheshti University. The stones ranged from 1.2 × 1.5 cm to 2.5 × 3.2 cm, and were mostly pink with some yellow-pink and yellow areas, as well as conspicuous black veining. Their RI values ranged
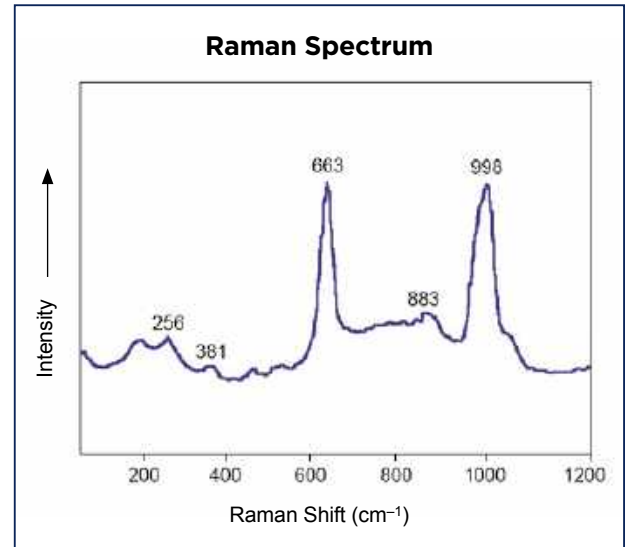
Figure 22: The Raman spectrum of a typical rhodonite sample from southern Iran reveals features that resemble those of rhodonite from other localities.

from 1.733 to 1.734, which are comparable to those of rhodonite from Val Malenco, Italy (RI = 1.73; Diella *et al.* 2014). The hydrostatic SG ranged from 3.4 to 3.7. Raman spectroscopy showed peaks at 256, 381, 663, 883 and 998 cm^{-1} (Figure 22), which resemble those seen in rhodonite reference spectra and in material from Val Malenco (Diella *et al.* 2014).

The carving and polishing done so far on the rhodonite from southern Iran shows that it has good potential for use as gemstones and *objets d'art*.

Bahman Rahinzadeh and Parisa Hadipanah
(b_rahimzadeh@sbu.ac.ir)
Gemmological Centre and Department of
Mineral Resources & Groundwater
School of Earth Sciences
Shahid Beheshti University
Tehran, Iran

Note: The correct spelling is Rahimzadeh.

References

Bauer, J. 1990. *Minerals, Rocks and Precious Stones*. Aventinum Publishing House, Prague, Czechoslovakia, 207 pp.

Diella, V., Adamo, I. & Bocchio, R. 2014. Gem-quality rhodonite from Val Malenco (central Alps, Italy). *Periodico di Mineralogia*, **83**(2), 207–221, https://doi.org/10.2451/2014PM0012.

Sepidbar, F., Lucci, F., Biabangard, H., Khedr, M.Z. & Jiantang, P. 2020. Geochemistry and tectonic significance of the Fannuj-Maskutan SSZ-type ophiolite (Inner Makran, SE Iran). *International Geology Review*, published online 27 April, 28 pp., https://doi.org/10.1080/00206814.2020.1753118.

Origin of Asterism in a Rare Four-Rayed Star Spessartine

Figure 23: This 37.78 ct spessartine cabochon displays a four-rayed star. Photo by M. P. Steinbach.

While attending the February 2008 Tucson gem shows, one of the authors (MPS) used a penlight to search through several thousand carats of spessartine cabochons from a new find at Loliondo, Tanzania, and was fortunate to discover one stone that showed a four-rayed star (Figure 23). The garnet was later documented in the author's book (Steinbach 2016, p. 537), and here we investigate the origin of its unusual asterism.

The oval cabochon weighed 37.78 ct and measured approximately 22 × 16 × 11 mm. Its body colour was orange, as is typical of spessartine. It displayed a weak four-rayed star showing acute and obtuse angles similar to those encountered in four-rayed star garnets of the pyrope-almandine series (e.g. Guinel & Norton 2006). The angles between the two branches of the star were approximately 70° and 110°, corresponding to two-fold

axes. Walcott (1937, p. 41, figure 20) demonstrated that such a garnet should display multiple symmetrically equivalent four-rayed stars. Indeed, four additional very weak stars could barely be observed along the rim of the cabochon, and one of them was distinct enough to show, as expected, a four-rayed star with the same angular characteristics. The weakness of all these stars corresponded to the low density of linear features present in the stone.

The gem was translucent rather than transparent, due to the presence of intersecting partially healed fractures and 'fingerprints', as depicted in Figure 24a. The fingerprints consisted of two-phase (liquid-gas) inclusions that displayed various shapes (Figure 24b); such secondary fluid inclusions are commonly encountered in spessartine (cf. Knox & Laurs 2001, p. 288; Gübelin & Koivula 2005, pp. 448–451). In the present stone, some of these fluid inclusions were elongated and parallel to one another (Figure 24b, top centre)—apparently being oriented according to the host crystal—and they contributed somewhat to the asterism.

Photomicrography of other inclusions was challenging, but we observed lamellar features in parallelogram shapes. Numerous bundles of such cavities were present throughout the gem (Figure 25a). They were quite reminiscent of the hopper growth exhibited by spessartine crystals (e.g. Gübelin & Koivula 2005, p. 448). Those with a high length:width ratio (i.e. similar to acicular inclusions; Figure 25b) clearly contributed to the asterism. Raman spectroscopy and optical microscopy revealed that these lamellar-like inclusions
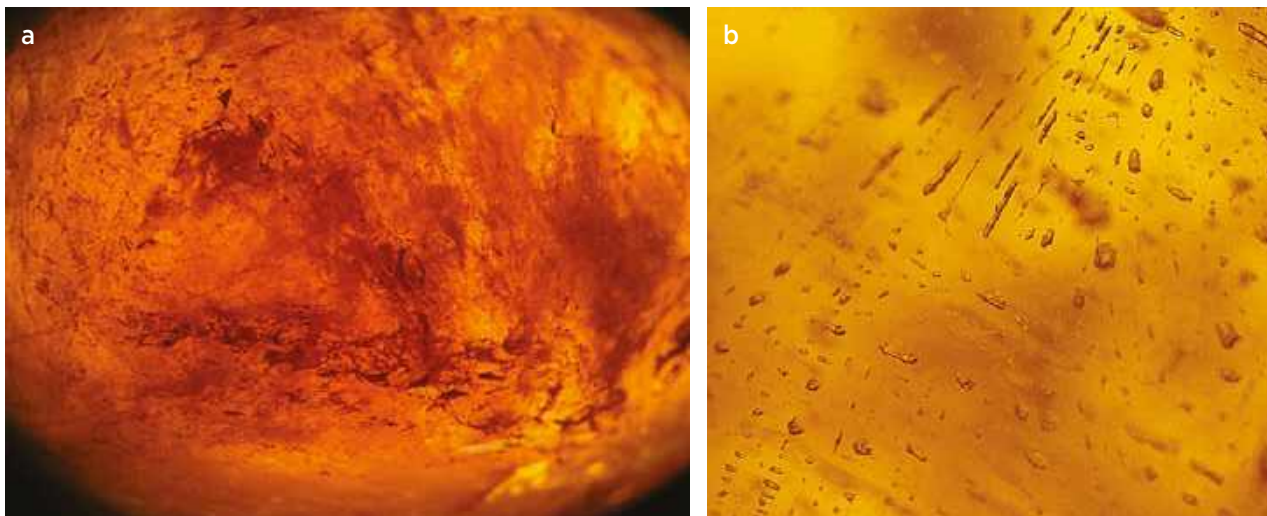
Figure 24: (a) Numerous partially healed fractures and 'fingerprints' cause the star spessartine to appear translucent. (b) The fingerprints consist of two-phase (liquid-gas) inclusions of various shapes. Photomicrographs by J.-P. Gauthier in transmitted light; field of view (a) 16 × 12 mm and (b) 0.9 × 1.0 mm.
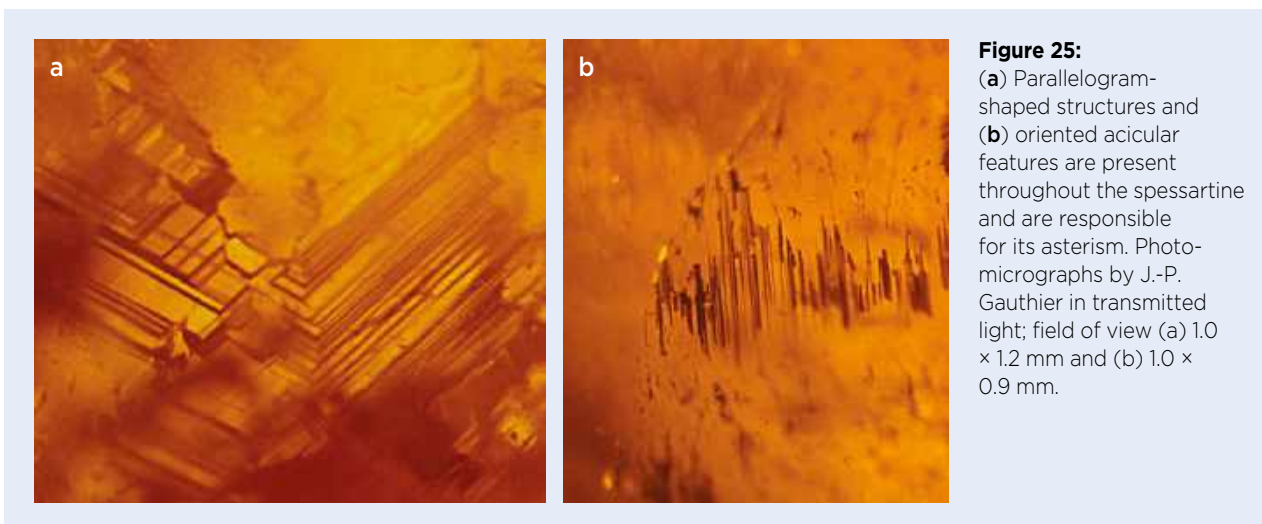
Figure 25: (**a**) Parallelogram-shaped structures and (**b**) oriented acicular features are present throughout the spessartine and are responsible for its asterism. Photomicrographs by J.-P. Gauthier in transmitted light; field of view (a) 1.0 × 1.2 mm and (b) 1.0 × 0.9 mm.

were thin fluid films. Similar flat fluid inclusions—less geometrical but characterised by 70° and 110° complementary angles—have been reported previously in spessartine from the USA (Knox & Laurs 2001, p. 288). Their submicron thickness is indicated by the presence of interference colours, as seen in the centre of Figure 26. It is likely that the asterism that was barely visible along other crystallographic directions at the rim of the cabochon was produced by light reflecting from different sides of the parallel arrays of these parallelograms. The transparency of these films is in agreement with the orangey appearance of the star, which owes its colour to the garnet matrix rather than to solid acicular inclusions. It also accounts for the weakness of the star, in contrast to the strong, sharp stars in garnets of the pyrope-almandine series that are caused by solid inclusions.

The present cabochon is possibly the only *four*-rayed star spessartine reported so far. Author MPS first encountered star spessartine shortly after the millennium, but that stone (which was from Sri Lanka) displayed a six-rayed star (Steinbach 2016, pp. 538–539).

Thanh Nhan Bui (tnhan93@gmail.com)
Université catholique de Louvain
Louvain-la-Neuve, Belgium

Aurélien Delaunay and Ugo Hennebois
Laboratoire Français de Gemmologie
Paris, France

Martin P. Steinbach
Steinbach – Gems with a Star
Idar-Oberstein, Germany

Prof. Jean-Pierre Gauthier
Centre de Recherches Gemmologiques
Nantes, France
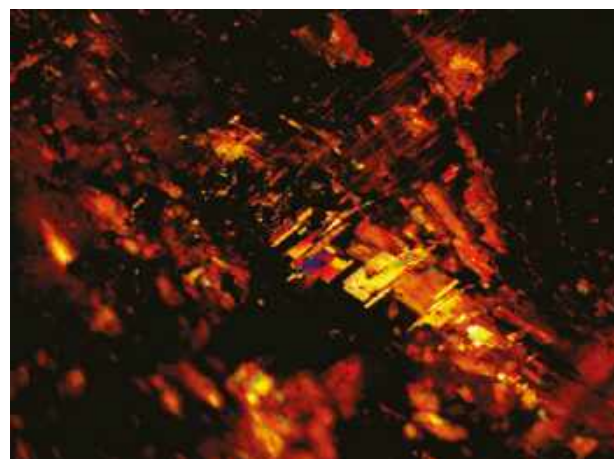
Figure 26: Parallelogram-shaped thin-film fluid inclusions in the spessartine show interference colours due to their submicron thickness. Photomicrograph by A. Delaunay in darkfield illumination; field of view 1.80 × 1.35 mm.

References

Gübelin, E.J. & Koivula, J.I. 2005. *Photoatlas of Inclusions in Gemstones*, Vol. 2. Opinio Publishers, Basel, Switzerland, 829 pp.

Guinel, M.J.F. & Norton, M.G. 2006. The origin of asterism in almandine-pyrope garnets from Idaho. *Journal of Materials Science*, **41**(3), 719–725, https://doi.org/10.1007/s10853-006-6500-4.

Knox, K. & Laurs, B.M. 2001. Spessartine garnet from Ramona, San Diego County, California. *Gems & Gemology*, **37**(4), 278–295, https://doi.org/10.5741/gems.37.4.278.

Steinbach, M.P. 2016. *Asterism – Gems with a Star*. MPS Publishing and Media, Idar-Oberstein, Germany, 896 pp.

Walcott, A.J. 1937. Asterism in garnet, spinel, quartz, and sapphire. *Geological Series of Field Museum of Natural History*, **7**(3), 39–57, https://archive.org/details/asterismingarnet73walc/page/n5/mode/2up.

A Rare Bicoloured Spinel

Recently, the GIT Gem Testing Laboratory (GIT-GTL) received for identification a bicoloured purple and greenish blue stone that weighed 0.57 ct and measured 7.02 × 3.32 × 2.27 mm (Figure 27). The stone was singly refractive with an RI of 1.718 and a hydrostatic SG value of 3.60. Observation with a gemmological microscope revealed oriented arrays of slender, short to elongate iridescent silk inclusions and minute particles in the purple colour zone (Figure 28), but no inclusions in the greenish blue portion. It was inert to both long- and short-wave UV radiation. The stone's RI and SG values, as well as its inclusion features, are typical for natural spinel.

UV-Vis-NIR spectroscopy, recorded with a Perkin-Elmer Lambda 950 spectrophotometer in the range of 300–1500 nm, showed absorption features at 371, 386, 458 and 555 nm for the purple zone, while the greenish blue portion displayed the same characteristics along with additional broad bands at 656 and 917 nm (Figure 29). These features were assigned by D'Ippolito *et al.* (2015) to Fe^{2+}, Fe^{3+} and Fe^{2+}-Fe^{3+} intervalence charge transfer (IVCT). In the spectrum of the purple zone, the absorptions at 371, 386 and 555 nm (all due to Fe^{2+}) create a transmission window in the blue-violet region which, combined with decreasing absorption in the red region, give rise to the purple colouration. The spectrum of the other colour zone, by contrast, shows stronger Fe^{2+} absorption at 371 and 386 nm, and the presence of a broad band at around 656 nm (due to Fe^{2+}-Fe^{3+} IVCT) combines to create a transmission window in the blue-green region, thus giving rise to the greenish blue colouration. We therefore infer that the greenish blue zone contains somewhat more Fe^{2+} and Fe^{3+} than the purple area, in agreement with a

Figure 27: This 0.57 ct bicoloured purple and greenish blue stone was identified as spinel. Photo by A. Buathong.

relatively higher total iron content in that portion of the sample (see below).

PL spectroscopy of both the purple and greenish blue zones of the spinel, measured by a Renishaw inVia Raman microspectrometer using 532 nm laser excitation at room temperature, showed a series of emission centres at 671, 673, 675, 685, 686, 695, 697, 699, 704, 706, 708, 718 and 722 nm (Figure 30). This emission series perfectly matched the reference PL spectrum for spinel in the RRUFF database, and is known to be due to Cr^{3+} substituting for Al^{3+} in the octahedral site (e.g. Gaft *et al.* 2005; Skvortsova *et al.* 2011). Furthermore, the rather sharp peaks associated with the Cr-related emission centres in the PL spectra also indicate this stone has not been subjected to heat treatment (Saeseaw *et al.* 2009; Smith 2012).

Semi-quantitative chemical analysis of the stone's purple and greenish blue zones by EDXRF spectroscopy (using an Eagle III instrument) revealed the expected major amounts of Mg and Al, along with minor Fe, Si and Zn, and traces of V, Cr and Ga (Table I). Overall, the chemical data, when normalised to 100 wt.%, are
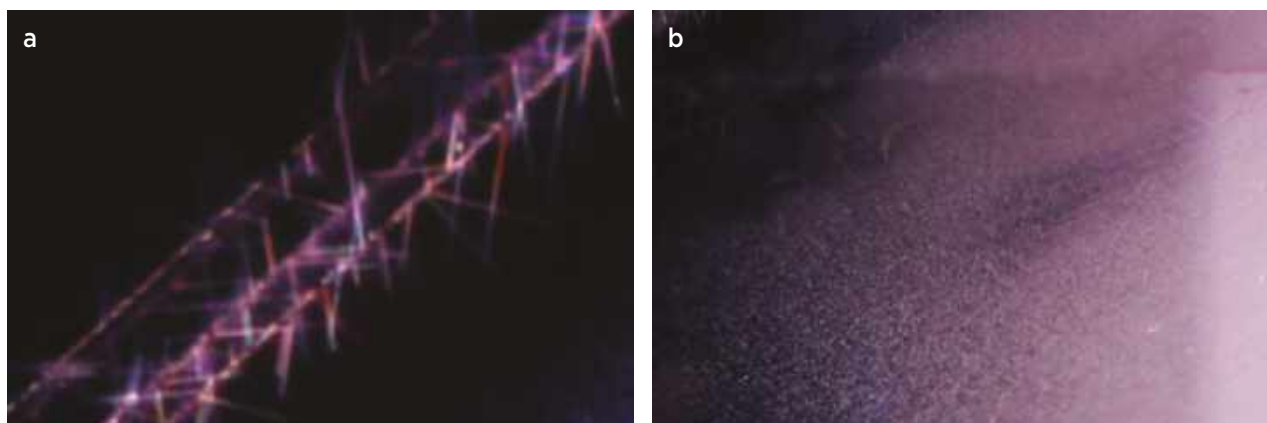
Figure 28: (**a**) Networks of iridescent silk and (**b**) minute particles were observed in the purple zone of the bicoloured spinel. Photomicrographs by A. Buathong; image widths 1.3 mm.
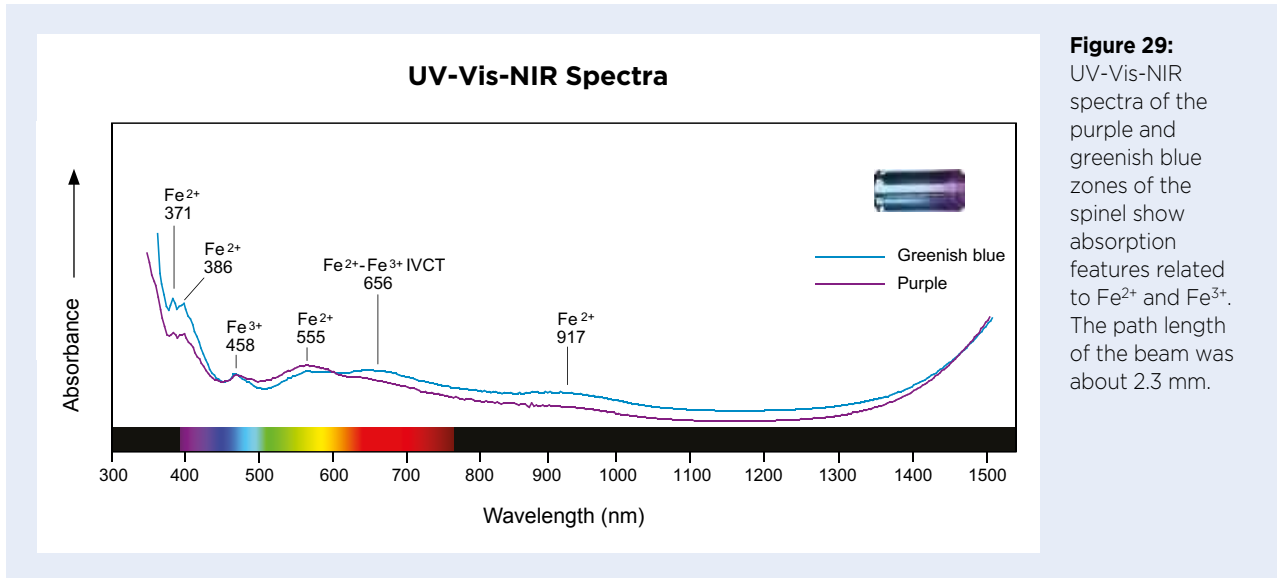
UV-Vis-NIR Spectra

Figure 29: UV-Vis-NIR spectra of the purple and greenish blue zones of the spinel show absorption features related to Fe^{2+} and Fe^{3+}. The path length of the beam was about 2.3 mm.
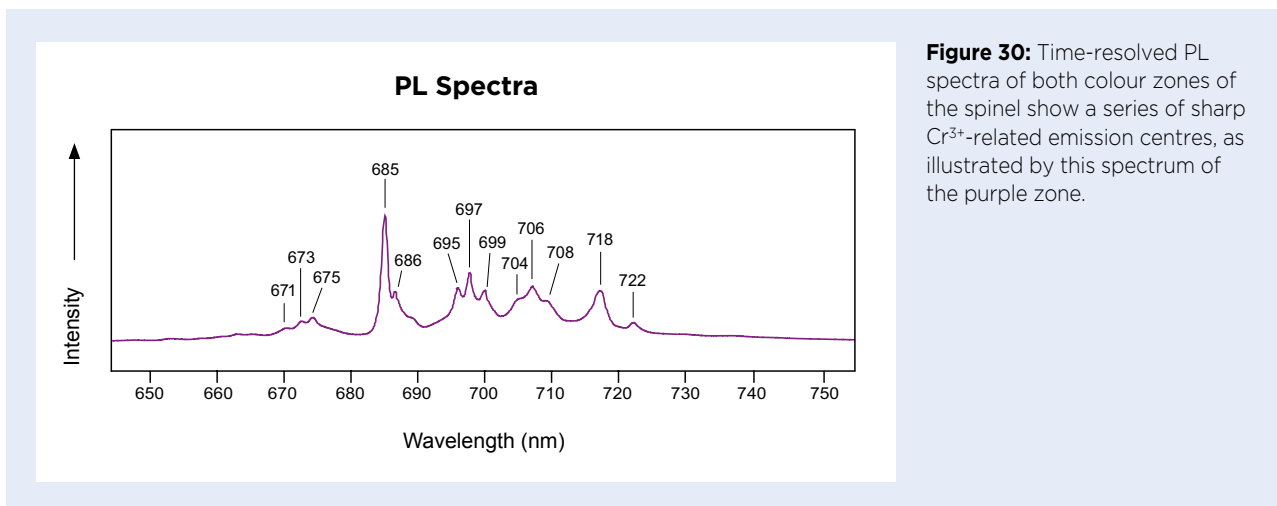
PL Spectra

Figure 30: Time-resolved PL spectra of both colour zones of the spinel show a series of sharp Cr^{3+}-related emission centres, as illustrated by this spectrum of the purple zone.

Table I: Minor- and trace-element composition of the bicoloured spinel by EDXRF spectroscopy.

Oxides (wt.%)	Purple zone	Greenish blue zone
SiO_2	1.64	1.33
V_2O_5	0.05	0.06
Cr_2O_3	0.03	0.03
Fe_2O_3 (total)	2.56	2.77
ZnO	1.01	0.69
Ga_2O_3	0.04	0.06

consistent with the spinel composition ($MgAl_2O_4$)—wherein minor Zn^{2+} and, probably, Fe^{2+} substitute for Mg^{2+} in the tetrahedral sites and traces of Fe^{3+}, Si^{4+}, Cr^{3+}, V^{3+} and Ga^{3+} replace Al^{3+} in the octahedral sites.

The chemical composition of this stone, with significant Zn content (Muhlmeister *et al.* 1993) and the series of sharp Cr-related emission features in the PL spectra, indicates that it is a natural, unheated spinel. Even though spinel has commonly been found in a rather wide colour range—including colourless, red, blue, violet, green, brown, pink and black—bicoloured specimens such as this stone are very scarce (cf. DuToit 2012).

Apitchaya Buathong and
Nalin Narudeesombat (nnalin@git.or.th)
GIT Gem Testing Laboratory
Bangkok, Thailand

References

D'Ippolito, V., Andreozzi, G.B., Hålenius, U., Skogby, H., Hametner, K. & Günther, D. 2015. Color mechanisms in spinel: Cobalt and iron interplay for the blue color. *Physics and Chemistry of Minerals*, **42**(6), 431–439, https://doi.org/10.1007/s00269-015-0734-0.

DuToit, G. 2012. Lab Notes: Bicolored spinel. *Gems & Gemology*, **48**(4), 304.

Gaft, M., Reisfeld, R. & Panczer, G. 2005. *Luminescence Spectroscopy of Minerals and Materials*. Springer-Verlag, Berlin, Germany, 356 pp.

Muhlmeister, S., Koivula, J.I., Kammerling, R.C., Smith, C.P., Fritsch, E. & Shigley, J.E. 1993. Flux-grown synthetic red and blue spinels from Russia. *Gems & Gemology*, **29**(2), 81–98, https://doi.org/10.5741/gems.29.2.81.

Saeseaw, S., Wang, W., Scarratt, K., Emmett, J.L. & Douthit, T.R. 2009. Distinguishing heated spinels from unheated natural spinels and from synthetic spinels. Gemological Institute of America, www.gia.edu/doc/distinguishing-heated-spinels-from-unheated-natural-spinels.pdf, 13 pp., 2 April, accessed 7 July 2020.

Skvortsova, V., Mironova-Ulmane, N. & Riekstiņa, D. 2011. Structure and phase changes in natural and synthetic magnesium aluminum spinel. *Environment. Technology. Resources. Proceedings of the 8th International Scientific and Practical Conference*, **2**, 100–106, https://doi.org/10.17770/etr2011vol2.1002.

Smith, C.P. 2012. Spinel and its treatments: A current status report. *InColor*, No. 19, 50–54.

Purple Tourmaline from Zambia

Tourmaline is not commonly encountered in the violet-to-purple colour range, so these authors were interested to see some new purple material that reportedly came from Zambia in 2019. A rough parcel of this tourmaline was obtained by Farooq Hashmi (Intimate Gems, Glen Cove, New York, USA) during the February 2020 Tucson gem shows. His supplier had about 100–150 g of rough material and Hashmi obtained several pieces that he kindly loaned for examination.

The crystals consisted of striated prisms with sharp edges and no evidence of alluvial transport (e.g. Figure 31). The ends of the prisms were formed by broken surfaces except for one that showed evidence of chemical resorption in the form of parallelogram-shaped etch pits. Most of the crystals had surface residues of rust-coloured material, as would be expected from lateritic soil. Their body colour was a fairly homogeneous medium-to-dark slightly greyish purple, and they showed strong dichroism in pale purple (lavender) and vivid purple. Internal features consisted of planar and irregular thin films, partially healed fractures marked by the presence of fluid inclusions ('trichites'), fissures, tubes and elongate colourless birefringent crystals; the last two features were oriented parallel to the *c*-axis.

Figure 31: This purple tourmaline (8.03 g) reportedly came from a new find in Zambia. Photo by B. M. Laurs.

Table II: SEM-EDS analyses of purple tourmaline from Zambia.*

Oxides (wt.%)	Average	Range
SiO_2	36.24	36.11–36.51
TiO_2	0.004	nd–0.02
B_2O_3 calc.	10.82	10.76–10.97
Al_2O_3	40.95	40.65–41.67
FeO	0.16	0.08–0.23
MnO	2.37	2.26–2.55
MgO	0.01	nd–0.02
CaO	0.46	0.39–0.56
ZnO	0.16	0.10–0.23
Li_2O calc.	1.67	1.64–1.70
Na_2O	1.80	1.64–1.89
K_2O	0.006	nd–0.01
H_2O calc.	3.47	3.35–3.69
F	0.65	0.50–0.81
Subtotal	98.68	97.97–99.90
–O=F	0.24	0.20–0.29
Total	98.44	97.94–99.67
Ions per 31 (O,OH,F)		
Si	5.813	5.764–5.828
Ti	0.001	nd–0.002
B	2.998	2.994–2.999
Al	7.743	7.714–7.78
Fe^{2+}	0.022	0.011–0.031
Mn	0.323	0.308–0.347
Mg	0.002	nd–0.005
Ca	0.079	0.067–0.095
Zn	0.019	0.013–0.028
Li	1.078	1.060–1.102
Na	0.559	0.531–0.590
K	0.001	nd–0.003
X-site vacancy	0.361	0.336–0.382
F	0.283	0.250–0.411
OH	3.713	3.642–3.964

* Five spots were analysed on the sample. All iron is reported as FeO, and Li_2O, B_2O_3 and H_2O were calculated by stoichiometry. Cr, Bi, V, Cu, Ba, Pb and Cl were analysed for but not detected (nd).

Figure 32: Faceting of a piece of the purple tourmaline yielded this 1.38 ct stone. Photo by Orasa Weldon.

Standard-based scanning electron microscopy-energy dispersive spectroscopy (SEM-EDS) chemical analysis of one of the crystals was performed by authors AUF and WBS using a JEOL JSM-6400 instrument with the Iridium Ultra software package by IXRF Systems Inc. The data showed the tourmaline was elbaite with a rather homogeneous composition (Table II). The main chromophoric element was Mn (average 2.37 wt.% MnO) and traces of Fe were also present (average 0.16 wt.% FeO). In addition, unusually high traces of Zn were measured (average 0.16 wt.% ZnO). This composition is similar to a violet elbaite from the DRC that was recently documented by Williams *et al.* (2018), except that the present tourmaline contained slightly less Mn, Ca and Mg.

Just before this issue was finalised, a piece of this tourmaline was faceted by Richard Vogl (Golden State Gem & Mineral, Huntington Beach, California, USA) into a 1.38 ct 'mini Portuguese' cut with 113 facets (Figure 32).

Brendan M. Laurs FGA

Alexander U. Falster and
Dr William 'Skip' B. Simmons
Maine Mineral & Gem Museum
Bethel, Maine, USA

Reference

Williams, C., Williams, B., Falster, A.U., Simmons, W.B. & Laurs, B.M. 2018. Gem Notes: Violet tourmaline from Democratic Republic of Congo. *Journal of Gemmology*, **36**(2), 106–107.

White to Beige Variscite from Kazakhstan

Variscite and metavariscite are hydrated aluminium phosphates ($AlPO_4 \cdot 2H_2O$) that form from the reaction of low-temperature phosphate-bearing surface waters with aluminium-rich rocks. The minerals typically occur as compact fine-grained aggregates; they appear white when pure, but usually show attractive yellowish to bluish green colouration (due to Cr^{3+}), and therefore may be confused with turquoise (Calas *et al.* 2005).

During the February 2020 Tucson gem shows, variscite showing unusual white to beige colouration was displayed by Rare Earth Mining Co. (Trumbull, Connecticut, USA). According to Rare Earth's Bill Heher, the material came from a new find in Kazakhstan and is being marketed as Ivory Creek variscite. He initially encountered it in August 2018, and first offered cabochons of this variscite at the September 2019 gem and mineral shows in Denver, Colorado, USA. From 180 kg of rough, Rare Earth has cut approximately 2,000 pieces (including 500 matched pairs) in various shapes that range from about 14 to 60 mm in maximum dimension. The material takes a good polish and displays black to yellowish brown veining in various patterns, similar to those seen in some 'spiderweb' turquoise. It reportedly has not been treated in any way.

Heher kindly loaned two samples for examination that showed the range of colouration available (Figure 33). Raman spectroscopy was performed by one of the authors (MR) using a Thermo Nicolet Almega micro-Raman system that employed a 532 nm solid-state laser and a thermoelectric-cooled CCD detector; the analyses confirmed that both samples were variscite.

Heher reported that the supply outlook for this material is good.

Brendan M. Laurs FGA

Melli Rose
University of Arizona
Tucson, Arizona, USA

Reference

Calas, G., Galoisy, L. & Kiratisin, A. 2005. The origin of the green color of variscite. *American Mineralogist*, **90**(5–6), 984–990, https://doi.org/10.2138/am.2005.1668.

Figure 33: These cabochons show the range of colour of variscite from Kazakhstan. The pear shape measures 42.2 × 13.3 mm and the oval cut is 38.5 × 15.5 mm. Photo by B. M. Laurs.

SYNTHETICS AND SIMULANTS

Doublets Featuring Dioptase, Chrysocolla and Shattuckite from the Democratic Republic of Congo

Minerals from secondary copper ores commonly display bright colouration, sometimes in combination with interesting textures, and therefore may be polished into attractive cabochons. However, due to their softness and/or brittle nature, it may be necessary to stabilise such specimens with epoxy-type substances (e.g. Zwaan 2015) or attach them to a sturdy backing material as doublets.

During the February 2020 Tucson gem shows, Rare Earth Mining Co. displayed colourful doublets—showing blue, green, black and brown areas—that were prepared from a new find of secondary copper minerals in the DRC. Rare Earth's Bill Heher indicated that the material mainly consists of dioptase, chrysocolla and shattuckite, and that malachite and cuprite may be present in some pieces. A limited amount of rough material was recovered in 2018 and eventually found its way on to the market in 2019. Rare Earth cut a few dozen pieces ranging from about 20 to 70 mm in maximum dimension. The rock was first sliced into thin slabs, which were then affixed to a black resin backing material before being cut into various shapes.

Heher kindly loaned one sample for examination (Figure 34), and Raman spectroscopy was performed by one of the authors (MR) using a Thermo Nicolet Almega micro-Raman system that employed a 532 nm solid-state laser and a thermoelectric-cooled CCD detector. The analyses confirmed the presence of dioptase (green), chrysocolla (light to medium blue) and shattuckite (dark blue). Raman spectra could not be obtained from the

Figure 34: This colourful doublet (58.2 × 45.1 × 4.7 mm) consists of an assemblage of dioptase (green), chrysocolla (light to medium blue) and shattuckite (dark blue), which has been affixed to a durable backing material. Photo by Jeff Scovil.

brown and black areas, which apparently consisted of matrix material.

The patterns and colours displayed by some of the doublets were reminiscent of landscapes. It is not clear how much of this material will be available in the future.

Brendan M. Laurs FGA
and Melli Rose

Reference

Zwaan, J.C. 2015. Gem Notes: Stabilized shattuckite and bisbeeite from the Democratic Republic of Congo. *Journal of Gemmology*, **34**(8), 663–666.

Glass Imitation of a Garnet Pebble

Glass imitations of rough gem materials having the appearance of water-worn pebbles are well known in the trade (e.g. Laurs & Fritz 2015). Their abraded surface prevents close examination for diagnostic internal features such as gas bubbles and swirl marks that are indicative of glass. In addition, high-property manufactured glass can have RI and SG values that overlap those of the material being imitated (Hurwit 2003), making their detection even more difficult.

During the February 2020 Tucson gem shows, rough

stone dealer Steve Ulatowski showed this author a 26.18 g purple 'pebble' that was offered as a garnet in Arusha, Tanzania, in December 2019 (Figure 35). Ulatowski knew it was an imitation because someone had polished a small window on its surface and examination with oblique illumination revealed a gas bubble in the otherwise clean interior, identifying it as manufactured glass. He took the gem to remove it from the market and once it was back in the USA he informed the dealer about its identity. Notably, Ulatowski obtained an RI of 1.76 and

Figure 35: Weighing 26.18 g, this gem 'pebble' was offered as a garnet in Arusha, Tanzania, and proved to consist of manufactured glass. Note the tiny gas bubble visible on the upper right side of the polished window. Photo by B. M. Laurs.

a hydrostatic SG value of 4.02, which are both consistent with a pyrope-almandine composition that would be expected for such a 'garnet' sample.

Ulatowski suspected that the piece may have been manufactured from a glass-ceramic material such as Nanosital, as described by Bergman (2017) for what appeared to be a water-worn pebble of colour-change garnet that was sold in Arusha in June 2017. That sample had an RI of 1.66, an SG of 3.48 and a Raman spectrum that was consistent with a glass-ceramic material. However, the present 'pebble' had higher properties than those typically encountered in glass-ceramics—which show an RI range of 1.61–1.72 and SG values of 2.91–3.98 (Vyshnevskyi et al. 2017)—and it therefore appears more likely that it was composed of a high-property manufactured glass.

This example serves as a reminder of the continued presence of convincing glass imitations of rough gem material on the international market.

Brendan M. Laurs FGA

References

Bergman, J. 2017. Trade Alert: Color-change glass sold as natural garnet rough. Primagem, Bangkok, Thailand, www.academia.edu/33940879/TRADE_ALERT_Color_Change_Glass_Sold_As_Natural_Garnet_Rough, 5 pp., 19 July, accessed 19 August 2020.

Hurwit, K.N. 2003. Lab Notes: Glass imitation of tsavorite garnet. *Gems & Gemology*, **39**(2), 146.

Laurs, B.M. & Fritz, E.W. 2015. Gem Notes: Glass imitations of Cu-bearing Mozambique tourmaline. *Journal of Gemmology*, **34**(6), 484–485.

Vyshnevskyi, O., Khomenko, V., Kosorukov, O., Ripenko, V. & Kalinichenko, T. 2017. Glass-ceramics as imitation of gems. I. Gemological characteristic, composition, physical properties. *Mineralogical Journal*, **39**(3), 32–42, https://doi.org/10.15407/mineraljournal.39.03.032 (in Ukrainian with English abstract).

An Unusual Synthetic Fancy Sapphire Coloured by Co^{2+} and Co^{3+}

Recently, an intriguing synthetic sapphire was sent to the American Gemological Laboratories (AGL) in New York for testing. The 3.73 ct round mixed cut possessed an appealing greenish blue colour, which at first glance resembled copper-bearing tourmaline, apatite or zircon (Figure 36). Indeed, the client informed the author that it had been sold to him as a Paraíba-type tourmaline. However, the standard gemmological properties readily identified the sample as corundum, with RIs of 1.761–1.770, a birefringence of 0.009 and a hydrostatic SG of 3.99. In addition, the specimen had a pink/red reaction to the Chelsea Colour Filter.

When observed with magnification, the sample appeared clean, with a weak doubling of the back facets. However, fibre-optic lighting revealed wispy formations of faint particles that produced a reddish sheen (Figure 37). Inhomogeneous colour zoning was created by a repeating pattern of broad bands of alternating more- and less-saturated zones of the same hue when viewed in

Figure 36: This 3.73 ct melt-grown synthetic sapphire has an unusual colour, which more closely resembles that of Paraíba-type tourmaline, apatite or zircon than a variety of natural corundum. Photo by Alex Mercado and Bilal Mahmood, AGL.
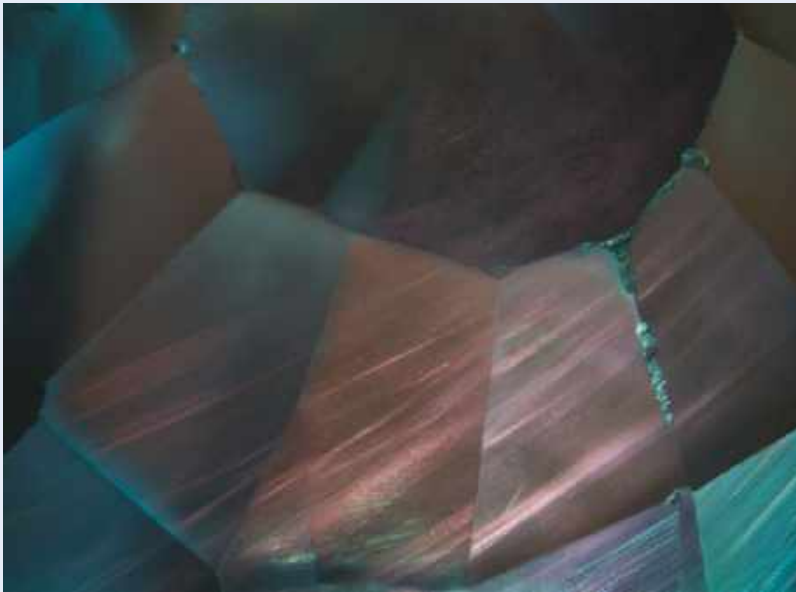
Figure 37: With fibre-optic lighting, faint wisp-like patterning of minute particles casts a reddish appearance in the synthetic sapphire. Photomicrograph by C. P. Smith; magnified 38×.

one direction; the more-saturated banding also followed a wispy distribution of faint particulates when viewed from another direction (cf. Zandi 2019).

Chemical analysis with EDXRF spectroscopy revealed traces of Fe (0.006 wt. %), Ti (0.002 wt. %) and Co (0.010 wt. %). Other trace elements commonly encountered in corundum—such as Cr, V and Ga—were not detected. Additionally, other elements that are sometimes encountered in blue-green synthetic corundum, such as Ni, were also not detected. Using PL spectroscopy, minute traces of Cr (i.e. below the detection limit of EDXRF spectroscopy) were revealed as an emission doublet at 693/694 nm.

All of these data readily confirmed the synthetic origin of this sapphire. However, its colour was unlike that of typical green Co-doped synthetic corundum that is occasionally encountered in the trade. As a result, a more in-depth spectral analysis was performed. UV-Vis spectroscopy recorded absorption bands at approximately 430/435, 470, 548, 590, 630 and 689 nm (see Table III and Figure 38a), as well as a broad band centred in the near-infrared at approximately 1380 nm (not shown). All of these features are related to divalent and trivalent cobalt (Co^{2+} and Co^{3+}; see, e.g., Schmetzer & Peretti 2000 and references therein). No absorptions were found that are related to other chromophores which may be present in synthetic corundum of various colours, such as Cr^{3+}, Fe^{3+}, V^{3+}, Ti^{4+}, Ni^{2+}/Ni^{3+} and Mn^{2+}. In the mid-infrared region of the spectrum, no structurally bonded OH groups were recorded.

As mentioned above, Co^{2+} and Co^{3+} are known contributors to colour in synthetic corundum (Table III).

Table III: UV-Vis-NIR absorption features (in nm) related to cobalt in synthetic corundum.

Vibronic progression	o-ray	e-ray
Co³⁺ absorptions		
Sharp band	689 (zero phonon)	—
Weak, broad band	~680 (2nd order)	—
Weak, broad band	~670 (3rd order)	—
Apex broad band	~655	~640
Apex broad band	~435	~430
Shoulder	—	~470 (unknown allocation)
Intensity comparison for the two dominant absorption bands	655 ≥ 435	640 << 430
Ill-defined bands (Co³⁺ or other potential contributors)		
Weak, broad band	530 (unknown allocation)	—
Faint, broad band	~500 (unknown allocation)	—
Shoulder on rising absorption	—	~345 (unknown allocation)
Co²⁺ absorptions (both o-ray and e-ray)		
Primary broad band	~630	
Secondary broad band	~590	
Tertiary broad band	~548	
Primary broad band	~1380	

Although not commonly seen as faceted samples, vibrant green colouration has been produced in synthetic corundum grown by the Verneuil method by doping with pure Co^{3+}, as well as with a combination of Co^{3+} and V^{3+} (see, e.g., Sandmeier 1930; Kammerling & Fritsch 1995; Kammerling 1996; Mayerson 2004). Figure 38b shows the spectral features of Co^{3+} in such a melt-grown green synthetic sapphire from the author's reference collection for which only cobalt (0.021 wt.%) was detected by EDXRF spectroscopy.
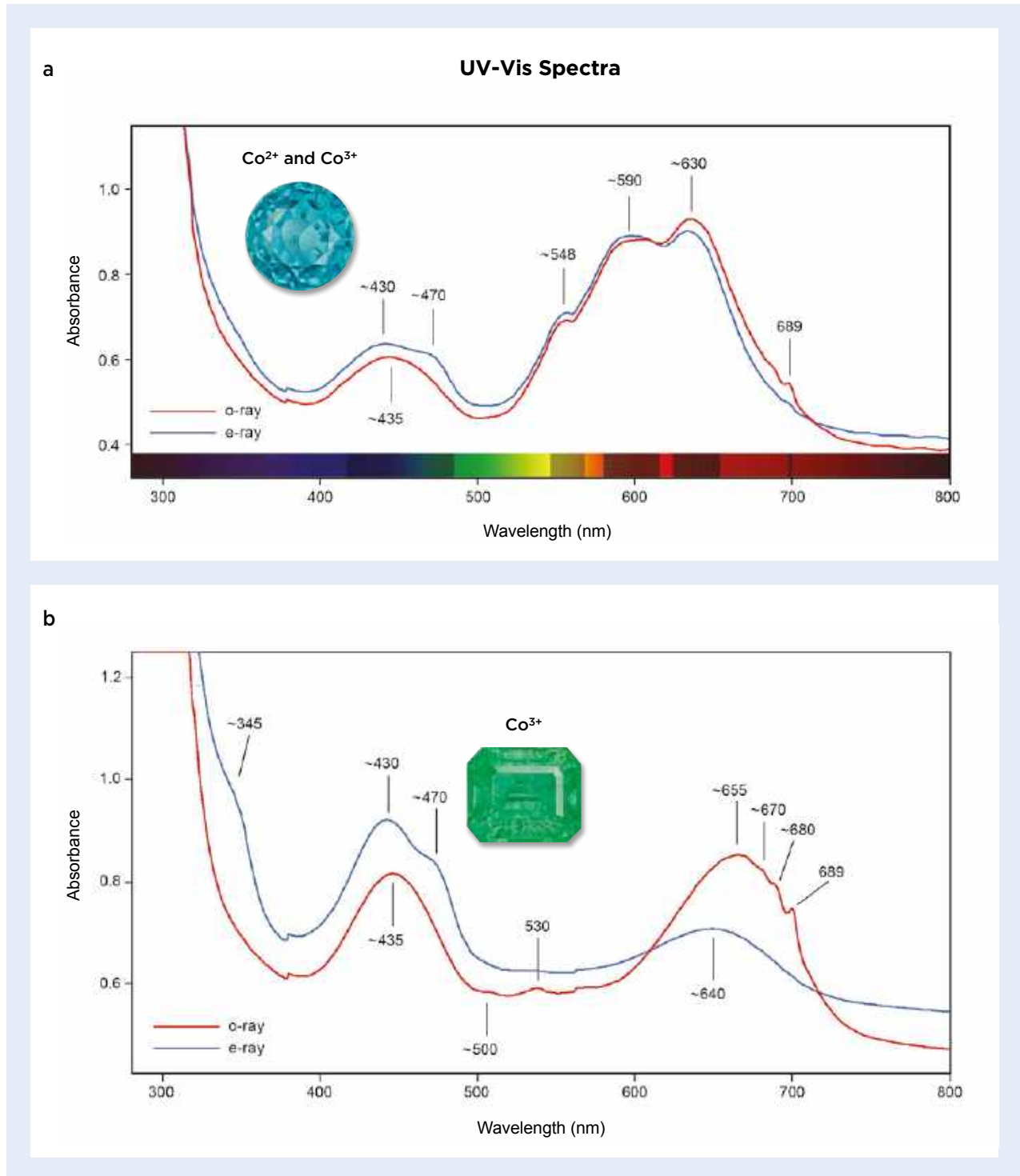
Figure 38: (**a**) Polarised UV-Vis spectroscopy of the 3.73 ct synthetic sapphire reveals a series of absorption bands associated with Co^{2+} and Co^{3+}. (**b**) Polarised spectra are shown for a vibrant green 8.38 ct synthetic sapphire predominantly coloured by Co^{3+} from the author's reference collection. The path length of the beam was approximately (a) 7.0 mm and (b) 7.7 mm. Inset photos by Alex Mercado and Bilal Mahmood, AGL.
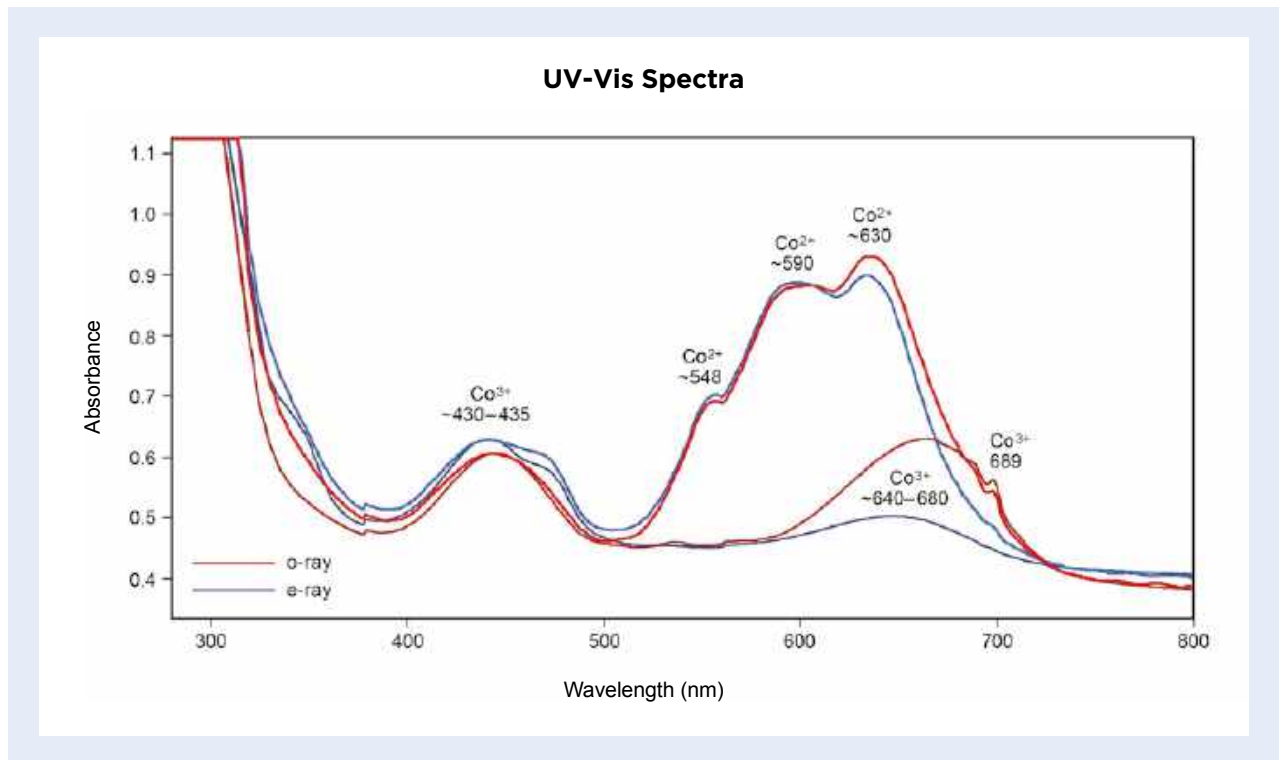
Figure 39: By overlaying the spectra in Figures 38a and 38b, the bands attributed to Co^{2+} and Co^{3+} can be more clearly distinguished. Additionally, the shoulder at approximately 470 nm is present in both samples and may or may not be due to Co^{3+}. Moreover, the position of this underlying band is not consistent with features associated with other well-known chromophores such as Cr^{3+}, V^{3+} or Fe^{3+}, or lesser-known chromophores such as Ti^{3+}, Ni^{3+} or Ni^{2+}.

By overlaying the spectra in Figures 38a and 38b, it is possible to differentiate between the bands that are related to Co^{2+} and Co^{3+} in the 3.73 ct synthetic sapphire (Figure 39). This also revealed some discrepancies with the band allocations for cobalt that have been reported in the literature (see, e.g., figure 6 in Schmetzer & Peretti 2000).

The intriguing and noteworthy aspect of this 3.73 ct synthetic sapphire is its unusual colour. This was the first time the author can recall seeing a synthetic sapphire of this particular colour—although it seems that a production has recently entered the marketplace (see also Zandi 2019)—and such examples demonstrate the addition of an intriguing new colour range to the existing synthetic corundum product line via a melt-growth process, such as flame-fusion (Verneuil) or pulling (Czochralski) techniques. Spectroscopy of this sample also clarified the allocation of spectral bands associated with Co^{2+} and Co^{3+}.

Christopher P. Smith FGA (chsmith@aglgemlab.com)
American Gemological Laboratories Inc.
New York, New York, USA

References

Kammerling, R.C. 1996. Gem Trade Lab Notes: Green synthetic sapphire. *Gems & Gemology*, **32**(1), 51.

Kammerling, R.C. & Fritsch, E. 1995. Gem Trade Lab Notes: Synthetic star sapphire with an unusual color. *Gems & Gemology*, **31**(1), 57–58.

Mayerson, W.M. 2004. Lab Notes: Synthetic sapphire with unusual yellowish green bodycolor. *Gems & Gemology*, **40**(2), 167–168.

Sandmeier, E.G. 1930. Synthetic oriental emerald or emerald-green sapphire. U.S. Patent assigned to Swiss Jewel Co. SA, issued 16 September.

Schmetzer, K. & Peretti, A. 2000. Characterization of a group of experimental Russian hydrothermal synthetic sapphires. *Journal of Gemmology*, **27**(1), 1–7, https://doi.org/10.15506/JoG.2000.27.1.1.

Zandi, F. 2019. Lab Notes: Paraíba-like synthetic sapphire. *Gems & Gemology*, **55**(1), 101.

MISCELLANEOUS

'Versatility of Genius' Cubic Zirconia

The author's 'World Heritage Collection of Gems' consists of a series of designs that honour different contributions by various countries to the world's cultural heritage. For instance, China is famous for its philosophy, Japan for its traditions, India for spiritual teachings and Spain for architecture. The pattern of facets conceived for each gem was inspired by renowned symbols or images from the respective countries. The collection currently consists of six designs—honouring China, Japan, Tibet, India, France and Italy—and the sixth one was displayed for the first time at the February 2020 Tucson gem shows. Called 'Versatility of Genius', it consists of a 387 ct cubic zirconia (CZ) that was completed at the end of January 2020. The conception and cutting of this gem—which honours Italy's contributions to cultural heritage—is described in this report.

Leonardo da Vinci (1452–1519) was an Italian artist and engineer who is best known for his paintings (e.g. the Mona Lisa and the Last Supper). Among Leonardo's architectural designs, the author was inspired by his sketches for a cathedral (Figure 40a). The mathematical harmony of his drawing, formed by the crossing of lines, continuing from one edge to another, served as the basis for the faceting design without needing significant changes (Figure 40b). It was clear, however, that faceting this pattern would be technically very difficult.
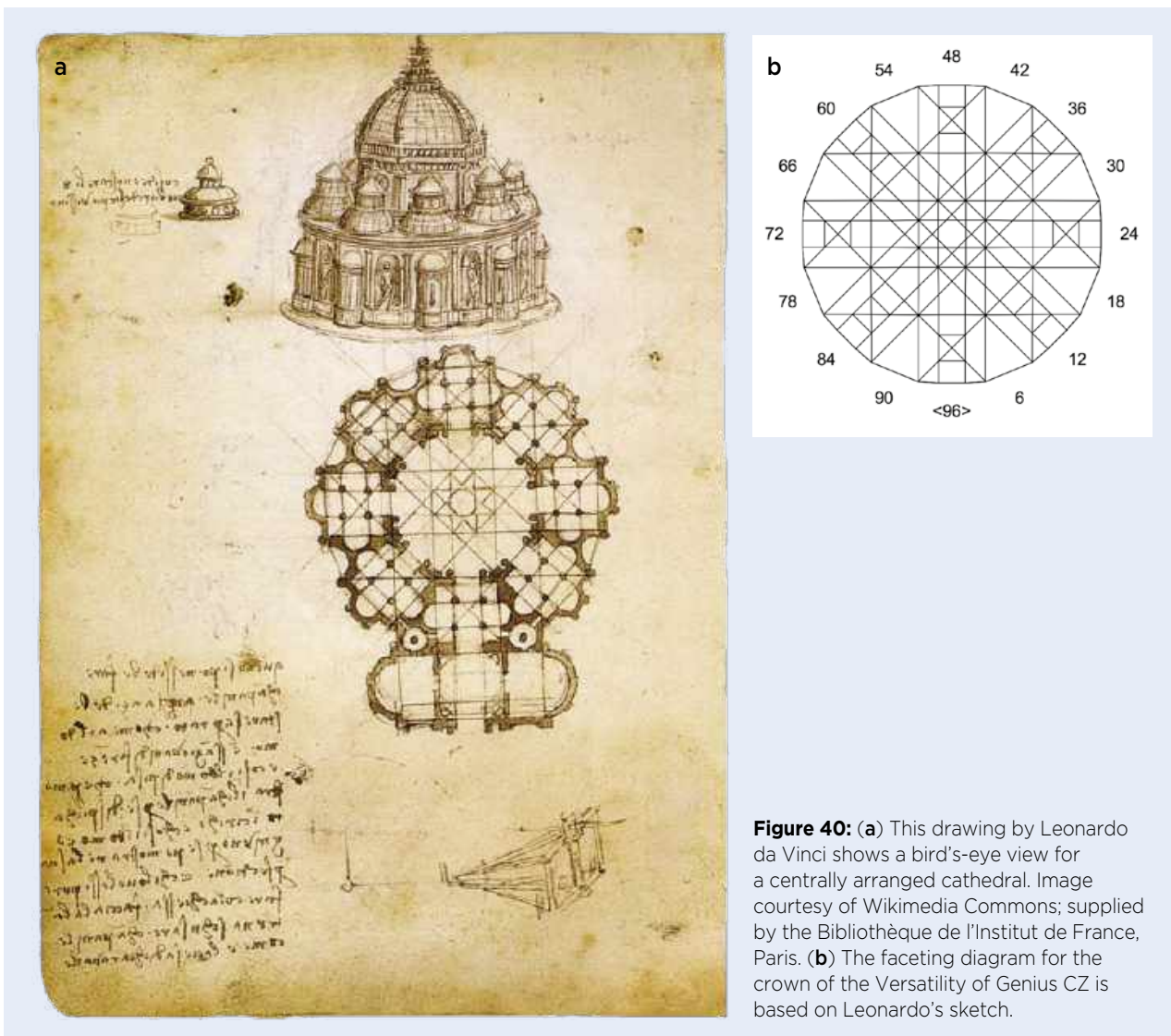
Figure 40: (**a**) This drawing by Leonardo da Vinci shows a bird's-eye view for a centrally arranged cathedral. Image courtesy of Wikimedia Commons; supplied by the Bibliothèque de l'Institut de France, Paris. (**b**) The faceting diagram for the crown of the Versatility of Genius CZ is based on Leonardo's sketch.
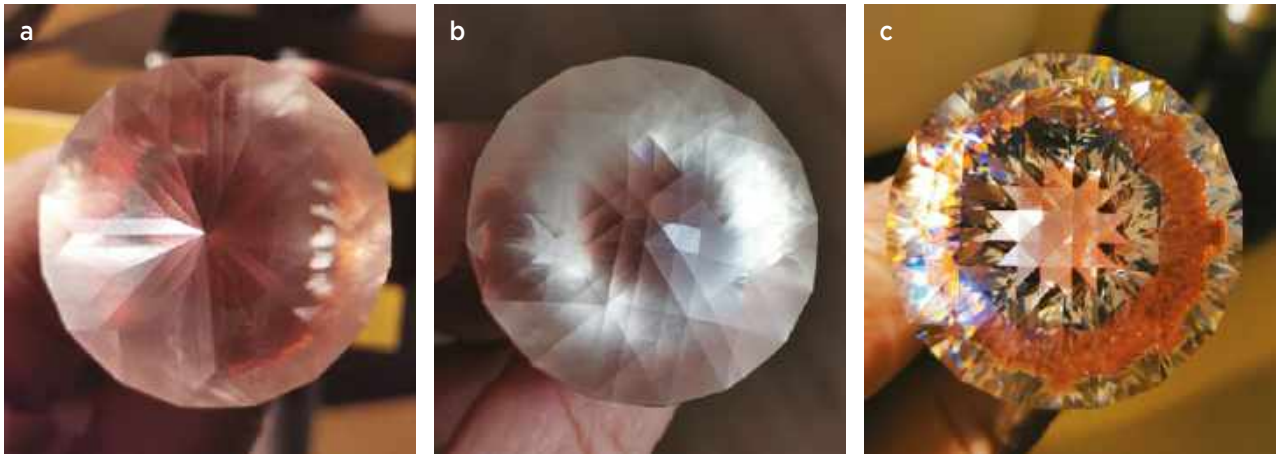
Figure 41: The steps in cutting the Versatility of Genius CZ include (**a**) forming the initial outline of the facets, as viewed here from the pavilion; (**b**) final cutting of the crown facets; and (**c**) pre-polishing. Photos by V. Tuzlukov.

After the design was drawn and the faceting diagram was constructed on a computer, the author studied the movement of a three-dimensional rendering and its incredible play of light. The synthetic material CZ was chosen for this work as being most suitable to fully express the beauty of this cut.

The primary condition for a successful outcome was precision. The faceting process consists of three stages: cutting the facets, pre-polishing and final polishing. Very often faceters approach the first stage casually, assuming they can correct things later, but this would not be possible in this case. Greater initial care is always needed on more complicated and very difficult designs such as this one.

It was first necessary to outline the pattern from which
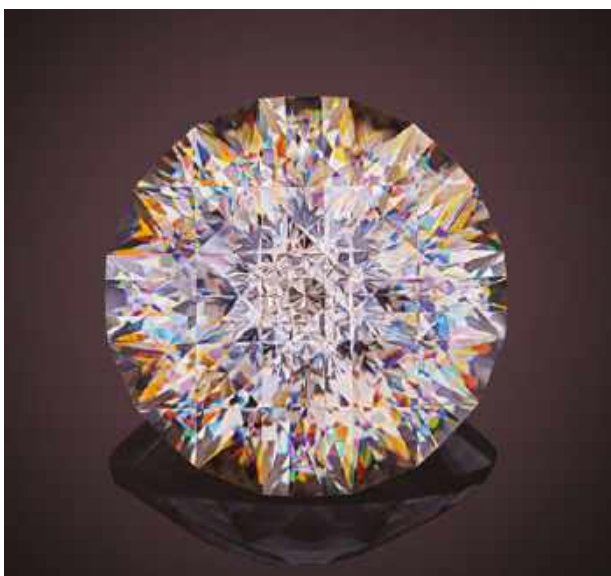
Figure 42: The Versatility of Genius CZ is the sixth contribution to the author's 'World Heritage Collection of Gems'. It weighs 387 ct and has 329 facets. Photo by Dmitry Stolyarevich.

to create the facets so they would conjoin to form the desired optical effects. A preliminary outline of the main facet lines was done first, around which the next facets were grouped. The photos in Figure 41 reflect the steps in this process: initial outline (Figure 41a), final cutting (Figure 41b) and pre-polish (Figure 41c). A final polish then brought the facets to a mirror-like condition to facilitate the play of light, in which multi-coloured flashes were created by numerous inner reflections (Figure 42).

After many long days of work, the finished gem was finally completed—with 329 facets and weighing 387 ct. Holding it in my hand I felt its pleasant heaviness, and my soul was filled with happiness that I had managed to embody in this work at least a shadow of the creation of the great master Leonardo da Vinci. I hope this 'Versatility of Genius' will serve as a source of inspiration to other masters, such as photographer Dmitry Stolyarevich, who captured the image in Figure 42, exactly portraying the meaning and character of this gem. Moreover, this exercise represents something new for gem faceting in my experience: using an ancient text to provide direction for one's imagination and then manifesting the gem that completes one's vision. I summarise the experience of its creation with the following: *When beauty of artistic images and precision of geometric drawings merge in the great Harmony, they reflect the multidimensional nature of Genius*.

Each design in the World Heritage Collection of Gems has been manifested in a natural stone and a synthetic one. After the CZ version of the Versatility of Genius was completed, the author also produced this cut in a 143.1 ct smoky quartz, which was completed in July 2020.

Victor Tuzlukov (vtuzlukov@hotmail.com)
Bangkok, Thailand

Gemmological and Mineralogical Characteristics of Chrysocolla Chalcedony from Taiwan, Indonesia and the USA, and Their Separation

Min Ye and Andy H. Shen

ABSTRACT: Chrysocolla chalcedony is the most valuable form of chalcedony. To distinguish samples from three commercially important localities—Taiwan, Indonesia and the USA—we studied the gemmological, mineralogical and trace-element characteristics of this gem material. UV-Vis-NIR absorption spectra verified the colour-causing inclusions to be chrysocolla. Chemical analysis by EPMA showed that Si and Cu are the main components of chrysocolla chalcedony, and FTIR spectroscopy indicated that α-quartz was dominant in all samples. Examination of petrographic thin sections revealed that quartz was present as fine crystallites, relatively coarser crystals and radiating fibres (i.e. chalcedony), while backscattered-electron images showed that the chrysocolla usually formed irregular patches or fibrous rims and clusters. Raman spectral identification of associated minerals and LA-ICP-MS chemical analyses provided useful information for distinguishing chrysocolla chalcedony samples from the three origins, according to their: (1) diagnostic impurities, such as copper mineral mixtures, manganite and a vernadite-like mineral; and (2) trace elements, specifically U and Mo, together with Fisher-LDA data processing, for specimens without obvious impurity minerals. Both of these criteria should be considered for the most reliable separation of samples' geographic origin.

Chrysocolla chalcedony[1], sometimes marketed as 'gem silica', is an attractive form of chalcedony that usually ranges from vivid blue to bluish green (e.g. Figure 1). The material is mainly coloured by the presence of chrysocolla inclusions (Shen *et al*. 2006). In recent years, the majority of fine-quality chrysocolla chalcedony on the Chinese market has come from Taiwan, Indonesia and the USA. Other sources include Peru, Mexico and Spain (Hyršl 2001; Emerson & Darley 2010; Koivula *et al*. 1992; Laurs 2015), from which material is gradually entering the Chinese market. Chrysocolla chalcedony from Taiwan usually has a more pleasing saturated blue colour, so its price is higher. Moreover, the authors are aware of material from other localities being represented as coming from Taiwan. As a result, there is a growing need to reliably identify the origin of chrysocolla chalcedony gems.

---

[1] The name *chrysocolla chalcedony* does not follow rigorous terminology according to the mineralogical nomenclature of silica minerals, in which granular fine-grained quartz is called *chert* and oriented fibrous quartz is termed *chalcedony* (Graetsch 1994). In this article we use *chrysocolla chalcedony* since this name is widely used and well known in the gemmological community.

Figure 1: A rough sample of chrysocolla chalcedony from Taiwan (8.47 g) is accompanied by four greenish blue cabochons that are (left to right) from the USA (1.82 ct), Taiwan (2.21 ct), Indonesia (1.07 ct) and the USA (3.16 ct). Samples courtesy of Songshan Lin; photo by Z. Zhang.

Until now, there have been few detailed studies of chrysocolla chalcedony. Earlier reports generally provided a brief description of the gemmological properties of material from specific origins (e.g. Koivula *et al*. 1992; Emerson & Darley 2010). Indonesian specimens were characterised in more detail by Einfalt and Sujatmiko (2006), who pointed out that varying proportions of chrysocolla and quartz may lead to a more uniform or mottled appearance. Detailed studies of Taiwan material were reported—in Chinese—by Lin (2008) and Chen *et al.* (2011).

This article describes the gemmological, mineral-ogical and trace-element characteristics of chrysocolla chalcedony from Taiwan, Indonesia and the USA. Specifically, we focus on the microstructure, chemical composition and impurity minerals. Finally, we compare relevant data and devise a set of criteria to help separate material from these three geographic origins.

LOCATION AND GEOLOGY

Chrysocolla forms as a secondary alteration product in the oxidation zone of copper sulphide mineralisation, with quartz as a common co-precipitate (Einfalt & Sujatmiko 2006). Therefore, chrysocolla chalcedony is mainly found co-existing with copper deposits.

Specimens from Taiwan mostly originate from the island's eastern coastal mountain range (Figure 2a), spanning from northern Hualien County to southern Taitung County. Currently, only the main Baofengxiang copper mine in Tungho township, located in Taitung County, is still active. Mineralisation took place during Miocene time, when late-stage hydrothermal fluids enriched in SiO_2 entered fractures associated with faults and penetrated gaps in andesitic breccia containing primary copper minerals, and then reacted to form chrysocolla chalcedony (Lin 2008). Due to lack of produc-tion, the availability of this gem material from Taiwan has rapidly diminished in recent years.

Indonesian chrysocolla chalcedony mostly comes from North Maluku Province. The deposits are located about 2,400 km east of Jakarta in the Bacan Archipelago, particularly on Kasiruta Island (Figure 2b). The mining sites are situated in pillow lavas of Oligocene age, occurring as chrysocolla-bearing quartz veins and small pods in the basaltic rock (Einfalt & Sujatmiko 2006).

Chrysocolla chalcedony from the USA is found in association with various copper deposits, including the Morenci, Inspiration and Ray mines in Arizona (Figure 2c; e.g. Laurs 2019). The Morenci mine is located in the Clifton-Morenci District, Greenlee County; the Inspiration

Figure 2: The locations of the chrysocolla chalcedony samples studied for this report are shown on these maps. (**a**) In Taiwan, the main deposit is located in the eastern coastal range. (**b**) In Indonesia, several localities are known in the Bacan Archipelago. (**c**) In the state of Arizona, USA, chrysocolla chalcedony is found at the Morenci, Inspiration and Ray mines.

mine is situated in the Globe-Miami District, Gila County; and the Ray mine is in the Ray District, Pinal County. At these localities, chrysocolla chalcedony is found in oxidised porphyry copper ore associated with intrusive igneous rocks ranging from granodiorite to quartz monzonite; the mineralisation took place about 75 to 50 million years ago during the Laramide orogeny (Creasey 1984; Enders 2000).

MATERIALS AND METHODS

For this study, we initially obtained 60 samples of chrysocolla chalcedony from Taiwan, Indonesia and the USA. The Taiwanese specimens were obtained from local private collectors. The Indonesian samples were donated by a major supplier of Indonesian gem material in Taiwan. The USA samples were purchased from a Taiwanese dealer who regularly visits the mining areas in the USA and South America, and we acquired samples immediately after he returned from trips to known USA localities.

After preliminary examination, we omitted approximately half of the samples because they were too pale (i.e. near-colourless) or too porous for gem use. We therefore focused on 29 samples (Figure 3), which included 10 from Taiwan (labelled TW), nine from Indonesia (labelled ID) and 10 from Arizona (labelled US-M for the Morenci mine and US-I/R for the Inspiration and Ray mines). All of them were doubly polished as 2–3 mm thick slabs for further testing.

The gemmological properties of all samples were documented using a refractometer, hydrostatic balance, standard gemmological long- and short-wave 4 W UV lamps, a Chelsea Colour Filter and a gemmological microscope at the Gemmological Institute, China University of Geosciences (Wuhan). Photomicrographs were taken with a Leica M205 A microscope. In addition, offcuts from all samples were prepared as petrographic thin sections and observed using an Olympus BX51 polarising microscope at the Resources Institute, China University of Geosciences (Wuhan).

Quantitative chemical analysis of all samples was conducted with a JEOL JXA-8100 electron probe micro-analyser (EPMA) at the State Key Laboratory of Geological Processes and Mineral Resources, China University of Geosciences (Wuhan). We used an accelerating voltage of 15 kV, beam current of 20 nA and beam diameter of 10 μm. One to three analyses were performed on each sample, consisting of more-transparent near-colourless areas, more-translucent blue portions and/or more-opaque whitish blue parts of the samples. We also obtained backscattered electron (BSE) images to help visualise the distribution of chrysocolla within the chalcedony.

Trace-element concentrations were determined for all samples by laser ablation inductively coupled plasma mass spectrometry (LA-ICP-MS) at the State Key Laboratory of Geological Processes and Mineral Resources, China University of Geosciences (Wuhan). The instrumentation consisted of an Agilent 7700 Series ICP-MS coupled with a GeoLasPro 193 nm excimer laser. The laser had a 3 Hz pulse rate and a 60 μm diameter spot size with a fluence of 6 J/cm^2. Reference materials included USGS glasses (BCR-2G, BHVO-2G and BIR-1G) and a NIST glass (SRM 610); ^{29}Si was used as the internal standard to calculate the concentrations of 55 trace elements with ICPMSDataCal software. One or two spots were analysed on each sample. Fisher linear discriminant analysis (Fisher-LDA) was performed using the SPSS (Statistical Product and Service Solutions) software package.

Ultraviolet-visible-near infrared (UV-Vis-NIR) absorption spectra in the range of 350–2500 nm were recorded for all samples with a JASCO MSV-5200 micro-spectrophotometer at the Gemmological Institute, China University of Geosciences (Wuhan). The sampling interval was 0.5 mm and the scan speed was 1,000 nm/min.

For infrared spectroscopy, a small area of each sample was ground into a fine powder and incorporated into KBr pellets (with a sample-to-KBr ratio of 1:200). For some samples showing variable diaphaneity, two areas were analysed: a more-translucent blue portion and a more-opaque whitish blue zone. The spectra were recorded in the 4000–400 cm^{-1} range with a Bruker Vertex 80 Fourier-transform infrared (FTIR) spectrometer at the Gemmological Institute, China University of Geosciences (Wuhan). The resolution was 8 cm^{-1} and 32 scans were collected for each sample. Spectra are presented in the range of 1600–400 cm^{-1}, where the most relevant features are seen.

Raman spectra of the chrysocolla chalcedony were obtained from smoothly polished blue areas of all samples using a Thermo Scientific DXR Raman microscope at the State Key Laboratory of Geological Processes and Mineral Resources, China University of Geosciences (Wuhan). The following parameters were used: 780 nm laser wavelength, 10 mW laser power, 25 μm aperture slit, 2.4–4.4 cm^{-1} resolution, 53–3300 cm^{-1} spectral range and 50 × objective lens. Spectra are presented in the 200–1200 cm^{-1} range, where the most diagnostic features occur. Selected impurity minerals in the chalcedony were identified using a Bruker Senterra R200-L Raman spectrometer at the Gemmological Institute, China
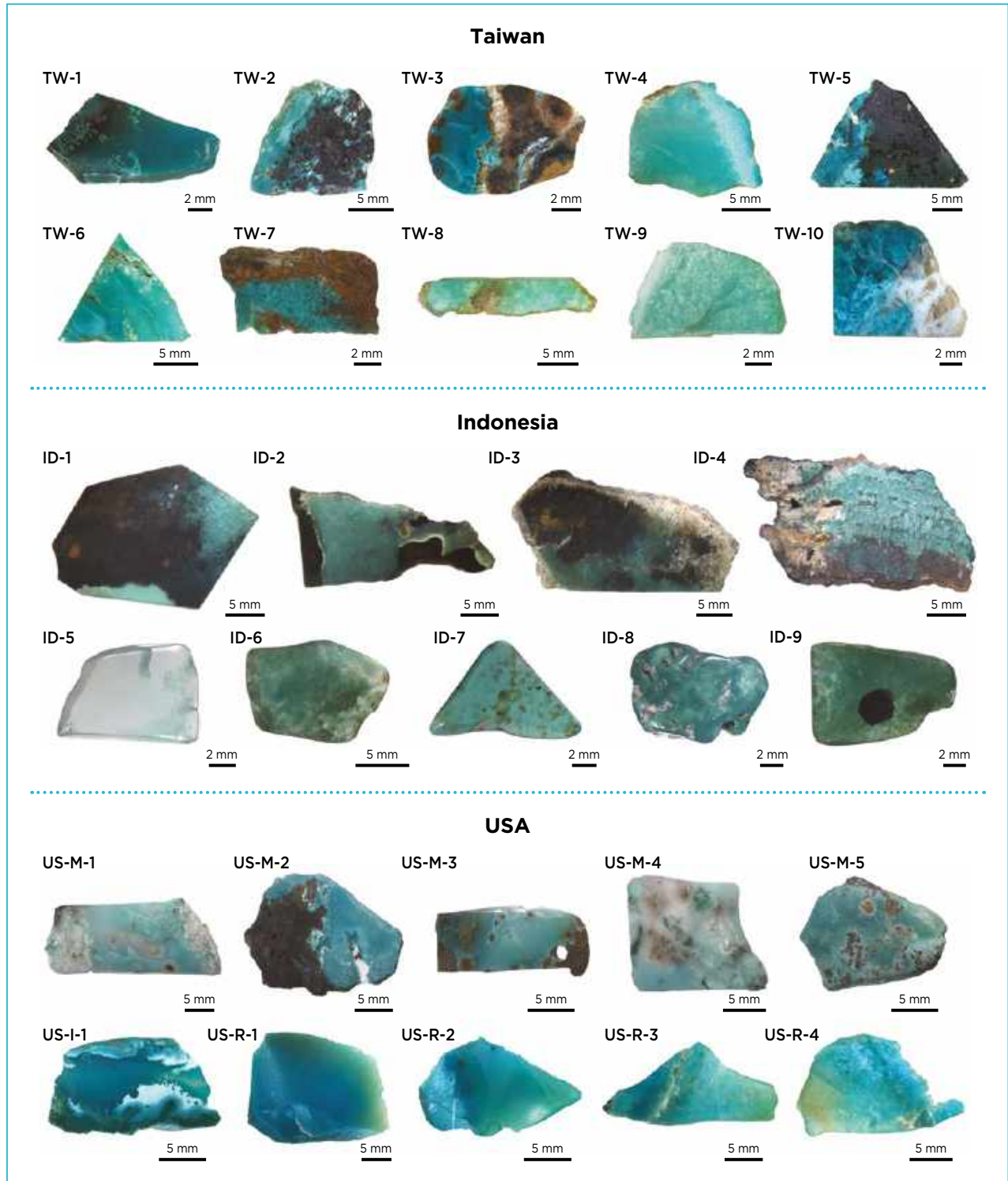
Figure 3: These 29 chrysocolla chalcedony specimens were characterised for this study. They are from Taiwan (TW), Indonesia (ID) and the USA (US-M = Morenci mine, US-I = Inspiration mine and US-R = Ray mine). Photos by M. Ye.

University of Geosciences (Wuhan), using the following parameters: 532 nm laser wavelength, 5 mW laser power, 50 × 1000 μm aperture slit, 3–5 cm⁻¹ resolution, 45–3600 cm⁻¹ spectral range and 50× objective lens.

Energy-dispersive X-ray fluorescence (EDXRF) chemical analysis of some dark impurity minerals was done using a Thermo Scientific ARL Quant'X spectrometer (equipped with an Rh tube and Peltier-cooled detector) at the Gemmological Institute, China University of Geosciences (Wuhan). We analysed for all elements that are available by this technique under various instrumental conditions.

RESULTS

Gemmological Characteristics

The gemmological properties of our samples are summarised in Table I. Material from the three localities had similar RIs, UV fluorescence and Chelsea filter reactions, but some differences were noted in their colour, diaphaneity, SG values and internal features.

Colour and Diaphaneity. The colour distribution in the chrysocolla chalcedony was generally not uniform. The Taiwanese samples ranged from intense blue to bluish green; the bright colouration of samples TW-5 and TW-10 was particularly attractive. The samples from Indonesia were pale blue to bluish green, and showed a limited range of brightness and saturation. Those from the USA were pale to highly saturated blue, with better colouration displayed by the US-I/R samples. The colouration was somewhat affected by the thickness of the slabs, with thin parts showing a less-saturated yellowish green.

Chrysocolla chalcedony is commonly not a very transparent gem material. The Taiwanese and USA samples ranged from translucent to semi-translucent. In general, the Indonesian samples showed greater transparency than those from the other two origins, ranging from semi-transparent to semi-translucent. Overall, an uneven diaphaneity was obvious in all samples.

In general, the colour and transparency depended on the proportions of chrysocolla and quartz. Too little chrysocolla resulted in pale colouration (although typically with good transparency), and too much chrysocolla also caused the material to appear pale coloured but with diminished transparency due to porosity and scattering of light from the chrysocolla inclusions. Samples containing a moderate amount of chrysocolla inclusions tended to show the most desirable combination of colour and transparency.

Specific Gravity. The SG range of samples from the different origins was quite broad and mostly overlapped. SG was mainly dependent on the different proportions of chrysocolla (SG about 2.00–2.40) and quartz (the major matrix material, SG = 2.65) in each sample. Those containing less chrysocolla commonly had higher SG values (e.g. ID-5: SG = 2.64). In some specimens, SG was affected by porosity (e.g. ID-8: SG = 2.39) or the presence of heavy impurity minerals (e.g. TW-1: SG = 2.70).

Internal Features. Observing the slabs with the gemmological microscope revealed their inhomogeneous nature. In the Taiwanese samples, chrysocolla was sometimes present as milky blue cloud-like inclusions (Figure 4a), or as globular or irregular cotton-like aggregates (Figure 4b). Green, yellowish brown and dark-coloured impurity minerals were also seen in some specimens, and fractures

Table I: Gemmological characteristics of the studied chrysocolla chalcedony samples from Taiwan, Indonesia and the USA.*

Property	Taiwan	Indonesia	USA
Colour	Intense blue to bluish green	Pale blue to bluish green	Pale to intense blue
Diaphaneity	Translucent to semi-translucent; usually low diaphaneity	Semi-transparent to semi-translucent; greater diaphaneity than those from Taiwan and the USA	Translucent to semi-translucent; generally low diaphaneity
RI	1.53–1.54	1.53–1.54	1.53–1.54
SG	2.26–2.70	2.30–2.64	2.38–2.63
Internal features	Chrysocolla formed cloud-like, globular or irregular aggregates. Green, yellowish brown and dark impurity minerals were present, and fractures were common. Malachite formed globular green aggregates.	Chrysocolla appeared mottled in the transparent matrix. Some dark or yellowish-to-orangey brown impurities were common. Pores and even small vugs were present. Malachite formed globular green aggregates.	US-M samples were quite mottled, with obvious unevenly distributed chrysocolla aggregates and dark impurity minerals; also malachite formed green needle-like radiating clusters. Some US-I/R samples contained irregular or rounded chrysocolla aggregates.

*Most samples were inert to long- and short-wave UV radiation except for TW-7 (moderate green to short-wave UV) and ID-4 (faint green to short-wave UV). None of the samples showed any reaction to the Chelsea Colour Filter. Internal features do not include minerals seen in areas of host rock adjacent to chrysocolla chalcedony. Abbreviations: US-M = Morenci mine and US-I/R = Inspiration and Ray mines, Arizona, USA.

were quite common. In the Indonesian samples, chryso-colla often created a mottled appearance within a rather transparent matrix (Figure 4c), usually with some dark or yellowish-to-orangey brown impurities (discussed in more detail below). Pores and even small vugs were present in some samples (Figure 4d). The US-M samples appeared quite mottled, with obvious uneven concentrations of chrysocolla aggregates and some dark impurities. In the US-I/R samples, the blue matrix was comparatively uniform and transparent; sometimes irregular or rounded pale blue chrysocolla aggregates were observed (Figure 4e, f).

Thin Section Observation

Examination of thin sections with cross-polarised light using a petrographic microscope revealed various microstructural features (Figure 5). In the Taiwanese specimens, quartz displayed three morphologies: fine crystallites (Figure 5a, mixed with inconspicuous chryso-colla); relatively coarser crystals, sometimes showing hexagonal growth striations (Figure 5a); and radiating fibres (i.e. chalcedony; Figure 5b, c). Chalcedony commonly surrounded the coarser-grained quartz and formed adjacent to chrysocolla aggregates (Figure 5b). Chrysocolla was sometimes not readily differentiable from quartz in cross-polarised light (i.e. where very fine grained; Figure 5a), but more commonly it showed

anomalous interference colours (often yellowish green; Figure 5b). Occasionally, chrysocolla formed radiating spherical aggregates displaying various anomalous inter-ference colours (Figure 5c).

In the thin sections from Indonesia, chrysocolla was seen dispersed in a fine-grained quartz matrix, and it commonly showed very pale green (Figure 5d, e) or brownish green (Figure 5f) anomalous interference colours. Similar to the Taiwanese samples, quartz was present as fine crystallites (Figure 5d, e; mixed with inconspicuous chrysocolla) or coarser crystals (Figure 5d–f), and sometimes as radiating fibres of chalcedony adjacent to chrysocolla aggregates (Figure 5e).

In the USA material, chrysocolla aggregates usually displayed brown anomalous interference colours in the US-M samples (Figure 5g), and yellowish green (Figure 5h) or dark green (Figure 5i) anomalous inter-ference colours in the US-I/R specimens. The size of the quartz crystals varied considerably: the coarsest ones sometimes exceeded 1 mm (Figure 5g), while the smallest ones were usually less than 50 μm (Figure 5h). In addition, quartz sometimes formed radiating fibres of chalcedony in the USA samples (Figure 5i).

EPMA and LA-ICP-MS Analysis

BSE Imagery. Bright areas in BSE images correspond to higher overall atomic weight, and therefore BSE imagery
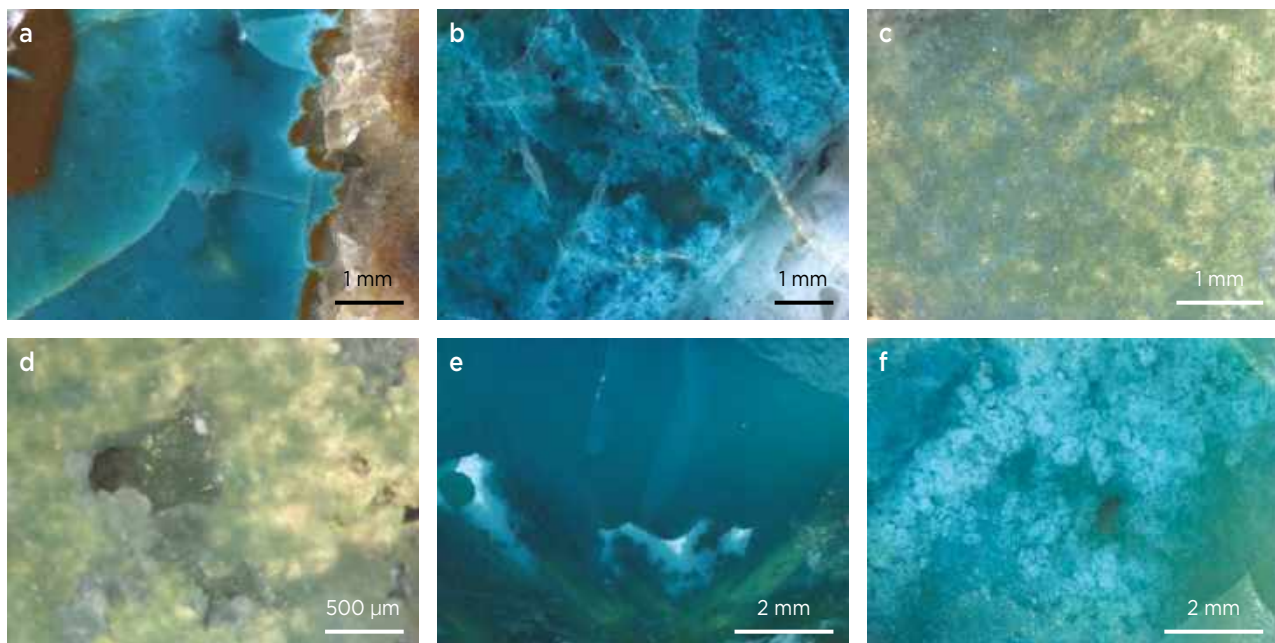
Figure 4: Viewed with the gemmological microscope, chrysocolla chalcedony commonly shows various inhomogeneities. (**a**) Cloud-like chrysocolla aggregates are present in sample TW-3. (**b**) Globular and irregular-shaped chrysocolla appears as cotton-like inclusions in specimen TW-10. (**c**) Chrysocolla in sample ID-3 occurs as mottled aggregates in a transparent matrix. (**d**) Small vugs also occur in specimen ID-3. (**e**) Irregular patches of whitish blue chrysocolla occur in a comparatively uniform blue matrix in sample US-I-1. (**f**) Rounded aggregates of whitish blue chrysocolla are present in specimen US-R-4. Photomicrographs by M. Ye in overhead lighting.
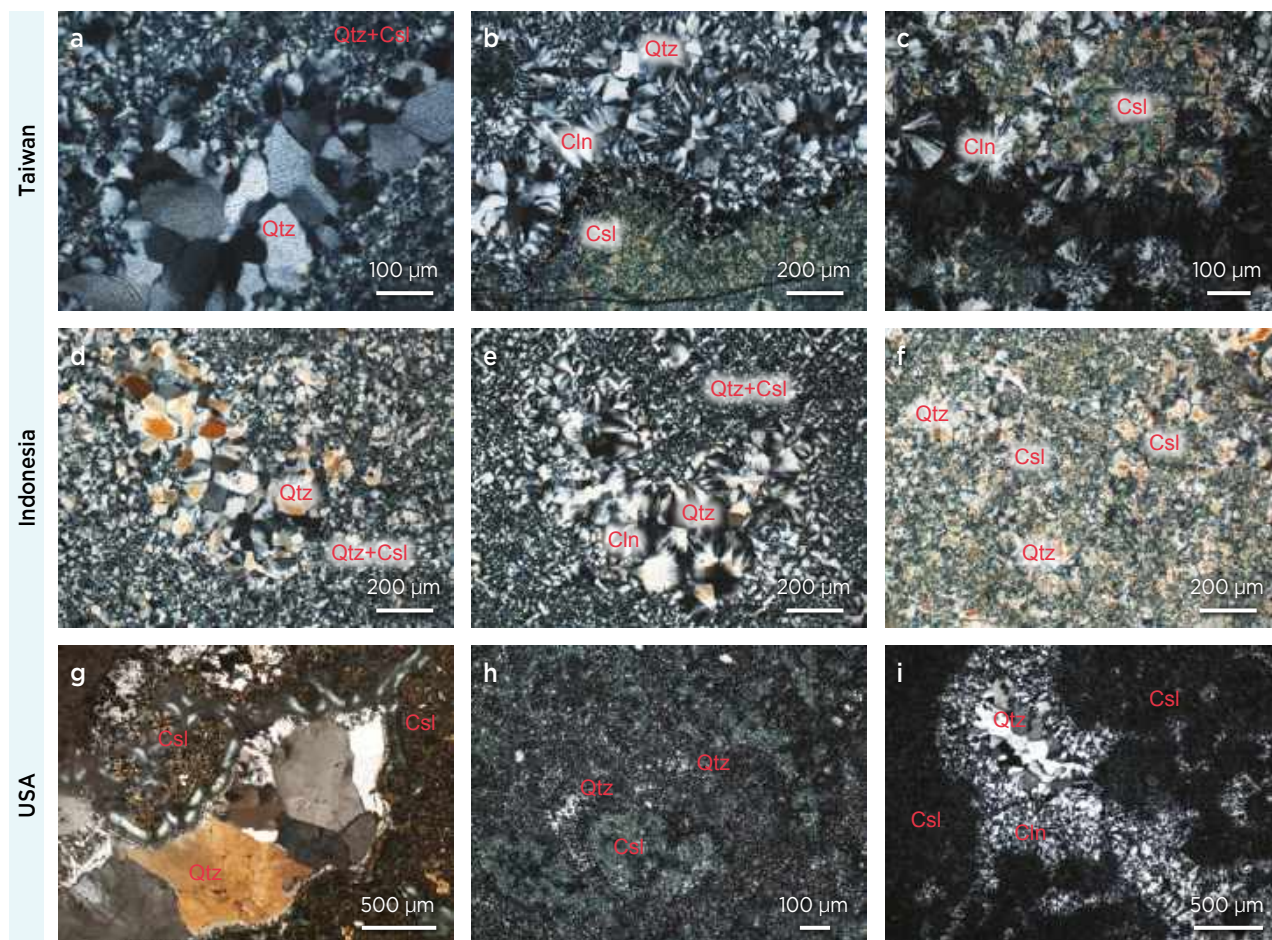
Figure 5: The typical appearance of chrysocolla chalcedony in petrographic thin sections is shown here in cross-polarised light for samples from Taiwan (a–c), Indonesia (d–f) and the USA (g–i). (**a**) The larger grains consist of crystalline quartz (Qtz) with hexagonal growth striations, which are surrounded by a mixture of fine-crystalline quartz and inconspicuous chrysocolla (Csl). (**b**) Chrysocolla aggregates show mostly yellowish green anomalous interference colours, while quartz occurs as fibrous chalcedony (Cln) and coarser crystals. (**c**) Chrysocolla forms distinct radiating spherical aggregates with bright anomalous interference colours, coexisting with spherical chalcedony. (**d**) An area of coarser-grained quartz is surrounded by a mixture of fine-grained quartz and chrysocolla. (**e**) Fine-grained chrysocolla aggregates surround chalcedony and locally coarser-crystalline quartz. (**f**) Fine-grained chrysocolla aggregates show brownish green anomalous interference colours. (**g**) An area of coarse-grained quartz (showing clear crystal boundaries and some growth striations) is surrounded by chrysocolla aggregates displaying anomalous interference colours that appear brown in finer-grained areas. (**h**) Chrysocolla aggregates displaying yellowish green interference colours are dispersed in micron-scale quartz. (**i**) Relatively coarse-grained quartz is surrounded by chalcedony and fine-grained chrysocolla aggregates showing dark green anomalous interference colours. (Note: In d–g, quartz shows some orange interference colours because those thin sections are a little thicker than the standard 30 μm.) Photomicrographs by M. Ye.

proved quite effective at revealing the distribution patterns of chrysocolla in chalcedony: the quartz-rich matrix appeared darker, while brighter areas had higher Cu, indicating greater chrysocolla content. Figure 6 shows representative BSE images of the blue areas of several samples.

In the Taiwanese specimens, chrysocolla usually formed irregular-shaped patches that were rimmed by a very thin layer of additional chrysocolla fibres (Figure 6a). Where the blue colour was relatively uniform, chrysocolla occurred as numerous small fibres forming various patterns (Figure 6b). Occasionally, chrysocolla

was present as radiating spherical masses (Figure 6c).

In the Indonesian samples, fibrous chrysocolla commonly grew around irregular chrysocolla-quartz patches, or formed fibrous clusters (Figure 6d). Occasionally, the chrysocolla fibres formed radiating spherical (Figure 6e) or botryoidal aggregates displaying more than one chrysocolla-quartz growth layer (Figure 6f).

In the USA specimens, chrysocolla generally was present as radiating fibres around quartz domains (Figure 6g) or formed irregular-shaped accumulations (Figure 6h). Sometimes, these two distribution patterns coexisted (Figure 6i).
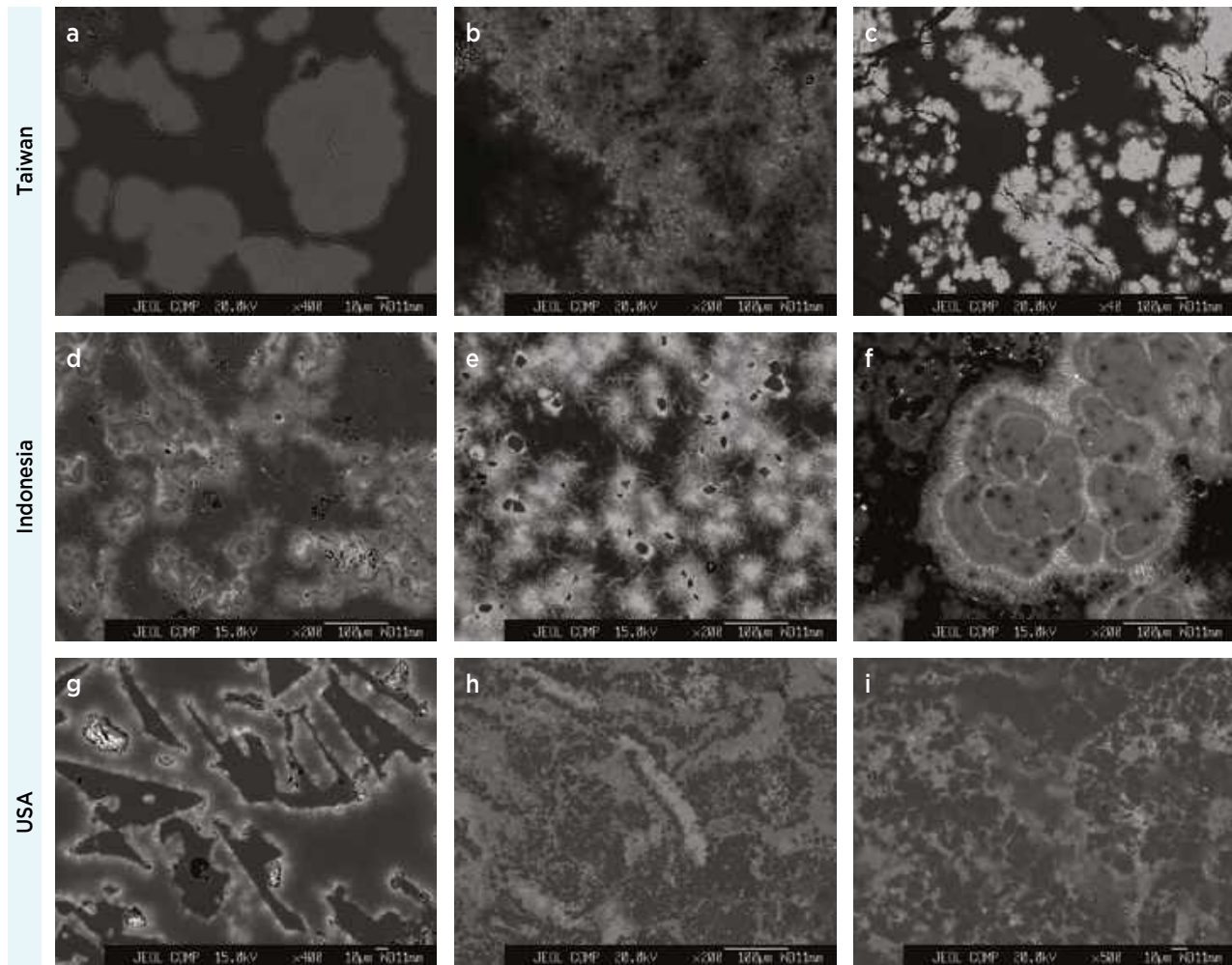
Figure 6: These representative BSE images are of samples from Taiwan (a–c), Indonesia (d–f) and the USA (g–i). (**a**) Irregular-shaped chrysocolla patches are surrounded by a very thin layer of chrysocolla fibres. (**b**) Aggregates of tiny chrysocolla fibres are present in some samples, as are (**c**) radiating spheres of chrysocolla. (**d**) Fibrous chrysocolla surrounds irregular chrysocolla-quartz patches. (**e**) Roughly spherical aggregates of fibrous chrysocolla are sometimes present. (**f**) Botryoidal aggregates sometimes have more than one chrysocolla-quartz layer, rimmed by radiating chrysocolla fibres. (**g**) Minute chrysocolla fibres radiate away from irregularly shaped quartz domains. (**h**) Irregular-shaped accumulations of chrysocolla also occur. (**i**) Fibrous chrysocolla is interspersed between irregular quartz-rich patches. Images by M. Ye.

Major Elements. The results of EPMA chemical analysis are listed in Table II. Si and Cu were the main components, and because of the presence of volatiles (such as water) the oxide sums were sometimes significantly less than 100 wt.%. The content of Si varied according to Indonesia > Taiwan > USA (averaging 87.42 > 80.77 > 76.89 wt.% SiO_2), while the amount of Cu showed the opposite trend of Indonesia < Taiwan < USA (averaging 11.27 < 16.38 < 19.02 wt.% CuO). Other elements such as Al, Mg and Ca were likely components of chrysocolla, as their values positively correlated with Cu in most samples; the concentrations of these elements were highest in the Taiwanese samples (averaging 0.42 wt.% Al_2O_3, 0.31 wt.% MgO and 0.38 wt.% CaO). The oxide concentrations of Na, K, Fe and Mn were all less than 0.1 wt.% (except for Fe in the USA samples, averaging 0.11 wt.% FeO).

Trace Elements. We analysed for 55 trace elements by LA-ICP-MS and then selected 14 of them that showed the best distinctions between the different origins; the results are summarised in Table III. The USA samples are separated into two groups (US-M and US-I/R) due to obvious compositional differences between them. One prominent feature of the Taiwanese samples was their abundant U content (averaging 5,040 ppmw), which was much higher than for our specimens from the other two origins (averaging less than about 50 ppmw). For the US-I/R samples, a high Mo content (averaging 7,720 ppmw) was diagnostic. Data for U and Mo are plotted in Figure 7, and show a distinct separation between the TW and US-I/R specimens. In addition, the Taiwanese samples contained more B (averaging 483 ppmw) and the US-I/R samples had greater Rb

Table II: Chemical composition by EPMA of chrysocolla chalcedony.*

Oxides (wt.%)	Taiwan	Indonesia	USA
SiO_2	38.55–99.54 (80.77)	49.51–99.21 (87.42)	39.09–98.40 (76.89)
CuO	0.09–48.18 (16.38)	0.22–46.71 (11.27)	0.36–48.74 (19.02)
Al_2O_3	<4.47 (0.42)	<0.16 (0.04)	<1.93 (0.27)
MgO	<2.36 (0.31)	<0.57 (0.08)	0.01–0.86 (0.24)
CaO	<2.14 (0.38)	<1.17 (0.20)	0.01–1.18 (0.29)
Na_2O	<0.30 (0.05)	0.01–0.47 (0.07)	<0.16 (0.03)
K_2O	<0.35 (0.06)	0.01–0.57 (0.07)	<0.10 (0.02)
FeO	<0.38 (0.04)	<0.04 (0.02)	<1.22 (0.11)
MnO	<0.27 (0.03)	<0.55 (0.09)	<0.10 (0.01)
Total	87.50–100.18 (98.46)	95.96–100.66 (99.18)	85.94–100.36 (96.89)

*Average concentrations are shown in parentheses.

(averaging 199 ppmw). Both the Taiwanese and US-I/R samples were rich in K (averaging 21,600 and 16,000 ppmw, respectively). Moreover, the Taiwanese samples were slightly higher in Na (averaging 1,160 ppmw), Sr (averaging 25.5 ppmw) and Ba (averaging 194 ppmw) than the specimens from the other two origins. Neither the Indonesian nor the US-M samples had much trace-element content (except Fe was greatest in the US-M samples, averaging 2,480 ppmw).

Spectroscopic Features

UV-Vis-NIR Absorption Spectra. All the samples showed very similar absorption spectra (e.g. Figure 8, red trace). A spectrum of a reference chrysocolla (blue trace, from author AHS's personal collection) showed the same absorption features: a broad band centred at 720 nm (due to Cu^{2+}; Shen *et al.* 2006), and three narrower bands at 1415, 1910 and 2257 nm. The narrower bands are attributed to various forms of hydroxyl bonds: the one at 2257 nm is from a combination of vibrations due to the bending and stretching of silanol groups (Si-OH); the

Figure 7: A logarithmic plot of U vs. Mo in chrysocolla chalcedony from the different localities shows high U with lower Mo in the Taiwanese samples, and low U with high Mo in the US-I/R specimens, making them easy to distinguish from the Indonesian and US-M samples (both of which contain much less U and Mo).

Table III: Selected trace-element concentrations by LA-ICP-MS in chrysocolla chalcedony.*

Elements (ppmw)	Taiwan	Indonesia	USA-M	USA-I/R
B	104–1170 (483)	<119 (68.4)	4.29–9.78 (7.34)	42.0–132 (83.8)
Na	142–3850 (1160)	71.1–742 (465)	59.0–208 (150)	142–445 (262)
K	585–48100 (21600)	105–518 (328)	19.2–291 (125)	8290–24500 (16000)
V	0.11–254 (75.9)	<65.0 (12.5)	16.9–74.2 (58.1)	4.83–66.3 (18.9)
Fe	<1610 (375)	<85.2 (20.9)	<12200 (2480)	<599 (232)
Ni	<37.4 (4.05)	<111 (30.4)	<4.81 (0.96)	<10.7 (7.39)
Ge	<3.02 (1.24)	<9.51 (2.56)	0.82–5.23 (3.55)	2.32–5.04 (3.72)
Rb	21.8–138 (70.9)	<1.17 (0.41)	0.06–3.70 (0.92)	110–347 (199)
Sr	2.23–96.3 (25.5)	<5.05 (2.64)	1.13–8.24 (4.44)	11.9–36.4 (22.9)
Mo	86.7–1010 (439)	<7.71 (2.14)	<30.3 (6.51)	**1030–20200 (7720)**
Ba	12.7–508 (194)	<4.22 (1.66)	<8.84 (2.52)	19.1–307 (142)
Ce	2.02–964 (157)	0.49–7.79 (2.41)	0.01–0.43 (0.14)	5.55–374 (101)
Sm	<3.99 (0.94)	<3.16 (0.68)	<0.36 (0.18)	0.07–23.7 (5.01)
U	**996–15300 (5040)**	9.98–147 (48.5)	2.28–58.2 (21.8)	11.2–90.0 (51.0)

*Average concentrations are shown in parentheses. Boldface numbers highlight high contents of U in Taiwanese samples and Mo in USA-I/R samples that are useful for distinguishing material from these localities.
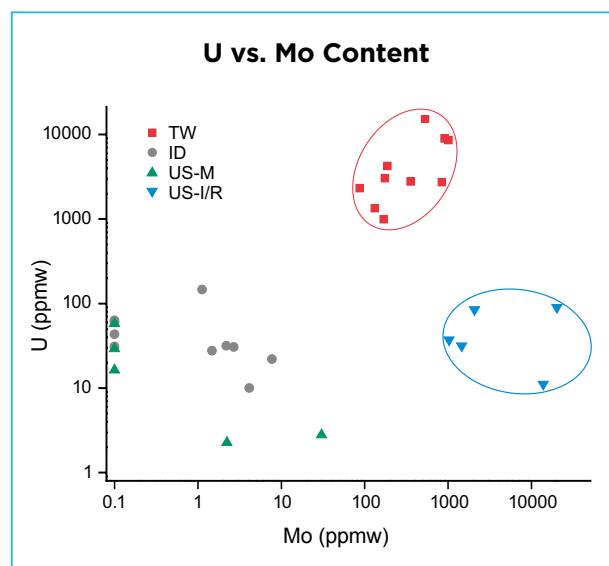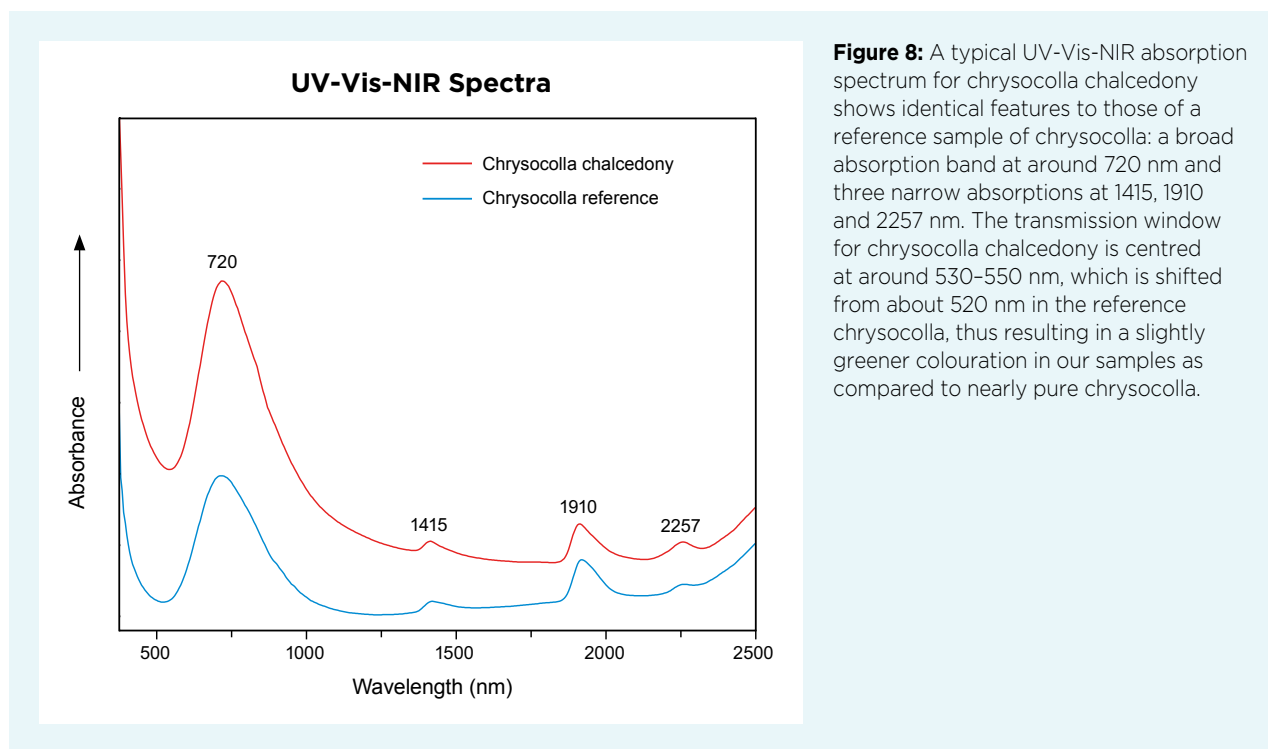
UV-Vis-NIR Spectra

Figure 8: A typical UV-Vis-NIR absorption spectrum for chrysocolla chalcedony shows identical features to those of a reference sample of chrysocolla: a broad absorption band at around 720 nm and three narrow absorptions at 1415, 1910 and 2257 nm. The transmission window for chrysocolla chalcedony is centred at around 530–550 nm, which is shifted from about 520 nm in the reference chrysocolla, thus resulting in a slightly greener colouration in our samples as compared to nearly pure chrysocolla.

one at 1910 nm corresponds to a combination of vibrations from bending and stretching of molecular water (H_2O); and the one at 1415 nm is the first overtone of O-H stretching vibrations of both molecular and silanol-group water (total OH; Graetsch 1994; Shen & Keppler 1995).

For the reference chrysocolla, the transmission window in the visible region ranged from about 400 to 600 nm and was centred at around 520 nm (with a calculated dominant wavelength of 500 nm, consistent with its blue colour; unpublished data), while for the chrysocolla chalcedony samples in the present study the transmission window was generally centred at around 530–550 nm, thus giving rise to their greener hue.

FTIR Spectroscopy. Figure 9 shows representative FTIR spectra for chrysocolla chalcedony samples from each locality (see Table DD-1 in *The Journal*'s online data depository for a summary of the main absorption bands). Sample numbers are accompanied by B to indicate the more-translucent blue areas and WB to denote the more-opaque whitish blue areas of a specimen. Most samples showed the dominant IR absorption features of α-quartz (e.g. TW-8 B, ID-1 B and US-M-1 B): a strong band at 1090 cm^{-1} with a shoulder at 1167 cm^{-1}; a pair of bands at 798 and 780 cm^{-1}; and additional bands at 515 and 465 cm^{-1}. Those in the 1200–600 cm^{-1} region are assigned to Si-O stretching vibrational modes, and those from 600 to 400 cm^{-1} are associated with Si-O bending vibrational modes (Etchepare *et al*. 1974).

Chrysocolla is an amorphous or poorly crystallised mineral, so it can be difficult to detect by vibrational spectroscopy. Samples with detectable chrysocolla showed features of both quartz and chrysocolla (the latter displaying a main absorption band centred at 1030 cm^{-1}; e.g. TW-3 B, ID-4 B and US-M-3 WB in Figure 9). In those spectra, the 1090 cm^{-1} band of quartz shifted to a slightly lower wavenumber of 1085 cm^{-1}. In addition, the main IR band of chrysocolla (typically 1025 cm^{-1}; RRUFF sample R050053) shifted to a slightly higher wavenumber of 1030 cm^{-1}.

For areas of a sample showing different diaphaneity, the more translucent portion (B) showed stronger quartz bands, while the more opaque zone (WB) displayed mixed features of quartz and chrysocolla, or even just chrysocolla (e.g. TW-4, US-M-3 and US-I-1 in Figure 9).

Raman Spectroscopy. Figure 10 shows representative Raman spectra for comparatively uniform blue areas of our samples (see Table DD-2 in the data depository for a summary of the main peaks). Most of the samples had a strong Raman peak for α-quartz near 464 cm^{-1} (e.g. TW-1, ID-1 and US-M-4), which involves the bending vibrations of O-Si-O (Etchepare *et al*. 1974). In addition, some spectra contained an obvious peak near 501 cm^{-1} (e.g. TW-6, ID-9 and US-R-4), corresponding to the Si-O-Si symmetric stretching-bending modes of moganite (a monoclinic quartz polymorph that is often present in the microcrystalline fibrous structure of chalcedony and agate;
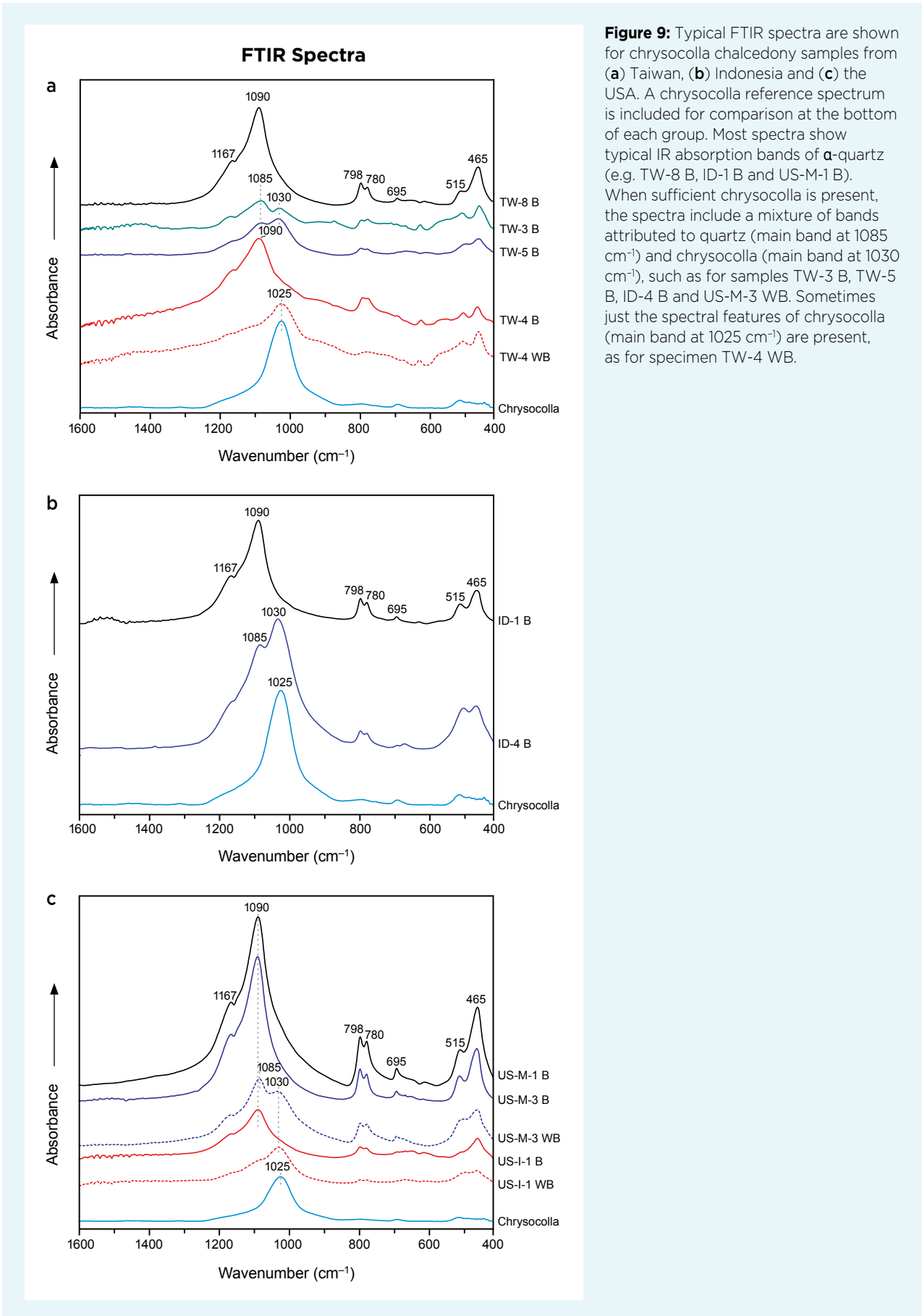
FTIR Spectra

Figure 9: Typical FTIR spectra are shown for chrysocolla chalcedony samples from (**a**) Taiwan, (**b**) Indonesia and (**c**) the USA. A chrysocolla reference spectrum is included for comparison at the bottom of each group. Most spectra show typical IR absorption bands of α-quartz (e.g. TW-8 B, ID-1 B and US-M-1 B). When sufficient chrysocolla is present, the spectra include a mixture of bands attributed to quartz (main band at 1085 cm⁻¹) and chrysocolla (main band at 1030 cm⁻¹), such as for samples TW-3 B, TW-5 B, ID-4 B and US-M-3 WB. Sometimes just the spectral features of chrysocolla (main band at 1025 cm⁻¹) are present, as for specimen TW-4 WB.
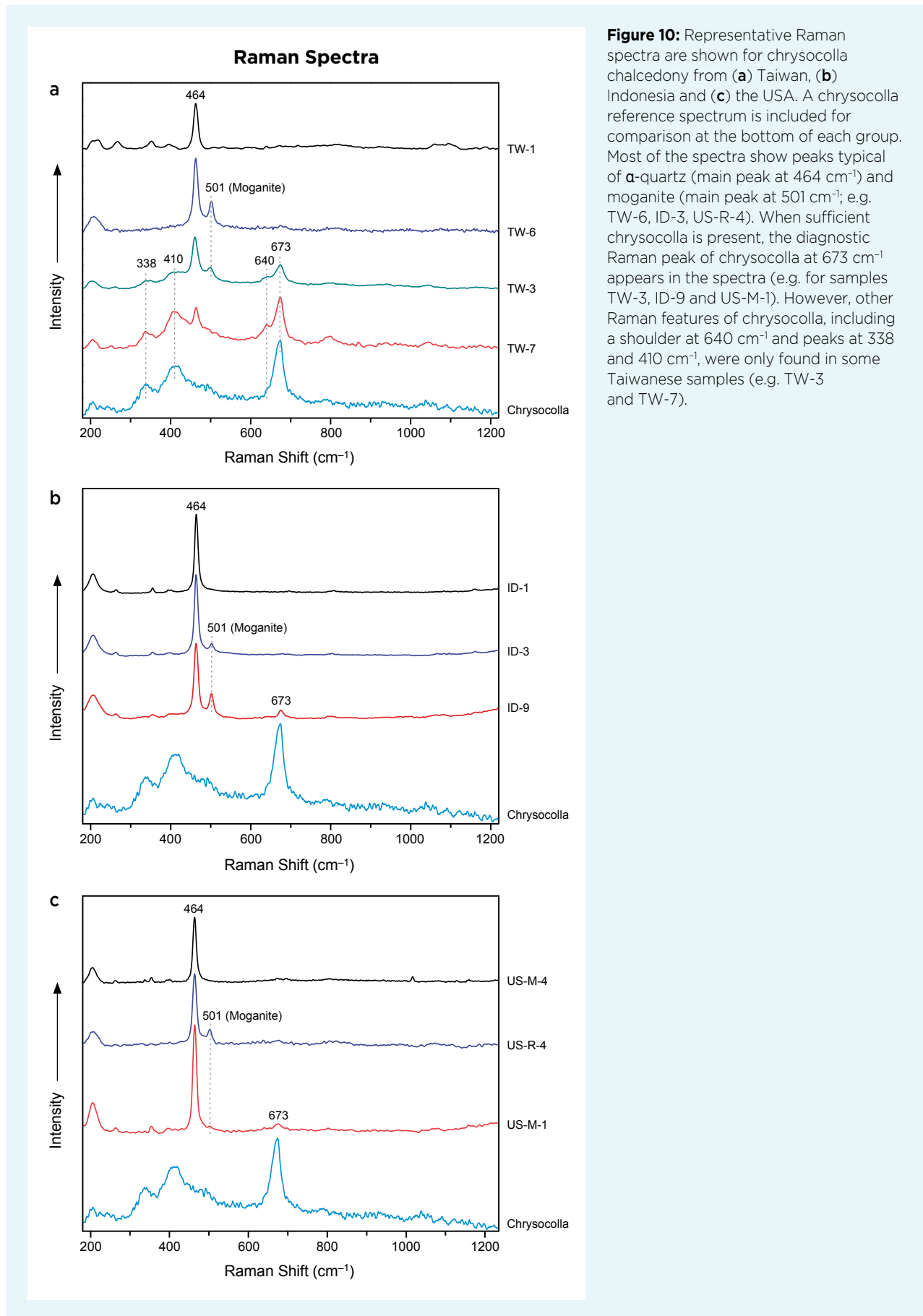
Raman Spectra

Figure 10: Representative Raman spectra are shown for chrysocolla chalcedony from (**a**) Taiwan, (**b**) Indonesia and (**c**) the USA. A chrysocolla reference spectrum is included for comparison at the bottom of each group. Most of the spectra show peaks typical of α-quartz (main peak at 464 cm^{-1}) and moganite (main peak at 501 cm^{-1}; e.g. TW-6, ID-3, US-R-4). When sufficient chrysocolla is present, the diagnostic Raman peak of chrysocolla at 673 cm^{-1} appears in the spectra (e.g. for samples TW-3, ID-9 and US-M-1). However, other Raman features of chrysocolla, including a shoulder at 640 cm^{-1} and peaks at 338 and 410 cm^{-1}, were only found in some Taiwanese samples (e.g. TW-3 and TW-7).

Kingma & Hemley 1994). The main chrysocolla peak at 673 cm^{-1} (RRUFF sample R050053) was present in some specimens (e.g. TW-3, ID-9 and US-M-1); again, chrysocolla is difficult to detect by vibrational spectroscopy. Other Raman peaks of chrysocolla at 338 and 410 cm^{-1} and the shoulder at 640 cm^{-1} were seen only in some Taiwanese specimens (e.g. TW-3 and TW-7), which might indicate better-crystallised chrysocolla in those samples.

Impurity Minerals

Most of the chrysocolla chalcedony specimens contained eye-visible inclusions, as well as some areas of host rock. Raman microspectroscopy was used to identify several of the corresponding impurity minerals.

Inclusions of malachite were present in the chrysocolla chalcedony of several specimens. In the Taiwanese and Indonesian samples, malachite formed globular green aggregates (Figure 11a, b), while in the US-M samples it occurred as needle-like radiating clusters (Figure 11c).

Other impurity minerals were identified in areas of host rock (Figure 12). In the Taiwanese samples, light yellowish brown calcite, yellowish brown goethite and brown hematite were common (Figure 12a, b), and

sometimes chalcopyrite was observed (Figure 12a). In sample TW-7, we identified some tiny grains of native copper dispersed in the chalcedony matrix or forming aggregates (Figure 12b). In some specimens, black manganite surrounded chrysocolla aggregates and, occasionally, the rhombic section of these crystals was visible in petrographic thin sections (Figure 12c).

The impurity minerals in the Indonesian samples were different, with most consisting of various copper minerals. Tiny red cuprite crystals were visible using oblique illumination within yellow or orange aggregates (Figure 12d, e). These aggregates were probably composed of a mixture of nanometre-sized cuprite and quartz, and were usually surrounded by dark areas containing cuprite and tenorite (Figure 12d). We also found some native copper in sample ID-4 that was locally surrounded by cuprite (Figure 12f).

The US-M samples commonly contained brownish black or reddish brown hematite (Figure 12g, h), as well as numerous minerals typical of propylitic alteration, such as epidote, albite and chlorite (Figure 12h). Black impurities in the US-I/R samples consisted of a vernadite-like mineral (Figures 12i and 13).
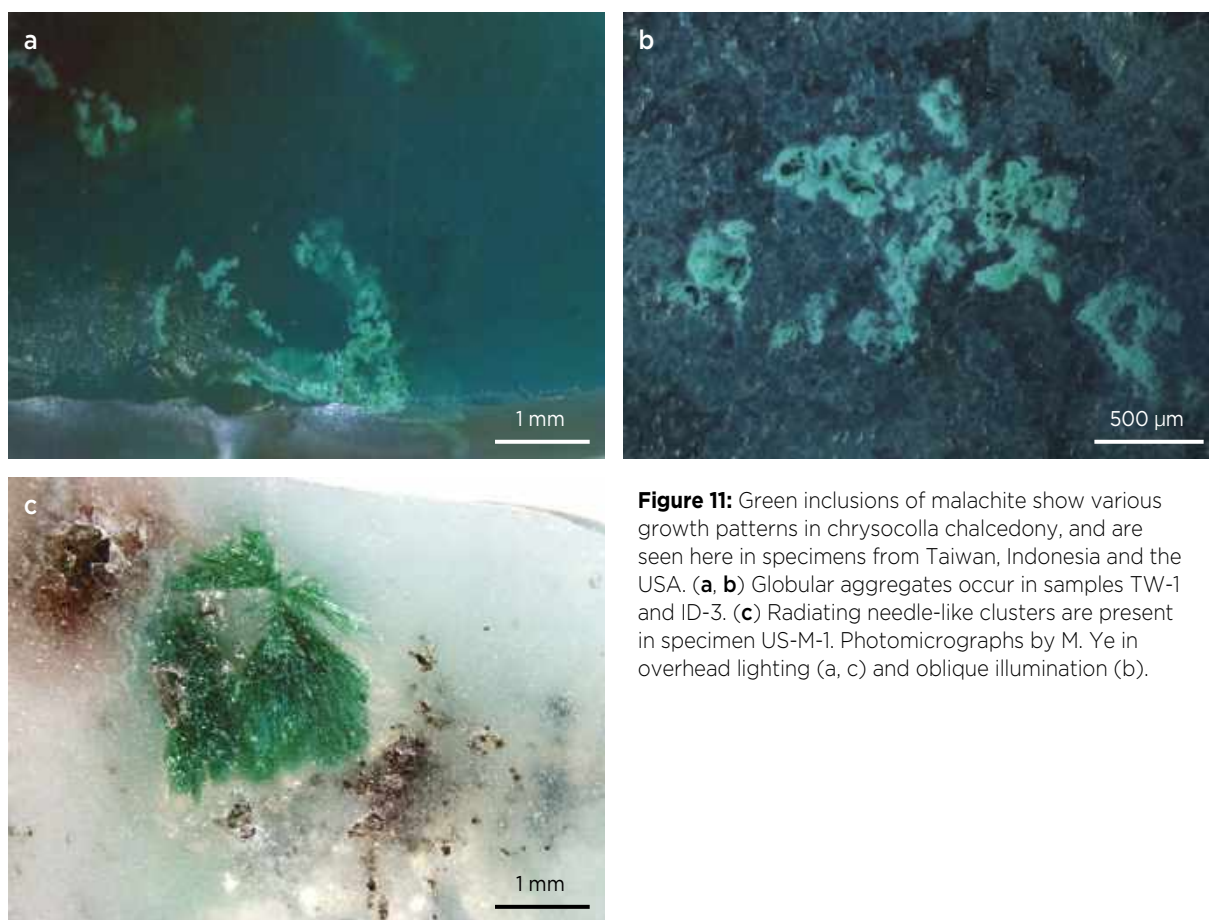
Figure 11: Green inclusions of malachite show various growth patterns in chrysocolla chalcedony, and are seen here in specimens from Taiwan, Indonesia and the USA. (**a**, **b**) Globular aggregates occur in samples TW-1 and ID-3. (**c**) Radiating needle-like clusters are present in specimen US-M-1. Photomicrographs by M. Ye in overhead lighting (a, c) and oblique illumination (b).
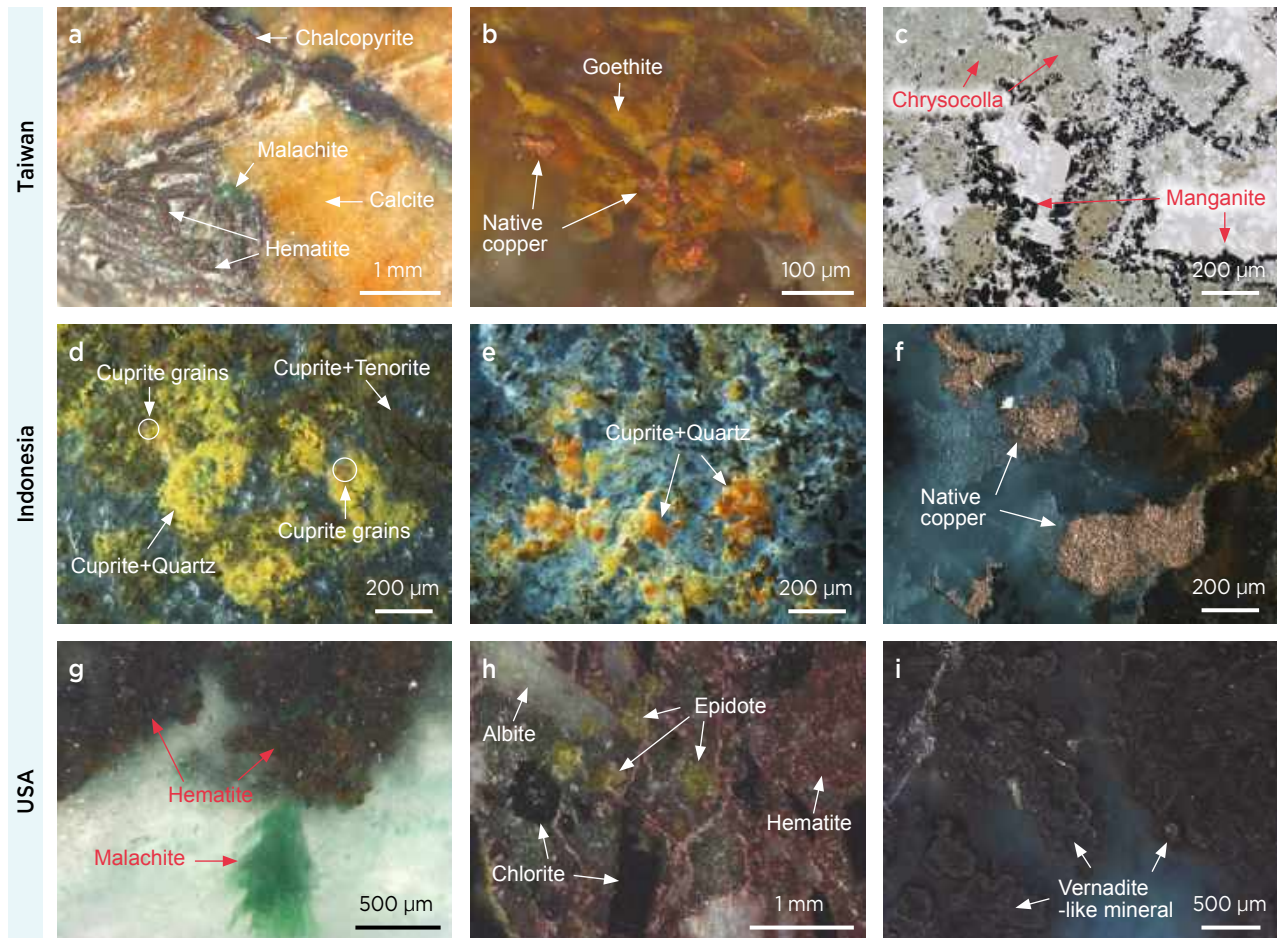
Figure 12: Various impurity minerals are observed in the host rock areas of the chrysocolla chalcedony. Images c–f were taken with a petrographic microscope from thin sections and the others were photographed with a gemmological microscope in polished slabs. (**a–c**) Samples from Taiwan contain calcite, goethite, hematite, malachite, chalcopyrite, native copper and manganite. (**d–f**) Specimens from Indonesia include various copper minerals, such as cuprite, tenorite and native copper. US-M samples show (**g**) areas of hematite (and adjacent malachite in the chrysocolla chalcedony), or (**h**) mineral assemblages that are typical of propylitic alteration. (**i**) A black vernadite-like mineral is present in some US-I/R samples. Photomicrographs by M. Ye with overhead lighting (a, b and g–i), plane-polarised light (c) and oblique illumination (d–f).

DISCUSSION

Major-Element Composition

The chemical constituents are consistent with a mixture of chrysocolla and quartz, with quartz being the main mineral. The Indonesian samples contained more quartz than those from the other two localities, which may be correlative with their better overall transparency. In the USA samples, chrysocolla was sometimes dispersed very unevenly (e.g. US-I-1 and US-R-2), thus leading to the high Cu averages.

We can estimate the proportion of chrysocolla and quartz in our samples using mineralogical methods (Zhao *et al.* 2004), considering that the chemical formula of chrysocolla is $(Cu,Al)_2H_2Si_2O_5(OH)_4 \bullet nH_2O$ (Anthony *et al.* 1990). EPMA results yielded the total Si contents of chrysocolla + quartz in more-translucent blue portions, more-opaque whitish blue zones and more-transparent near-colourless areas of our samples. Based on the Cu, Al, Mg and Ca concentrations, we calculated the Si content needed for chrysocolla. Then the Si content attributed to quartz was estimated by subtracting the Si in chrysocolla from the total Si content. This enabled us to calculate the following chrysocolla:quartz ratios:

Taiwan = from about $1:419_{(NC)}$ to $31:1_{(WB)}$
Indonesia = from about $1:504_{(NC)}$ to $3:1_{(WB)}$
USA = from about $1:176_{(NC)}$ to $40:1_{(WB)}$

Therefore, the more-transparent near-colourless portions (denoted above as NC) are dominated by quartz while the more-opaque whitish blue zones (WB) are enriched in chrysocolla. In the more-translucent blue areas, the chrysocolla:quartz ratios were intermediate between those of the other two types of areas.

Origin Determination Using Trace Elements

There are some obvious differences in trace-element composition between the samples from the different origins. Features that appear diagnostic for the Taiwanese samples are high U and lower Mo, and for the US-I/R samples, low U and high Mo (again, see Figure 7). To help further separate Indonesian and US-M samples, we performed statistical processing of our rather limited number of analyses using Fisher-LDA (see Li & Wang 2014; Zhang *et al*. 2019). Six trace elements were selected (B, V, Ni, Ge, Ce and Sm) by the software, and the following Fisher linear discriminant function equations were generated:

$$Y_{(ID)} = -6508.535 + (115.988 \times [B]) - (40.612 \times [V]) + (14.382 \times [Ni]) - (180.849 \times [Ge]) + (2179.482 \times [Ce]) + (3502.914 \times [Sm])$$

$$Y_{(US-M)} = -69.125 - (10.345 \times [B]) + (4.051 \times [V]) - (1.306 \times [Ni]) + (19.009 \times [Ge]) - (205.922 \times [Ce]) - (312.968 \times [Sm])$$

The cross-validation results were encouraging—nearly 100%—and three randomly selected 'unknown' samples fell into their correct origins. Nevertheless, the limited number of samples analysed means that this particular methodology is preliminary.

Identity of Impurity Minerals

Although cuprite crystals are intrinsically red, when the crystal size is very small (on the order of hundreds of nanometres), their apparent colour can range from yellow to orange to red (Markina *et al*. 2016). Both Raman spectra and chemical data showed that the yellow and orange aggregates in our Indonesian samples were composed of a mixture of cuprite and quartz, so they probably consist of nanometre-size cuprite dispersed in quartz.

Raman microspectroscopy of the dark areas of the US-I/R samples yielded a spectral pattern that was similar to vernadite (except for the 468 cm⁻¹ quartz peak; Figure 13), but not identical. EDXRF analysis of those same areas showed the presence of Mn, Si, Cu and Co. The chemical formula of vernadite is $(Mn,Fe,Ca,Na)(O,OH)_2 \cdot nH_2O$ (Anthony *et al*. 1990), and trivalent Fe, Cu, Co and Ni can isomorphously substitute for quadrivalent Mn (Hu *et al*. 2009), which makes this mineral difficult to characterise chemically. Therefore, we make a general assumption that the dark areas of those samples are due to a vernadite-like mineral.

Genesis of Chrysocolla Chalcedony

Based on the identities and textures of the impurity minerals in chrysocolla chalcedony, we infer that the following genetic mechanisms took place (cf. Einfalt & Sujatmiko 2006): (1) the oxidation and dissolution of primary or
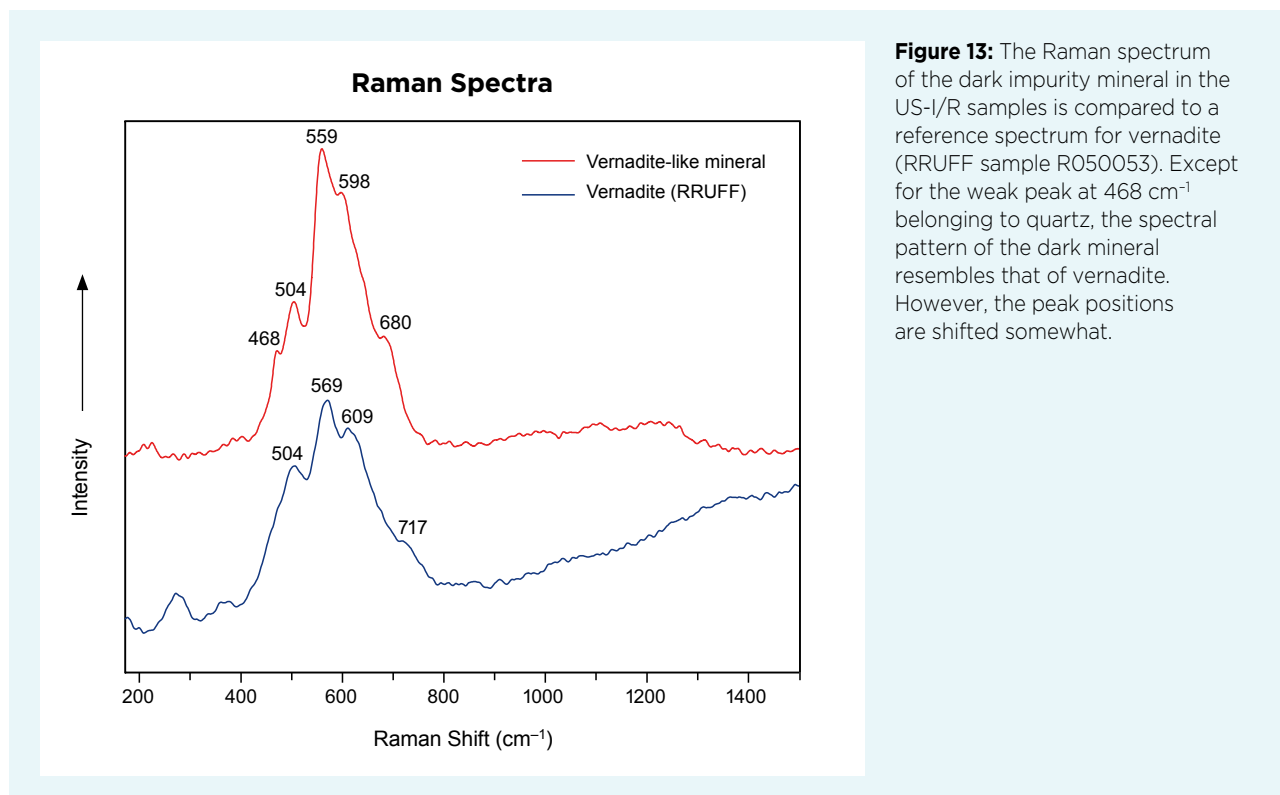
Figure 13: The Raman spectrum of the dark impurity mineral in the US-I/R samples is compared to a reference spectrum for vernadite (RRUFF sample R050053). Except for the weak peak at 468 cm⁻¹ belonging to quartz, the spectral pattern of the dark mineral resembles that of vernadite. However, the peak positions are shifted somewhat.

secondary Cu-sulphides (e.g. chalcopyrite) resulted in an assemblage consisting of malachite, native copper, cuprite and tenorite; and (2) malachite and Cu-oxides reacted with silicic fluids to form Cu-silicates, and during this process chrysocolla co-precipitated with quartz.

From the observation of our thin sections, the following crystallisation sequence is inferred for chrysocolla chalcedony: (1) crystal growth initially proceeded rapidly in a Cu-bearing and strongly siliceous aqueous solution or gel, from which fine-crystalline quartz co-precipitated with chrysocolla; (2) the crystallisation rate slowed down as Si and Cu were depleted from the growth medium, yielding chrysocolla-quartz aggregates surrounded by fibrous quartz; and (3) coarser crystalline quartz (and even vugs) followed in a low-concentration siliceous solution or gel (cf. Wang & Merino 1990; Einfalt & Sujatmiko 2006).

The actual crystallisation and precipitation processes are likely to be more complex than described above.

CONCLUSIONS

Using various gemmological, mineralogical and geochemical techniques, we identified several differences in the impurity minerals and trace-element contents between chrysocolla chalcedony from Taiwan, Indonesia and the USA. Figure 14 provides a preliminary identification flow chart for differentiating samples from these localities:

(1) If impurity minerals are visible with an optical microscope, Raman analysis should be used

to identify them. Material without observable impurity minerals should undergo trace-element analysis by LA-ICP-MS.

(2) For impurity minerals identified by Raman analysis:
- A copper mineral mixture (e.g. cuprite, tenorite and native copper) suggests Indonesian material.
- Black manganite occurs in Taiwanese material.
- An assemblage of iron (hydr)oxides, copper minerals (chalcopyrite and native copper) and calcite is also common in samples from Taiwan.
- A vernadite-like mineral occurs in material from the Inspiration and Ray mines in the USA.
- Minerals associated with propylitic alteration (epidote, albite and chlorite) may coexist with radiating malachite aggregates in samples from the Morenci mine in the USA.

(3) For trace-element concentrations determined by LA-ICP-MS:
- High U and lower Mo values typify samples from Taiwan.
- Low U and high Mo values are indicative of material from the Inspiration and Ray mines in the USA.
- Low U and low Mo values appear common in samples from Indonesia and the Morenci mine.
- Fisher-LDA analysis may be necessary to separate samples from Indonesia and the Morenci mine.

Origin Determination Flow Chart
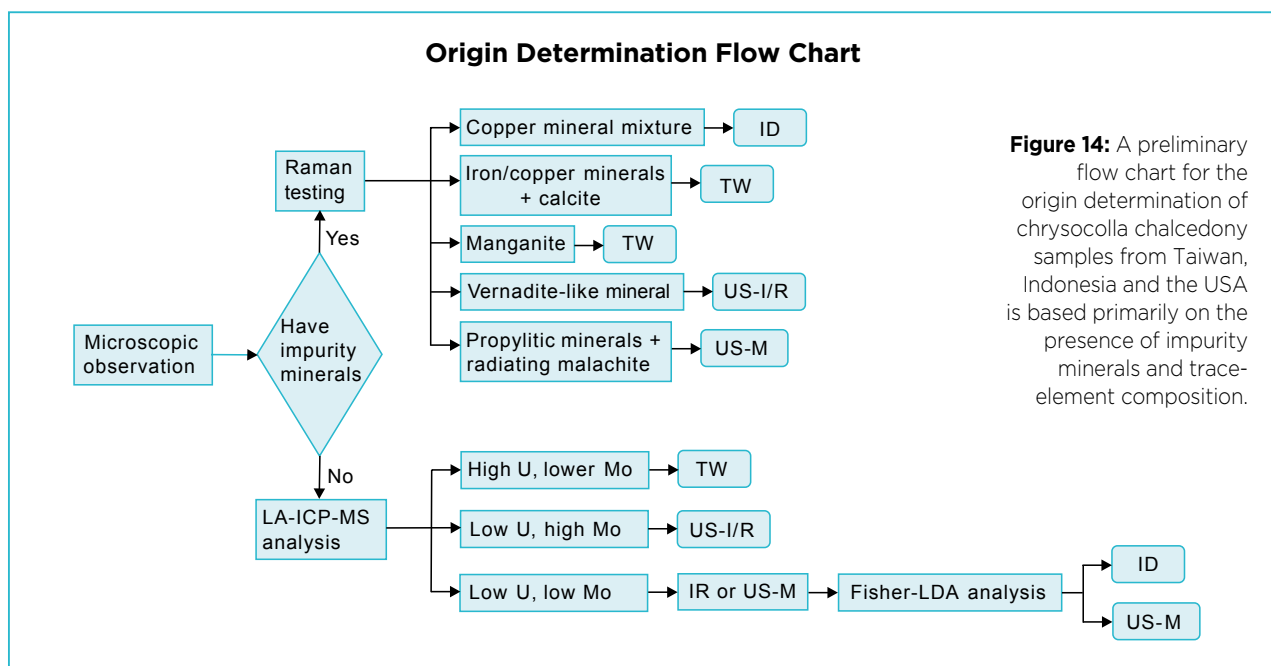
Figure 14: A preliminary flow chart for the origin determination of chrysocolla chalcedony samples from Taiwan, Indonesia and the USA is based primarily on the presence of impurity minerals and trace-element composition.

Figure 15: This necklace features chrysocolla chalcedony from Indonesia and Taiwan (approximately 8–15 ct) accompanied by diamonds and pink sapphires and set in 18 ct white gold. Photo courtesy of Taiwan She Say Jewellery Co.

Applying a combination of the approaches described above will help give a clearer determination of a sample's origin. The Fisher-LDA model established in this research is still at its early stage and further development is needed. In addition, more samples should be examined from the localities studied here and from other deposits (Peru and Mexico).

Chrysocolla chalcedony can be incorporated into beautiful jewellery pieces (see, e.g., Figure 15) that can be quite valuable, particularly when they contain well-matched stones. With decreasing production of high-quality material from some deposits, we expect that chrysocolla chalcedony from certain origins will become rarer (and also more valuable) in the future. Therefore, systematic research on the similarities and differences between chrysocolla chalcedony from various geographic locations is timely and necessary.

REFERENCES

Anthony, J.W., Bideaux, R.A., Bladh, K.W. & Nichols, M.C. 1990. *Handbook of Mineralogy*. Mineral Data Publishing, Tucson, Arizona, USA.

Chen, Q., Yuan, X. & Jia, L. 2011. Study on the vibrational spectra characters of Taiwan blue chalcedony. *Spectroscopy and Spectral Analysis*, **31**(6), 1549–1551 (in Chinese with English abstract).

Creasey, S.C. 1984. *The Schultze Granite, the Tea Cup Granodiorite, and the Granite Basin Porphyry; a Geochemical Comparison of Mineralized and Unmineralized Stocks in Southern Arizona*. U.S. Geological Survey Professional Paper 1303, 41 pp., https://doi.org/10.3133/pp1303.

Einfalt, H.C. & Sujatmiko, H. 2006. Chrysocolla quartz from the Bacan Archipelago, South Halmahera Regency, North Maluku Province, Indonesia. *Journal*

of Gemmology, **30**(3–4), 155–168, https://doi.org/10.15506/JoG.2006.30.3.155.

Emerson, E. & Darley, J. 2010. Gem News International: Chrysocolla chalcedony from Acarí, Peru. *Gems & Gemology*, **46**(2), 148–149.

Enders, M.S. 2000. *The evolution of supergene enrichment in the Morenci porphyry copper deposit, Greenlee County, Arizona*. PhD dissertation, University of Arizona, Tucson, Arizona, USA, 517 pp., https://repository.arizona.edu/handle/10150/289155.

Etchepare, J., Merian, M. & Smetankine, L. 1974. Vibrational normal modes of SiO_2. I. α and β quartz. *Journal of Chemical Physics*, **60**(5), 1873–1876, https://doi.org/10.1063/1.1681287.

Graetsch, H. 1994. Chapter 6. Structural characteristics of opaline and microcrystalline silica minerals. *In*: Heaney, P.J., Graetsch, H., Prewitt, C.T. & Gibbs, G.V. (eds) *Silica: Physical Behavior, Geochemistry, and Materials Applications*. Mineralogical Society of America, Washington DC, USA, 209–232, https://doi.org/10.1515/9781501509698-011.

Hu, D., Chu, F. & Yao, J. 2009. Study on vernadite in Co-rich crust from the central Pacific Ocean. *Journal of Jilin University (Earth Science Edition)*, **39**(4), 706–710 (in Chinese with English abstract).

Hyršl, J. 2001. Gemstones of Peru. *Journal of Gemmology*, **27**(6), 328–334, https://doi.org/10.15506/jog.2001.27.6.328.

Kingma, K.J. & Hemley, R.J. 1994. Raman spectroscopic study of microcrystalline silica. *American Mineralogist*, **79**(3–4), 269–273, www.minsocam.org/ammin/AM79/AM79_269.pdf.

Koivula, J.I., Kammerling, R.C. & Fritsch, E. (eds) 1992. Gem News: Chrysocolla-colored chalcedony from Mexico. *Gems & Gemology*, **28**(1), 59–60.

Laurs, B.M. 2015. Gem Notes: Chrysocolla chalcedony from Spain. *Journal of Gemmology*, **34**(6), 472–473.

Laurs, B.M. 2019. Gem Notes: Chrysocolla from the Ray mine, Arizona, USA. *Journal of Gemmology*, **36**(6), 499.

Li, C. & Wang, B. 2014. Fisher linear discriminant analysis. Lecture notes, CS 6140: Machine Learning, Northeastern University Khoury College of Computer Sciences, Boston, Massachusetts, USA, www.ccs.neu.edu/home/vip/teach/MLcourse/5_features_dimensions/lecture_notes/LDA/LDA.pdf, 31 August, accessed 12 June 2020.

Lin, S. 2008. Blue chalcedony from Taiwan province. *Journal of Gems & Gemmology*, **10**(2), 5–8 (in Chinese with English abstract).

Markina, N.E., Pozharov, M.V. & Markin, A.V. 2016. Synthesis of copper(I) oxide particles with variable color: Demonstrating size-dependent optical properties for high school students. *Journal of Chemical Education*, **93**(4), 704–707, https://doi.org/10.1021/acs.jchemed.5b00563.

Shen, A. & Keppler, H. 1995. Infrared spectroscopy of hydrous silicate melts to 1000 °C and 10 kbar: Direct observation of H_2O speciation in a diamond-anvil cell. *American Mineralogist*, **80**(11–12), 1335–1338, https://doi.org/10.2138/am-1995-11-1223.

Shen, A., Fritz, E., DeGhionno, D. & McClure, S. 2006. Identification of dyed chrysocolla chalcedony. *Gems & Gemology*, **42**(3), 140.

Wang, Y. & Merino, E. 1990. Self-organizational origin of agates: Banding, fiber twisting, composition, and dynamic crystallization model. *Geochimica et Cosmochimica Acta*, **54**(6), 1627–1638, https://doi.org/10.1016/0016-7037(90)90396-3.

Zhang, Z., Ye, M. & Shen, A.H. 2019. Characterisation of peridot from China's Jilin Province and from North Korea. *Journal of Gemmology*, **36**(5), 436–446, https://doi.org/10.15506/JoG.2019.36.5.436.

Zhao, S.R., Bian, Q.J. & Ling, C. (eds) 2004. *Crystallography & Mineralogy*. Higher Education Press, Beijing, China, 478 pp. (in Chinese).

The Authors

Min Ye and Prof. Andy H. Shen
Gemmological Institute and Center for Innovative Gem Testing Technology, China University of Geosciences, No. 388 Lumo Rd., 430074 Wuhan, China
Email: shenxt@cug.edu.cn
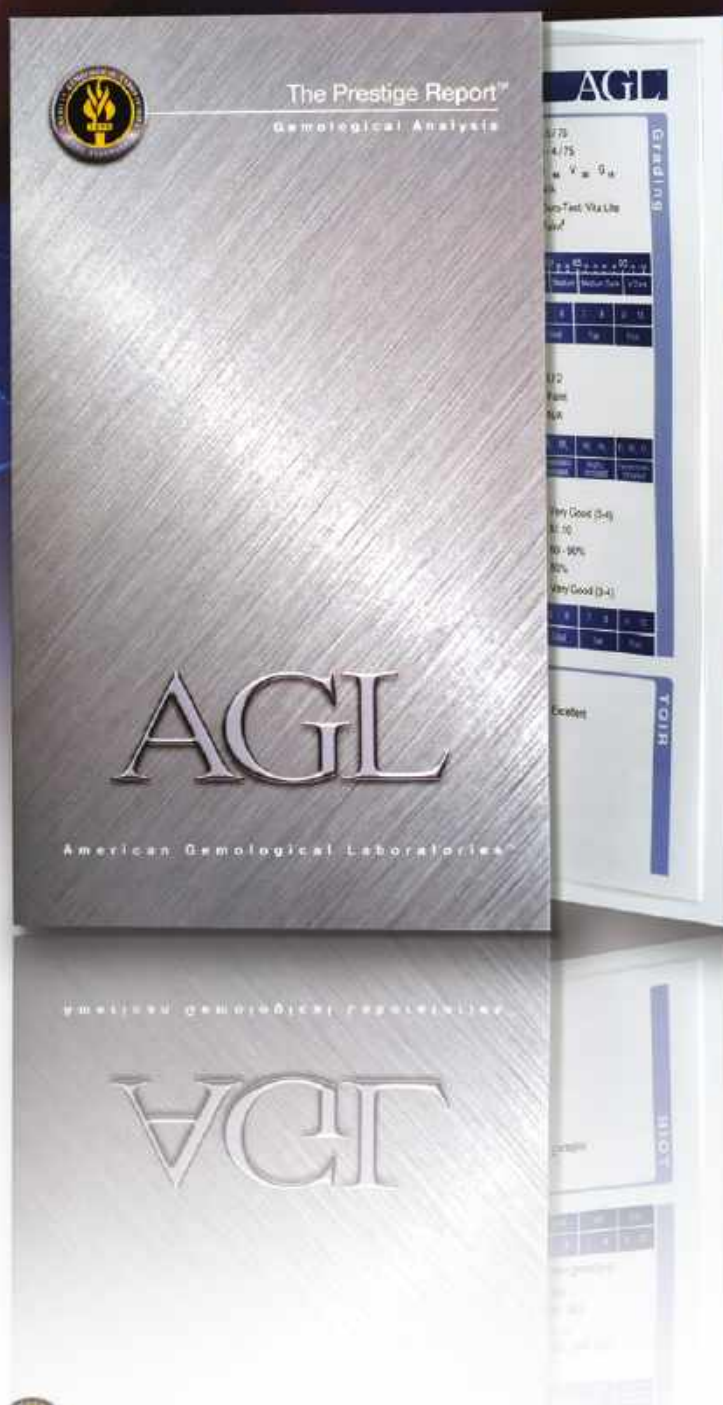
A Case Study of Ivory Species Identification Using a Combination of Morphological, Gemmological and Genetic Methods

Laurent E. Cartier, Michael S. Krzemnicki, Mario Gysi, Bertalan Lendvay and Nadja V. Morf

ABSTRACT: Twenty-one items sold as mammoth ivory in China were submitted to the Zurich Institute of Forensic Medicine (University of Zurich, Switzerland) and SSEF for testing. The aim of this case study was to identify these samples using macroscopic morphological diagnostics, microscopic examination, FTIR spectroscopy, trace-element analysis and additional minimally destructive DNA analysis (of approximately 100 mg of powder) of a region of the cytochrome *b* gene to assign taxonomic identification. Morphological features (Schreger angles) shown by five of the samples were characteristic of extinct Proboscideans (mammoths), and one other specimen displayed unnatural layering that identified it as an ivory imitation. FTIR spectroscopy further showed the imitation was an artificial resin, while infrared spectra of the other samples displayed overlapping features characteristic of carbonated hydroxyapatite (i.e. ivory or bone). Like FTIR spectroscopy, trace-element chemistry cannot be used to separate species. DNA analysis could in some cases differentiate extinct (mammoth) from extant (African and Asian elephant) Proboscidean species, and also identified one specimen as cattle bone. Combining morphological, gemmological and genetic approaches can increase the amount of evidence available to identify the species origin of ivory.

Ivory (e.g. Figure 1), a mammalian tooth or tusk of commercial interest, has been valued since ancient times (Espinoza & Mann 2000). Ivory is produced by a large number of animal taxa (e.g. walrus, warthog and whale), among which elephant ivory is the most studied due to its value, popularity and cultural importance (Campbell Pedersen 2015). African (*Loxodonta* spp.) and Asian (*Elephas maximus*) elephants, along with their extinct relatives (e.g. mammoths, *Mammuthus* spp.), belong to the mammalian taxonomic order Proboscidea. These taxa produce ivory that is made up of collagen and carbonated hydroxyapatite (Edwards *et al.* 2006), which can be finely carved and is therefore sought after.

Among the extinct Proboscidea species, only the ivory of the woolly mammoth (*Mammuthus primigenius*) is suitable for carvings and jewellery use, as this is the only species with tusks that have been well preserved since the end of the Pleistocene (10,000–11,000 years ago) in high-latitude permafrost areas (Nikolskiy *et al.* 2011). Ivory from *Mammuthus primigenius* is abundant in certain parts of Siberia and Alaska, and mammoth ivory has appeared more widely on the market in recent years (Vigne & Martin 2014), as restrictions on the international trade of elephant ivory have taken force (e.g. under the Convention on International Trade in Endangered Species of Wild Fauna and Flora, or CITES; www.cites.org/eng/niaps).

Figure 1: The 21 specimens submitted for testing (including a strand of 108 beads that are grouped together as sample no. 13) were purchased in China, where they were represented as 'mammoth ivory'. See Table I for sample weights. Photo by Vito Lanzafame, SSEF.

Given the regulations on elephant ivory, and the free trade in mammoth ivory, it is necessary to develop and apply scientific methods that can assign an ivory sample to its correct taxonomic species.

This article presents a case study exploring a range of methods used collectively to identify the species of 21 samples that were sold on the Chinese market as mammoth ivory. Our examination included morphological evaluation based on Schreger angles, Fourier-transform infrared (FTIR) spectroscopy and trace-element analysis of six selected specimens. When morphological assessment of the species was not possible, we performed DNA analysis.

BACKGROUND

Currently, the identification of elephant and mammoth ivories, and their distinction from other forms of ivory or imitations, rests largely on macroscopic morphological observation, although it can be supplemented by DNA analysis depending on the context. Morphological identification was outlined by Espinoza & Mann (2000) in a document that is widely used by customs agents and wildlife forensic scientists worldwide; this

reference guide was updated in August 2020 (Baker *et al.* 2020). The main criterion to identify ivory is the presence of Schreger lines, which are present only in Proboscidean material. The angle formed by the Schreger lines can be used to differentiate between extant (recently living) African and Asian elephants, and extinct Proboscidea (mammoths), as explained below. However, Schreger lines are often not visible enough on processed (carved and polished) samples to make a conclusive identification.

Ivory has been studied using techniques such as Raman and Fourier-transform infrared spectroscopy (Edwards & Farwell 1995; Shimoyama *et al.* 2004; Edwards *et al.* 2006), along with detailed visual analysis and trace-element studies (Singh *et al.* 2006; Yin *et al.* 2013). However, as outlined by the United Nations in its *Guidelines on Methods and Procedures for Ivory Sampling and Laboratory Analysis* (UNODC 2014), FTIR and Raman spectroscopy can be employed to distinguish genuine carbonated hydroxyapatite-based ivory from ivory imitations such as resin, but FTIR spectroscopy should not be used to determine the animal species. Therefore, UNODC (2014) recommends that morphological and genetic methods be used for the forensic species identification of ivory.

Table I: Results of the morphological analysis of the 21 samples.

Sample no.	Item	Weight (ct)	Schreger lines visible?	CDJ[a] visible?	Schreger angle[b] (average and min.–max.)	Taxonomic identification[c]
1	Ring, carved	6.71	Yes	No	—	Proboscidea
2	Ring, carved	4.33	Yes	No	—	Proboscidea
3	Ring, carved	71.59	Yes	No	—	Proboscidea
4	Bangle	117.42	Yes	No	—	Proboscidea
5	Ring, carved	63.42	Yes	No	—	Proboscidea
6	Bead, carved	19.50	Yes	No	—	Proboscidea
7	Head and stand, carved	74.81	Yes	Yes (head)	83.2° (77°–87°)	Extinct Proboscidea
8	Plaque, carved	70.98	Yes	No	—	Proboscidea
9	Plaque, carved	211.13	Yes	Yes	94.2° (91°–99°)	Extinct Proboscidea
10	Plaque, carved	52.21	Yes	No	—	Proboscidea
11	Slab	10.36	No	No	—	Not possible
12	Plaque, carved	109.20	Yes	Yes	72.6° (53°–86°)	Extinct Proboscidea
13	Beads (108), drilled	~1.2 each	Yes	Yes (seven beads)	Two beads: 72.6° (70°–75°), 84.5° (82°–88°)	Extinct Proboscidea
14	Plaque, polished	17.91	Yes	No	—	Proboscidea
15	Snuff bottle	150.53	No	No	—	Not possible
16	Mammoth, carved	70.27	Yes	Yes (tusks)	Not possible (too small)	Proboscidea
17	Pipe mouthpiece, carved	47.62	No	No	—	Not possible
18	Bead, carved	59.46	Yes	No	—	Proboscidea
19	Stamp, carved	247.02	No	No	—	Ivory imitation
20	Stamp, carved	151.59	No	No	—	Not possible
21	Block, painted	82.78	Yes	Yes	82.2° (77°–86°)	Extinct Proboscidea

[a] CDJ = cementum-dentine junction.
[b] Schreger angles are provided only for samples on which the CDJ was visible.
[c] The standalone term 'Proboscidea' indicates that it was not possible to differentiate whether a specimen consisted of extant or extinct Proboscidean ivory.

Various genetic methods have been developed and used to identify species of Proboscidean ivory (Gupta *et al.* 2011; Wozney & Wilson 2012; Lee *et al.* 2013; Kitpipit *et al.* 2016, 2017; Conte *et al.* 2019; Ngatia *et al.* 2019). However, among these studies, only Lee *et al.* (2013) used the so-called *DNA barcoding* methodology—that is, using a specific and targeted genome region, which allows identification of both extinct and extant Proboscidean species, as well as the species of other types of ivory or ivory imitations (e.g. bone). All other previously applied techniques simply give a negative result (i.e. not Proboscidean ivory) if the ivory item originated from taxa other than those specifically targeted by the assay. Applying DNA barcoding methodology using universal primers[1] can be less sensitive than a species-specific assay, but it can provide additional information about a tested item, as it allows for the identification of a broad array of species. Such markers show variations between species, but are generally invariable within species; this makes them ideal for differentiating species

---

[1] For definitions of some terminology related to genetic testing, see the glossary on p. 157 of Cartier *et al.* (2018).

based on DNA (Tobe & Linacre 2010). Nevertheless, analysing these markers (based on Sanger sequencing) is not possible if a sample contains a mixture of DNA from different species. This is often the case when a specimen is very old and/or has little DNA (such as ivory from extinct Proboscideans), for which various contaminants (e.g. bacterial DNA, polishing residues or human DNA) can make up significant portions of the total DNA. To help deconvolute such species mixtures, a technique called *massive parallel sequencing* can be used (Budowle *et al.* 2016).

Although not employed in this study, isotopic analysis of ivory samples (van der Merwe *et al.* 1990; Ziegler *et al.* 2016) has been applied as an investigative technique to combat elephant poaching by further narrowing the geographic source region of an ivory sample. Another test—also beyond the scope of this article—to determine whether unknown specimens are from extinct or extant Proboscideans is age dating (e.g. carbon-14). This technique has been used to determine the age of seized elephant ivory (Schmied *et al.* 2012; Cerling *et al.* 2016), and has also been applied to mammoth samples (Basilyan *et al.* 2011), and could thus be useful to distinguish recent elephant ivory from extinct mammoth ivory. Furthermore, radiocarbon age dating can determine whether or not an elephant lived before or after the atomic 'bomb peak' (around 1950), and can thus be used to determine whether ivory should be classified as pre-CITES material (i.e. before 1 July 1975 for the Asian elephant and before 26 February 1976 for the African elephant; Brunnermeier *et al.* 2012; Schmied *et al.* 2012). Importantly, these dates and laws are not the same in every country; some are stricter or date further back than CITES regulations. For example, the UK has banned the sale of elephant ivory worked after 1947 (Harris *et al.* 2019).

MATERIALS AND METHODS

Twenty-one specimens (including multiple beads sold as a strand and classified as one sample; Figure 1 and Table I) were purchased as mammoth ivory from different dealers and shops in China and submitted to the Zurich Institute of Forensic Medicine and SSEF for testing.

Morphological Analysis Using Schreger Angles

The Schreger pattern was first described by Bernard Schreger (1800), and consists of sets of intersecting lines that radiate in a spiral fashion from the axis of a tusk (Trapani & Fisher 2003), as for example in Figure 2. According to Trapani and Fisher (2003, p. 429), 'light and dark regions forming these lines are thought to be macroscopic manifestations of systematic shifts in undulatory pathways of dentinal tubules, produced by odontoblasts as they move towards the tusk axis during dentin [*sic*] deposition'. The Schreger angle is the angle at which dextral and sinistral Schreger lines intersect. Outer Schreger angles (i.e. those closest to the outside of the tusk) are acute in extinct Proboscideans (i.e. mammoths) and obtuse in extant Proboscideans (i.e. elephants; Espinoza & Mann 1993, 2000). Mammoth ivory samples examined by Espinoza & Mann (2000) consistently showed outer Schreger angles that averaged below 100° (typically 73°), whereas the tested elephant specimens exhibited angles with averages above 100° (typically 124°). For samples with angles falling in the range of 90°–110°, it is important that multiple angle measurements be carried out and averaged (Espinoza & Mann 2000).
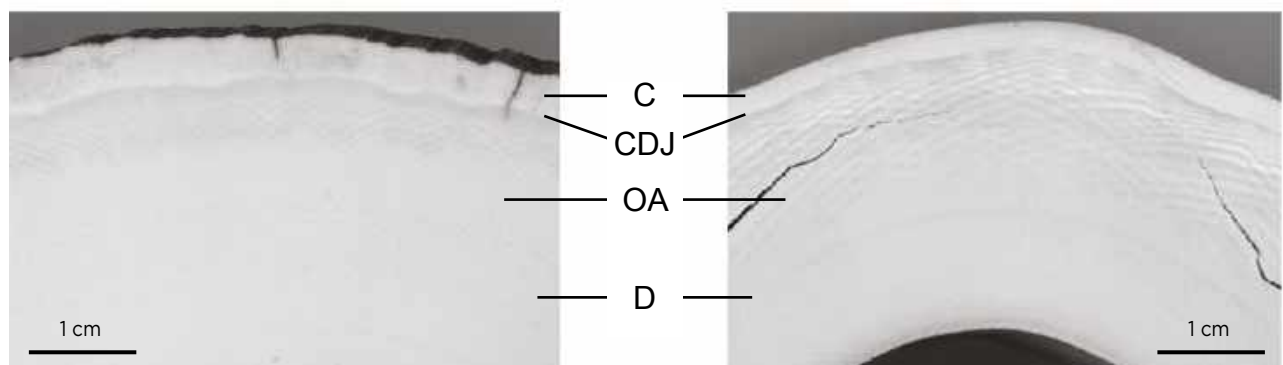

Figure 2: The angles formed by Schreger lines are shown here in extinct (left) and extant (right) Proboscidean ivory cross-sections. The outer Schreger angles (OA) in the dentine (D) closest to the cementum (C) show diagnostic differences. The cementum-dentine junction (CDJ) must be present in a sample for Schreger angles to be used reliably. Photos by Ed Espinoza.

The cementum (a layer of mineralised dental tissue which covers the outside of the tusk) must be visible for the correct reading of Schreger angles, in order to orient the sample within the tusk. Unfortunately, the cementum-dentine junction (CDJ) is not always present in worked specimens. Because only the outer Schreger lines can be used for diagnostic angle measurement, it is vital to orient a sample based on the presence of the CDJ. Research by Trapani and Fisher (2003) on specimens with and without cementum confirmed that if a sample cannot be oriented, and if the Schreger angles are measured from inner lines, then misidentifications can occur.

All 21 specimens in this study were subjected to meticulous microscopic and morphological characterisation, but only six of them were found to contain the CDJ and were therefore potentially useful for Schreger angle measurements.

Infrared and Chemical Analysis

All 21 samples were investigated by infrared spectroscopy at the Swiss Gemmological Institute SSEF using a Nicolet 550 FTIR spectrometer in transmission mode with the KBr pellet method (Khoshhesab 2012). An average of 0.5 mg of powdered material was taken from each ivory sample for each measurement. Spectra were collected in the range of 6000–400 cm^{-1} with a resolution of 0.5 cm^{-1} and 32 scans per spectrum at room temperature (25ºC).

Trace-element chemistry cannot be used to clearly separate ivory species (more research and a larger data set are needed), and is thus provided here to contribute to the further chemical characterisation of ivory samples in general. Laser ablation inductively coupled plasma time-of-flight mass spectrometry (LA-ICP-TOF-MS) was used to determine the trace-element composition of six selected specimens (nos. 10, 11, 14, 16, 17 and 21). These were considered to be representative of the sample lot, and also nos. 11 and 17 could not be conclusively identified using other techniques and were thus selected for trace-element characterisation to obtain additional data. The analyses were performed at SSEF using a 193 nm ArF excimer laser (ESI/New Wave Research NWR193UC) coupled to a commercial ICP-TOF-MS unit (Tofwerk icpTOF) with helium as the carrier gas. A detailed description of this method and set-up can be found in Wang *et al.* (2016). TOF-MS allows simultaneous analysis of the full range of masses (from ^{7}Li to ^{238}U), so no pre-selection of elements (isotopes) of interest was necessary. To calculate element concentrations, we used NIST610 glass as an external standard and the stoichiometry of Ca in hydroxyapatite as an internal standard. Although not matrix-matched, this approach using NIST glass standards has been applied in numerous previous studies on biogenic calcium carbonates and phosphates (Lee *et al.* 1999; Cucina *et al.* 2007; Limbeck *et al.* 2015; and references therein). Each sample was measured at two different locations using an ablation spot size of 75 µm and 20 Hz ablation frequency.

Genetic Analysis

Genetic analysis was performed on 16 samples (i.e. those for which morphological analysis was not possible) at the Zurich Institute of Forensic Medicine, University of Zurich, Switzerland. The method for DNA extraction and the polymerase chain reaction (PCR) set-up selected to analyse the ivory specimens were standardised and validated in the ISO 17025 accredited laboratory facilities where this work was carried out. Although this methodology may not be typical for identifying Proboscidean ivory, it allows species identification also for non-Proboscidean samples.

Prior to DNA extraction, the samples were cleaned with Dr. Weigert 5% neodisher LM 3 detergent and rinsed with deionised water and 70% ethanol. About 100 mg of ivory powder were acquired from each specimen by drilling a small hole on the back or base of the sample. We used a Proxxon Micromot 50 (E) drill with a 4–6 mm diameter cone-shaped grinding bit, taking care to avoid heating up the specimen by not pressing hard and including regular pauses to let the drill head cool down. To avoid contamination, the powder produced from the initial external surface was discarded. The size and shape of some samples, and especially the desire to not alter the item's appearance, made the cleaning and drilling process very challenging.

DNA was isolated from the powdered ivory samples using a Thermo Fisher Scientific PrepFiler BTA Forensic DNA Extraction Kit, following the manufacturer's protocol for the extraction of DNA from calcified tissues (bone or tooth). For species identification, a region of the cytochrome *b* gene was amplified as described by Morf *et al.* (2013). A Beckman Coulter AMPure XP bead system was used to purify the PCR products, which were then quantified with a Thermo Fisher Scientific Qubit 4 fluorometer. To explore the utility of the massive parallel sequencing technique for performing species identification, sequencing libraries were constructed with the Thermo Fisher Scientific Ion Plus Fragment Library Kit and Ion Xpress barcode adapters, beginning with the end repair of the purified PCR products. End repair and all subsequent steps of the manufacturer's protocol were conducted by reducing all reaction volumes to one quarter and using 2.4 ng DNA input if possible.

The barcoded libraries were then quantified with a Thermo Fisher Scientific Ion Library TaqMan Quantitation Kit, and all samples were pooled with equimolar concentrations. The 26 micromolar pooled libraries were used for templating on a Thermo Fisher Scientific Ion OneTouch 2 System. Sequencing was carried out on a Thermo Fisher Scientific Ion PGM platform. Adapter-trimmed sequence data were exported to FASTQ files using the FileExporter Plugin within Torrent Suite 5.10 software. The sequences were quality filtered using USEARCH (Edgar & Flyvbjerg 2015) and clustered into operational taxonomic units (OTUs) with UPARSE (Edgar 2013) at 97% minimal identity threshold (default setting; other values were tested but did not make significant differences) and a minimal OTU size of 100 sequence reads (to analyse major components and exclude noise sequences).

The resulting sequences of the OTUs were then compared to DNA sequences stored in the online GenBank database of the National Center for Biotechnology Information (NCBI; Bethesda, Maryland, USA). We identified DNA sequence entries of the GenBank database that were most similar to the DNA sequences obtained from our samples by searching the database with the MegaBLAST function of NCBI. That way, each OTU was assigned to a taxonomic rank; ideally an OTU would correspond to a species. For each sample, read numbers pertaining to different taxonomic ranks were expressed as a percentage of the entire sequence read number. Sequences belonging to the domain of bacteria and OTUs that could not be identified via the MegaBLAST function were grouped together into one category. To exclude rare contaminants, taxonomic ranks below 10%

of the total read number were not considered during evaluation of the sample. To see the relationship of the ivory DNA sequences of this study to those of extant Proboscideans and *Mammuthus primigenius*, a Bayesian phylogenetic tree was constructed using MrBayes version 3.2.7 software (Ronquist *et al.* 2012), as described by Lendvay *et al.* (2020). As reference data, we used five homologous DNA sequences of each extant Proboscidean species and *Mammuthus primigenius*, respectively. Furthermore, DNA sequences of the closely related rock hyrax (*Procavia capensis*) and dugong (*Dugong dugon*) were included as outgroup taxa. All reference data were downloaded from the GenBank database.

RESULTS AND DISCUSSION

Morphological Analysis

Schreger angles were successfully measured on five of the samples (with one sample [no. 5] consisting of two beads; see Table I). Figure 3 illustrates the location of the CDJ in one of these specimens, which is a prerequisite for morphological identification based on Schreger angles. The range of average measurements obtained from the five samples was 72.6°–94.2°. All of these measurement averages are below 100°, which according to Espinoza & Mann (2000) corresponds to the suggested limit to separate elephant ivory (above 100° average) from mammoth ivory (below 100° average). These five samples were thus conclusively identified as ivory originating from extinct Proboscideans. Therefore, further DNA analysis was not deemed necessary and was thus not carried out on those specimens.
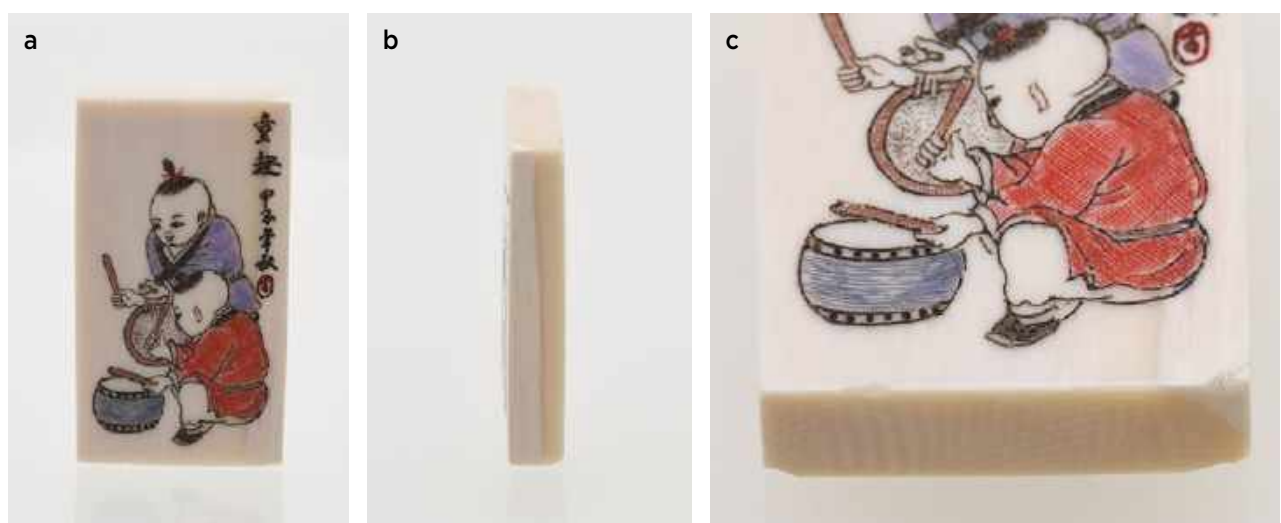
Figure 3: Sample 21 is a carved block of ivory (about 4 cm tall) that is decorated by a painting (**a**). Views of the side (**b**) and base (**c**) clearly show the cementum-dentine junction. The white part to the left in the side view is cementum, whereas the beige material on the right side is dentine. Image (c) shows cementum (white) at the upper right, next to the outer Schreger lines. The Schreger angle of these lines averaged 82.2°, which is characteristic of mammoth ivory. Photos by Vito Lanzafame, SSEF.

Although Schreger lines were observed in 11 other samples, their intersection angle could not be used due to orientation issues (absence of visible CDJ). Nevertheless, based only on the presence of the Schreger lines, these specimens could be identified as being Proboscidean.

The remaining five samples showed no Schreger lines, and no. 19 was visually identified as an ivory imitation based on the presence of a distinct layered structure intended to simulate the Schreger lines of ivory.

FTIR SPECTROSCOPY

All samples except for the ivory imitation showed FTIR spectral characteristics of carbonated hydroxyapatite (Figures 4 and 5; cf. Chang & Tanaka 2002; Grunenwald *et al.* 2014; Chappard *et al.* 2016). Figure 4 highlights a particular case (ivory bangle sample no. 4) where Schreger lines were visible but not conclusive for species identification (due to the absence of the CDJ). By contrast, specimen no. 19 yielded a very different FTIR spectrum dominated by sharp peaks (Figure 6) and was readily identified as an ivory imitation made of artificial resin (by comparison to the Thermo Scientific spectral library). The FTIR spectrum of sample no. 17 (see Figure 5) showed a characteristic carbonated hydroxyapatite spectrum, suggesting that it is of dentine or bone origin, but it could not be attributed to a specific species or species group with the methods used.

As (mammoth) ivory ages over time, carbonated hydroxyapatite can recrystallise. Furthermore, as weathering occurs, amide/phosphate ratios and carbonate/phosphate ratios can change (Jacob *et al.* 2008). Multiple factors can influence an FTIR spectrum (age, weathering state, crystallinity, collagen content and location of the sample in a tusk), so FTIR spectroscopy is not a reliable method to determine the species of ivory (see also UNODC 2014). This case study—and further unpublished research by the authors on elephant ivory from the SSEF reference collection—confirm this fact, as we could not identify clear distinguishing factors to separate elephant ivory from fossilised mammoth ivory based on FTIR spectral features.

This result is, however, different from that of Yin *et al.* (2013), who suggested a possible separation of modern elephant ivory from mammoth ivory based on FTIR spectroscopy, mainly by attributing observed differences in the spectra to the burial of mammoth ivory and related loss of water and degradation of collagen. Although such weathering-related processes are possible, their influence on FTIR spectra remains unclear (O'Connor *et al.* 2011). Our FTIR spectra of both modern elephant ivory and extinct (buried) mammoth ivory samples from the SSEF reference collection did not reveal any notable or conclusive difference in the hydroxyl range (3500–2900 cm^{-1}) or in the CH-range (3000–2800 cm^{-1}). Based on our analyses, we thus presume that the spiky 'peaks' in the 3500–2900 cm^{-1} range of the FTIR spectra reported by Yin *et al.*

Figure 4: The FTIR spectrum of sample no. 4 (mammoth ivory bangle) shows absorption bands characteristic of carbonated hydroxyapatite (e.g. ivory and bone) and collagen. Peak attributions are after Hassan *et al.* (2016) and the artefact at 2360 cm^{-1} is from atmospheric CO_2. The inset shows Schreger lines in the bangle (which is approximately 1 cm thick; photo courtesy of SSEF), but the absence of the CDJ precludes identification based on Schreger angles.

Figure 5: FTIR spectra (in the 1800–500 cm^{-1} range) of mammoth ivory (nos. 4 and 16) and undifferentiated Proboscidea (no. 18) are compared to cattle bone (no. 15, identified using DNA analysis) and one unidentified sample (no. 17). Regardless of their taxa, all these specimens show very similar spectral features characteristic of carbonated hydroxyapatite.
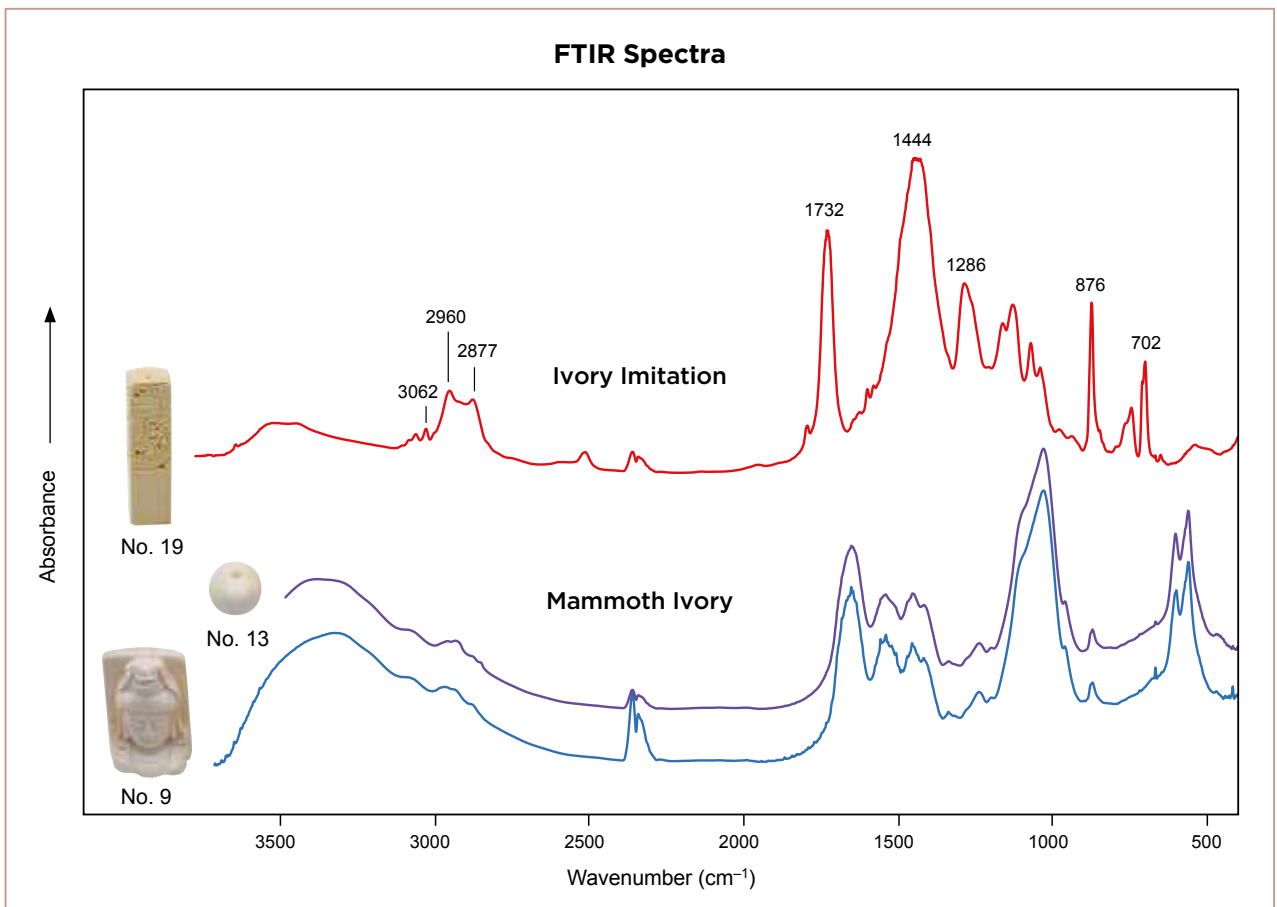
Figure 6: The FTIR spectrum of an ivory imitation (artificial resin, no. 19) is dominated by sharp polymer-related bands, and is compared to two samples of mammoth ivory (nos. 9 and 13) that display characteristic features of carbonated hydroxyapatite. Inset photos by Vito Lanzafame, SSEF; the specimens are 3.5 cm wide (no. 9), about 0.5 cm in diameter (no. 13) and 7 cm tall (no. 19).

(2013)—which were described by them as a result of water loss—are in fact artefacts due to total absorption in the hydroxyl range of their mammoth sample. In any case, the present study clearly reveals that species identification or age estimation (modern vs. fossil) of ivory based on FTIR spectroscopy is not reliable.

Trace-Element Analysis

Polycrystalline hydroxyapatite can accommodate a broad range of trace elements, primarily as substitutions for the large Ca^{2+} cation (Brown & Constantz 1994). A selection of relevant elements is listed in Table II for the six samples analysed by LA-ICP-TOF-MS. A comparison of our data to the literature (Kohn *et al.* 1999 and references therein) reveals high consistency with reported concentration ranges for fossil dentine. Each specimen was analysed on two randomly selected areas, and our data suggest that each one was very homogeneous in its trace-element concentrations. Interestingly, three of

the samples (nos. 14, 16 and 21, all identified as extinct Proboscidea by their morphology or DNA testing, as covered below) showed distinctly higher Mg but lower concentrations of Fe, Sr and Ba compared to sample no. 10 (undifferentiated Proboscidea). Specimen no. 11 (which could not be identified) was characterised by relatively high Mn, Fe and, to some extent, Sr, Ba and rare-earth elements (REEs). This might be related to alteration during burial in soil (diagenesis), as this sample looked weathered and was reddish brown (Figure 7), as if stained by Fe-Mn (hydr)oxides. Specimen no. 17 (also not identifiable) differed in having higher Na, Zn, Ba and REEs compared to the other samples.

Genetic Analysis Based on a Region of the Cytochrome b Gene

DNA analysis was carried out on 16 of the 21 samples, and was successful for 15 of them. For one specimen (no. 11), no PCR product could be amplified, most likely

Table II: LA-ICP-TOF-MS trace-element data (in ppmw) for six selected samples.[a]

Sample no.	Spot	B	Na	Mg	Si	Cr	Mn	Fe	Zn	Sr	Ba	REE	Pb	U/Pb	Taxonomic identification (based on morphology or DNA)
10	1	7.85	4415	7653	266.3	1.186	153.9	639.2	34.17	994.3	95.28	0.208	0.153	0.10	Proboscidea
	2	7.45	4372	7381	265.7	1.054	147.6	614.4	36.62	971.9	92.89	0.193	0.166	0.12	
11	1	5.46	2700	1470	343.8	0.539	4808	26300	38.89	1315	768.8	1.236	0.061	0.30	Not possible
	2	5.90	2770	1468	321.6	1.132	4758	26260	40.24	1311	767.9	1.228	0.054	0.21	
14	1	8.28	3081	43370	339.3	1.124	0.899	31.69	25.81	318.3	48.16	0.125	0.108	0.12	Extinct Proboscidea
	2	7.61	3172	37830	281.7	0.902	0.850	24.41	27.36	316.9	46.74	0.083	0.180	0.10	
16	1	14.07	4172	42690	255.7	1.150	0.924	28.55	34.92	385.8	15.52	0.021	0.030	na	Extinct Proboscidea
	2	14.02	4297	41460	288.3	0.790	0.913	25.07	34.79	386.1	15.67	0.045	0.031	0.19	
17	1	5.95	8423	5554	218.4	0.653	0.931	26.94	121.9	609.4	719.7	1.112	0.633	0.01	Not possible
	2	6.05	8262	5467	199.4	0.451	1.164	25.47	136.8	599.7	752.9	1.221	0.755	na	
21	1	11.19	4905	39250	292.6	0.908	0.948	20.11	28.22	345.6	45.47	0.130	0.185	0.08	Extinct Proboscidea
	2	11.83	5205	36220	314.6	0.782	0.971	22.42	31.52	356.1	44.50	0.142	0.200	0.15	
Reference values (Kohn *et al.* 1999)		>10–10s	1000s	1000s	10–~100s	nr	nr	nr	100s–1000s	100s–~100	10s–~100	<1	nr	<1	Fossil dentine[b]

[a] Abbreviations: na = not applicable because U was below the detection limit; nr = not reported by Kohn *et al.* (1999).
[b] Range of values from Burchell's zebra (*Equus burchellii*), Guenther's dik-dik (*Rhynchotragus guentheri*) and Grant's gazelle (*Gazella granti*).

Figure 7: This weathered sample (no. 11; about 2 cm wide) was found to contain relatively high Fe and Mn concentrations. Its colour and chemistry might be related to alteration during burial in soil, resulting in impregnation with Fe-Mn (hydr)-oxides. Photo by V. Lanzafame, SSEF.

due to too little or too degraded DNA. By using massive parallel sequencing to analyse the genetic data, we were able to deconvolute mixtures and infer the different DNA contents of a specimen. Detected bacterial species were excluded as a possible origin. Any human DNA detected as a minor component in a mixture was considered a contaminant and was not included in the final taxonomic identification.

The taxonomic origin of nine samples was identified as extinct Proboscidea, one specimen originated from the genus *Bos* (wild and domestic cattle) and the DNA analysed for another sample was of human origin (Table III). The DNA extracts of the remaining four specimens were identified as DNA mixtures in which human DNA accounted for the largest part. The minor parts of these mixtures originated from the following taxonomic ranks: *Mammuthus* sp. (mammoths), *Loxodonta* sp. (African elephants), *Gallus gallus* (junglefowl, e.g. chickens) and bacteria.

Table III: Results for 16 samples based on DNA analysis, including total number of sequence reads per sample.*

Sample no.	Total no. of reads	*Mammuthus* sp.	*Homo sapiens*	*Loxodonta* sp.	*Bos* sp.	*Gallus gallus*	Bacterial or unidentifiable sequences	Sequences below threshold	Taxonomic identification
1	1012	70.7	14.7					14.7	Extinct Proboscidea
2	6850		73.1	13.2			13.3	0.3	Mixture
3	17855	98.8						1.2	Extinct Proboscidea
4	20580	98.5						1.5	Extinct Proboscidea
5	20285	98.5						1.5	Extinct Proboscidea
6	12070	95.3						4.7	Extinct Proboscidea
8	3251	30.2	66.7					3.1	Mixture
10	996		62.3			37.3		0.4	Mixture
11									Not possible
13	2939	99.5						0.5	Extinct Proboscidea
14	13931	73.9	21.3					4.8	Extinct Proboscidea
15	6317				62.9		33.2	3.9	*Bos* sp.
16	10958	56.7	41.8					1.6	Extinct Proboscidea
17	5974		81.5			12.0		6.6	Mixture
18	10833		93.1					6.9	*Homo sapiens*
20	14908	97.8						2.2	Extinct Proboscidea

* The read numbers pertaining to different taxonomic ranks are expressed as percentages of the entire sequence read number, and sequences of OTUs with less than 100 reads are grouped together with sequences of taxonomic ranks with less than 10% of the total read number in the category titled 'Sequences below threshold'.
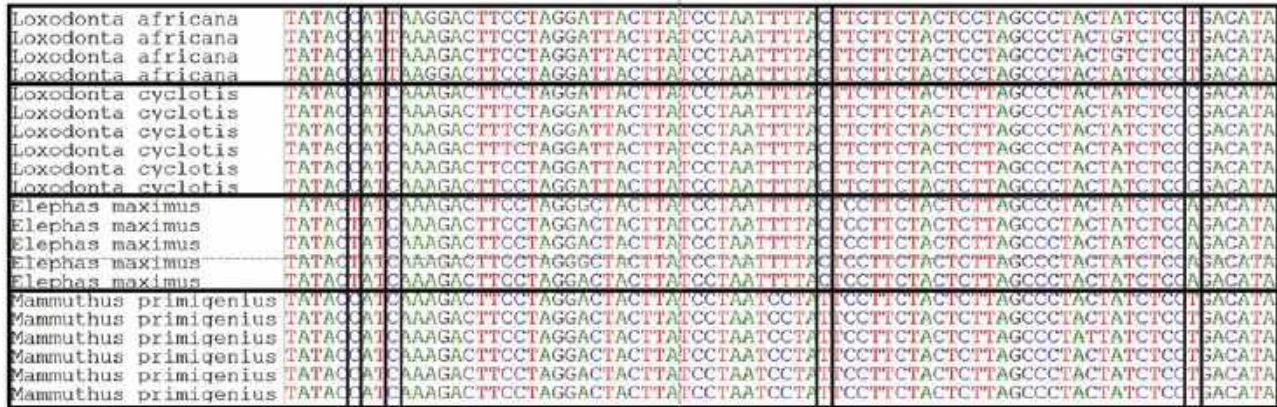
Figure 8: Nucleotide differences between extant Proboscidean species and the woolly mammoth (*Mammuthus primigenius*) are bracketed by vertical lines in this DNA sequence alignment of a short fragment of the mitochondrial cytochrome *b* gene.

Separating Mammoth and Elephant Ivory Using Genetic Analysis

To demonstrate how our genetic analysis is able to differentiate between elephant and mammoth ivory, we compared sequences from different Proboscideans in the online NCBI database. Figure 8 shows examples of nucleotide (A, C, G, T) differences between the extant Proboscidean species and the woolly mammoth (*Mammuthus primigenius*) in a short fragment (length:

78 base pairs) of the mitochondrial cytochrome *b* gene. The sequences of the extinct Proboscidea (length: 359 base pairs) obtained in this study showed 10 or more nucleotide differences from the sequences of African or Asian elephants found in the NCBI database.

These sequences from the extinct Proboscidean samples were included in a Bayesian phylogenetic tree containing sequences of extant Proboscideans and *Mammuthus primigenius* (Figure 9). A phylogenetic tree

Figure 9: This Bayesian phylogenetic tree displays the taxonomic position of our ivory samples identified as extinct Proboscidea. With high probability, these specimens group together with those of *Mammuthus primigenius*. Species names for the reference samples are followed by their NCBI GenBank accession numbers. Bayesian posterior probability values next to the branches indicate the levels of support that the specimens in that branch group together; a value greater than 0.95 is generally accepted as well-supported clustering.

Bayesian Phylogenetic Tree

is a diagram representing evolutionary relationships among organisms. The included species are found at the tips of lines, referred to as tree branches. The pattern in which these branches connect represents how the species evolved from different common ancestors; a node represents a divergence event. In our phylogenetic tree, the identical DNA sequences obtained from nine of our tested samples grouped together, with high probability, with sequences of *Mammuthus primigenius*.

Combining the Results of the Morphological, Gemmological and Genetic Methods

By combining the results of all the analyses we conducted, we were able to determine the origin of all but two of the 21 samples (Table IV). Thirteen specimens

were attributed to extinct Proboscideans (*Mammuthus* sp.). Five of these were identified by their morphological features (Schreger angles) and nine as a result of DNA analysis (different beads in sample no. 13 were identified by both techniques).

DNA analysis could not be used to specify the exact species of origin of four samples exhibiting inconclusive Schreger angles because their DNA extract consisted of a mixture of species. These samples were therefore identified as simply 'Proboscidean' since their extinct or extant origin could not be determined. Although the major component shown by genetic testing was ascribed to *Homo sapiens*, a human origin was ruled out due to the observed Schreger lines, so the presence of human DNA is considered contamination. Surprisingly, one of

Table IV: Taxonomic identification of the samples based on the methods used in this case study.

Sample no.	Taxonomic identification based on morphological analysis	Taxonomic identification based on DNA analysis	FTIR analysis	Taxonomic identification, considering results from all analyses
1	Proboscidea	Extinct Proboscidea	Carbonated hydroxyapatite	Extinct Proboscidea
2	Proboscidea	Mixture	Carbonated hydroxyapatite	Proboscidea
3	Proboscidea	Extinct Proboscidea	Carbonated hydroxyapatite	Extinct Proboscidea
4	Proboscidea	Extinct Proboscidea	Carbonated hydroxyapatite	Extinct Proboscidea
5	Proboscidea	Extinct Proboscidea	Carbonated hydroxyapatite	Extinct Proboscidea
6	Proboscidea	Extinct Proboscidea	Carbonated hydroxyapatite	Extinct Proboscidea
7	Extinct Proboscidea	Not performed	Carbonated hydroxyapatite	Extinct Proboscidea
8	Proboscidea	Mixture	Carbonated hydroxyapatite	Proboscidea
9	Extinct Proboscidea	Not performed	Carbonated hydroxyapatite	Extinct Proboscidea
10	Proboscidea	Mixture	Carbonated hydroxyapatite	Proboscidea
11	Not possible	Not conclusive	Carbonated hydroxyapatite	Not possible
12	Extinct Proboscidea	Not performed	Carbonated hydroxyapatite	Extinct Proboscidea
13	Extinct Proboscidea	Extinct Proboscidea	Carbonated hydroxyapatite	Extinct Proboscidea
14	Proboscidea	Extinct Proboscidea	Carbonated hydroxyapatite	Extinct Proboscidea
15	Not possible	*Bos* sp.	Carbonated hydroxyapatite	*Bos* sp.
16	Proboscidea	Extinct Proboscidea	Carbonated hydroxyapatite	Extinct Proboscidea
17	Not possible	Mixture	Carbonated hydroxyapatite	Not possible
18	Proboscidea	*Homo sapiens*	Carbonated hydroxyapatite	Proboscidea
19	Imitation	Not performed	Ivory imitation	Ivory imitation (artificial resin)
20	Not possible	Extinct Proboscidea	Carbonated hydroxyapatite	Extinct Proboscidea
21	Extinct Proboscidea	Not performed	Carbonated hydroxyapatite	Extinct Proboscidea

these specimens (no. 10) had a minor component attributed to the species *Gallus gallus*, but again because of the observed Schreger lines we know this sample did not originate from a chicken. A possible source of contamination could be residual chicken grease used to polish the specimen during manufacturing.

One sample originated from the genus *Bos* (no. 15; cattle bone) according to DNA analysis, and another (no. 19) was conclusively identified as an imitation of ivory made of artificial resin based on microscopic and FTIR analyses. Finally, two specimens (nos. 11 and 17) did not exhibit any Schreger angles, nor any other morphological characteristics indicative for ivory. DNA analysis of these items was also not successful—one sample exhibited too little or too degraded DNA, and the DNA extract of the other consisted of a mixture—so their taxonomic identification was not possible.

CONCLUSIONS

Various types of ivory may be encountered by gemmologists as *objets d'art*, jewellery and other items (e.g. Figures 1 and 10). This case study shows the challenges and limitations of distinguishing between these gem materials. To identify the nature (e.g. ivory or imitation) and species of 'ivory' samples, a combined approach using multiple techniques (in this study, morphological, gemmological and genetic) can be helpful in many instances. For this case study, determination began with morphological analysis (macroscopic and microscopic), which is the most readily available testing method. Samples not displaying orientable Schreger lines were tested further using DNA analysis. Techniques available in well-equipped gemmological laboratories (FTIR and LA-ICP-TOF-MS) were applied to further characterise

Figure 10: The carved mammoth-ivory leaves in these gold earrings are accented by diamonds and accompanied by ~2.4 ct of pink sapphires. Courtesy of Paul Farmer Goldsmith, Vail, Colorado, USA; photo by Jeff Scovil.

and document a selection of the samples, but they were not useful for identifying whether a specimen was from an extinct or extant Proboscidean species. Importantly for gemmologists, the presence of a cattle bone sample that had FTIR features similar to those of ivory shows the importance of integrating DNA analysis into origin determination when Schreger lines are not clearly visible or measurable.

Jacob *et al.* (2008) showed that the distribution of chemical elements in tusks is heterogeneous. They also proposed that isotopic rather than trace-element analysis might be more suitable for identifying the geographic source region of ivory species, but this method is outside the scope of this study. The portion of the tusk being analysed should be taken into account when carrying out trace-element and isotopic analysis of ivory specimens; if the CDJ is not present, then establishing a consistent sampling position is not possible. Furthermore, the degree of weathering (and presence of associated elements) in fossilised ivory samples, which can be 10,000 years or older, is a considerable factor to take into account. A larger reference database would be needed before attempting to use trace elements, and more specifically ultra-trace elements (e.g. REEs), to identify different ivory species.

Although the ivory trade has changed due to more stringent international regulations, material continues to be misrepresented on the market, and research such as outlined here is important to support elephant conservation work worldwide. Making techniques available to conclusively identify ivory species can help limit fraud, as in cases where poached elephant ivory is falsely declared as mammoth ivory. During an August 2019 CITES conference in Switzerland, a proposal was made (although ultimately retracted) to include mammoth ivory in CITES appendices. The ongoing interest in differentiating between extinct vs. extant ivory demonstrates the need for the reliable identification of ivory in the trade.

REFERENCES

Baker, B.W, Jacobs, R.L., Mann, M.-J., Espinoza, E.O. & Grein, G. 2020. *Identification Guide for Ivory and Ivory Substitutes*, 4th edn. CITES Secretariat, Geneva, Switzerland and World Wildlife Fund, Washington DC, USA, 108 pp., https://wwfeu.awsassets.panda.org/downloads/r8_ivoryguide_07162020_low_res.pdf.

Basilyan, A.E., Anisimov, M.A., Nikolskiy, P.A. & Pitulko, V.V. 2011. Wooly mammoth mass accumulation next to the Paleolithic Yana RHS site, Arctic Siberia: Its geology, age, and relation to past human activity. *Journal of Archaeological Science*, **38**(9), 2461–2474, https://doi.org/10.1016/j.jas.2011.05.017.

Brown, P.W. & Constantz, B. 1994. *Hydroxyapatite and Related Materials*. CRC Press, Boca Raton, Florida, USA, 368 pp., https://doi.org/10.1201/9780203751367.

Brunnermeier, M.J., Schmied, S.A.K., Müller-Boge, M. & Schupfner, R. 2012. Dating of ivory from 20th century by determination of ^{14}C by the direct absorption method. *Applied Radiation and Isotopes*, **70**(8), 1595–1602, https://doi.org/10.1016/j.apradiso.2011.10.006.

Budowle, B., Churchill, J.D. & King, J.L. 2016. The next state-of-the-art forensic genetics technology: Massively parallel sequencing. *In*: Amorim, A. & Budowle, B. (eds) *Handbook of Forensic Genetics: Biodiversity and Heredity in Civil and Criminal Investigation*. World Scientific, London, 249–291, https://doi.org/10.1142/9781786340788_0013.

Campbell Pedersen, M. 2015. *Ivory*. Robert Hale Ltd, London, 240 pp.

Cartier, L.E., Krzemnicki, M.S., Lendvay, B. & Meyer, J.B. 2018. DNA fingerprinting of pearls, corals and ivory: A brief review of applications in gemmology. *Journal of Gemmology*, **36**(2), 152–160, http://doi.org/10.15506/jog.2018.36.2.152.

Cerling, T.E., Barnette, J.E., Chesson, L.A., Douglas-Hamilton, I., Gobush, K.S., Uno, K.T., Wasser, S.K. & Xu, X. 2016. Radiocarbon dating of seized ivory confirms rapid decline in African elephant populations and provides insight into illegal trade. *Proceedings of the National Academy of Sciences*, **113**(47), 13330–13335, https://doi.org/10.1073/pnas.1614938113.

Chang, M.C. & Tanaka, J. 2002. FT-IR study for hydroxyapatite/collagen nanocomposite cross-linked by glutaraldehyde. *Biomaterials*, **23**(24), 4811–4818, https://doi.org/10.1016/S0142-9612(02)00232-6.

Chappard, C., André, G., Daudon, M. & Bazin, D. 2016. Analysis of hydroxyapatite crystallites in subchondral bone by Fourier transform infrared spectroscopy and powder neutron diffraction methods. *Comptes Rendus Chimie*, **19**(11–12), 1625–1630, https://doi.org/10.1016/j.crci.2015.03.015.

Conte, J., Potoczniak, M.J., Mower, C. & Tobe, S.S. 2019. ELEquant: A developmental framework and validation of forensic and conservation real-time PCR assays. *Molecular Biology Reports*, **46**(2), 2093–2100, https://doi.org/10.1007/s11033-019-04660-7.

Cucina, A., Dudgeon, J. & Neff, H. 2007. Methodological strategy for the analysis of human dental enamel by LA-ICP-MS. *Journal of Archaeological Science*, **34**(11), 1884–1888, https://doi.org/10.1016/j.jas.2007.01.004.

Edgar, R.C. 2013. UPARSE: Highly accurate OTU sequences from microbial amplicon reads. *Nature Methods*, **10**(10), 996–998, https://doi.org/10.1038/nmeth.2604.

Edgar, R.C. & Flyvbjerg, H. 2015. Error filtering, pair assembly and error correction for next-generation sequencing reads. *Bioinformatics*, **31**(21), 3476–3482, https://doi.org/10.1093/bioinformatics/btv401.

Edwards, H.G.M. & Farwell, D.W. 1995. Ivory and simulated ivory artefacts: Fourier transform Raman diagnostic study. *Spectrochimica Acta Part A: Molecular and Biomolecular Spectroscopy*, **51**(12), 2073–2081, https://doi.org/10.1016/0584-8539(95)01455-3.

Edwards, H.G.M., Hassan, N.F.N. & Arya, N. 2006. Evaluation of Raman spectroscopy and application of chemometric methods for the differentiation of contemporary ivory specimens I: Elephant and mammalian species. *Journal of Raman Spectroscopy*, **37**(1–3), 353–360, https://doi.org/10.1002/jrs.1458.

Espinoza, E.O. & Mann, M.-J. 1993. The history and significance of the Schreger pattern in Proboscidean ivory characterization. *Journal of the American Institute for Conservation*, **32**(3), 241–248, https://doi.org/10.1179/019713693806124866.

Espinoza, E.O. & Mann, M.-J. 2000. *Identification Guide for Ivory and Ivory Substitutes*, 3rd edn. Ivory Identification Inc., Richmond, Virginia, USA, 33 pp.

Grunenwald, A., Keyser, C., Sautereau, A.M., Crubézy, E., Ludes, B. & Drouet, C. 2014. Revisiting carbonate quantification in apatite (bio)minerals: A validated FTIR methodology. *Journal of Archaeological Science*, **49**, 134–141, https://doi.org/10.1016/j.jas.2014.05.004.

Gupta, S.K., Thangaraj, K. & Singh, L. 2011. Identification of the source of ivory idol by DNA analysis. *Journal of Forensic Sciences*, **56**(5), 1343–1345, https://doi.org/10.1111/j.1556-4029.2011.01750.x.

Harris, L., Gore, M. & Mills, M. 2019. Compliance with ivory trade regulations in the United Kingdom among traders. *Conservation Biology*, **33**(4), 906–916, https://doi.org/10.1111/cobi.13277.

Hassan, M.N., Mahmoud, M.M., El-Fattah, A.A. & Kandil, S. 2016. Microwave-assisted preparation of nano-hydroxyapatite for bone substitutes. *Ceramics International*, **42**(3), 3725–3744, https://doi.org/10.1016/j.ceramint.2015.11.044.

Jacob, D.E., Stracke, A., Wiegand, B. & Dindorf, W. 2008. Tracing ivory by its chemical and isotopic composition. *In*: Roth, J. & Bortolaso, G. (eds) *Elfenbein und Artenschutz. INCENTIVS – Tagungsbeiträge der Jahre (2004 - 2007)/Ivory and Species Conservation. Proceedings of INCENTIVS – Meetings (2004 - 2007)*. Bundesamt für Naturschutz, Bonn, Germany, **228**, 93–99, www.bfn.de/fileadmin/BfN/service/Dokumente/skripten/skript228.pdf.

Khoshhesab, Z.M. 2012. Reflectance IR spectroscopy. *In*: Theophile, T. (ed) *Infrared Spectroscopy – Materials Science, Engineering and Technology*. IntechOpen, London, 233–244, https://doi.org/10.5772/37180.

Kitpipit, T., Penchart, K., Ouithavon, K., Satasook, C., Linacre, A. & Thanakiatkrai, P. 2016. A novel real time PCR assay using melt curve analysis for ivory identification. *Forensic Science International*, **267**, 210–217, https://doi.org/10.1016/j.forsciint.2016.08.037.

Kitpipit, T., Thongjued, K., Penchart, K., Ouithavon, K. & Chotigeat, W. 2017. Mini-SNaPshot multiplex assays authenticate elephant ivory and simultaneously identify the species origin. *Forensic Science International: Genetics*, **27**, 106–115, https://doi.org/10.1016/j.fsigen.2016.12.007.

Kohn, M.J., Schoeninger, M.J. & Barker, W.W. 1999. Altered states: Effects of diagenesis on fossil tooth chemistry. *Geochimica et Cosmochimica Acta*, **63**(18), 2737–2747, https://doi.org/10.1016/s0016-7037(99)00208-2.

Lee, K.M., Appleton, J., Cooke, M., Keenan, F. & Sawicka-Kapusta, K. 1999. Use of laser ablation inductively coupled plasma mass spectrometry to provide element versus time profiles in teeth. *Analytica Chimica Acta*, **395**(1–2), 179–185, https://doi.org/10.1016/s0003-2670(99)00319-0.

Lee, E., Lee, Y., Moon, S., Kim, N., Kim, S., Yang, M., Choi, D. & Han, M. 2013. The identification of elephant ivory evidences of illegal trade with mitochondrial cytochrome b gene and hypervariable D-loop region. *Journal of Forensic and Legal Medicine*, **20**(3), 174–178, https://doi.org/10.1016/j.jflm.2012.06.014.

Lendvay, B., Cartier, L.E., Gysi, M., Meyer, J.B., Krzemnicki, M.S., Kratzer, A. & Morf, N.V. 2020. DNA fingerprinting: An effective tool for taxonomic identification of precious corals in jewelry. *Scientific Reports*, **10**, article 8287 (12 pp.), https://doi.org/10.1038/s41598-020-64582-4.

Limbeck, A., Galler, P., Bonta, M., Bauer, G., Nischkauer, W. & Vanhaecke, F. 2015. Recent advances in quantitative LA-ICP-MS analysis: Challenges and solutions in the life sciences and environmental chemistry. *Analytical and Bioanalytical Chemistry*, **407**(22), 6593–6617, https://doi.org/10.1007/s00216-015-8858-0.

Morf, N.V., Wood, K.L., Köppel, R., Felderer, N., Daniels, M., Tenger, B. & Kratzer, A. 2013. A multiplex PCR method to identify bushmeat species in wildlife forensics. *Forensic Science International: Genetics Supplement Series*, **4**(1), e202–e203, https://doi.org/10.1016/j.fsigss.2013.10.104.

Ngatia, J.N., Lan, T.M., Ma, Y., Dinh, T.D., Wang, Z., Dahmer, T.D. & Chun Xu, Y. 2019. Distinguishing extant elephants ivory from mammoth ivory using a short sequence of cytochrome b gene. *Scientific Reports*, **9**, article 18863 (12 pp.), https://doi.org/10.1038/s41598-019-55094-x.

Nikolskiy, P.A., Sulerzhitsky, L.D. & Pitulko, V.V. 2011. Last straw versus Blitzkrieg overkill: Climate-driven changes in the Arctic Siberian mammoth population and the Late Pleistocene extinction problem. *Quaternary Science Reviews*, **30**(17–18), 2309–2328.

O'Connor, S., Edwards, H.G.M. & Ali, E. 2011. An interim investigation of the potential of vibrational spectroscopy for the dating of cultural objects in ivory. *ArcheoSciences*, **35**, 159–165, https://doi.org/10.4000/archeosciences.3091.

Ronquist, F., Teslenko, M., van der Mark, P., Ayres, D.L., Darling, A., Höhna, S., Larget, B., Liu, L. *et al*. 2012. MrBayes 3.2: Efficient Bayesian phylogenetic inference and model choice across a large model space. *Systematic Biology*, **61**(3), 539–542, http://doi.org/10.1093/sysbio/sys029.

Schmied, S.A.K., Brunnermeier, M.J., Schupfner, R. & Wolfbeis, O.S. 2012. Dating ivory by determination of ^{14}C, ^{90}Sr and $^{228/232}$Th. *Forensic Science International*, **221**(1–3), 5–10, https://doi.org/10.1016/j.forsciint.2012.02.017.

Schreger, B.N.G. 1800. Beitrag zur Geschichte der Zähne. *Beiträge für die Zergliederungkunst*, **1**, 1–7.

Shimoyama, M., Morimoto, S. & Ozaki, Y. 2004. Non-destructive analysis of the two subspecies of African elephants, mammoth, hippopotamus, and sperm whale ivories by visible and short-wave near infrared spectroscopy and chemometrics. *Analyst*, **129**(6), 559–563, https://doi.org/10.1039/b401003e.

Singh, R.R., Goyal, S.P., Khanna, P.P., Mukherjee, P.K. & Sukumar, R. 2006. Using morphometric and analytical techniques to characterize elephant ivory. *Forensic Science International*, **162**(1–3), 144–151, https://doi.org/10.1016/j.forsciint.2006.06.028.

Tobe, S.S. & Linacre, A. 2010. DNA typing in wildlife crime: Recent developments in species identification. *Forensic Science, Medicine, and Pathology*, **6**(3), 195–206, https://doi.org/10.1007/s12024-010-9168-7.

Trapani, J. & Fisher, D.C. 2003. Discriminating Proboscidean taxa using features of the Schreger pattern in tusk dentin. *Journal of Archaeological Science*, **30**(4), 429–438, https://doi.org/10.1006/jasc.2002.0852.

United Nations Office on Drugs and Crime (UNODC) 2014. *Guidelines on Methods and Procedures for Ivory Sampling and Laboratory Analysis*. United Nations, Vienna, Austria, 119 pp., www.unodc.org/res/cld/bibliography/guidelines-on-methods-and-procedures-for-ivory-sampling-and-laboratory-analysis_html/Guidelines_Ivory.pdf.

van der Merwe, N.J., Lee-Thorp, J.A., Thackeray, J.F., Hall-Martin, A., Kruger, F.J., Coetzee, H., Bell, R.H.V. & Lindeque, M. 1990. Source-area determination of elephant ivory by isotopic analysis. *Nature*, **346**(6286), 744–746, https://doi.org/10.1038/346744a0.

Vigne, L. & Martin, E. 2014. *China Faces a Conservation Challenge: The Expanding Elephant and Mammoth Ivory Trade in Beijing and Shanghai*. Save the Elephants and The Aspinall Foundation, Nairobi, Kenya and Lympne, Nr Hythe, Kent, 89 pp., http://savetheelephants.org/wp-content/uploads/2014/12/2014_ChinaConservationChallenge.pdf.

Wang, H.A.O., Krzemnicki, M.S., Chalain, J.-P., Lefèvre, P., Zhou, W. & Cartier, L. 2016. Simultaneous high sensitivity trace-element and isotopic analysis of gemstones using laser ablation inductively coupled plasma time-of-flight mass spectrometry. *Journal of Gemmology*, **35**(3), 212–223, https://doi.org/10.15506/JoG.2016.35.3.212.

Wozney, K.M. & Wilson, P.J. 2012. Real-time PCR detection and quantification of elephantid DNA: Species identification for highly processed samples associated with the ivory trade. *Forensic Science International*, **219**(1–3), 106–112, https://doi.org/10.1016/j.forsciint.2011.12.006.

Yin, Z., Zhang, P., Chen, Q., Luo, Q., Zheng, C. & Li, Y. 2013. A comparison of modern and fossil ivories using multiple techniques. *Gems & Gemology*, **49**(1), 16–27, https://doi.org/10.5741/gems.49.1.16.

Ziegler, S., Merker, S., Streit, B., Boner, M. & Jacob, D.E. 2016. Towards understanding isotope variability in elephant ivory to establish isotopic profiling and source-area determination. *Biological Conservation*, **197**, 154–163, https://doi.org/10.1016/j.biocon.2016.03.008.

The Authors

Dr Laurent E. Cartier FGA
Swiss Gemmological Institute SSEF, Aeschengraben 26, 4051 Basel, Switzerland, and Institute of Earth Sciences, University of Lausanne, 1015 Lausanne, Switzerland
Email: laurent.cartier@ssef.ch

Dr Michael S. Krzemnicki FGA
Swiss Gemmological Institute SSEF, Aeschengraben 26, 4051 Basel, Switzerland

Mario Gysi, Dr Bertalan Lendvay and Nadja V. Morf
Zurich Institute of Forensic Medicine, University of Zurich, Winterthurerstrasse 190/52, 8057 Zurich, Switzerland

Stereoscopy in Asteriated Gemstones Revisited

Thanh Nhan Bui, Pascal Entremont, Francesco Mazzero
and Jean-Pierre Gauthier

ABSTRACT: This article documents an optical illusion displayed by the asterism of one of the largest-known star garnets. This dark brownish purple gem weighs 5,737 ct and exhibits a sharp, classical four-rayed star. The three-dimensional phenomenon—in which some or all branches of the asterism appear to float above the stone—is mainly visible due to the stone's large size. Such an illusion was partially documented for star and cat's-eye gemstones by Killingback (2005), who invoked the concept of stereoscopy to explain the effect. We report new observations of the phenomenon displayed by this garnet, as well as a star rose quartz, through stereoscopic images and anaglyphs. These show that the amplitude of the floating effect depends on the orientation of the star with respect to the observation plane.

Asterism is an optical phenomenon that has been broadly reported in the gemmological literature, and comprehensively documented in a recent book on star gemstones (Steinbach 2016). Various authors have studied the optical effect that produces asterism and chatoyancy (e.g. Wüthrich & Weibel 1981; Killingback 2005). The effect is caused by the scattering of incident light from acicular inclusions near a stone's surface that are oriented in parallel directions depending primarily on the crystallographic symmetry of the host mineral.

The star or cat's-eye that is seen when such a sample is cut *en cabochon* may appear as if slightly above the stone, giving the impression that it floats over the cabochon (Moon & Phillips 1984). Using a large star rose quartz sphere as an example, Killingback (2005) demonstrated that the floating effect is present on all star and cat's-eye gemstones. When we observe a cabochon using both eyes together (whether unaided or through a binocular microscope), the visibility of the floating-effect optical illusion depends on the angle of the cat's-eye or the branches of the star relative to the observation plane (formed by both eyes), as well as the size of the stone.

Here, we describe this phenomenon in detail in a large four-rayed star garnet (Figure 1). Author PE noticed that

Figure 1: The 5,737 ct 'Two Pound Star' from the collection of author PE is a cabochon-cut garnet displaying a sharp four-rayed star. The size of this stone makes it easy to observe the stereoscopic effect of the star with unaided eyes, as documented in this article. Photo by T. N. Bui.

when observing the stone at certain angles, it sometimes gives the impression that it would be possible to insert an object between the two branches of the four-rayed star. This optical phenomenon can be explained by invoking the concept of stereoscopy. We also examine this effect using a six-rayed star rose quartz.

Stereoscopy dates back to the 19th century when Charles Wheatstone lectured to the Royal Society in London on this topic (Wheatstone 1838, 1852). Today, stereoscopy is widely exploited for three-dimensional (3D) imaging in numerous fields.

MATERIALS AND METHODS

The studied garnet was obtained in Jaipur, India, by author PE in around 1985. The stone is cabochon cut and weighs approximately 5,737 ct (about 95 × 82 × 68 mm), making it one of the largest-known star garnets; its weight gave author PE the idea to name it 'Two Pound Star'. The gem's existence was reported in the French press in the 1980s (e.g. de La Taille 1987, p. 83) and it was also published in the *Guinness Book of World Records* (McWhirter 1986). In addition, the stone has been illustrated in the gemmological literature (Schmetzer *et al*. 2002a, b), and it was recently displayed as part of the Entremont Collection at the first temporary exhibition of the new 'DIVA, Antwerp Home of Diamonds' museum in Belgium (Bui 2018). The garnet is accompanied by a 2015 report from GGTL Laboratories stating that it consists of pyrope-almandine with physical and chemical characteristics that are similar to those garnets from India.

For comparison, we also examined a six-rayed star rose quartz that was purchased by author FM in Madagascar in 2001. It consists of a semi-transparent pink sphere with a diameter of 45.20 mm and weight of 633.50 ct.

Both specimens were studied by means of visual observation, and the optical effects are explained using stereoscopy principles and techniques. A stereoscope is a device by which two photographs of the same object taken at slightly different angles are juxtaposed (a stereogram or stereograph) and viewed together. It mainly consists of a pair of lenses and a divider, which is placed between the images and the observer in order to force each eye to see the respective parts of the stereogram separately. Due to the similarity of the two images in the stereogram, the brain reconstructs them into a single image, creating a 3D effect.

Stereoscopic images are an effective way of illustrating the 'floating' asterism seen in star stones. A stereogram's pair of images—left and right—represents what is seen separately by the left eye and right eye, respectively. The difference in what the two eyes see is called *stereoscopic parallax*; it allows the brain to interpret what the eyes see as having depth (or depth perception). Usually, stereoscopic cameras have two objectives; a set-up using two cameras can also produce stereoscopic pictures. For this study, we used a single camera on a tripod affixed to a 7-cm-long slider to obtain pairs of pictures taken from different perspectives while keeping both the stone and the light source motionless. The gem in each pair of pictures was systematically positioned to simulate the convergence of two eyes. We used an average human interpupillary distance of about 65 mm and a distance of about 650 mm between the observer and the stone, yielding an angle of 2.87° for the eyes' convergence. The star rose quartz was photographed from the side, where a large partially healed fracture is located, to provide a frame of reference for the reader while observing the stereograms.

To see the 3D effect in stereograms with unaided eyes (i.e. without the use of a stereoscope): (1) place the image pair about 20 cm from your eyes (with the PDF sized at 75% if viewing them on a computer screen); (2) allow your eyes to relax, as if staring into the distance; (3) as your eyes defocus, the images of the stone will float sideways; (4) pay attention to the image that coalesces at the centre, where the 3D effect should be visible.

RESULTS

Four-Rayed Star Garnet

Figure 1 shows the overall appearance of the star garnet, illuminated at its centre with a torch, revealing the dark brownish purple body colour of the huge cabochon and highlighting its four-rayed star, which is caused by the presence of acicular inclusions oriented along crystallographic directions in the garnet. The piece is opaque, due partly to the abundance of needles that are responsible for the asterism, and also to other, opaque inclusions and the overall dark colour of the garnet. The two branches of the star intersect at approximately 70° and 110°, in agreement with the previous studies of star garnets (e.g. Guinel & Norton 2006 and references therein).

The branches of the four-rayed star garnet are shown as seen by each eye in the stereograms in Figure 2. In the particular orientation of the star relative to the observation plane in Figure 2a, the illusion is that the short horizontal branch is on the surface of the cabochon and the other one is floating above it. In other words, the horizontal branch and the surface of the cabochon appear as the

background, with the oblique branch floating above on a virtual surface. When the eye moves in a sideways direction relative to the fixed cabochon and light source, the oblique branch moves in the opposite direction. The illusion of depth between the two branches of the star is produced by the displacement of the oblique branch—in this case by a significant amount—due to binocular vision (the distance between the eyes) combined with certain observation conditions (the distance between the stone and the eyes), compared to the fixed horizontal branch, which lies along the observation plane. The phenomenon is strongly enhanced in this sample for this particular orientation of the branches because of the cabochon's large size.

The oval shape of the cabochon and, thus, the different curvature radii along its width and length do not contribute to the optical illusion. Instead, it is exclusively due to the stereoscopic effect. When one eye
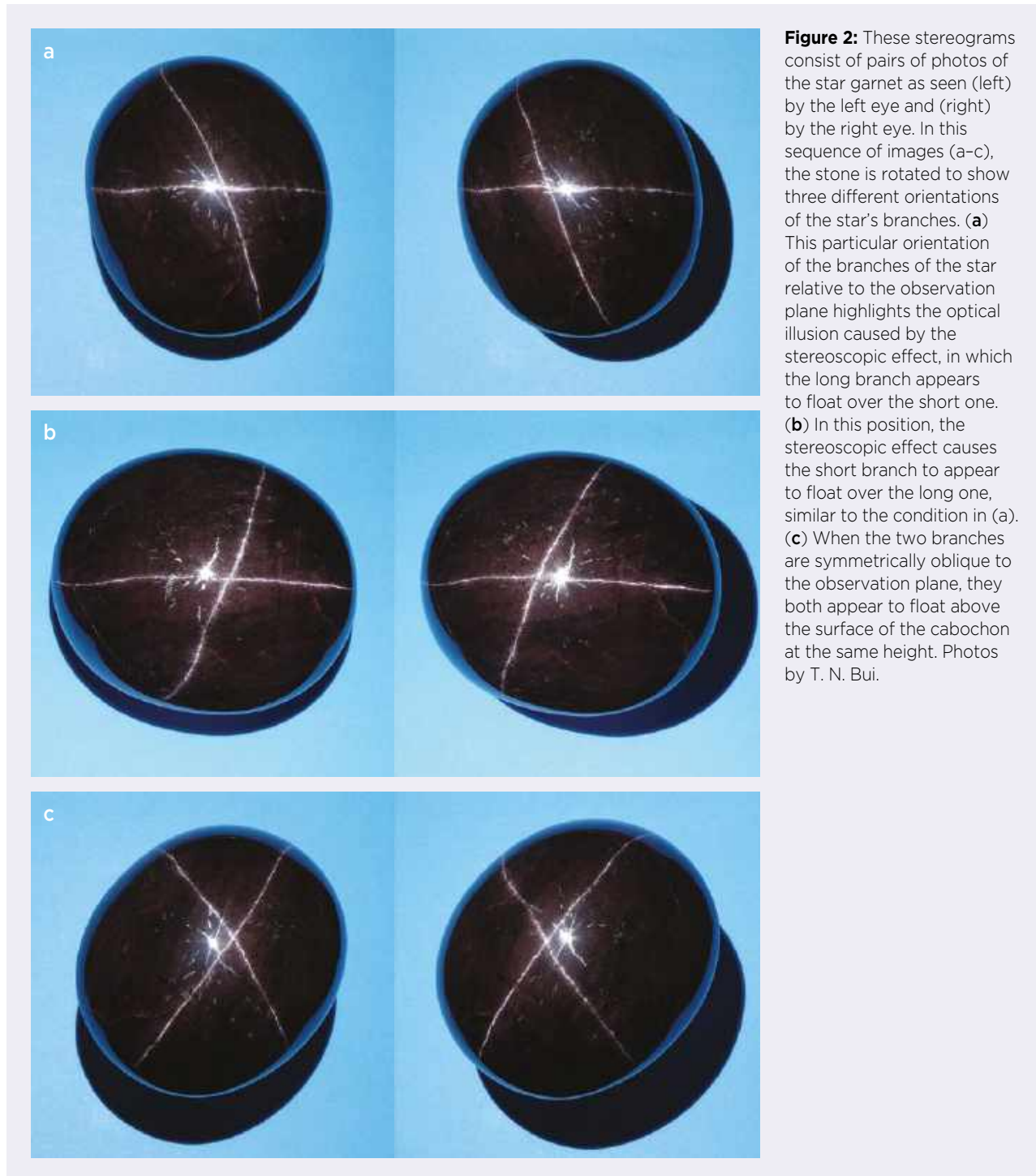

Figure 2: These stereograms consist of pairs of photos of the star garnet as seen (left) by the left eye and (right) by the right eye. In this sequence of images (a–c), the stone is rotated to show three different orientations of the star's branches. (**a**) This particular orientation of the branches of the star relative to the observation plane highlights the optical illusion caused by the stereoscopic effect, in which the long branch appears to float over the short one. (**b**) In this position, the stereoscopic effect causes the short branch to appear to float over the long one, similar to the condition in (a). (**c**) When the two branches are symmetrically oblique to the observation plane, they both appear to float above the surface of the cabochon at the same height. Photos by T. N. Bui.

is closed, the optical illusion disappears, and the eye remaining open observes a two-dimensional image.

The additional stereograms in Figure 2 show the star garnet in two other orientations: with the branch along the length of the cabochon horizontal (Figure 2b) and with both branches at symmetrically oblique angles (Figure 2c). When aligning the longer branch horizontally, it remains at a fixed position for both eyes (as previously illustrated in Figure 2a for the shorter branch), and the illusion is that the shorter branch floats above and in front of the longer horizontal one. When both branches are symmetrically oblique, the apparent gap between them disappears, but the impression is that both are floating above the cabochon. With further rotation of the stone, the relative position of these two branches above the cabochon appears to shift so that one branch is seen below the other one (and vice versa when turning it in the other direction).

So, by rotating the stone through 360°, beginning with the last-described orientation (Figure 2c), the branches are initially both seen floating above the cabochon, and then they appear to separate, such that the branch which appears to move in front of the other is the one rotating towards vertical. When one branch reaches the horizontal position, the two branches theoretically reach their maximum apparent separation distance (Figures 2a and 2b), where the horizontal branch seems stuck on the surface of the cabochon and the other one is floating above it. By continuing to rotate the stone in the same direction, the two branches get closer and once more are both seen floating above the cabochon when they again reach one of the four symmetrically oblique positions (e.g. Figure 2c).

Six-Rayed Star Rose Quartz

The floating effect reported by Killingback (2005) concerned the vertical branch of a six-rayed star in a rose quartz sphere. However, the observations we describe here consider the interactions among all the branches of the star. We photographed our rose quartz sphere by rotating it into three different orientations, in which one of the three branches is vertical (Figure 3a), one is at 45° to the vertical plane (Figure 3b) and one is horizontal (Figure 3c).

In the stereogram in Figure 3a, all three branches are seen as floating above the surface of the stone. (The vertical branch may appear slightly higher than the two others, but not by a significant amount.) In Figure 3c, the horizontal branch remains practically at the same position for both eyes and therefore seems stuck on the cabochon's surface, while the other two branches are

symmetrically oblique and appear to float together at the same level above the horizontal branch. In Figure 3b, all three branches appear to float at different heights, but the illusion of depth between the branch closest to horizontal and the other two is more pronounced. These observations are similar to those described for the four-rayed star garnet, and correspond to a combination of the different viewing conditions.

Another representation of the stereoscopic effect can be seen by using '3D glasses' to view an anaglyph, in which both pictures comprising a stereogram are superimposed in the same frame. The 'left' picture is generally in red and the 'right' one in cyan. The interpretation of an anaglyph is accomplished with two colour filters—red for the left eye and cyan for the right eye, as used to create the traditional 3D glasses that at one time were widely used for watching 3D films (subsequently replaced by the current polarisation 3D systems). These complementary colours also allow 3D pictures to be reproduced in static images when viewed with these glasses.

This effect is illustrated in Figure 4a–c using the same conditions for the star rose quartz as in Figure 3a–c. The slightly different positions of the six-rayed star seen by each eye are responsible for the floating and stereoscopic effects, but they are more clearly illustrated in these anaglyphs. The illusion of depth between two branches is caused by the amount of their apparent displacement. Figure 4a shows a larger displacement for the vertical branch compared to the two oblique branches [1]. The floating effect reaches its maximum when a branch is vertical, weakens in the branch that gets closer to horizontal (Figure 4b) and is nil when a branch is horizontal (Figure 4c). The different amounts of displacement for each of the three oblique branches in Figure 4b express the different apparent heights of the floating effect observed in the corresponding stereogram (Figure 3b).

DISCUSSION

Star Garnets Showing Asterism

Star garnets of pyrope-almandine composition are known from various world localities such as Andhra Pradesh, India (Kumar *et al.* 1992), Ilakaka, Madagascar (Schmetzer & Bernhardt 2002), and Idaho, USA (Guinel & Norton 2006).

---

[1] The relative distance between the red and cyan representations of the same branch is consistent in one anaglyph but cannot be compared from one anaglyph to another because we used slightly different vertical axes for each orientation of the star to best highlight the stereoscopic effect.

The origin of asterism in almandine(-pyrope) has been described in detail (see, e.g., Walcott 1937; Schmetzer *et al.* 2002a; Guinel & Norton 2006). Walcott (1937) studied the crystallographic orientations of the needle-like inclusions in star garnets showing four rays, as well as displaying both four- and six-rayed asterism in the same sample. Schmetzer *et al.* (2002a) used Raman spectroscopy and Guinel and Norton (2006) employed electron diffraction to identify the needles in star garnets as rutile; the latter study also established the crystallographic orientation relationship between the inclusions and the host garnet.
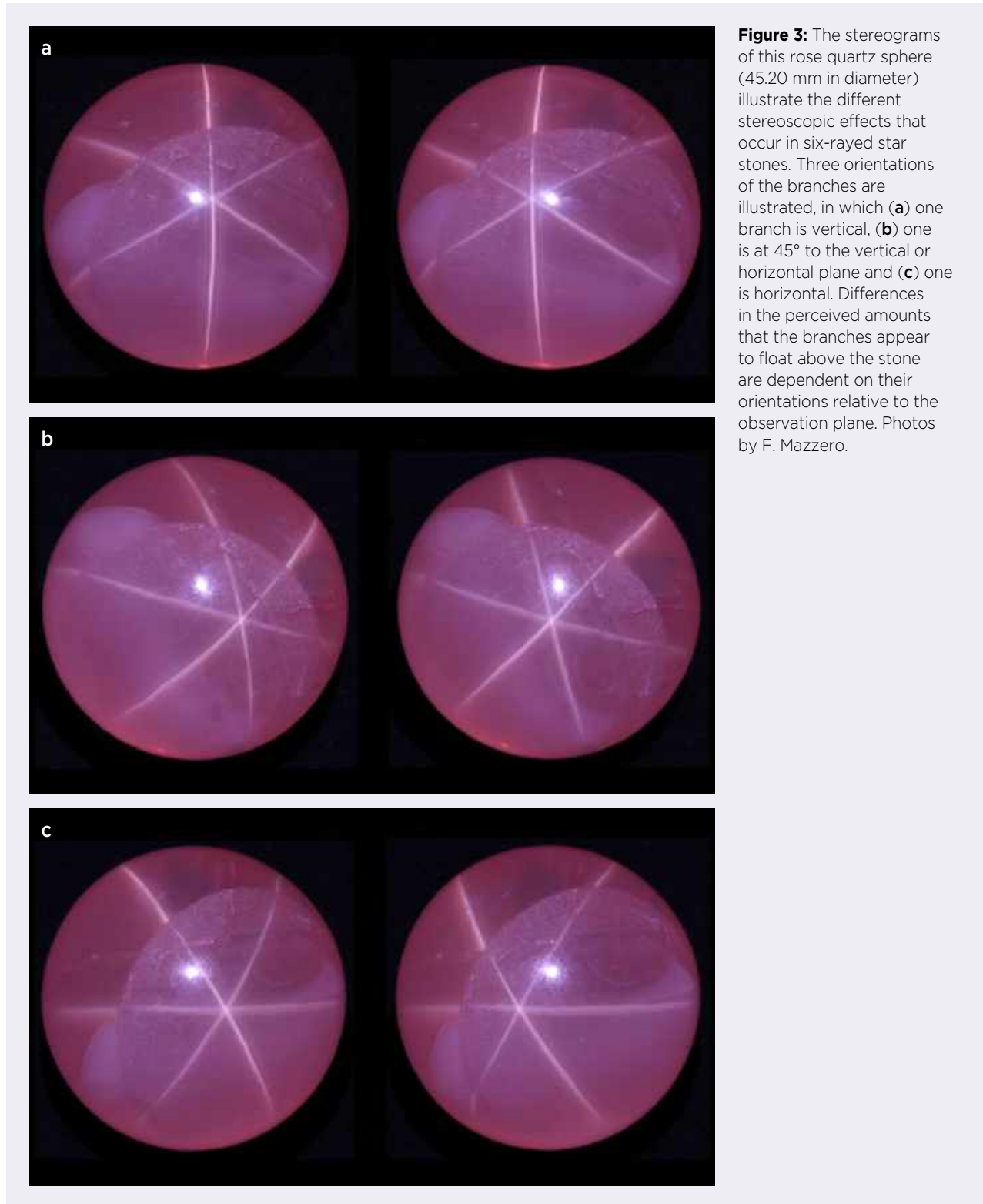

Figure 3: The stereograms of this rose quartz sphere (45.20 mm in diameter) illustrate the different stereoscopic effects that occur in six-rayed star stones. Three orientations of the branches are illustrated, in which (**a**) one branch is vertical, (**b**) one is at 45° to the vertical or horizontal plane and (**c**) one is horizontal. Differences in the perceived amounts that the branches appear to float above the stone are dependent on their orientations relative to the observation plane. Photos by F. Mazzero.
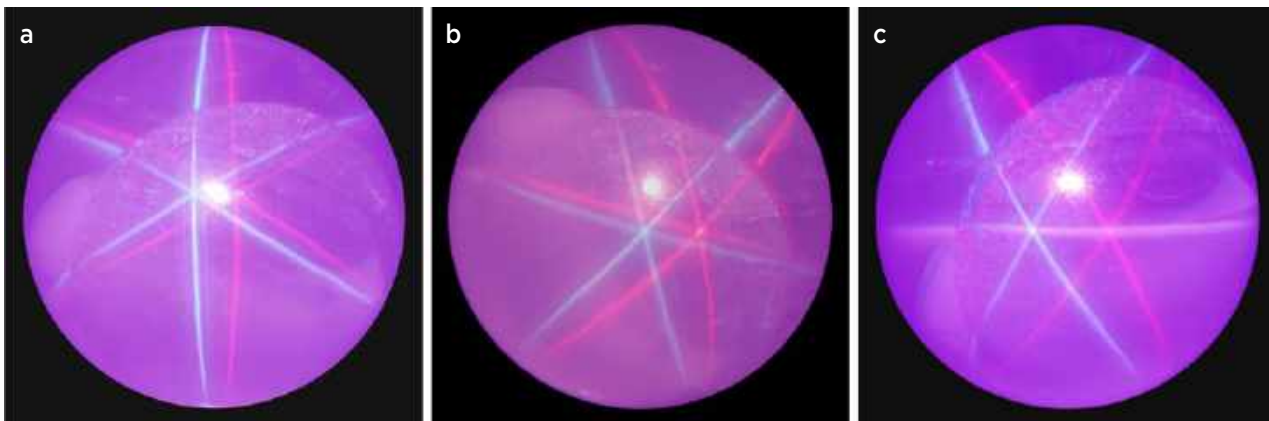
Figure 4: These three anaglyphs of the rose quartz sphere (a–c, corresponding to the stereograms in Figure 3a–c) show the separation of the rays that is responsible for the floating effect of a particular branch of the star and the illusion of variable depth between branches. Anaglyphs by F. Mazzero.

Origin of the Optical Phenomenon

To provide an explanation for the optical effects described in this article, it is convenient to trace the path of light using a ray diagram. Figure 5 provides a sketch of the entire light path, from the source to the eyes, which produces the cat's-eye phenomenon (or each branch of a star). The light is first refracted at the surface of the cabochon at B, then is reflected by an included needle at C and emerges at D towards the left eye L. Conversely, the light reaching the right eye R is first refracted at the surface of the cabochon at B', then is reflected by an included needle at C' and emerges at D'. Only the last parts of the light path (D–L and D'–R) need to be considered to explain the optical effects.

Figure 6 illustrates the anaglyph of one branch of the star in three different positions: (a) vertical, (b) oblique and (c) horizontal. Figure 6a corresponds to the condition illustrated in Figure 5, where the horizontal needles (C–C') are parallel to the observation plane and the resulting branch is thus vertical. D and D' belong to the two images of the vertical branch comprising the anaglyph (as seen in Figure 4a), which are clearly separated. The brain
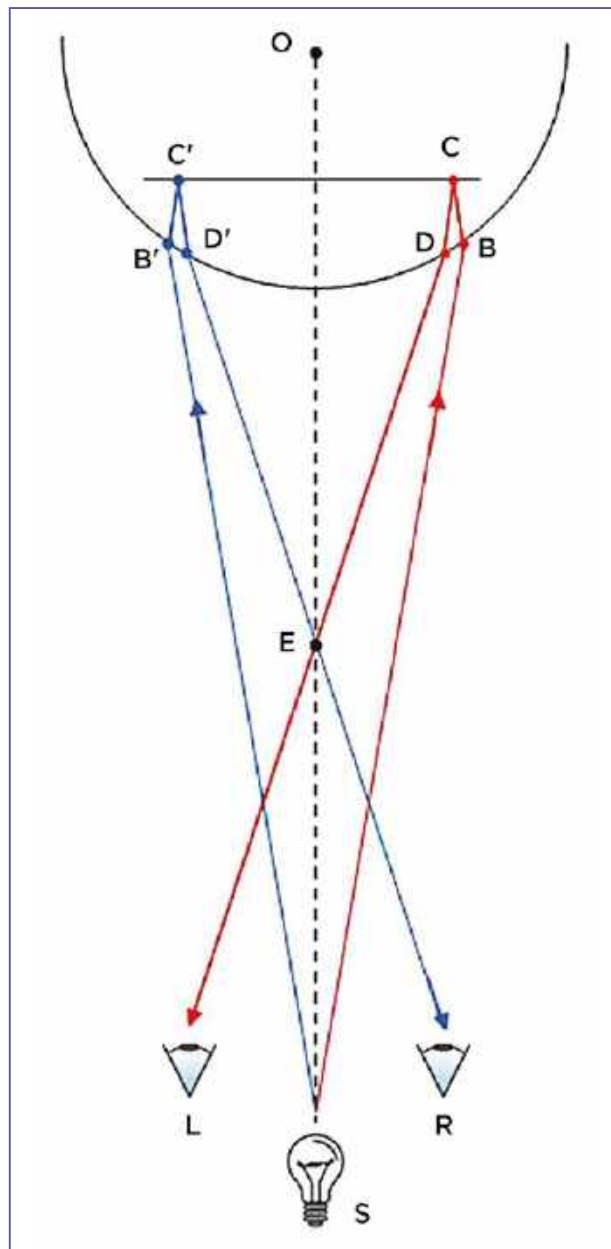

Figure 5: This diagram shows the entire light paths from the light source (S) to the eyes (L and R) for a set of horizontal needle inclusions parallel to the observation plane. The light reaches the sphere at B (red path) and is refracted on entering the stone and then is reflected from an included needle at C. It then returns to the surface of the sphere at D where it is refracted and travels to the left eye. In doing so, it crosses the axis OS at position E. Light reaching the other eye takes a mirror-image path (blue), entering the stone at B', reflecting at C', refracting at D' and crossing the axis at E to reach the right eye. The viewer's brain merges these two images into one so that the centre of the star appears to float above the sphere at E. This is the effect originally demonstrated by Killingback (2005).
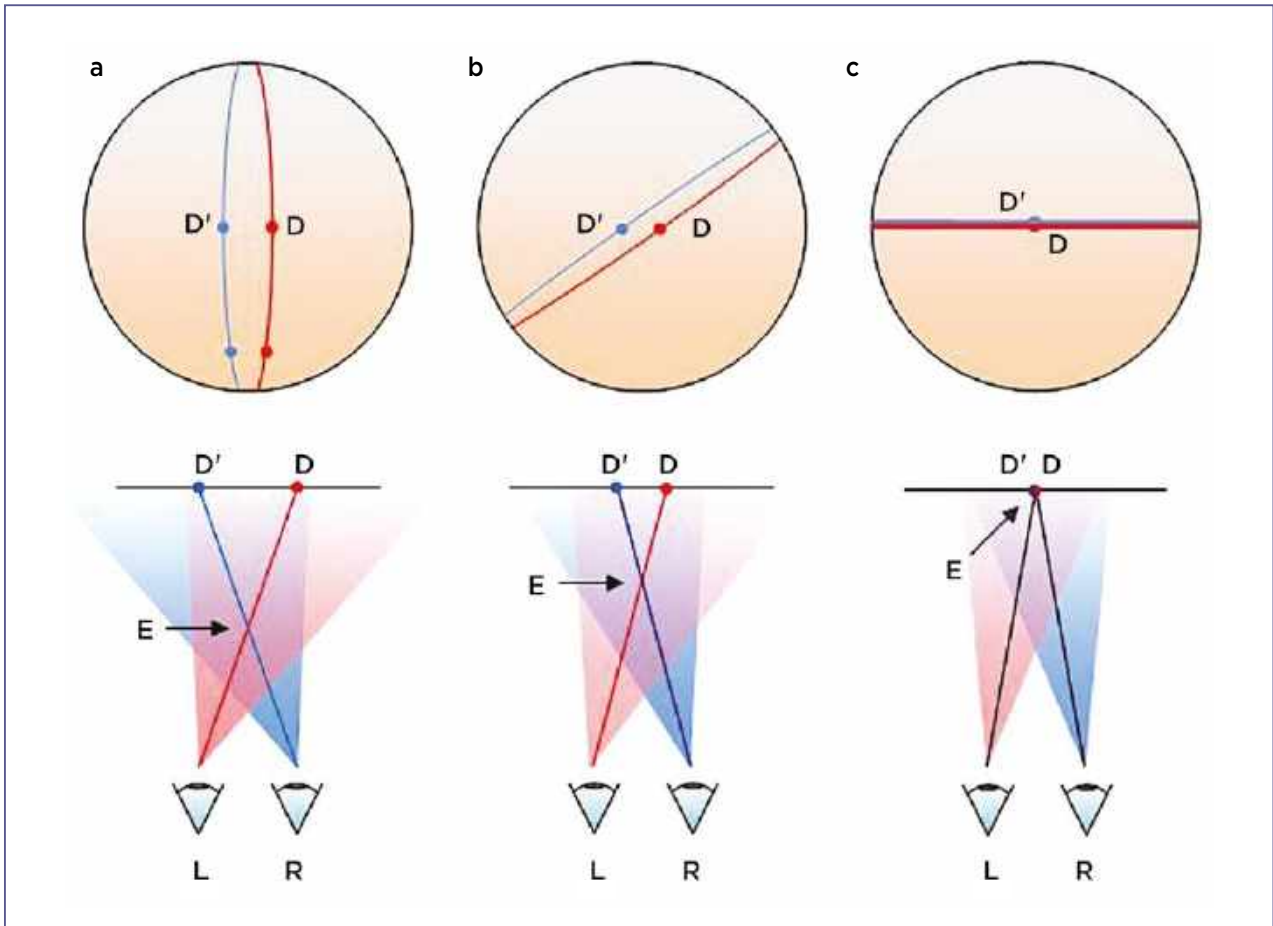
Figure 6: This sketch illustrates various positions for one branch of a star, corresponding to the orientations shown by the anaglyphs in Figure 4: (**a**) vertical, (**b**) oblique and (**c**) horizontal. The diagrams below show where the eyes focus at different levels E for each orientation of the stone. The colour convention is the same as that of classical anaglyphs (red for the left eye and cyan for the right eye). The vertical axis of the sphere is perpendicular to the drawing plane. These diagrams show only the last part of each light path, emerging from the stone at D and D' (see Figure 5) and then reaching each eye.

gathers them together above the stone's surface at the focal point of the light path reaching each eye (located at E). As the stone rotates around its vertical axis (O–S in Figure 5), the needles angularly shift away from the observation plane. The branch is then at an oblique angle, so the distance between the two equatorial dots is shorter and the focal point E thus moves closer to the stone (Figure 6b). Finally, when the stone is rotated so the needles are perpendicular to the observation plane, D and D' coincide (Figure 6c). The distance between the two equatorial dots is reduced to zero and the focal point is on the surface.

For the two pairs of dots in Figure 6a, the distance is greater between the two equatorial dots than between the subpolar ones. Consequently, the focus level should appear to get closer to the stone as the branch extends from the equator to the poles.

In a large cabochon or sphere such as those examined here, the stereoscopic phenomenon is visible to unaided

eyes and is impressive to observe when slowly moving the stone. Thus, it is possible to observe a gradual transition between the different conditions described above.

CONCLUSION

This article expands on the stereoscopic phenomenon previously reported by Killingback (2005) for a cat's-eye or the branch of a star perpendicular to the observation plane. We observed additional features when considering all branches of a star, using both a four-rayed star garnet and a six-rayed star rose quartz as examples. Depending on the orientation of the branches relative to the observation plane, one branch appears to be in front of the other, and their separation distance and relative positions oscillate through a full 360° rotation of the sample.

Readily observable on cabochons of large size, the floating effect occurs in all chatoyant and asteriated

gemstones. However, it is less perceptible to unaided eyes on jewellery-size cabochons of a few tens of carats or less. Indeed, the distance from the observer and the small size of the stone are such that differences between the two images of the star, as perceived by each eye, are not sufficient for the brain to interpret them as having a stereoscopic effect. Nevertheless, on these smaller stones, stereoscopic pairs of photomicrographs could be taken to highlight the effect. In addition, this optical phenomenon is usually visible with a binocular microscope.

While the floating effect can be observed on all cat's-eye and star gemstones, the variable distance between branches, of course, is only seen in star stones. Along with the appeal of the asterism itself, the stereoscopic phenomenon constitutes an additional interesting feature displayed by large star stones.

REFERENCES

Bui, T.N. 2018. What's New: New diamond museum in Antwerp. *Journal of Gemmology*, **36**(4), 278.

de La Taille, R. 1987. Les pierres plus que précieuses. *Science & Vie*, No. 839, 80–85.

Guinel, M.J.-F. & Norton, M.G. 2006. The origin of asterism in almandine-pyrope garnets from Idaho. *Journal of Materials Science*, **41**(3), 719–725, https://doi.org/10.1007/s10853-006-6500-4.

Killingback, H. 2005. Stereoscopic effect in asterism and chatoyancy. *Journal of Gemmology*, **29**(5–6), 312–315, https://doi.org/10.15506/JoG.2005.29.5.312.

Kumar, K.K., Balaram, V. & Sirdeshmukh, L. 1992. Characterization and dielectric properties of almandine-pyrope garnet. *Bulletin of Materials Science*, **15**(3), 279–284, http://doi.org/10.1007/bf02927506.

McWhirter, N. 1986. *Guinness Book of World Records*. Sterling Publishing Co., New York, New York, USA, 480 pp.

Moon, A.R. & Phillips, M.R. 1984. The physics of asterism in sapphire. *Schweizerische Mineralogische und Petrographische Mitteilungen*, **64**(3), 329–334.

Schmetzer, K. & Bernhardt, H.-J. 2002. Star garnets from Ilakaka, Madagascar. *Australian Gemmologist*, **21**(5), 202–206.

Schmetzer, K., Bernhardt, H.-J. & Kiefert, L. 2002a. Star garnets and star garnet cat's-eyes from Ambatondrazaka, Madagascar. *Journal of Gemmology*, **28**(1), 13–23, https://doi.org/10.15506/JoG.2002.28.1.13.

Schmetzer, K., Glas, M. & Bernhardt, H.-J. 2002b. Sterngranate aus Madagaskar. *Lapis*, **27**, 20–27 (in German).

Steinbach, M. 2016. *Asterism: Gems with a Star*. MPS Publishing and Media, Idar-Oberstein, Germany, 896 pp.

Walcott, A.J. 1937. Asterism in garnet, spinel, quartz, and sapphire. *Geological Series of Field Museum of Natural History* [Chicago, Illinois, USA], **7**(3), 39–57, https://archive.org/details/asterismingarnet73walc/page/n5/mode/2up.

Wheatstone, C. 1838. Contributions to the physiology of vision.—Part the first. On some remarkable, and hitherto unobserved, phenomena of binocular vision. *Philosophical Transactions of the Royal Society of London*, **128**, 371–394, https://doi.org/10.1098/rstl.1838.0019.

Wheatstone, C. 1852. The Bakerian Lecture.—Contributions to the physiology of vision.—Part the second. On some remarkable, and hitherto unobserved, phenomena of binocular vision (continued). *Philosophical Transactions of the Royal Society of London*, **142**, 1–17, https://doi.org/10.1098/rstl.1852.0001.

Wüthrich, A. & Weibel, M. 1981. Optical theory of asterism. *Physics and Chemistry of Minerals*, **7**(1), 53–54, https://doi.org/10.1007/bf00308202.

The Authors

Thanh Nhan Bui
Université catholique de Louvain,
Louvain-la-Neuve, Belgium
Email: tnhan93@gmail.com

Pascal Entremont and Prof. Jean-Pierre Gauthier
Centre de Recherches Gemmologiques,
Laboratoire de Planétologie et Géodynamique,
2 rue de la Houssinière, BP 92208, 44322 Nantes Cedex 3, France

Francesco Mazzero
Holaster, Kleindal, Longeville-lès-Saint-Avold,
57740, France

Identification of Type IIa Blue CVD Synthetic Diamonds from Huzhou SinoC Semiconductor Co. in China

Zhonghua Song, Taijin Lu, Hongming Liu, Huiru Dai, Jie Ke, Wenfang Zhu and Jian Zhang

ABSTRACT: Gemmological and spectroscopic characteristics are reported for two type IIa blue CVD synthetic diamonds from Huzhou SinoC Semiconductor Science and Technology Co. Ltd, China. These are the first relatively large (1.76 and 2.63 ct) blue CVD synthetics examined in NGTC's laboratories, and their colour was slightly brighter than other blue synthetic diamonds that we have encountered. In the DiamondView, they fluoresced blue (with purple-red in one sample), which is unusual for CVD synthetics. The mid- and near-IR absorption spectra of one sample showed no hydrogen-related features, while the other synthetic diamond showed a weak absorption at 6853 cm^{-1} attributed to hydrogen. The spectra of both samples had a very weak line at 1332 cm^{-1} due to isolated nitrogen and a distinct band at 9282 cm^{-1} related to radiation. A very strong GR1 absorption feature was detected by UV-Vis-NIR spectroscopy. Photoluminescence spectra obtained at liquid-nitrogen temperature recorded emissions related to radiation (mainly in the 480–510 nm region), N-V and [Si-V]$^-$ centres, and several unassigned weak emissions. This combination of optical centres strongly suggests that these samples underwent post-growth treatment to improve their transparency before they were irradiated to produce blue colouration.

China is the world's largest producer of industrial and gem-quality synthetic diamonds, particularly those grown under high-pressure, high-temperature (HPHT) conditions (Lu *et al*. 2019). Chemical vapour deposition (CVD) synthetic diamond growth technology in China is less well developed, and factory-scale production was lacking until 2012 (Song *et al*. 2012). However, in the past five years, many Chinese companies have begun producing CVD synthetic diamonds, and their products and growth technologies have rapidly developed. Some of these companies mainly produce relatively large, high-quality colourless or near-colourless material, such as Shanghai Zhengshi Technology, Hangzhou Chaoran and others (see, e.g., Lu *et al*. 2019). In addition to these products, other companies—such as Ningbo CrysDiam Industrial Technology and Huzhou SinoC Semiconductor Science and Technology Co. Ltd—can also produce relatively large fancy-colour CVD synthetic diamonds.

Blue CVD synthetic diamonds appeared on the market during the past several years, in sizes ranging from melee (0.007 ct) to 1.34 ct (Ardon & Want 2014; Åström & Scarani 2015; Moe *et al*. 2015; Eaton-Magaña 2018; Odake 2018). Their blue colour is due to irradiation. In March 2020, National Gemstone Testing Center's (NGTC) Beijing laboratory tested two relatively

Figure 1: The two type IIa blue CVD synthetic diamonds (1.76 ct loose and 2.63 ct mounted) examined for this study owe their colour to irradiation treatment. Photos by Z. Song.

large blue CVD synthetic diamonds from Huzhou SinoC Semiconductor Science and Technology Co. Ltd, and this article reports their gemmological and spectroscopic properties.

MATERIALS AND METHODS

The two CVD synthetic diamonds consisted of round brilliants weighing 1.76 ct (loose) and 2.63 ct (mounted in a ring; Figure 1). According to Huzhou SinoC Semiconductor Science and Technology Co. Ltd, which provided the samples, they are representative of commercial products being produced by the company. They were grown at a rate of about 21 μm per hour using the microwave plasma CVD growth technique with 6 kW power, 15–20 kPa pressure and 900–950°C temperature. The company also indicated that the samples had been HPHT treated to improve their transparency before being electron irradiated to produce their blue colour.

The following testing and analysis procedures were performed on both samples. A gemmological microscope was used to examine inclusions and anomalous birefringence. Fluorescence and phosphorescence were observed with the DiamondView instrument developed by De Beers Group. Fourier-transform infrared (FTIR) spectroscopy was performed using a Thermo Nicolet 6700 spectrometer in the range of 6000–400 cm⁻¹ (128 scans at a resolution of 2 cm⁻¹). A QSpec Gem-3000 spectrophotometer was used to obtain ultraviolet-visible-near infrared (UV-Vis-NIR) absorption spectra at liquid-nitrogen temperature. A Renishaw inVia Raman microspectrometer was used to collect photoluminescence (PL) spectra with four laser excitations (325, 473, 532 and 830 nm) at liquid-nitrogen temperature.

RESULTS

The two synthetic diamonds had colour grades equivalent to Fancy blue (1.76 ct) and Fancy Intense blue (2.63 ct), and overall they showed brighter blue colouration than other synthetic diamonds we have encountered. The clarity grades of both samples were equivalent to VS_1. A few irregular dark inclusions were visible with magnification in both specimens (e.g. Figure 2) and appeared to consist of non-diamond carbon, as described for CVD synthetic diamond by Martineau *et al.* (2004).

With cross-polarised light, strong birefringence was another important feature of these CVD samples. The loose one showed low- to moderate-order interference colours, and the mounted specimen displayed moderate-
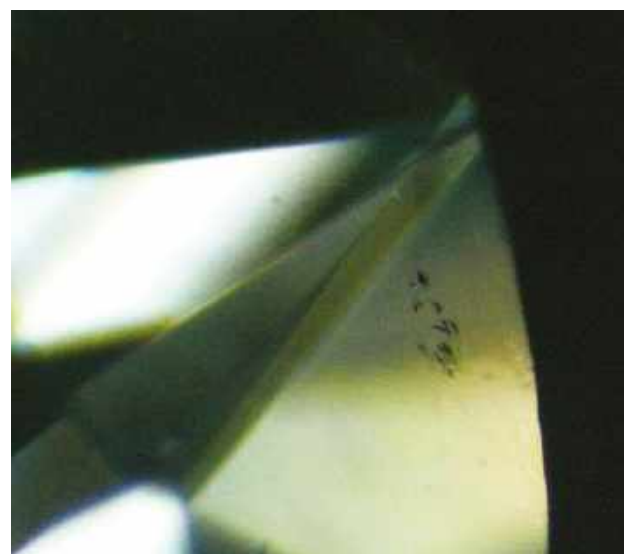

Figure 2: Dark inclusions (probably non-diamond carbon) are present in the blue CVD synthetic diamonds, as shown here in the 1.76 ct sample. Photomicrograph by Z. Song; magnified 50×.
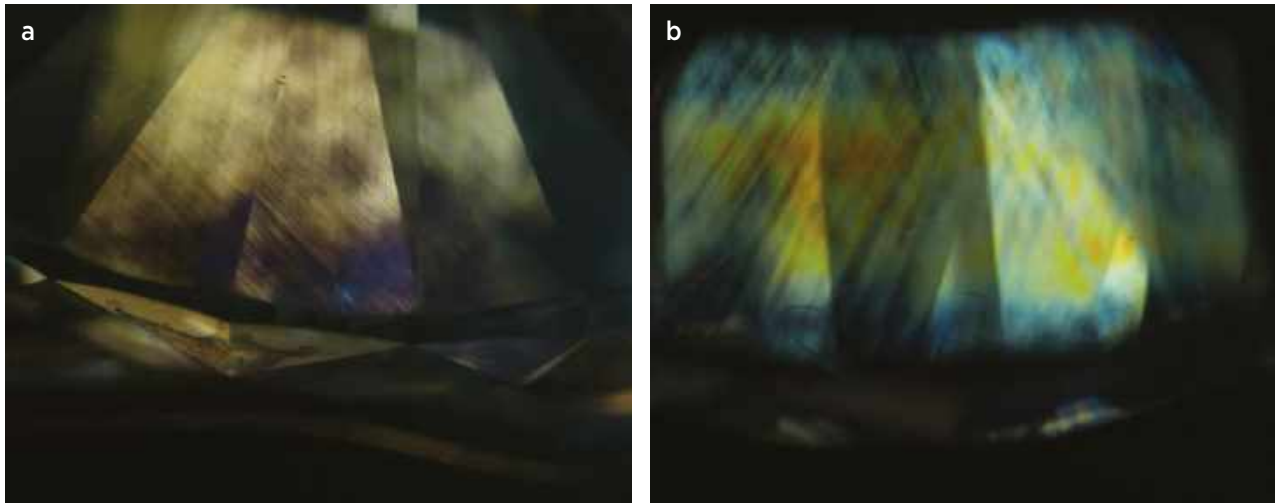
Figure 3: Strong birefringence is displayed by the (**a**) loose and (**b**) mounted CVD synthetic diamonds when observed with crossed polarisers. Photomicrographs by Z. Song; magnified 16×.

to high-order interference colours (Figure 3). The patterns were linear or grid-like, but not the Tatami structure typical of type IIa natural diamonds (Howell 2012).

Luminescence Features

As observed with a DiamondView, the loose sample fluoresced blue (with obscure growth structure), which is not typical for CVD synthetic diamonds. The mounted specimen fluoresced mottled blue and purple-red, and showed a distinct grid-like structure (Figure 4). The purple-red luminescence was different from the orange-red fluorescence commonly shown by as-grown CVD synthetic diamonds. In addition, the blue with added purple-red luminescence is seldom seen in natural diamonds (Eaton-Magaña & Shigley 2016). No phosphoresce was seen in either sample.

Spectroscopic Features

IR Spectra. In the mid-infrared region (Figure 5), neither sample showed significant absorption features related to nitrogen or boron impurities, except they both exhibited a very weak line at 1332 cm^{-1} attributed to isolated nitrogen (Zaitsev 2001); nevertheless, both samples were classified as type IIa. In the 3500–3000 cm^{-1} region there was no evidence of any H-related absorptions.

In the near-infrared range, we recorded a band at 9282 cm^{-1} in both samples and a very weak absorption at 6853 cm^{-1} in the 2.63 ct specimen (Figure 6).

UV-Vis-NIR Spectra. The UV-Vis-NIR spectra of both samples (Figure 7) displayed a distinct GR1 absorption at 741 nm, indicating exposure of these synthetics to radiation. Greater GR1 absorption was present in the
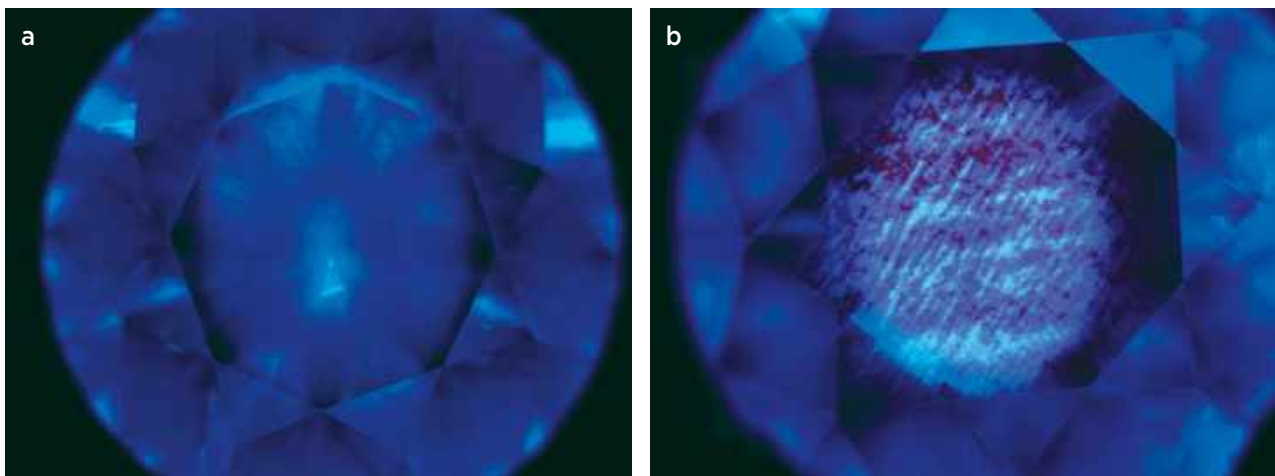
Figure 4: In the DiamondView, (**a**) the 1.76 ct synthetic diamond fluoresces blue and displays an indistinct structure, while (**b**) the 2.63 ct sample fluoresces mottled blue and purple-red and has a distinct grid-like structure. Photos by Z. Song.

Figure 5: The mid-infrared spectrum of the synthetic diamonds reveals that they are type IIa, with a very weak 1332 cm⁻¹ feature due to isolated nitrogen.

Figure 6: The near-IR spectrum of each synthetic diamond at room temperature shows the 9282 cm⁻¹ (1077 nm) absorption band as an indicator of irradiation—as seen here for the 2.63 ct sample, which also has a very weak absorption at 6853 cm⁻¹ attributed to hydrogen.

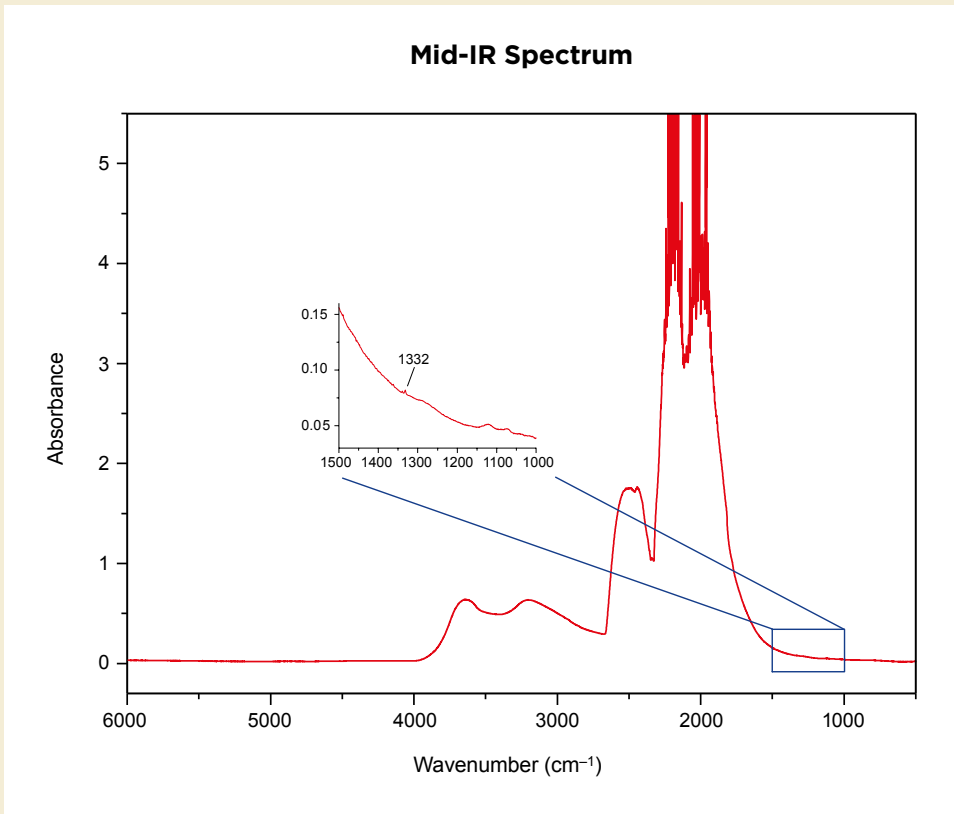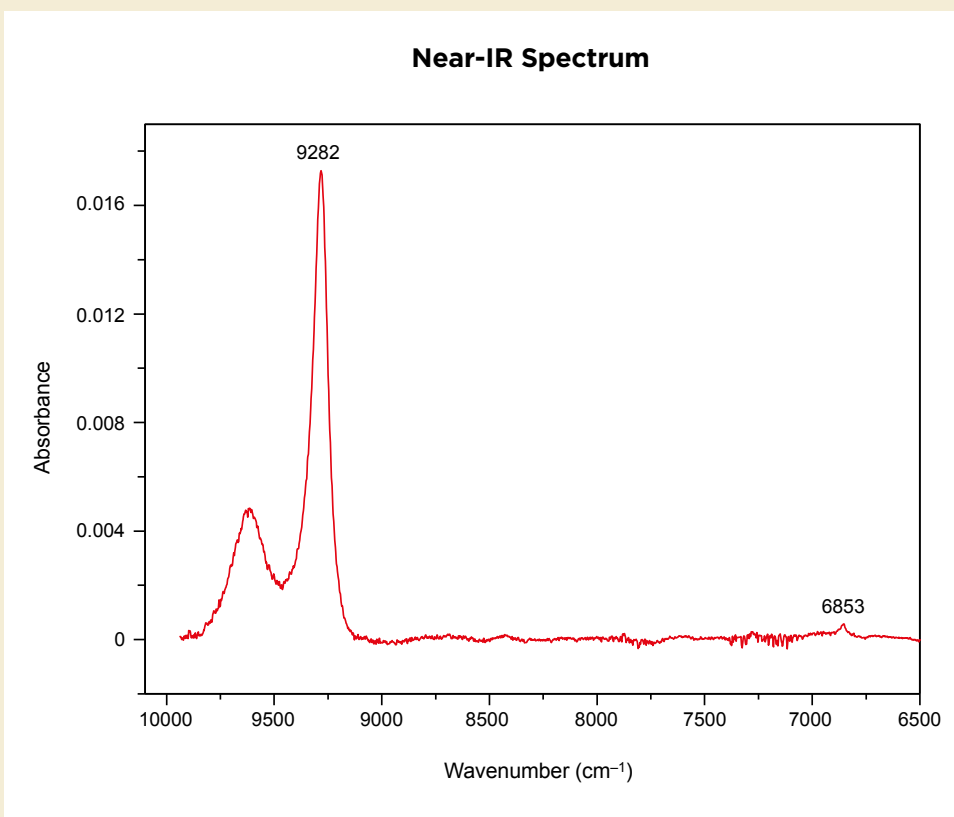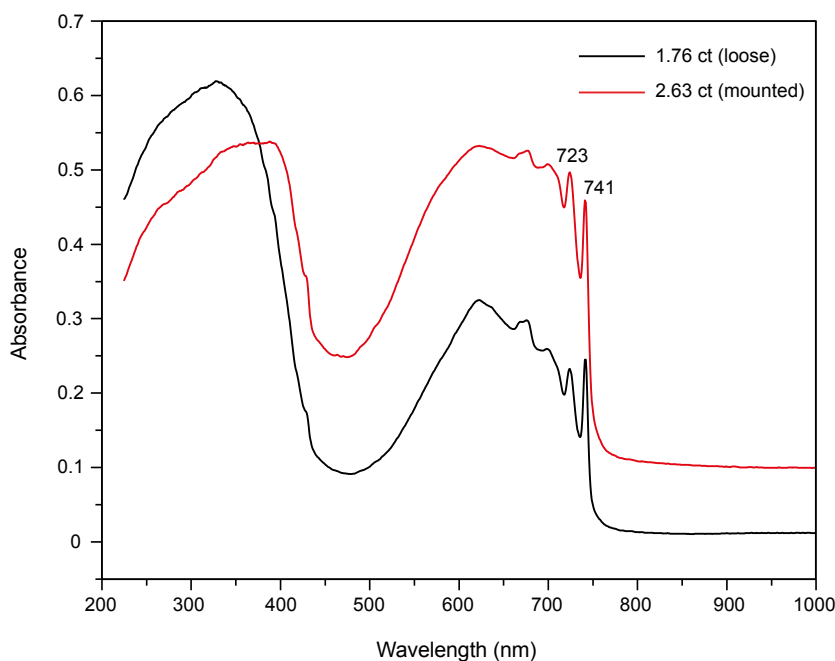**UV-Vis-NIR Spectra**

Figure 7: The UV-Vis-NIR spectra of both synthetic diamonds show strong absorption due to the GR1 centre. The slightly more intense blue colour of the 2.63 ct specimen correlates with its overall greater GR1 absorption.

more intensely blue sample. The blue colour of these synthetic diamonds is due to the transmission window at about 470 nm, which is related to strong absorptions due to irradation (i.e. GR1 and others).

PL Spectra. Both samples showed similar PL spectra, and numerous emission lines were recorded with the different lasers (although no notable emissions were seen with 830 nm excitation).

With the 325 nm laser, both samples showed strong GR1 peaks related to irradiation and a distinct 777 nm luminescence line (Figure 8a).

With blue laser excitation (473 nm; Figure 8b), both samples displayed sharp peaks at 486.3, 488, 488.9, 490.7, 492 and 503.5 nm (3H); weak but sharp peaks at 489.9, 500.8, 503.2 (H3), 523.6, 530.7 and 531.6 nm; and (not labelled on Figure 8b) weak peaks at 494.1, 496.2, 498.5, 510.9, 515.9 nm and elsewhere. The main features excited by this laser are related to irradiation, including the ones at 488, 488.9, 492 and 503.5 nm (Breeding & Wang 2015).

Green laser excitation (532 nm) revealed moderate emission systems (compared to the intensity of the diamond Raman line) of N-V centres at 575 and 637 nm (Figure 8c). We did not observe the doublet emissions at 596.5 and 597.0 nm that usually occur in as-grown CVD

samples (Martineau *et al*. 2004). An additional strong peak at 580 nm was also seen. The samples also showed strong silicon-related emissions at 736.6 and 736.9 nm (see inset in Figure 8c) due to the negative silicon-vacancy defect (Zaitsev 2001). Compared to the intensity of the diamond Raman line, both samples showed a very strong GR1 peak at 741 nm (i.e. much greater than the intensity of the Si-related emission at 737 nm: 741 nm/573 nm = 24 vs. 737 nm/573 nm = 1).

DISCUSSION

Most previously documented as-grown CVD synthetic diamonds have been colourless, near-colourless or brownish (Martineau *et al*. 2004; Wang *et al*. 2007). Specific absorptions in the mid-IR and near-IR regions, and doublet PL emissions at 596.5 and 597.0 nm, are important for separating as-grown from post-growth-treated CVD synthetics.

The specimens in this study had distinctly different characteristics from as-grown CVD synthetics. The 3123 cm⁻¹ band is commonly observed in N-doped as-grown CVD synthetics, but was notably absent from the present samples. Very weak absorption at 1332 cm⁻¹ due to isolated nitrogen was observed in the IR spectra of both samples (Figure 5). The 2.63 ct sample revealed a very
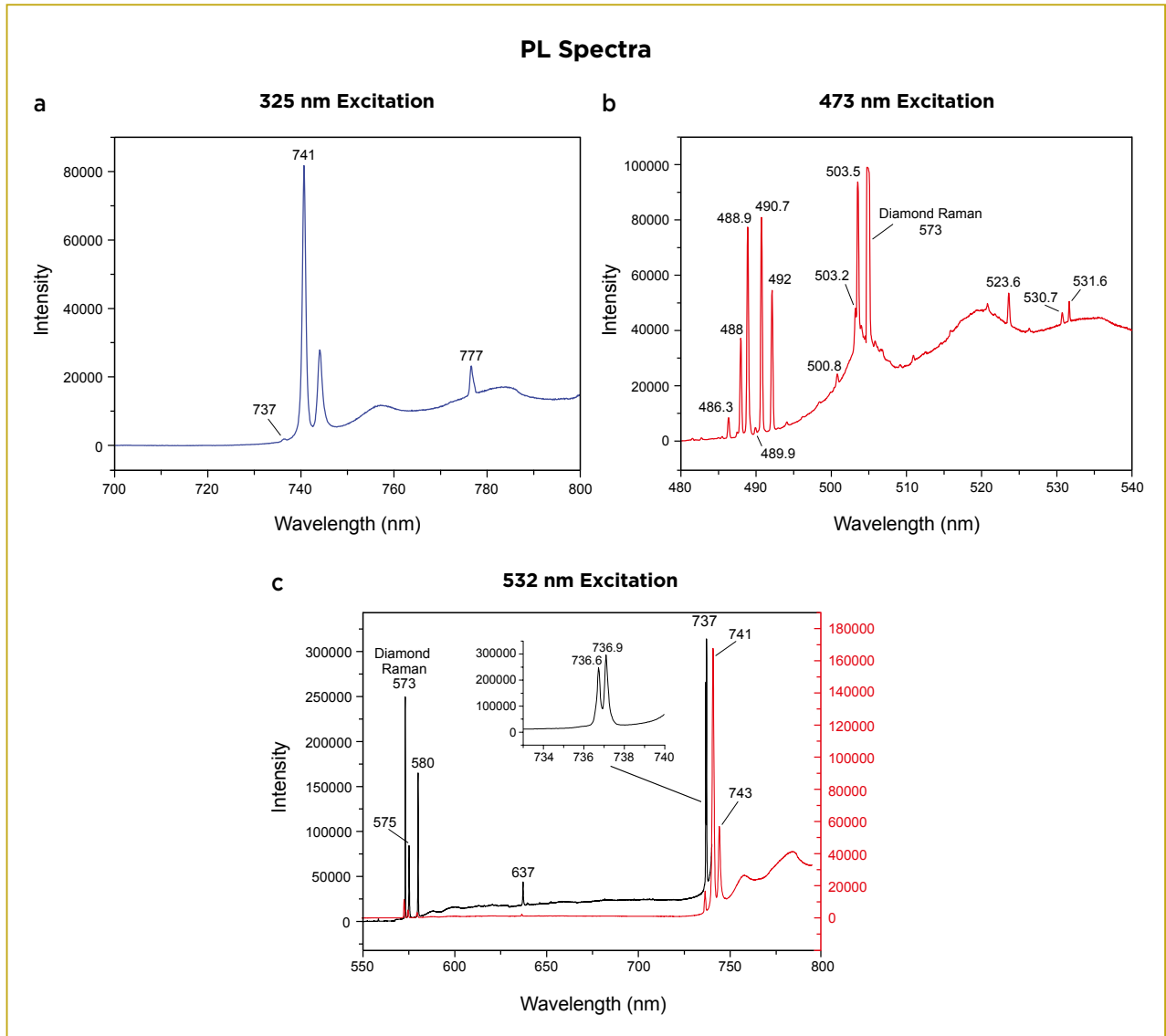
PL Spectra

a   **325 nm Excitation**

b   **473 nm Excitation**

c   **532 nm Excitation**

Figure 8: Numerous emission lines are present in the PL spectra of the synthetic diamonds obtained with (**a**) 325 nm, (**b**) 473 nm and (**c**) 532 nm excitations. The two traces shown for 532 nm excitation are from different test conditions, resulting in more distinct 575, 637 and 737 nm peaks exhibited by the black spectral line.

weak H-related line at 6853 cm^{-1}; the other one did not show any H-related features. All of these mid- and near-IR absorption features indicate that the two CVD samples had been HPHT treated before electron radiation, as indicated by the company that supplied them.

In the near-IR region, an absorption feature at 1077 nm (or 9282 cm^{-1} in Figure 6) was observed in both of the blue CVD synthetic diamonds. This feature is often observed in type Ia and IIa natural and synthetic diamonds after irradiation (Lyu *et al.* 2015). This centre is not associated with nitrogen, but possibly relates to a multi-vacancy complex (Zaitsev 2001). Vasilev *et al.* (2018) documented naturally irradiated diamonds showing absorption at 1077 nm. At room temperature this feature was weak compared to the absorption in

the visible region, and it almost disappeared at 77 K. Although the spectrum in figure 2b of Vasilev *et al.* (2018) is not shown clearly, Prof. A. Collins (pers. comm. 2020) examined the original data files, which were kindly made available by Dr Vasilev, and the room-temperature spectrum was very similar to that shown in Figure 6 of the present article. We can therefore conclude that distinct 1077 nm absorption is a strong indicator of irradiation. However, the absence of absorption at 1077 nm does not mean that a synthetic or natural diamond has not been irradiated. There are examples of less heavily irradiated diamonds in which the 1077 nm centre was not detected when the absorption spectra were measured at 77 K (A. Collins, pers. comm. 2020).

PL spectroscopy of the two samples in the present

study showed that several centres were introduced during the electron-irradiation process, including those at 486.3, 488, 488.9, 492, 503.5, 515.9, 523.6, 580, 741 and 777 nm. In addition, a strong 490.7 nm peak was observed in the PL spectra of both samples (Figure 8b). Breeding and Wang (2015) found that this feature was not observed in diamonds with less than 25 ppm A aggregates. Because we did not examine the present specimens before they were irradiated, we cannot be sure whether this feature was introduced by irradiation. Therefore, more work is required to determine whether the irradiation process can introduce the 490.7 nm PL peak.

Both the 488.9 and 523.6 nm PL emissions can occur in irradiated type I and II diamonds (Collins & Rafique 1979; Breeding & Wang 2015; Hainschwang & Pamies 2019). The 488.9 nm line has been attributed to complexes involving carbon interstitials and isolated nitrogen (Collins & Rafique 1979) and will anneal out by 375°C. The authors have tested some irradiated natural rough diamonds with a weak 488.9 nm line, but after they were faceted it was no longer detected and a new line appeared at 488.4 nm. Although Hainschwang and Pamies (2019) reported that the 523.6 nm peak is related to nitrogen concentration and plastic deformation, but not to any specific form of nitrogen, the present study shows that a weak 523.6 nm line can be detected in CVD synthetic diamonds that contain a small amount of isolated nitrogen.

We detected a very strong 503.5 nm peak (3H centre) in the PL spectra of both samples. Along with the GR1, the 3H centre is a typical feature of irradiated diamond, often accompanied by a peak at 492 nm (Breeding & Wang 2015; Zaitsev et al. 2017). Although the 3H defect can be detected in some untreated natural type IIa and IIb diamonds (Eaton-Magaña & Lu 2011), a strong 3H is still a good indicator of irradiation. The other typical features of the 3H centre at 540.7 and 552.4 nm (Steeds et al. 1999; not shown in Figure 8) were also present in both samples.

We found that the intrinsic optical centre with its zero-phonon line at 580 nm can be very strong in irradiated CVD synthetic diamond. This 580 nm centre relates to a negatively charged interstitial vacancy pair (I-V⁻; Zaitsev et al. 2017).

With 325 and 532 nm excitation, the PL spectra of both samples revealed the strong presence of the GR1 radiation centre, a defect correlated with an isolated vacancy. The intensity of the GR1 peak was about 24 times that of the diamond Raman line; this is much more intense than in untreated natural diamonds.

Breeding and Wang (2015) proposed that the 777 nm centre is introduced by radiation and should disappear when A-aggregate concentration increases up to 10%; this centre does not correlate to B or C centres. However, we have found the 777 nm centre in many untreated natural type IIa diamonds and occasionally in naturally irradiated type Ia diamonds. In addition, according to our unpublished research, the 777 nm peak can be introduced during irradiation of HPHT-treated type IIa diamonds. There is some relationship between the intensity of the GR1 centre and the presence of the 777 nm peak: the stronger the GR1 feature, the clearer the 777 nm peak. More work is needed to understand the exact structure of the 777 nm feature.

CONCLUSIONS

This is the first time NGTC has examined CVD synthetic diamonds that were irradiated to a blue colour. In the DiamondView, the loose sample described here showed blue florescence, as well as no observable layered growth structure typical of CVD products, which indicates how such material can be difficult to identify by this technique alone. The presence of a 9282 cm⁻¹ band in the near-infrared spectral region, and the distinct GR1 and other lines displayed by these two CVD synthetic diamonds, proved that they were indeed irradiated. Moreover, there are no natural blue diamonds in which the colour is due to the presence of GR1 absorption, and so the blue colour, together with the UV-Vis-NIR spectral features, unambiguously show that these type IIa synthetic diamonds have been treated.

These two irradiated blue CVD synthetic diamonds provide a lot of information about defects produced during irradiation. The 3H system (503.5, 540.7 and 552.4 nm PL peaks), as well as the 488.9 and 523.6 nm PL features, exemplify that irradiated diamonds may display various combinations of defects, which reveal information about the production of such material. As CVD synthetic diamonds become more available and more complicated to identify, the most reliable option is to send samples to a gemmological laboratory.

REFERENCES

Ardon, T. & Want, W. 2014. Lab Notes: Heavily irradiated CVD synthetic diamond. *Gems & Gemology*, **50**(3), 240–241.

Åström, M. & Scarani, A. 2015. Application Note: Large amount of pink and blue CVD-grown synthetic diamonds on the market. Magilabs, 8 pp., www.gemmoraman.com/Articles/AppNoteBluePinkCVD.aspx, 22 February, accessed 21 May 2020.

Breeding, C.M. & Wang, W. 2015. The influence of nitrogen aggregates on PL-active diamond defects introduced during electron irradiation and annealing including 490.7 nm. *The 66th Diamond Conference*, Warwick, West Midlands, 6–9 July, O28.1 (unpublished).

Collins, A.T. & Rafique, S. 1979. Optical studies of the 2.367 eV vibronic absorption system in irradiated type Ib diamond. *Proceedings of the Royal Society of London. A. Mathematical and Physical Sciences*, **367**(1728), 81–97, https://doi.org/10.1098/rspa.1979.0077.

Eaton-Magaña, S. 2018. Lab Notes: Three irradiated CVD synthetic diamonds. *Gems & Gemology*, **54**(2), 215–216.

Eaton-Magaña, S. & Lu, R. 2011. Phosphorescence in type IIb diamonds. *Diamond and Related Materials*, **20**(7), 983–989, https://doi.org/10.1016/j.diamond.2011.05.007.

Eaton-Magaña, S. & Shigley, J.E. 2016. Observations on CVD-grown synthetic diamonds: A review. *Gems & Gemology*, **52**(3), 222–245, https://doi.org/10.5741/gems.52.3.222.

Hainschwang, T. & Pamies, G. 2019. Diamond treatments revisited: A complete study of the behaviour of diamonds and their defects upon irradiation and annealing up to HPHT treatment. *The 70th Diamond Conference*, Warwick, West Midlands, 8–11 July, O24.1–O24.4 (unpublished).

Howell, D. 2012. Strain-induced birefringence in natural diamond: A review. *European Journal of Mineralogy*, **24**(4), 575–585, https://doi.org/10.1127/0935-1221/2012/0024-2205.

Lu, T., Ke, J., Lan, Y., Song, Z., Zhang, J., Tang, S., Su, J., Dai, H. *et al*. 2019. Current status of Chinese synthetic diamonds. *Journal of Gemmology*, **36**(8), 748–757, https://doi.org/10.15506/JoG.2019.36.8.748.

Lyu, X., Lu, T., Yang, L., Song, Z., Zhang, J. & Chen, C. 2015. Identification of irradiated coloured diamonds by 9287 cm^{-1} absorption band. *2015 China International Gem & Jewelry Academic Conference*, Beijing, China, 30 November, 36–41 (in Chinese with English abstract).

Martineau, P.M., Lawson, S.C., Taylor, A.J., Quinn, S.J., Evans, D.J.F. & Crowder, M.J. 2004. Identification of synthetic diamond grown using chemical vapor deposition (CVD). *Gems & Gemology*, **40**(1), 2–25, https://doi.org/10.5741/gems.40.1.2.

Moe, K.S., D'Haenens-Johansson, U. & Wang, W. 2015. Lab Notes: Irradiated green-blue CVD synthetic diamonds. *Gems & Gemology*, **51**(3), 320–321.

Odake, S. 2018. Lab Notes: An irradiated CVD synthetic melee diamond found in irradiated natural melee diamonds. *Gems & Gemology*, **54**(4), 436–437.

Song, Z., Lu, T., Lan, Y., Shen, M., Ke, J., Liu, J. & Zhang, Y. 2012. The identification features of undisclosed loose and mounted CVD synthetic diamonds which have appeared recently in the NGTC laboratory. *Journal of Gemmology*, **33**(1), 45–48, https://doi.org/10.15506/JoG.2012.33.1.45.

Steeds, J.W., Davis, T.J., Charles, S.J., Hayes, J.M. & Butler, J.E. 1999. 3H luminescence in electron-irradiated diamond samples and its relationship to self-interstitials. *Diamond and Related Materials*, **8**(10), 1847–1852, https://doi.org/10.1016/s0925-9635(99)00144-2.

Vasilev, E.A., Kozlov, A.V. & Petrovsky, V.A. 2018. Volume and surface distribution of radiation defect in natural diamonds. *Journal of Mining Institute*, **230**, 107–115, https://doi.org/10.25515/PMI.2018.2.107.

Wang, W., Hall, M.S., Moe, K.S., Tower, J. & Moses, T.M. 2007. Latest-generation CVD-grown synthetic diamonds from Apollo Diamond Inc. *Gems & Gemology*, **43**(4), 294–312, https://doi.org/10.5741/gems.43.4.294.

Zaitsev, A.M. 2001. *Optical Properties of Diamond*. Springer-Verlag, Berlin, Germany, 502 pp., https://doi.org/10.1007/978-3-662-04548-0.

Zaitsev, A.M., Moe, K.S & Wang, W. 2017. Optical centers and their depth distribution in electron irradiated CVD diamond. *Diamond and Related Materials*, **71**, 38–52, https://doi.org/10.1016/j.diamond.2016.11.015.

The Authors

Zhonghua Song, Dr Taijin Lu, Huiru Dai, Jie Ke and Jian Zhang
National Gemstone Testing Center, Technology Innovation Center of Gems & Jewelry Inspection and Appraisal, MNR, 22F, Building C, Global Trade Center, 36 North 3rd Ring East Road, Beijing 100013, China
Email: songzh@ngtc.com.cn

Hongming Liu
Huzhou SinoC Semiconductor Science and Technology Co. Ltd, No. 888 Axiang Road, Huzhou, Zhejiang Province, China

Wenfang Zhu
National Gemstone Testing Center Shenzhen Lab, 4 Libei South Road, Luohu District, Shenzhen, Guangdong Province, China

Amber from Khamti, Sagaing Region, Myanmar

Thet Tin Nyunt, Tay Thye Sun, Murali Krishnaswamy, Loke Hui Ying, Cho Cho, Naing Bo Bo Kyaw, Wai Yang Lai Aung and Chutimun Chanmuang N.

ABSTRACT: In the Pat-tar Bum area near Khamti in the Sagaing Region of northern Myanmar, amber is mined from Cretaceous limestone using underground and open-pit methods. Most of the amber ranges from yellow to dark brown, and it shows typical gemmological properties for amber. Inclusions in our samples consisted of flattened gas bubbles, fractures and brownish material (probably organic debris), and the authors have also seen pieces containing various types of animal remains such as an insect wing, spider and bird feather. FTIR and Raman spectra show features consistent with Burmese amber.

Burmese amber, or Burmite, is sought after as a gem material and is also well known for hosting a wide variety of interesting invertebrate and plant inclusions. It is mainly recovered from deposits near Tanai (or Danai) in the Hukawng Valley of Kachin State, northern Myanmar, where several different amber varieties are found (e.g. Jiang *et al.* 2020). Other Burmese amber localities, which were discovered more recently, include Hti Lin (Tilin) in the Magway Region of western central Myanmar, and Pat-tar Bum (Pat-ta Bum) near Khamti (Hkamti) in the Sagaing Region of northern Myanmar.

The Pat-tar Bum deposits were initially mined during the British colonial period, but were abandoned in the 19th century and reopened in 2010. Due to an increase in amber demand from mainland China, mining activities increased at Pat-tar Bum in 2012–2013. This amber was briefly described by Liu (2018), and in January 2018 some of the present authors (TTN, CC and NBBK) visited several sites in the Pat-tar Bum area. Initial results of the authors' research were briefly presented by Thet Tin Nyunt *et al.* (2019), and this article provides more details on the geology, mining and gemmological properties of this amber (e.g. Figure 1).

Figure 1: This amber pendant (7.2 × 3.3 × 1.6 cm) from Khamti, Myanmar, displays attractive patterns formed by trapped organic debris. Photo by Thet Tin Nyunt.
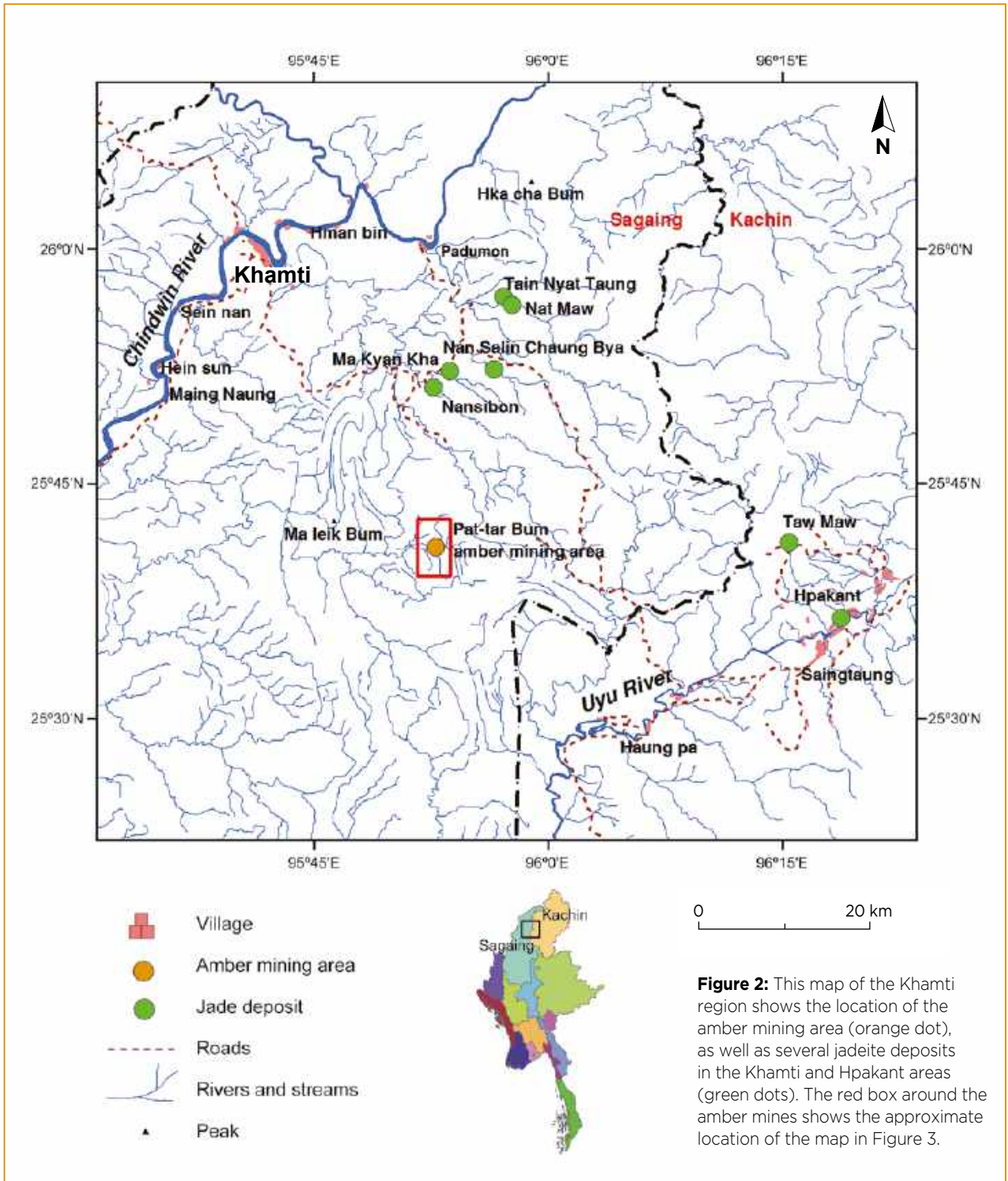
Figure 2: This map of the Khamti region shows the location of the amber mining area (orange dot), as well as several jadeite deposits in the Khamti and Hpakant areas (green dots). The red box around the amber mines shows the approximate location of the map in Figure 3.

LOCATION AND GEOLOGY

The Pat-tar Bum amber deposit is located near Nampilin stream about 40 km south-east of the town of Khamti (25°41′ N, 95°50′ E; Figure 2) and about 112 km south-west of Tanai. The specific sites visited by some of the authors include Lachun (also spelled Laychun and Lachon) Maw, which was the most productive mining area, as well as Kyat Maw, Shan Maw, Gyar (also spelled Kyar) Maw and Kyauk Tan Maw (Figure 3). ('Maw' means 'mine' in Burmese.)

The Khamti area is mostly underlain by Paleocene to Eocene molasse-type sedimentary units of the Paunggyi Formation. Cretaceous units are locally present, including

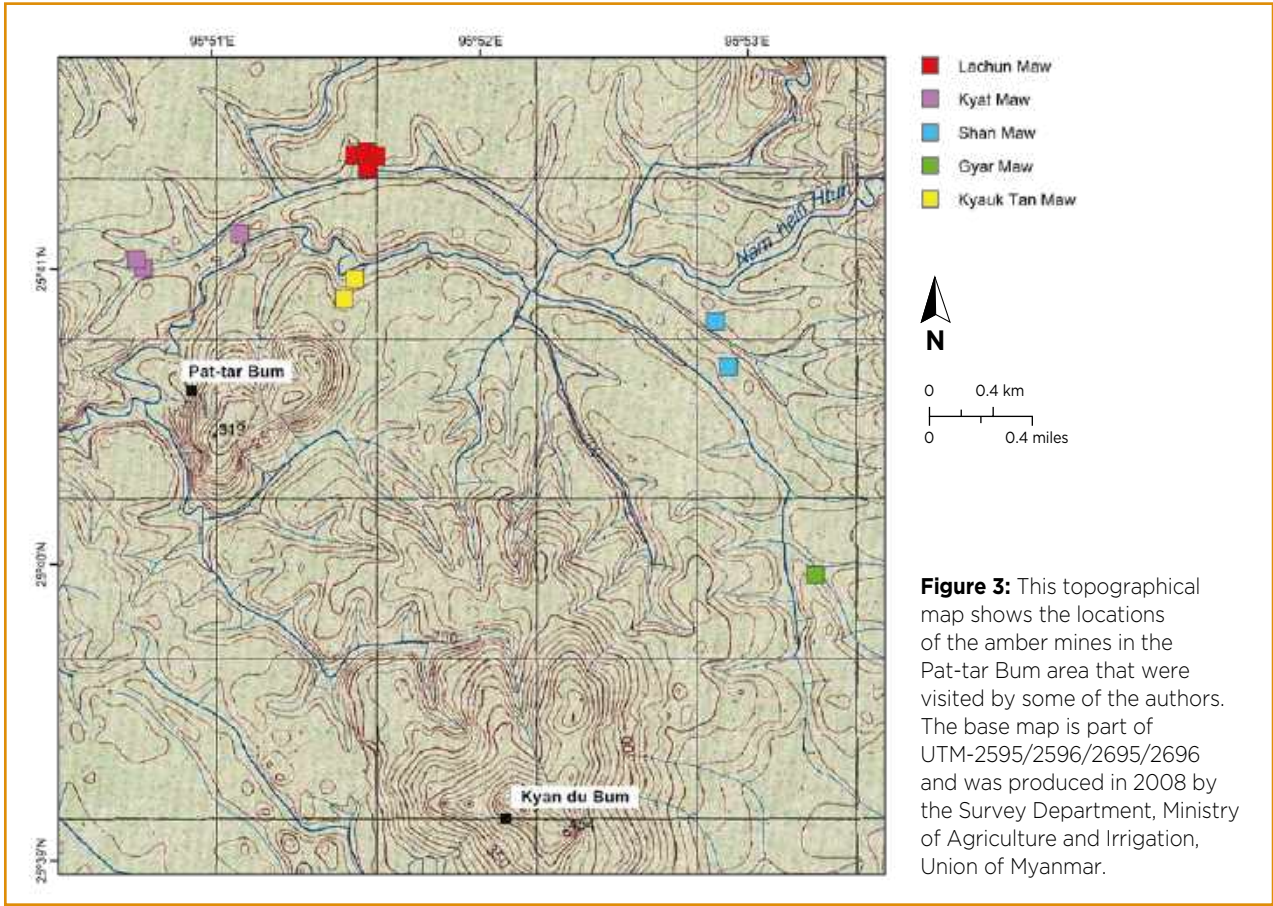**Figure 3:** This topographical map shows the locations of the amber mines in the Pat-tar Bum area that were visited by some of the authors. The base map is part of UTM-2595/2596/2695/2696 and was produced in 2008 by the Survey Department, Ministry of Agriculture and Irrigation, Union of Myanmar.

the Kalaw Red Beds, the Kabaw Formation and other marine units including limestone; also occurring in the area are ultramafic and mafic intrusions of mostly Jurassic age (Soe Thura Tun *et al.* 2014). The intrusions are mainly represented by peridotite and serpentinite, and commercially important jadeite deposits are locally associated with the latter rock type (e.g. near Nansibon; Thin 2016).

The amber deposits are hosted by the Cretaceous limestone, which contains fossils that are of late Albian age (*Orbitolina* sp.; Mitchell 2018). The thickness of the amber-bearing limestone horizons ranges from several centimetres to nearly 1 m, and they are locally intercalated with sandstone and carbonaceous shaley limestone, sometimes together with carbonaceous materials (Figures 4 and 5).

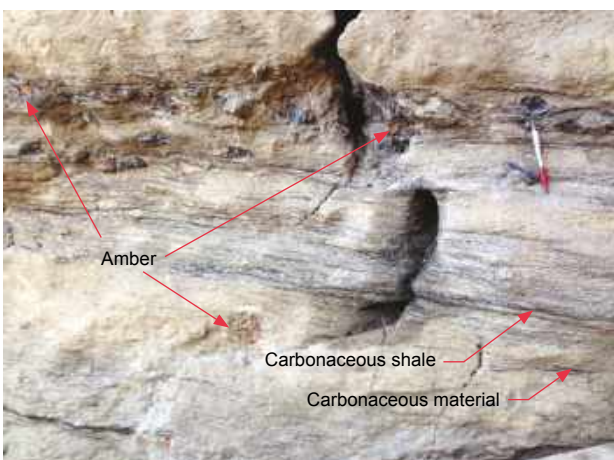**Figure 4:** Khamti amber is hosted by limestone (shown here at Lachun Maw) that is sometimes intercalated with sandstone and locally contains carbonaceous material. See pen for scale; photo by Thet Tin Nyunt.

Figure 5: A miner exposes pieces of amber within limestone at Lachun Maw. The amber from this locality is typically yellow, yellowish brown, brown and dark brown. Photo by Thet Tin Nyunt.

Figure 6: This view of Lachun Maw shows the entrance of an adit that explores the amber-bearing limestone at a shallow angle along bedding planes. Photo by Thet Tin Nyunt.

Figure 7: A pulley system (see ropes and orange bucket) is being used to remove amber-bearing limestone from this adit at Lachun Maw. The mining crew then breaks open the pieces of limestone in search of amber. Photo by Thet Tin Nyunt.

MINING AND PRODUCTION

The Pat-tar Bum amber mining area covers 1,500 hectares and contains five major production sites (listed in the previous section), including 13 claim blocks where mining has been organised by Sea-Sun-Star Co. Ltd (Myitkyina, Myanmar) since 2010.

At Lachun Maw, amber mining is carried out by drilling and blasting a series of tunnels (adits or inclines) that follow the 20°–35° dip of the limestone (e.g. Figure 6). The blasted material is transported to the surface using a pulley system, and the limestone is then broken into smaller pieces to extract the amber (Figure 7). Vertical shafts called *lay-pin* are also used to reach the amber-bearing horizons (Figure 8). Each shaft measures 4 × 4 feet (1.2 × 1.2 m) and may attain depths greater than 5 m, such

as at Kyat Maw. Upon reaching an amber-bearing layer, the miners then drive an adit along the bedding plane of the limestone. Open-pit mining is also carried out at Kyat Maw (Figure 9), Shan Maw and Gyar Maw, where 3–5 m of overburden must be removed to reach the amber-bearing limestone.

Although amber mining at Pat-tar Bum started in 2010, official production data began with fiscal year 2014–2015 (Table I). From 2014 to 2019, the total official production from Pat-tar Bum was about 6,655 kg with an appraised value of about MMK76,800,000 (Myanmar kyats; 1 kyat = 0.00055 British pound). According to a 1995 Myanma Gems Enterprise (MGE) law, the royalty for amber is 10% of the value established by MGE appraisers.

Figure 8: Vertical shafts are also used to reach the amber-bearing limestone, as shown here at Kyat Maw. This shaft is more than 5 m deep. Photo by Thet Tin Nyunt.

Figure 9: Open-pit mining for amber sometimes takes place, as shown here at Kyat Maw. The miners must use pumps to keep the pits from flooding with water. Amber from this mine tends to be dark brown, brown and yellow. Photos by Thet Tin Nyunt.

Table I: Approximate official production and appraised value of amber from Pat-tar Bum near Khamti, Myanmar.[a]

Fiscal year	Weight (kg)	Value (MMK)
2014–2015	555	6,400,000
2015–2016	2,400	6,900,000
2016–2017[b]	90	8,500,000
2017–2018	1,850	30,000,000
2018–2019	1,760	25,000,000

[a] Data obtained in 2019 from Myanma Gems Enterprise.
[b] Lower production was due to expiration of the mining licence in 2017 (nevertheless, a higher value than the previous year may have been due to greater demand). Operations were then carried out under a limited licence until a new mining licence was obtained during the 2017–2018 fiscal year.

MATERIALS AND METHODS

We characterised 21 amber samples (0.45–2.49 ct; Figure 10) that were obtained from the miners during the authors' visit to the Pat-tar Bum mining area. All of them were examined using basic gemmological tools such as a binocular microscope, refractometer, hydrostatic balance, and long- and short-wave UV lamps (Miner-alight UVSL-25) at the Far East Gem Lab in Singapore.

Eleven of the samples (nos. KT01–KT10 and KT21) were prepared as doubly polished plates (about 0.80 mm thickness), and Fourier-transform infrared (FTIR) absorption spectra were obtained from those specimens in attenuated total reflectance (ATR) mode using a Bruker Tensor 27 spectrometer at the University of Vienna. Spectra were collected in the 370–4000 cm^{-1} range with an aperture of 1.5 mm and a resolution of 4 cm^{-1}.

Figure 10: The 21 samples of amber examined for this report range from 0.45 ct (small brownish piece at centre) to 2.49 ct (yellow sample on the far left). Photo by Tay Thye Sun.

Raman analysis of amber and other fossil resins is typically hampered by strong laser-induced luminescence, which virtually covers the entire visible range, so FT Raman is commonly preferred (Brody *et al.* 2001; Jehlička *et al.* 2004). For the present study, by contrast, we used a dispersive Raman system that consisted of a Horiba LabRAM HR Evolution spectrometer. Analyses were performed at the University of Vienna on the same 11 samples that were used for FTIR spectroscopy. In the spectral region of 100–2250 cm^{-1}, Raman shift was measured with a 785 nm diode laser (3 mW power at the sample surface), and in the region of 2250–4000 cm^{-1} Raman shift was analysed using a 633 nm He-Ne laser (8 mW power). In both cases the laser power was well below the threshold of any sample changes due to local absorption-induced heating. A grating with 1,800 grooves/mm (for 633 nm excitation) or 600 grooves/mm (for 785 nm excitation) was used to disperse the scattered light, resulting in a spectral resolution of about 0.7 cm^{-1} and 2 cm^{-1}, respectively. For further analytical details on the Raman spectroscopy system used, see Zeug *et al.* (2018).

RESULTS AND DISCUSSION

Standard Gemmological Properties

Our amber samples were mostly transparent and showed various colours including yellow, greenish yellow, 'golden' yellow, orange-yellow, brownish yellow and brown (Figure 10). The RI ranged from 1.53 to 1.54 (spot readings) and the SG commonly varied from 1.03 to 1.09. Both of these ranges are typical of amber (O'Donoghue 2006). Specimens yielding SG values greater than 1.09 consisted of amber associated with some matrix.

Microscopic examination revealed small areas of white matrix (probably carbonate material) attached to the amber (Figure 11a), flattened gas bubbles, step-like fractures (Figure 11b), irregular brownish inclusions (probably organic debris; Figure 11c) and surface patterns suggesting an imprint against another material (Figure 11d). No insect inclusions were found in the samples studied, although author NBBK previously acquired Khamti amber specimens from a local miner that contained biogenic materials, such as those having the appearance of a bird feather (Figure 12a), a spider (Figure

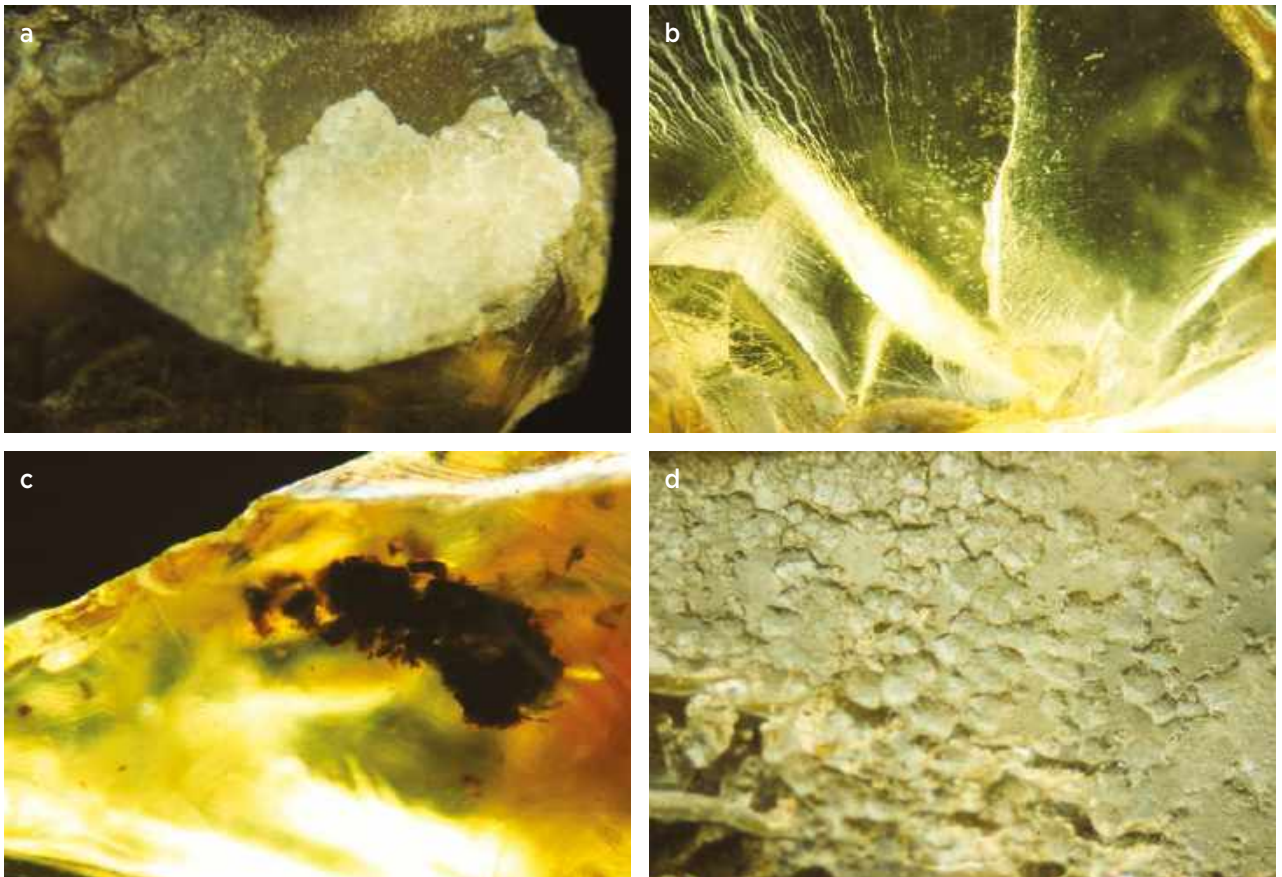**Figure 11:** (**a**) White matrix material is sometimes attached to the amber. (**b**) This sample contains several flattened gas bubbles and its broken surface displays step-like fractures. (**c**) These irregular-shaped brownish inclusions probably consist of organic debris. (**d**) Surface patterns on some of the amber suggest contact with another material. Photomicrographs by Tay Thye Sun; magnified 10×.

Figure 12: Various biogenic inclusions can be found in Khamti amber, as shown by these polished examples that were obtained from a local miner by author NBBK, including those resembling (**a**) a bird feather, (**b**) a spider and (**c**) bits of insect wing with some organic debris. The samples measure (a) 3 × 2 cm, (b) 1.5 cm wide and (c) 4.5 × 2.5 cm. Photomicrographs by Tay Thye Sun.

12b) and bits of insect wing with some organic debris (Figure 12c). In addition, Liu (2018) reported various types of plant and animal remains in Khamti amber.

Most of our samples luminesced strong chalky blue under long-wave UV and weak chalky blue or greenish blue under short-wave UV radiation, which are typical of amber (see, e.g., Kocsis *et al.* 2020). Some of the darker brownish samples showed weak chalky blue or yellow emissions under long-wave UV radiation, whereas they appeared to be inert under short-wave UV. These observations differ appreciably from the pink UV-induced luminescence reported for some samples of Khamti amber by Liu (2018) and the unique violet fluorescence to long-wave UV that was recently documented in some Burmese amber (Zhang & Shen 2019; Jiang *et al.* 2020).

IR and Raman Spectroscopy

IR absorption and Raman spectra of the 11 analysed specimens of Khamti amber were quite similar to one another, and representative spectra are presented in Figure 13 for sample KT21. The IR features were dominated by a group of absorption bands at around 2800–3000 cm^{-1}, relatively narrow bands in the range of 950–1750 cm^{-1} overlaying a broad hump at 800–1400 cm^{-1}, and a weak broad band at around 3420 cm^{-1}. The positions and relative intensities of these features are similar to those seen in the IR spectra of Burmese amber reported by various authors (e.g. Tay *et al.* 2015; Liu 2018; Chen *et al.* 2019; Jiang *et al.* 2020). Likewise, the Raman spectral features shown by our samples resembled those of Burmese amber reported

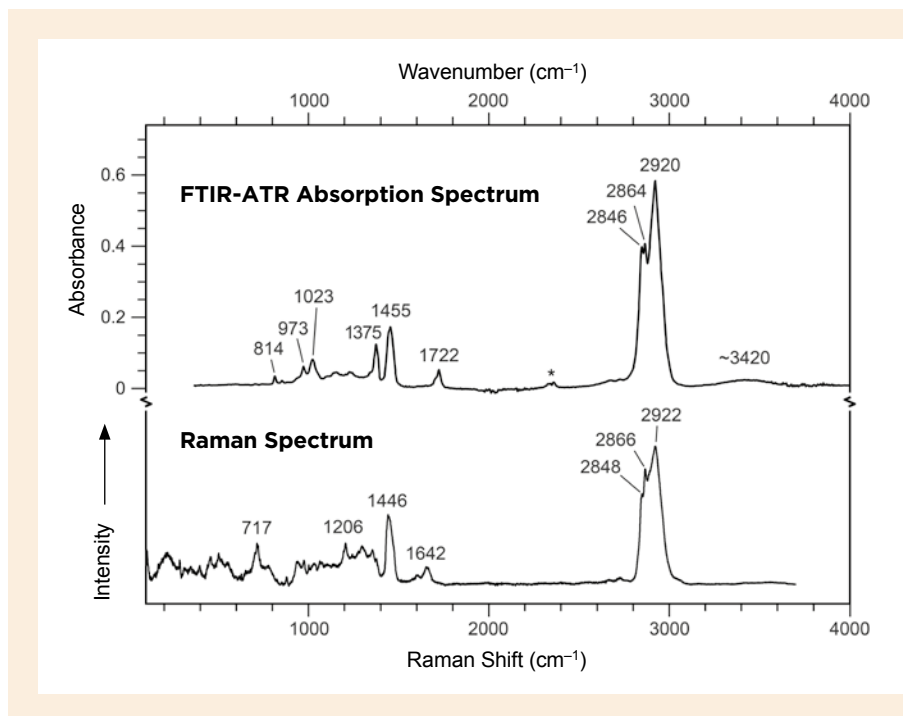**Figure 13:** The FTIR-ATR spectrum of amber sample no. KT21 (top) shows features that are similar to those of Hti Lin and Tanai amber. The Raman spectrum of the same sample (bottom; with background corrected) shows no absorption bands at 3048, 1642 and 887 cm^{-1}, which confirms that it is amber and not copal. The asterisk in the IR spectrum marks an analytical artefact (absorption by CO_2 in the air).

by Brody *et al.* (2001). Compared to the FTIR spectrum obtained by Liu (2018), our samples did not show significant absorption in the 1050–1250 cm^{-1} region, and an additional band at 1764 cm^{-1} reported by Liu (2018) was not detected in our spectra.

The vibrational bands in the 2800–3000 cm^{-1} range can be attributed to symmetric and asymmetric stretching vibrations of saturated C–H bonds, such as in methylene (CH$_2$) and methyl (CH$_3$) groups. Also, the absence of any IR absorption band at around 3080 cm^{-1} caused by C=C bonds indicates a lack of unsaturated or aromatic organic compounds (see Brody *et al.* 2001; Abduriyim *et al.* 2009; Wagner-Wysiecka 2018; and references therein). The narrow, intense IR absorption band at 1722 cm^{-1} has been assigned to C=O stretching of carbonyl groups. Infrared absorption and Raman bands below 1500 cm^{-1} are due to diverse stretching and deformation vibrations; a detailed list of assignments was provided by Montoro *et al.* (2020). As expected, no features were observed at 3048, 1642 and 887 cm^{-1} in either the FTIR and Raman spectra, which would indicate (young) copal (Guiliano *et al.* 2007; Abduriyim *et al.* 2009; Wang *et al.* 2015); this is consistent with the mid-Cretaceous age of the amber, as indicated by the *Orbitolina* sp. fossils in the host limestone.

A broad absorption at around 3500 cm^{-1} (3420 cm^{-1} in our samples) can be attributed to O–H stretching (see Montoro *et al.* 2020 and reference therein). Considering the presence of carbonyl groups, this hydroxyl can be assigned to carboxylic acid, rather than molecular water, in Khamti amber. A similar O–H stretching band has been recorded in the FTIR spectra of Tanai amber (Jiang *et al.* 2020). Also, a broad band at 3400–3460 cm^{-1} has been observed in amber from the Dominican Republic, Colombia and Madagascar, and in some specimens from the Baltic (A. Abduriyim, pers. comm. 2019).

CONCLUSIONS

Khamti amber (e.g. Figure 14) resembles material from other Burmese deposits, and our samples also showed similar gemmological properties—such as RI, SG and UV fluorescence—to those of typical amber from the Hti Lin and Tanai regions. The occurrence of Khamti amber in *Orbitolina* sp. fossil-bearing limestone indicates that it must have formed prior to or during mid-Cretaceous times when it was incorporated into the marine sediments that formed the limestone. More samples should be studied to further investigate variations in UV fluorescence and IR spectra that have been documented in Khamti amber, and also for comparison with material from other localities in Myanmar and elsewhere.

Figure 14: This bracelet made of Khamti amber illustrates some of the colours and textures that can be found in material from this area of Myanmar. The largest pieces forming the bracelet are each about 1.5 × 3.0 cm. Photo by Thet Tin Nyunt.

REFERENCES

Abduriyim, A., Kimura, H., Yokoyama, Y., Nakazono, H., Wakatsuki, M., Shimizu, T., Tansho, M. & Ohki, S. 2009. Characterization of "green amber" with infrared and nuclear magnetic resonance spectroscopy. *Gems & Gemology*, **45**(3), 158–177, https://doi.org/10.5741/gems.45.3.158.

Brody, R.H., Edwards, H.G.M. & Pollard, A.M. 2001. A study of amber and copal samples using FT-Raman spectroscopy. *Spectrochimica Acta Part A: Molecular and Biomolecular Spectroscopy*, **57**(6), 1325–1338, https://doi.org/10.1016/s1386-1425(01)00387-0.

Chen, D., Zeng, Q., Yuan, Y., Cui, B. & Luo, W. 2019. Baltic amber or Burmese amber: FTIR studies on amber artifacts of Eastern Han dynasty unearthed from Nanyang. *Spectrochimica Acta Part A: Molecular and Biomolecular Spectroscopy*, **222**, article 117270 (5 pp.), https://doi.org/10.1016/j.saa.2019.117270.

Guiliano, M., Asia, L., Onoratini, G. & Mille, G. 2007. Applications of diamond crystal ATR FTIR spectroscopy to the characterization of ambers. *Spectrochimica Acta Part A: Molecular and Biomolecular Spectroscopy*, **67**(5), 1407–1411, https://doi.org/10.1016/j.saa.2006.10.033.

Jehlička, J., Jorge Villar, S.E. & Edwards, H.G.M. 2004. Fourier transform Raman spectra of Czech and Moravian fossil resins from freshwater sediments. *Journal of Raman Spectroscopy*, **35**(89), 761–767, https://doi.org/10.1002/jrs.1191.

Jiang, X., Zhang, Z., Wang, Y. & Kong, F. 2020. Gemmological and spectroscopic characteristics of different varieties of amber from the Hukawng Valley, Myanmar. *Journal of Gemmology*, **37**(2), 144–162, http://doi.org/10.15506/jog.2020.37.2.144.

Kocsis, L., Usman, A., Jourdan, A.-L., Hassan, S.H., Jumat, N., Daud, D., Briguglio, A., Slik, F. *et al.* 2020. The Bruneian record of "Borneo amber": A regional review

of fossil tree resins in the Indo-Australian Archipelago. *Earth-Science Reviews*, **201**, article 103005 (21 pp.), https://doi.org/10.1016/j.earscirev.2019.103005.

Liu, S.I 2018. Gem Notes: Burmese amber from Khamti, Sagaing Region. *Journal of Gemmology*, **36**(2), 107–110.

Mitchell, A. 2018. Hukawng Basin, the amber mines, and the *Orbitolina* limestone. *In*: Mitchell, A. (ed) *Geological Belts, Plate Boundaries, and Mineral Deposits in Myanmar*. Elsevier, Amsterdam, the Netherlands, 433–438, https://doi.org/10.1016/b978-0-12-803382-1.00013-4.

Montoro, O.R., Tortajada, J., Lobato, Á., Baonza, V.G. & Taravillo, M. 2020. Theoretical (DFT) and experimental (Raman and FTIR) spectroscopic study on communic acids, main components of fossil resins. *Spectrochimica Acta Part A: Molecular and Biomolecular Spectroscopy*, **224**, article 117405 (11 pp.), https://doi.org/10.1016/j.saa.2019.117405.

O'Donoghue, M. (ed) 2006. *Gems*, 6th edn. Butterworth-Heinemann, Oxford, 873 pp.

Soe Thura Tun, Maung Thein, Nyunt Htay & Kyaing Sein 2014. *Geological Map of Myanmar 1:2,250,000*. Myanmar Geosciences Society, Yangon, Myanmar.

Tay, T.S., Kleišmantas, A., Thet Tin Nyunt, Minrui, Z., Krishnaswamy, M. & Loke, H.Y. 2015. Burmese amber from Hti Lin. *Journal of Gemmology*, **34**(7), 606–615, https://doi.org/10.15506/JoG.2015.34.7.606.

Thet Tin Nyunt, Tay, T.S., Cho Cho, Naing Bo Bo Kyaw and Wai Yang Lai Aung 2019. Amber from Khamti, Sagaing Region, Myanmar. *36th International Gemmological Conference*, Nantes, France, 27–31 August, 219–221.

Thin, K.K. 2016. *Mineralogy and occurrences of jadeite jade from Nansibon area, Hkamti township, Sagaing Region*. MSc thesis, University of Yangon, Myanmar, 94 pp.

Wagner-Wysiecka, E. 2018. Mid-infrared spectroscopy for characterization of Baltic amber (succinite). *Spectrochimica Acta Part A: Molecular and Biomolecular Spectroscopy*, **196**, 418–431, https://doi.org/10.1016/j.saa.2018.02.053.

Wang, Y., Shi, G., Shi, W. & Wu, R. 2015. Infrared spectral characteristics of ambers from three main sources (Baltic, Dominica and Myanmar). *Spectroscopy and Spectral Analysis*, **35**(8), 2164–2169, https://doi.org/10.3964/j.issn.1000-0593(2015)08-2164-06 (in Chinese with English abstract).

Zeug, M., Nasdala, L., Wanthanachaisaeng, B., Balmer, W.A., Corfu, F. & Wildner, M. 2018. Blue zircon from Ratanakiri, Cambodia. *Journal of Gemmology*, **36**(2), 112–132, https://doi.org/10.15506/JoG.2018.36.2.112.

Zhang, Z. & Shen, A.H. 2019. Amber with violet fluorescence from Myanmar. *36th International Gemmological Conference*, Nantes, France, 27–31 August, 232–234.

The Authors

Dr Thet Tin Nyunt
Director General, Department of Geological Survey and Mineral Exploration, Ministry of Natural Resources and Environmental Conservation, Myanma Gems Museum, Nay Pyi Taw 15011, Myanmar
E-mail: thettinnyunt@gmail.com

Tay Thye Sun and Loke Hui Ying
Far East Gem Lab, 12 Arumugam Road #04-02, LTC Building B, Singapore 409958
E-mail: tay@gem.com.sg

Murali Krishnaswamy
Department of Chemistry, NUS High School of Mathematics and Science, 20 Clementi Ave. 1, Singapore 129957

Cho Cho and Naing Bo Bo Kyaw
Myanma Gems Enterprise, Ministry of Natural Resources and Environmental Conservation, Myanma Gems Museum, Nay Pyi Taw 15011, Myanmar

Wai Yang Lai Aung
Department of Geology, University of Yangon, Kamayut 11041, Yangon, Myanmar

Dr Chutimun Chanmuang N.
Institut für Mineralogie und Kristallographie, University of Vienna, Althanstraße 14, 1090 Vienna, Austria

Gem-A Notices

Spencer Currie FGA 1934–2020

It is with sadness that I report the passing of Spencer Currie.

A well-known and much-respected member of the gemmological community in New Zealand and Australia, Spencer first trained as a manufacturing jeweller. He then studied with Gem-A and passed his Diploma exam in 1978, travelling that year to London to receive his Diploma.

He was a founding member of the Gemmological Association of New Zealand in 1980, became President and an Honorary Member of this organisation, and sat on countless committees. He gave many lectures to students and fellow gemmologists, both in New Zealand and Australia. Highlights of Spencer's career include attending a Gem-A organised trip to Idar-Oberstein (Germany, 1998), giving presentations at the International Gemmological Conference in Goa (India, 1999) and Moscow (Russia, 2007), and being invited to speak at the Asian Gemmological Institute and Laboratory's 25th anniversary conference in Hong Kong (2008).

Spencer studied, documented and published on New Zealand copal (Kauri gum), determining that some ancient specimens found in coal deposits were in fact amber (see *The Journal*, Vol. 25, No. 6, 1997, pp. 408–416). He also wrote two other articles for *The Journal*, titled 'An unusual star diamond' (Vol. 20, No. 1, 1986, p. 52) and 'The brilliant cut – Analysis of weight by calculation' (Vol. 20, No. 3, 1986, pp. 171–176).

Spencer was also a keen lapidarist, was much involved with the South Auckland Rock and Mineral Club and won awards for some of his nephrite carvings. He was keen on photography (in general and pertaining to the photomicrography of gems) and was an avid collector of rocks and all things gemmological.

A truly gentle character, Spencer will be sadly missed by us in New Zealand. Spencer is survived by his wife Brenda, their three children and many grandchildren and great-grandchildren.

Donald Francey FGA
Auckland, New Zealand

A Webinar with the Editor

Go behind the scenes at *The Journal of Gemmology* by tuning in to our webinar session with Editor-in-Chief, Brendan Laurs FGA, on 24 September 2020 at 17:00 BST. Join us as we hear Brendan discuss the current issue of *The Journal*, explaining how the issue was assembled and focusing in greater detail on some of the fascinating feature articles and Gem Notes. To register your place, head to: https://linktr.ee/gemaofgb.

Did you miss our last session of Gem-A Live with Brendan? Head to the Gem-A You Tube Channel and watch it online now: https://youtu.be/-xTbMbZDtSo.

Learning Opportunities

CONFERENCES AND SEMINARS

Association for the Study of Jewelry and Related Arts (ASJRA) Annual Conference
10–11 October 2020
Online
www.jewelryconference.com

2020 American Society of Appraisers (ASA) International Conference
12–13 October 2020
Online
www.appraisers.org/Education/events/
asa-international-conference

Geological Society of America (GSA) Connects Online
26–30 October 2020
Online
https://community.geosociety.org/
gsa2020/home
Session of interest: Gemological Research in the 21st Century: Gem Minerals and Localities

Munich Show: Mineralientage München
30 October–1 November 2020
Munich, Germany
https://munichshow.de/?lang=en
Note: Includes a seminar programme

Scottish Gemmological Association Conference
November 2020 (exact dates TBA)
Cumbernauld, Scotland
www.scottishgemmology.org

Chicago Responsible Jewelry Conference
6–7 November 2020
Chicago, Illinois, USA
https://responsiblejewelryconference.com

14th International Conference on New Diamond and Nano Carbons (NDNC)
10–14 January 2021
Kanazawa, Japan
www.ndnc2020.org

23rd FEEG Symposium—25th Anniversary
23–24 January 2021
Paris, France
www.feeg-education.com/symposium

NAJA 55th Ace© It Annual Winter Conference
31 January–1 February 2021
Tucson, Arizona, USA
www.najaappraisers.com/html/conferences.html

AGTA Gemfair Tucson
2–7 February 2021
Tucson, Arizona, USA
https://agta.org/agta-gem-fair-tucson
Note: Includes a seminar programme

Tucson Gem and Mineral Show
11–14 February 2021
Tucson, Arizona, USA
www.tgms.org/show
Note: Includes a seminar programme

Inhorgenta Munich
19–22 February 2021
Munich, Germany
www.inhorgenta.com/index.html
Note: Includes a seminar programme

International Colored Gemstone Association (ICA) Congress
March 2021 (exact dates TBA)
Shenzhen, China
www.icacongress2021.com

MJSA Expo
March 2021 (exact dates TBA)
New York, New York, USA
https://mjsa.org/eventsprograms/mjsa_expo
Note: Includes a seminar programme

10th National Opal Symposium
31 March–1 April 2021
Coober Pedy, Australia
www.opalsymposium.org

American Gem Society Conclave
26–28 April 2021
Louisville, Kentucky, USA
www.conclave2021.americangemsociety.org

**37th International Gemmological Conference
(IGC 2021)**
17–21 May 2021
Tokyo, Japan
www.igc-gemmology.org
Note: Includes field trips to jadeite deposits
and a pearl farm

Swiss Gemmological Society Conference
30 May–1 June 2021
St Gallen, Switzerland
http://gemmologie.ch/en/current

JCK Las Vegas
4–7 June 2021
Las Vegas, Nevada, USA
https://lasvegas.jckonline.com
Note: Includes a seminar programme

Diamonds – Source to Use 2021
9–10 June 2021
Johannesburg, South Africa
www.saimm.co.za/saimm-events/upcoming-events/
diamonds-source-to-use-2020

Jewellery in Texts: Texts in Jewellery
19 June 2021
London
www.societyofjewelleryhistorians.ac.uk/news

NAJ Summit
19–21 June 2021
Northampton, East Midlands
www.naj.co.uk/summit
Note: Includes the IRV Valuers' Conference

(19–21 June) and the JBN Retail Jewellers'
Congress (21 June)

Sainte-Marie-aux-Mines Mineral & Gem Show
24–27 June 2021
Sainte-Marie-aux-Mines, France
www.sainte-marie-mineral.com
Note: Includes a seminar programme

**The Goldsmiths' Company Jewellery
Materials Congress**
18–20 July 2021
London
www.assayofficelondon.co.uk/events/
event-programme-202021

**9th International Conference Mineralogy
and Museums**
24–26 August 2021
Sofia, Bulgaria
www.bgminsoc.bg
Note: Gem minerals and archaeogemmology are
among the topics that will be covered.

**3rd European Mineralogical Conference
(emc2020)**
29 August–2 September 2021
Krakow, Poland
https://emc2020.ptmin.eu
Sessions of interest: The Geology of Gem Deposits:
A Session in Honour of Gaston Giuliani; Materials
Sciences and Archaeometry for Cultural Heritage

**31st International Conference on Diamond
and Carbon Materials**
5–9 September 2021
Palma, Mallorca, Spain
www.elsevier.com/events/conferences/international-
conference-on-diamond-and-carbon-materials

**3rd International Conference on Tourmaline
(TUR2021)**
9–11 September 2021
Elba Island, Italy
www.tur2021.com

**Canadian Gemmological Association
(CGA) Conference**
22–24 October 2021
Vancouver, British Columbia, Canada
https://canadiangemmological.com

OTHER EDUCATIONAL OPPORTUNITIES

Gem-A Workshops and Courses
Gem-A, London
https://gem-a.com/education

Lectures with The Society of Jewellery Historians
Society of Antiquaries of London,
Burlington House, London
www.societyofjewelleryhistorians.ac.uk/current_lectures

- Niamh Whitfield—The 'Tara' Brooch: The Making of an Early Medieval Masterpiece from Ireland
22 September 2020 (online)

- Lynne Bartlett—Titanium the Magical Metal
27 October 2020

- Charlotte Gere—Colour in Victorian Jewellery
24 November 2020

- Jonathan Boyd—His Work as a Jeweller
26 January 2021

- Jack Ogden—Presidential Address (following AGM)
23 February 2021

- Carol Michaelson—Chinese Jade Jewellery and Ornaments from the Neolithic to the Present
27 April 2021

- Gonçalo de Vasconclo e Sousa—Portuguese Jewellery
25 May 2021

- Karl Schmetzer—The Late 14th-Century Royal Crown of Blanche of Lancaster
22 June 2021

- TBA
28 September 2021

- Three Speakers TBA—New Research on Jewellery
26 October 2021

- Ute Decker—Sculptural Minimalism & Fairtrade Gold: Philosophy, Provenance and Process
23 November 2021

New Media
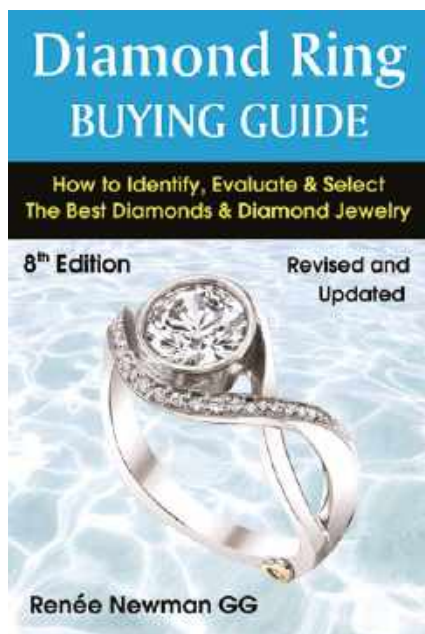
Diamond Ring Buying Guide, 8th edn.

By Renee Newman, 2020. International Jewelry Publications, Los Angeles, California, USA, www. reneenewman.com/diamond.htm, 149 pages, illus., ISBN 978-0929975542 or e-ISSN 978-0929975559. USD19.95 softcover or USD9.99 eBook.

The previous (7th) edition of the *Diamond Ring Buying Guide* was published 12 years ago, and it has been out of print for four years. This new edition retains a lot of the original information, but also includes many updates.

In the first chapter, the author proposes a set of price factors to judge diamond value by replacing the 'Four Cs' criteria of colour, clarity, cut and carat weight with a more complex value system consisting of six 'Cs' and two 'Ts': cut quality, colour, carat weight, cutting style, clarity and creator (natural vs. laboratory grown), plus transparency (cloudiness) and treatment status. The 'creator' factor is new in this edition, reflecting the upsurge of synthetic diamonds being used in jewellery.

Chapter 2 has been shortened and focuses on why diamonds are so valued. Distinctive and prized properties include diamond's exceptional hardness; its resistance to high temperatures, radiation and chemicals; its electrical and heat conduction properties, as well as insulation from heat; and the aesthetic allure of its brightness and fire.

The next several chapters deal with each of the six 'Cs' and two 'Ts'. Chapter 3 covers carat weight and includes a useful table compiled by the Gemological Institute of America displaying corresponding weights and diameters of well-cut round-brilliant diamonds. A chapter on shape and cutting style describes these aspects and explains branded and non-traditional diamond cuts, accompanied by photos of examples. Excellent images also help illustrate an extended discussion on how shape affects price.

Chapter 5 deals with colour, with revised text and new photos. It includes the effect of fluorescence on colour and price, the subjectivity of diamond colour grades, fancy-colour diamonds and treatments that affect colour. An updated table provides recently realised auction prices. The following chapter, on cut quality, explains how to judge the quality of cut for fancy-shape diamonds as well as round-brilliant cuts. It includes what to look for in face-up and profile views, with new photos that demonstrate specific examples. Next comes a chapter on how to evaluate clarity and transparency, with photos illustrating how to search for inclusions, graining, surface features and more. Lighting, magnification, positioning and focus can all affect success in locating inclusions and other features. Photos also illustrate differences in transparency.

Chapter 8 focuses on synthetic diamonds, reviews various growth methods, and discusses the benefits of both laboratory-grown and natural diamonds. A section on how to detect synthetic diamonds lists the basic gemmological tests that are currently available. All-new photographs help make this chapter current.

The following chapter on diamond imitations is very helpful, with tips on how to spot simulants using a little observation, without expensive tools or equipment. A separate section deals with synthetic moissanite, warning that it can show up as 'diamond' on a thermal tester. Some of the newer synthetic moissanites even fool moissanite detectors.

A chapter on diamond treatment covers all the important types: laser drilling, fracture filling, coatings and irradiation with heat, along with descriptions of low-pressure, high-temperature (LPHT) treatment and high-pressure, high-temperature (HPHT) treatment. It also includes a new section on the factors involved in pricing colour-enhanced diamonds, accompanied by new colour photos.

A new chapter on diamond-grading reports helps the reader know what to look for on a report, but with a warning that not all grading labs are equal.

A chapter on gold, platinum and palladium helps the consumer decide on the characteristics they prefer in their setting, accompanied by terminology pertaining to precious metals. A well-organised chart contrasts white gold with platinum. The benefits and cautions of 14-ct vs. 18-ct gold are compared, as are the pros and cons of the different metals. The metalworking procedure of Japanese origin known as *mokume gane* is also profiled.

A new chapter on silver has been added, explaining its history and standards. It includes a review of various brand names of silver that have been treated with anti-tarnish alloys such as those containing copper or germanium. Another new chapter covers alternative metals, which are quickly finding acceptance on the marketplace. Short descriptions of each metal are accompanied by a discussion of their advantages and disadvantages, including stainless steel, tungsten, tungsten carbide, titanium, cobalt-chrome and tantalum.

A chapter on setting styles describes popular mounting techniques, including prong, channel, bezel, bead, pavé, flush and bar settings, along with invisible setting, a method of displaying stones without visible metal support. Situations reveal which mountings might be best for people with different wearing needs. New to this edition is a section with tips on what to look for in a well-made, secure setting. Selecting a ring style is also a personal choice, but the author poses practical questions to consider when choosing such a significant piece of jewellery. Many new photos are featured in this chapter.

The next chapter covers how to clean and store a diamond, along with how to prevent it from being 'switched'. The latter entails knowing your diamond's unique characteristics and establishing a long-term relationship with your jeweller. The book concludes with a chapter that gives shopping pointers, followed by a new section on the chemical, physical and optical properties of diamond and a thorough bibliography.

This book can be used by consumers who are not necessarily interested in becoming diamond experts, but who want to feel more informed about the material and the industry in general when considering a purchase. The book is also a helpful sales tool for those in the retail jewellery industry. It outlines what a consumer should know and what information a salesperson should be responsible for. An amazing amount of excellent information has been packed into this portable paperback that can accompany the prospective buyer to the jewellery store or sales office. The numerous updated photographs help illustrate current styles, and the streamlined text addresses commonly asked questions and concerns.

Jo Ellen Cole
Cole Appraisal Services
Los Angeles, California, USA
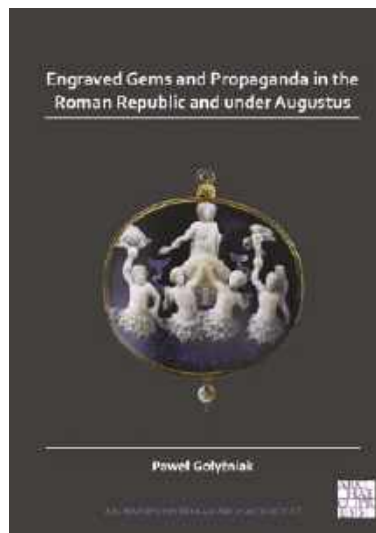
Engraved Gems and Propaganda in the Roman Republic and Under Augustus

This lengthy volume is a revised version of a PhD thesis presented to Jagiellonian University, Krakow, Poland. The author charts the development and use of engraved gems from the earliest Roman Republic, when they signified self-advertisement of the owner and wearer. From the time of Sulla onwards they conveyed a political message that could be distributed to or worn by followers and allies. Pompey, Caesar and Octavian (who became Augustus) were especially adept at this. With Octavian we are in very familiar territory, made well known by Paul Zanker in his classic work *The Power of Images in the Age of Augustus* (1988).

Gołyźniak's achievement has been to place Imperial propaganda on gems into the context of a long history. To my knowledge only one previous author has attempted

anything like this—Marie-Louise Vollenweider in her *Die Porträtgemmen der römischen Republik* (1974), which only deals with portraits—while Gołyźniak covers a whole range of pictorial and symbolic subject matter. And with more than a thousand figures (mainly colour photographs) spread over 130 pages, he has provided a veritable *musée imaginaire* for the gem enthusiast.

Following an introductory section dealing with the research aims and methodology is a short theoretical discussion on the nature of propaganda. Next is a general section on how gems were used by the Romans of the Republic: in triumphs, collected for their own sake and presented to temples, for personal branding and self-pro-motion, and to promote family and political faction, often emphasising abstract ideas by the use of symbols. In later periods the gems acquired by close supporters of those with supreme power, especially Octavian (63 BC–14 AD), were extremely precious items—often cameos carved in the round or cameo vessels.

The bulk of the book collects, illustrates and evaluates the evidence for the use of engraved gems as propaganda. The beginnings in the 3rd and 2nd centuries BC were concerned with Italic gems, following the Etruscan tradition. Then we are on more familiar ground, as Roman glyptic takes on a more Hellenised appearance, as with the well-known portrait in a gold setting (probably of Scipio Africanus) cut by Herakleides, and a garnet signed by Daidalos perhaps depicting Titus Quinctius Flamininus, both of the 2nd century BC. However, in that time of increasing conflict and Roman expansion, the many gems depicting warriors and battle scenes took on a particular resonance, and sometimes they related to particular events.

It is with Sulla (138–78 BC), who sealed documents with an image of himself receiving Jugurtha bound from Bocchus, as reproduced on coins struck for him, that we can begin to see a wider use of gems as propaganda. Here, as elsewhere, Gołyźniak sees how coins—which are, when all is said and done, pieces of bullion sealed by an authority as a guarantee of fineness—contribute to the theme and often depict subjects also seen on intaglios. Marius, Sulla's great rival, does not seem to have used glyptic to the same degree. However, during the period of the civil wars, both Pompey and Caesar became increasingly involved in this sort of propaganda, with gem engravers working for them, and disseminating images to ordinary soldiers and others by means of glass copies. Apart from portraiture, gems depicting Romans being victorious over Celts allude to Caesar's Gallic Wars, while symbols of victory and prosperity might bear charged political overtones. Cameos then began to

come in, including a strongly Hellenising one evidently from Spain in the Content Family Collection that depicts jugate busts of Caesar and his divine ancestor, Venus. A cameo formerly in the Ionides Collection shows an elephant trampling a fish, which recalls Caesar's famous coins of an elephant trampling a serpent.

However, only after Caesar's assassination in 44 BC does the book reach its climax. Brutus and the Repub-licans employed gems to a limited degree, as did Mark Antony, after their defeat, but it is clear that Octavian was the supreme master of using gems of all sorts as a medium to secure and maintain power. His engraved gems employed portraiture, myth and symbolism to ally himself with the divine, as had Julius Caesar to a lesser extent.

Useful distribution maps of the Roman Empire show where provenanced gems associated with particular personalities have been found. Not surprisingly, in many cases they cluster around Rome and central Italy, the centre of power where reputations were won and lost.

I have only two criticisms. First, as with other books on gems, users will often find themselves browsing the plates. The list of associated figure credits is daunting, and it is very hard to relate those plates to the extensive catalogue, let alone to the text, because the figures are in a separate section at the end of the book rather than being dispersed throughout, near their relevant text. Second, and this is especially pertinent to readers of this journal, it would be good to know how the gems used in propaganda at the higher end of the market related to the gem trade at the time. My own favourite gem is a sapphire cameo with which Vollenweider began her great study of gem engraving in the Late Republic and early Empire, in *Die Steinschneidekunst und ihre künstler in Spätrepublikanischer und Augusteischer zeit* (1966). This gem is illustrated in colour in my catalogue of the Fitzwilliam Museum in Cambridge (*Classical Gems in the Fitzwilliam Museum*, 1994), but here (in figure 972) it is only in black and white. As other exotic and beautiful gems show, it was only under Augustus that the use of gems in propaganda achieved its full potential.

With these small caveats, this volume—splendidly produced at an extraordinarily low price for what it contains (and actually free to download in PDF format)—is a book of enduring worth. Gołyźniak deserves our gratitude for writing one of the best books on Roman gems to have been published for a very long time.

Dr Martin Henig
Wolfson College, Oxford
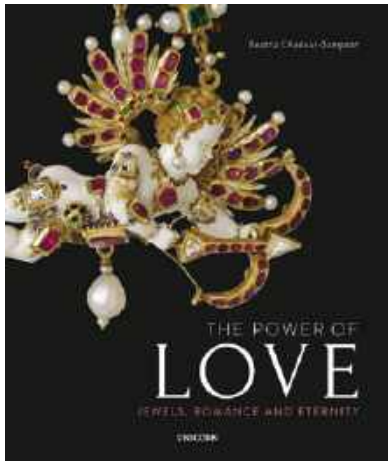
The Power of Love: Jewels, Romance and Eternity

By Beatriz Chadour-Sampson, 2019. Unicorn Publishing Group, London, www.unicornpublishing.org/page/detail/The-Power-of-Love/?k=9781911604464, 144 pages, illus., ISBN 978-191164464. GBP25.00 hardcover.

Jewellery and the themes of love and marriage have inspired goldsmiths and artists for millennia. In this well-written and beautifully illustrated book, renowned jewellery historian Beatriz Chadour-Sampson explores romance, love and courtship translated into jewellery. To explore the intimate relation we have with jewellery and how it is worn and created, the reader is taken on a journey from antiquity to the Middle Ages and from the early modern period to the modern era in six chapters. The focus of the book is on jewellery from western Europe and several famous examples are reviewed. The crown of Princess Blanche from the late 14th century (extensively discussed in a feature article of *The Journal*, Vol. 37, No. 1, 2020, pp. 26–64) is but one of the stunning pieces that can be admired for their symbolism, craftsmanship and use of materials.

Rings take centre stage in this publication, which is not surprising, considering the author's role as curator and researcher for the Alice and Louis Koch Collection of rings in Switzerland. As symbols of enduring love and worn directly on the body, rings are considered intimate pieces of jewellery and are therefore particularly suitable to tell the story of love and marriage. And perhaps there is a more pragmatic reason for the number of rings depicted in this publication. Rings are easy to keep, cherished by multiple generations and small enough that they tend to survive better under archaeological circumstances.

In discussing the development of marriage and betrothal, the use and meaning of diamonds is very important. The author shares an interesting reference from the 1st century AD that differs from the common idea that diamonds were used for wedding and betrothal rings only from the Late Middle Ages onwards. Physical examples and references from the 8th to 11th centuries could shed more light on this fascinating topic, but the scarcity of material from this period is a well-known gap in European jewellery history.

This book is full of wonderful pieces of sumptuous jewellery, but one of my favourites is actually very humble: a ring given by Napoleon Bonaparte to his first consort, Joséphine de Beauharnais (1763–1814). A simple golden band with the initials 'NB', some light blue enamel and the inscription *amour sincère* (sincere love) tells us that deep and profound love does not always have to be translated into big jewels covered in gemstones. Whether this was Joséphine's actual engagement ring is unclear, because a sapphire- and diamond-set *toi e moi* ring auctioned in 2013 was claimed as the official one given to her by Napoleon in 1796. This was one of the times when, in reading this book, I missed the use of notes. Luckily, the select bibliography offers enough sources to continue the quest.

Because love is such a universal theme, it would have been nice to include examples other than just western European ones, but perhaps this is an idea for a follow-up publication. This book is not written as a reference catalogue, nor is discussing the pieces in detail the aim of this publication. That being said, this book is a must-read for anyone interested in the jewellery of love. And because so many pieces of jewellery have survived since they are love-related, this book could serve well as a general introduction to students of jewellery history.

Suzanne van Leeuwen FGA
Rijksmuseum
Amsterdam, The Netherlands

Rubellite— Tourmaline Rouge

Ed. by William B. Simmons, Gloria A. Staebler, David W. Bunk, Alexander U. Falster, Sarah L. Hanson and Karen W. Webber, 2019. Mineral Monograph No. 20, Lithographie, Arvada, Colorado, USA, https://tinyurl.com/yxvmf6hl, 148 pages, illus., ISBN 978-0983632399. USD40.00 softcover.

*R*ubellite—*Tourmaline Rouge* is a 138-page extravaganza of superb images, illustrations, information and anecdotes about the aesthetically outstanding red tourmaline, as well as the tourmaline mineral group in general. The monograph is structured in a logical and easy-to-read fashion, beginning with a history of rubellite and followed by in-depth sections on tourmaline—its chemistry, colour and sources—with examples of rubellite found across the globe. The various sections are written by 13 expert authors, with illustrations contributed by more than 40 other individuals. The ensemble is harmoniously orchestrated by chief editors Gloria Staebler and Dr William (Skip) Simmons into an informative and illustrative text that could equally complement a tourmaline scholar's bookshelf or adorn someone's living-room table. Although titled 'Rubellite'—the pink-to-red variety of tourmaline that is known to occur in various species (i.e. elbaite, liddicoatite, rossmanite, darrellhenryite and uvite)—this work is, in reality, an overview of tourmaline, with a special emphasis on this colour range.

Who cannot appreciate the outstanding beauty of tourmaline? The sharp, intricate terminations, the perfectly aligned striations and, above all, the intense and varied colours make it special. I'm personally fascinated by this mineral, and I'm extremely lucky to have access to an outstanding suite of specimens in the Mineralogical and Geological Collections at Harvard University. Despite feeling quite well versed in the tourmaline mineral group, I nonetheless found myself immersed in *Rubellite*. I have personally seen some of the most spectacular specimens of rubellite pictured in the monograph, yet I learned a great deal about some of the most important localities and their discoveries, geology, and history of mining and production.

The monograph starts with an historical overview of rubellite, including its misidentification as 'ruby' in jewellery pieces and a fascinating discussion about what may be the oldest worked rubellite as an intaglio of Alexander the Great. The following sections explain tourmaline's structure and crystallography, its varied colouration and its formation in granitic pegmatites. These are accompanied by photos of beautiful gem-quality rubellite crystals. Next, the reader is treated to a nearly chronological 'tour' of some of the most important rubellite-bearing pegmatite localities, beginning with the 1668 discovery of tourmaline in the Ural Mountains of Russia. There are three main areas for rubellite and multi-colour tourmaline in Russia: the central Ural Mountains, the Malkhan range and the Borschovochny Ridge. Red tourmalines from

Russia, similar to those from the Jonas mine in Brazil, are of a unique deep colour intensity. The next section covers rubellite from the Czech Republic, especially a pegmatite at Rožná, which is the type locality for lepidolite mica and rossmanite tourmaline. This section includes a wonderful short biography of Prof. George Rossman, after whom this tourmaline species was named. A shorter article on rubellite from Italy's Elba Island depicts some excellent examples of multicoloured specimens in matrix.

In the USA, there are two main localities for tourmaline, and both compete in terms of colour and quality of material produced. These are California (Pala and Mesa Grande Districts), where some of the largest and most abundant elbaites have been found, and the Dunton Quarry in Maine. The history of these localities is described, including the connection between California tourmaline and the Chinese Qing dynasty. The descriptions outline the various ownership of the mines throughout the years, important discoveries and decisions that factored into their successes.

Four sections are dedicated to 'Pan-African' pegmatites. One of them, on tourmaline from Madagascar, provides a detailed account of the different districts and characteristics of each deposit, including Anjanabonoina, the well-known producer of colourful liddicoatite that is typically sliced perpendicular to the *c*-axis. Two sections on Minas Gerais, Brazil, cover the Serra do Cruzeiro (Cruzeiro and Chiá mines, sources of outstanding rubellite specimens and bicoloured elbaite) and the Jonas mine (which produced some of the largest and most aesthetically pleasing rubellite crystals ranging up to 1 m long, including the 'Rocket' and other famous pieces such as the 'Joninha'). The last section, on Pan-African pegmatites, covers Nigeria's Abuja mine, which has produced intense red as well as bicoloured tourmalines.

The final sections of the monograph consider examples from Vietnam and a summary of other worldwide localities such as Malaga in Spain. Located only 150 km from where I grew up, I am ashamed to say I never knew about this Spanish locality for tourmaline, but I am now keen to return and visit! The book ends with an informative reference list that mostly pertains to tourmaline localities.

Until now I did not realise that some of the most important pegmatitic rubellite discoveries of the last 50 years were clustered in the 1970s: the 'Blue Cap' pocket from California in 1972, the 'Jolly Green Giant' tourmaline from the 'Big Pocket' in Maine during the same year and the famous Jonas pocket in Brazil in 1978. When, I wonder, will the next big rubellite discovery be made?

What makes this monograph exceptional is the excellent use of maps, illustrations of gem-bearing pockets, pictures of miners and amazing specimens, together with all of the fascinating histories, which leads to an immersive experience. The colour illustrations range from single crystals with perfect terminations, to crystal clusters and aesthetically pleasing matrix specimens, to ancient carvings and modern artistic gem cutting. This is an essential book for any aficionado, collector or scientist interested in tourmaline.

Dr Raquel Alonso-Perez FGA
Harvard Mineralogical & Geological Museum
Cambridge, Massachusetts, USA
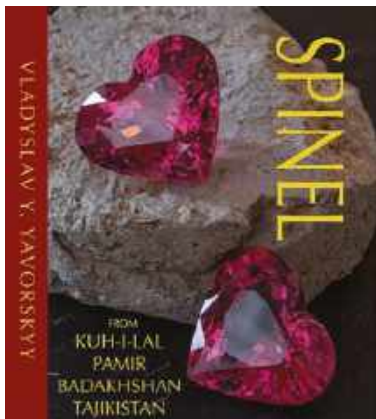
Spinel from Pamir

By Vladyslav Y. Yavorskyy, 2019. Yavorskyy Co. Ltd.,
Hong Kong, www.gemstonesbook.com,
236 pages, illus., ISBN 978-1733486002.
USD180.00 hardcover.

Vladyslav Yavorskyy's sixth volume on gemstones covers the remarkable spinels from Kuh-i-Lal in the Pamir Mountains of Tajikistan. Those who are familiar with Yavorskyy's other books know that text is minimal and great photos abound—perhaps more so in this volume than in previous ones. The text of the five chapters was written by Anne Carroll Marshall, with photo captions by Vladyslav and Samantha Yavorskyy. The photos were captured by the author in colour and black-and-white using a Leica M6 film camera, and the spinels are indicated as all being natural and untreated.

Chapter 1 covers history, with an excellent summation of Pamir spinel from times before Marco Polo. This is followed by the great spinels set in crown jewels, including those of Iran, Russia and England, especially the famous Timur 'Ruby', a 352.5 ct spinel set for Queen Victoria in 1853. Also pictured are wonderful spinel necklaces sold at auction.

Chapter 2, on mining, offers a fascinating excerpt from the 2015 dissertation *Mineralogical Features and Genesis of the Kuh-i-Lal Spinel Deposit* (translated from Russian).

This chapter is filled with photos of miners and beautiful, faceted red and pink spinel gems on facing pages.

Chapter 3 covers legends of the Pamirs. One of these legends includes Alexander the Great, who crossed the Panj River in 329 BC and met his third wife, Roxanne, in Tajikistan. This chapter contains spectacular photos of the Pamir Mountains and colourful faceted spinels, some mounted in fine jewellery.

Chapter 4, on Kuh-i-Lal village, contains mostly black-and-white candid photographs of the local people taken by the author, with each facing page showing colourful faceted spinels. The text on page 108 covers some historic spinels, including the famous 170 ct Black Prince's 'Ruby'—mounted as the central decoration in the Imperial State Crown of England—which is thought to be of Kuh-i-Lal origin. Page 144 mentions the biggest discovery at Kuh-i-Lal when, in 1985, the largest known red spinel—26,000 ct—was found. A photo shows the piece being held by export company officials.

Chapter 5 is about the people of the Pamir Mountains. It features images of the local inhabitants (mostly in colour), accompanied by photos of fashioned spinels, often in pairs or even preformed rough sets. I particularly enjoyed a close-up photo of the boots of a local shepherd 'made from car tyres'. Then on pages 177 and 178 are two half-page pictures: on the left 'from rough crystal 380 ct' and on the right a '180 ct world's largest faceted red spinel'. Okay, that's just showing off!

The final pages include endnotes, further reading and some additional text from the Russian study mentioned in chapter 2, followed by photos of several more faceted spinels and the author's afterword.

This book is a labour of love by an artist. Everyone who enjoys gemstones should have this and Yavorskyy's other volumes in their library. My only small critique is that the quantity of spinels shown here makes them look almost too common!

Bill Larson FGA
Pala International
Fallbrook, California, USA

Other Book Titles

CULTURAL HERITAGE

Byzantinische Goldschmiedearbeiten im Römisch-Germanischen Zentralmuseum [Byzantine Goldsmith Work in the Roman-Germanic Central Museum]
Ed. by Mechthild Schulze-Dörrlamm, 2020. Kataloge: Vor- und Frühgeschichtlicher Altertümer **42**, Verlag des Römisch-Germanisches Zentralmuseums, Mainz, Germany, 336 pages, ISBN 978-3795423513 (in German). EUR90.00 hardcover.

New Research on Late Byzantine Goldsmiths' Works (13th–15th Centuries)
Ed. by Antje Bosselmann-Ruickbie, 2019. Byzanz zwischen Orient und Okzident **13**, Verlag des Römisch-Germanisches Zentralmuseums, Mainz, Germany, 188 pages, ISBN 978-3884673157. EUR43.00 hardcover.

The Staffordshire Hoard: An Anglo-Saxon Treasure
Ed. by Chris Fern, Tania Dickinson and Leslie Webster, 2019. Research Report of the Society of Antiquaries of London No. 80, 595 pages, ISBN 978-1527233508, https://doi.org/10.26530/20.500.12657/39941. GBP45.00 hardcover or free PDF.

GEM LOCALITIES

Mineral Collections of Brazil/Coleçóes Minerais do Brasil
By Carlos Cornejo and Andrea Bartorelli, 2020. Solaris Edições Culturais, São Paulo, Brazil, 792 pages, ISBN 978-8589820134 (English) or ISBN 978-8589820127 (Portuguese). USD120.00 hardcover.

GENERAL REFERENCE

Gemstones Identification BlueChart (updated edn.)
By Hervé Nicolas Lazzarelli, 2019. Self-published, no ISBN, 26 pages. GBP29.50 softcover.

JEWELLERY HISTORY

Ancient Egyptian Jewelry: 50 Masterpieces of Art and Design
By Nigel Fletcher-Jones, 2020. The American University in Cairo Press, Cairo, Egypt, and New York, New York, USA, 116 pages, ISBN 978-9774169656. USD19.95 hardcover.

Chaumet in Majesty: Jewels of Sovereigns Since 1780 (English edn.)
By Christophe Vachaudez, Karine Huguenaud and Romain Condamine, 2019. Flammarion, Paris, France, 288 pages, ISBN 978-2080204301. USD35.00 softcover.

'A Marvel to Behold': Gold and Silver at the Court of Henry VIII
By Timothy Schroder, 2020. Boydell & Brewer Ltd, Martlesham, Suffolk, 400 pages, ISBN 978-1783275076. GBP45.00 hardcover.

JEWELLERY AND *OBJETS D'ART*

Eastern Treasures: Ottoman, Oman, Yemen and Turkoman Jewellery
By Oytun Camcigil, 2020. Gilgamesh Art Publishing, London, 312 pages, ISBN 978-1908531575. GBP49.96 hardcover.

Guía Completa de Engastado en Joyería: Técnicas, Estilos y Materiales [Complete Guide to Setting in Jewelry: Techniques, Styles and Materials]
By Anastasia Young, 2020. Promopress, Barcelona, Spain, 208 pages, ISBN 978-8492810833 (in Spanish). EUR35.00 hardcover.

Shaun Leane
By Joanna Hardy, Vivienne Becker and Claire Wilcox, 2020. Arnoldsche Art Publishers, Stuttgart, Germany, 320 pages, ISBN 978-3897905955. EUR68.00 hardcover.

ORGANIC/BIOGENIC MATERIALS

Lungo le Vie del Corallo. Collezione Antonino de Simone [Along the Coral Road. Antonino de Simone Collection]
By Cristina Del Mare, 2019. Arte'm, Naples, Italy, 176 pages, ISBN 978-8856906936 (in Italian and English). EUR35.00 softcover.

PEARLS

Biomineralization Mechanism of the Pearl Oyster, *Pinctada fucata*
By Zhang Rongqing, Xie Liping, and Yan Zhenguang, 2019. Springer Nature, Singapore, 737 pages, ISBN 978-9811314582 (hardcover), ISBN 978-9811346361 (softcover) or ISBN 978-9811314599 (eBook), https://doi.org/10.1007/978-981-13-1459-9. EUR179.99 hardcover or softcover, or EUR149.79 eBook.

Literature of Interest

COLOURED STONES

Chemical constituents and spectra characterization of demantoid from Russia. J. Pei, W. Huang, Q. Zhang and S. Zhai, *Spectroscopy and Spectral Analysis*, **39**(12), 2019, 3849–3854 (in Chinese with English abstract).

Coexisting rubies and blue sapphires from major world deposits: A brief review of their mineralogical properties. A.C. Palke, *Minerals*, **10**(5), 2020, article 472 (20 pp.), https://doi.org/10.3390/min10050472.*

Color characteristics of blue to yellow beryl from multiple origins. Y. Hu and R. Lu, *Gems & Gemology*, **56**(1), 2020, 54–65, https://doi.org/10.5741/gems.56.1.54.*

Comments on beryl colors and on other observations regarding iron-containing beryls. L.O. Andersson, *Canadian Mineralogist*, **57**(4), 2019, 551–566, https://doi.org/10.3749/canmin.1900021.

Detailed luminescence spectra interpretation of selected oxides: Spinel from Myanmar and chryso-beryl – var. alexandrite from Tanzania. I. Malíčková, P. Bačík, J. Fridrichová, R. Hanus, J. Štubňa, S. Milovská and R. Škoda, *Acta Geologica Slovaca*, **12**(1), 2020, 69–74, https://tinyurl.com/y39wz6gs.*

Étoiles de 6 à 12 branches dans des saphirs noirs astériés thaïlandais [6- and 12-rayed asterism in Thai black star sapphires]. J.-P. Gauthier, J. Fereire and T.N. Bui, *Revue de Gemmologie A.F.G.*, No. 208, 2019, 4–10 (in French with English abstract).

An evaluation of the potential for determination of the geographic origin of ruby and sapphire using an expanded trace element suite plus Sr–Pb isotope compositions. M. Krebs, M. Hardman, D. Pearson, Y. Luo, A. Fagan and C. Sarkar, *Minerals*, **10**(5), 2020, article 447 (37 pp.), https://doi.org/10.3390/min10050447.*

Explanation of the alexandrite effect of Zultanite: From the view of colorimetry and chemical analysis. D. Zhou, T. Lu, R. Sun, G. Shi, H. Chen and J. Ke, *Color Research & Application*, **44**(6), 2019, 925–931, https://doi.org/10.1002/col.22412.

Faceted fluorite. M. Mauthner, *Rocks & Minerals*, **95**(4), 2020, 357–361, https://doi.org/10.1080/00357529.2020.1744096.

The gem/rock conundrum. G. Choudhary, *Gems&Jewellery*, **29**(3), 2020, 20–21.

The genesis of agates and amethyst geodes. I.N. Kigai, *Canadian Mineralogist*, **57**(6), 2019, 867–883, https://doi.org/10.3749/canmin.1900028.

Investigation on the gemological, physical and compositional properties of some green opals from eastern Rhodopes, Bulgaria. F. Caucia, L. Marinoni and G. Bruni, *Rendiconti Lincei. Scienze Fisiche e Naturali*, **31**(1), 2019, 153–163, https://doi.org/10.1007/s12210-019-00855-z.

Jade: In search of heaven. R.W. Hughes, *Gems&Jewellery*, **29**(3), 2020, 22–24.

A lesser-known treasure [trapiche spinel from Mogok, Myanmar]. Thet Tin Nyunt and May Tin Zaw Win, *Gems&Jewellery*, **29**(3), 2020, 36–37.

Mineralogical characteristics of Japanese rainbow garnet. J. Lei, F. Bai and X. Ling, *Acta Petrologica et Mineralogica*, **38**(5), 2019, 733–742 (in Chinese with English abstract).

Mineralogy, geochemistry, and petrogenesis of nephrite from Panshi, Jilin, northeast China. F. Bai, G. Li, J. Lei and J. Sun, *Ore Geology Reviews*, **115**, 2019, article 103171 (14 pp.), https://doi.org/10.1016/j.oregeorev.2019.103171.

Orange-yellow inclusion in spinel from Man Sin, Myanmar. S. Zhai, J. Pei and W. Huang, *Journal of Gems & Gemmology*, **21**(6), 2019, 24–30 (in Chinese with English abstract).

Origine de la chatoyance dans une obsidienne noire du Mexique [Origin of chatoyancy in black obsidian from Mexico]. J.-P. Gauthier, J. Fereire and T.N. Bui, *Revue de Gemmologie A.F.G.*, No. 208, 2019, 28–30 (in French with English abstract).

Quality assessment of natural jadeite: Process and tips for appraisers. R. Schluessel, *GemGuide*, **39**(4), 2020, 4–10, www.gemguide.com/wp-content/uploads/pdf/2020GGJulAugNatJadeite.pdf.*

A quantitative description of the causes of color in corundum. E.V. Dubinsky, J. Stone-Sundberg and J.L. Emmett, *Gems & Gemology*, **56**(1), 2020, 2–28, https://doi.org/10.5741/gems.56.1.2.*

Replacement degree of Al³⁺ and Cr/V ratio in high-V emeralds from Malipo, Yunnan, China. F. Bai, H. Pan and X. Li, *Arabian Journal of Geosciences*, **12**(12), 2019, article 377 (9 pp.), https://doi.org/10.1007/s12517-019-4465-2.

Research of zonation characteristics of emeralds from Malipo, Yunnan Province, China. D. Bui, Z. Liao, Z. Zhou, Q. Zhong, M. Lai and L. Li, *Acta Mineralogica Sinica*, **39**(5), 2019, 601–608 (in Chinese with English abstract).

Ruby deposits: A review and geological classification. G. Giuliani, L.A. Groat, A.E. Fallick, I. Pignatelli and V. Pardieu, *Minerals*, **10**(7), 2020, article 597 (83 pp.), https://doi.org/10.3390/min10070597.*

Study on the spectral characteristics of the Menzies emerald from Australia. H. Wang, R. Liang, Y. Lan, H. Pan, X. Ai and H. Lin, *Acta Mineralogica Sinica*, **39**(6), 2019, 657–663 (in Chinese with English abstract).

The study on UV-Vis spectrum of a special color-changed [*sic*] sapphire. C. Chen, W. Huang, T. Shao, C. Shen, Z. Li and A.H. Shen, *Spectroscopy and Spectral Analysis*, **39**(8), 2019, 2470–2473 (in Chinese with English abstract).

Trace elements in almandine garnet, Vemireddipalle area, Krishna District, Andhra Pradesh, India. N. Sultana, *International Journal of Scientific Research in Science and Technology*, **6**(4), 2019, 184–187, https://doi.org/10.32628/ijsrst196438.*

CULTURAL HERITAGE

Gems. V. Dasen and Á.M. Nagy, in D. Frankfurter, Ed., *Guide to the Study of Ancient Magic*. Brill, Leiden, the Netherlands, 2019, 416–455, https://doi.org/10.1163/9789004390751_018.

"Palaeoshellomics" reveals the use of freshwater mother-of-pearl in prehistory. J. Sakalauskaite, S.H. Andersen, P. Biagi, M.A. Borrello, T. Cocquerez, A.C. Colonese, F. Dal Bello, A. Girod *et al.*, *eLife*, **8**, 2019, article 45644 (65 pp.), https://doi.org/10.7554/eLife.45644.*

The reliquary bust of Saint Lambert from the Liège Cathedral, Belgium: Gemstones and glass beads analysis by pXRF and Raman spectroscopy. Y. Bruni, F. Hatert, P. George and D. Strivay, *Archaeometry*, **62**(2), 2019, 297–313, https://doi.org/10.1111/arcm.12527.

Studying gems: Collectors and scholars. C. Wagner, in R. Morais, D. Leão, D.R. Pérez & D. Ferreira, Eds., *Greek Art in Motion: Studies in Honour of Sir John Boardman on the Occasion of his 90th Birthday*. Archaeopress, Oxford, 2019, 37–45, https://doi.org/10.2307/j.ctvndv598.8.

DIAMONDS

Diamonds from the Deep: Diamonds are not forever! Diamond dissolution. *Gems & Gemology*, **56**(1), 2020, 148–155, www.gia.edu/gg-issue-search?ggissueid=1495312555038&articlesubtype=diamondsfromthedeep.*

Features of the impurity composition of diamonds from placers of the northeastern Siberian craton. V.S. Shatsky, V.A. Nadolinny, O.P. Yuryeva, M.I. Rakhmanova and A.Y. Komarovskikh, *Doklady Earth Sciences*, **486**(2), 2019, 644–646, https://doi.org/10.1134/s1028334x19060096.

History, heritage…and hype [Indian diamonds]. J. Ogden, *Gems&Jewellery*, **29**(3), 2020, 38–40.

L'analyse du diamant mêlé incolore et de couleur : Alertes pour le marché du diamant [Analysis of colourless and coloured diamond melee: Alert for diamond merchants]. T. Hainschwang, *Revue de Gemmologie A.F.G.*, No. 208, 2019, 22–27 (in French).

Multi-analytical characterization of Fe-rich magnetic inclusions in diamonds. M. Piazzi, M. Morana, M. Coïsson, F. Marone, M. Campione, L. Bindi, A.P. Jones *et al.*, *Diamond and Related Materials*, **98**, 2019, article 107489 (9 pp.), https://doi.org/10.1016/j.diamond.2019.107489.

Pyramids <001> and <011> in natural diamond. V.P. Mironov, *AIP Conference Proceedings*, **2069**(1), 2019, article 040006 (7 pp.), https://doi.org/10.1063/1.5089849.

Round brilliant cut beauty and light performance Part 1. M.D. Cowing, *Gemmology Today*, June 2020, 60–66, www.worldgemfoundation.com/GTJUNE2020DV.*

A song of ice and diamonds [mining in Sakha, Russia]. J. Kozenko, *Gems&Jewellery*, **29**(3), 2020, 28–31.

The story of one diamond: The heterogeneous distribution of the optical centres within a diamond crystal from the Ichetju placer, northern Urals. E. Vasilev, V. Petrovsky, A. Kozlov, A. Antonov, A. Kudryavtsev and K. Orekhova, *Mineralogical Magazine*, **83**(4), 2019, 515–522, https://doi.org/10.1180/mgm.2019.32.

Structural and mineralogical features of diamonds from the Lomonosov deposit (Arkhangelsk Province): New data and interpretation. G.Y. Kriulina, E.A. Vasiliev and V.K. Garanin, *Doklady Earth Sciences*, **486**(2), 2019, 627–629, https://doi.org/10.1134/s1028334x19060291.

Tickled pink [Argyle pink diamonds]. J. Asplund, *Gemmology Today*, June 2020, 72–75, www.worldgemfoundation.com/GTJUNE2020DV.*

GEM LOCALITIES

Age determination of zircon inclusion in Kashmir sapphire with U-Pb dating. W. Xu, K. Link, C. Liu and L. Kiefert, *Journal of Gems & Gemmology*, **22**(1), 2020, 1–12.

The colored gemstone mining industry in Africa – 25 years of evolution. C. Simonet, *InColor*, No. 46, 2020, 20–27, www.gemstone.org/incolor/46.*

Connoisseur's Choice: Diaspore, Muğla Province, Turkey. M. Southwood, *Rocks & Minerals*, **95**(2), 2020, 145–153, https://doi.org/10.1080/00357529.2020.1689336.

Connoisseur's Choice: Tsavorite, the green gem variety of grossular, Merelani Hills, Manyara District, Tanzania. B. Cairncross, *Rocks & Minerals*, **95**(3), 2020, 252–259, https://doi.org/10.1080/00357529.2020.1716171.

Digging in the dirt – Fossicking [in Australia]. K. Rix, *Gemmology Today*, June 2020, 77–85, www.worldgemfoundation.com/GTJUNE2020DV.*

Ediacaran emerald mineralization in northeastern Brazil: The case of the Fazenda Bonfim deposit. J.S. Santiago, V. da Silva Souza, E.L. Dantas and C. Gouveia de Oliveira, *Brazilian Journal of Geology*, **49**(4), 2019, article 2317 (14 pp.), https://doi.org/10.1590/2317-4889201920190081.*

Fluorite from the North Pennines orefield England. J. Fisher, *Rocks & Minerals*, **95**(4), 2020, 306–347, https://doi.org/10.1080/00357529.2020.1744094.

Formation conditions and $^{40}Ar/^{39}Ar$ age of the gem-bearing Boqueirão granitic pegmatite, Parelhas, Rio Grande do Norte, Brazil. P.S. Palinkaš, L. Palinkaš, F. Neubauer, R. Scholz, S.B. Šoštarić and V. Bermanec, *Minerals*, **9**(4), 2019, article 233 (16 pp.), https://doi.org/10.3390/min9040233.*

The gems of Chanthaburi [Thailand]. J. Zheng, *JNA*, No. 417, 2019, 79–82, 84, https://jewellerynet.com/uploads/ebook/jna/2019/issue417_sep2019/V6.*

Glorious in green [peridot from China]. P. Tonna, *Gems&Jewellery*, **29**(3), 2020, 16–18.

History of the Chivor emerald mine, Part 1 (1880–1925): From rediscovery to early production. K. Schmetzer, G. Martayan and J.G. Ortiz, *Gems&Gemology*, **56**(1), 2020, 66–109, https://doi.org/10.5741/gems.56.1.66.*

Mineralogy, geochemistry and petrogenesis of nephrite from Tieli, China. S. Gao, F. Bai and G. Heide, *Ore Geology Reviews*, **107**, 2019, 155–171, https://doi.org/10.1016/j.oregeorev.2019.02.016.

A Persian paradise [turquoise]. M.M. Salimi, *Gems&Jewellery*, **29**(3), 2020, 26–27.

Rhodonite-pyroxmangite from Tanatz Alp, Switzerland. F. Caucia, L. Marinoni, M.P. Riccardi, O. Bartoli and M. Scacchetti, *Gems & Gemology*, **56**(1), 2020, 110–123, https://doi.org/10.5741/gems.56.1.110.*

INSTRUMENTATION AND TECHNOLOGY

Application of infrared spectrum detection technology in jewelry inspection and testing institutes. Y. Yang and Z. Yan, *Superhard Material Engineering*, **31**(5), 2019, 49–54 (in Chinese with English abstract).

Assessing color of gemstones. S. De Meo, A. Plutino and A. Rizzi, *Color Research & Application*, **45**(2), 2020, 224–234, https://doi.org/10.1002/col.22472.

Exploring natural gems and minerals by multiphoton microscopy. B.M. Cromey, R.J. Knox, E. Fritz and K. Kieu, *Proceedings of SPIE 11099: Light in Nature VII*, 2019, article 1109902 (8 pp.), https://doi.org/10.1117/12.2528764.

Near infrared spectrum analysis of nesosilicate gemstone minerals. H. Song, X. Guo, H. Tan and E. Zu, *Bulletin of the Chinese Ceramic Society*, **11**, 2019, 3592–3596, https://doi.org/10.16552/j.cnki.issn1001-1625.20190905.001 (in Chinese with English abstract).

LAPIDARY TECHNIQUES

The evolution of Chinese jade carving craftsmanship. M. Wang and G. Shi, *Gems & Gemology*, **56**(1), 2020, 30–53, https://doi.org/10.5741/gems.56.1.30.*

The evolution of the lapidary tradition. J.K. Prim, *InColor*, No. 46, 2020, 54–57, www.gemstone.org/incolor/46.*

The lapidary revolution. G.W. Lehrer, *InColor*, No. 46, 2020, 58–65, www.gemstone.org/incolor/46.*

MISCELLANEOUS

Education in gemology – A historical review. R. Galopim de Carvalho, *InColor*, No. 46, 2020, 78–81, www.gemstone.org/incolor/46.*

The evolution of pricing & value of gems and jewelry. H. Molesworth, *InColor*, No. 46, 2020, 44–53, www.gemstone.org/incolor/46.*

Evolution of the study of gem deposit geology. A.C. Palke and W. Vertriest, *InColor*, No. 46, 2020, 14–18, www.gemstone.org/incolor/46.*

Field gemology – The evolution of data collection. V. Pardieu, *InColor*, No. 46, 2020, 36–42, www.gemstone.org/incolor/46.*

Gold & silver recovery from jewelry waste with combination of physical and physicochemical methods. F. Burat, H. Baştürkcü and M. Özer, *Waste Management*, **89**, 2019, 10–20, https://doi.org/10.1016/j.wasman.2019.03.062.

Mastering jewellery [Wallace Chan]. *Gems&Jewellery*, **29**(3), 2020, 42–44.

Mine to market – Evolution of the rough trade. S.-F. Hashmi, *InColor*, No. 46, 2020, 28–35, www.gemstone.org/incolor/46.*

NEWS PRESS

The great diamond glut: Miners stuck with gems worth billions. T. Biesheuvel, Bloomberg, 7 June 2020, www.bloomberg.com/news/articles/2020-06-07/the-great-diamond-glut-miners-stuck-with-gems-worth-billions.*

Largest tanzanite gemstones in history sold for $3m. E. Shaban and S. Spary, CNN, 30 June 2020, https://edition.cnn.com/2020/06/30/africa/tanzanite-largest-gems-scli-intl/index.html.*

Mummy of ancient Egyptian teenager, buried in fine jewelry, discovered in Luxor. L. Geggel, LiveScience, 29 April 2020, www.livescience.com/ancient-egyptian-teenage-mummy.html.*

ORGANIC/BIOGENIC GEMS

An ammonite trapped in Burmese amber. T. Yu, R. Kelly, L. Mu, A. Ross, J. Kennedy, P. Broly, F. Xia, H. Zhang *et al.*, *Proceedings of the National Academy of Sciences*, **116**(23), 2019, 11345–11350, https://doi.org/10.1073/pnas.1821292116.

Green [Baltic] amber? M. Kosior, *Bursztynisko (The Amber Magazine)*, No. 44, 2020, 126–127, https://issuu.com/internationalamberassociation/docs/b44_issuu_teaser (in English and Polish).*

Lighting the ivory track: Are near-infrared and chemometrics up to the job? A proof of concept. A. Power, S. Ingleby, J. Chapman and D. Cozzolino, *Applied Spectroscopy*, **73**(7), 2019, 816–822, https://doi.org/10.1177/0003702819837297.

Structural evolution of Burmese amber during petrifaction based on a comparison of the spectral characteristics of amber, copal, and rosin. F. Bai, H. Liang and H. Qu, *Journal of Spectroscopy*, 2019, article 6904541 (11 pp.), https://doi.org/10.1155/2019/6904541.*

PEARLS

Long live [Akoya cultured] pearls. T. Atsumi, *Gems&Jewellery*, **29**(3), 2020, 14–15.

Overview of the development and modern landscape of marine pearl culture in the South Pacific. W. Johnston, D. Hine and P.C. Southgate, *Journal of Shellfish Research*, **38**(3), 2019, 499–518, https://doi.org/10.2983/035.038.0301.

Pearls – Evolution in the sector, production and technology. K. Scarratt, *InColor*, No. 46, 2020, 82–86, www.gemstone.org/incolor/46.*

Les perles de Bahrein [Pearls from Bahrain]. K. Scarratt, *Revue de Gemmologie A.F.G.*, No. 208, 2019, 11–20 (in French).

Trivalent iron is responsible for the yellow color development in the nacre of akoya pearl oyster shells. M. Kakinuma, K. Yasumoto, M. Suzuki, C. Kasugai, M. Koide, K. Mitani, K. Shidoji, S. Kinoshita *et al.*, *Marine Biotechnology*, **22**(1), 2019, 19–30, https://doi.org/10.1007/s10126-019-09927-5.

SYNTHETICS

Diamonds in the rough: Synthetic gems from Pliny to Lightbox. L. Pyne, *Athenaeum Review,* No. 3, 2020, 166–170, https://athenaeumreview.org/wp-content/uploads/2019/10/Pyne.pdf.*

A study in [emerald] synthesis. J. Beeley, *Gems&Jewellery*, **29**(3), 2020, 32–35.

Synthesis and characterization of gem diamond single crystals in Fe-C system under high temperature and high pressure. Z. Wang, H. Ma, S. Fang, Z. Yang, X. Miao, L. Chen and X. Jia, *Journal of Crystal Growth*, **531**, 2020, article 125371 (5 pp.), https://doi.org/10.1016/j.jcrysgro.2019.125371.

Synthesis and color centers study on diamond doping with CH_4N_2S under high pressure. J. Liao, Y. Li, D. Tan, Y. She, Y. Wang and T. Deng, *Journal of Synthetic Crystals*, **48**(9), 2019, 1626–1630 (in Chinese with English abstract).

TREATMENTS

The characterization study on quantity of filled glass material in ruby. Z. Xiang, Z. Yin and X. Zheng, *Spectroscopy and Spectral Analysis*, **39**(4), 2019, 1274–1279 (in Chinese with English abstract).

Effect of beryllium heat treatment in synthetic ruby. N. Monarumit, T. Lhuaamporn, S. Satitkune and W. Wongkokua, *Journal of Applied Spectroscopy*, **86**(3), 2019, 486–492, https://doi.org/10.1007/s10812-019-00845-x.

Filled turquoise and its corresponding filling solution. J. Liu, M. Yang, C. He and F. Cao, *Journal of Gems & Gemmology*, **21**(5), 2019, 56–64 (in Chinese with English abstract).

Gamma irradiation on rubellite tourmaline. N. Bunnag and T. Sripoonjan, *Chiang Mai Journal of Science*, **46**(6), 2019, 1249–1255, https://epg.science.cmu.ac.th/ejournal/journalDetail.php?journal_id=10432.*

Gemmological characteristic of electron irradiated amethyst. T. Shao, J. Zhang and A.H. Shen, *Journal of Gems & Gemmology*, **21**(5), 2019, 48–55 (in Chinese with English abstract).

Heat treatment experiments of corundum – Development of a before/after collection. T. Stephan, B. Huaysan and S. Müller, *GemGuide*, **39**(4), 2020, 11–15.

COMPILATIONS

G&G **Micro-World.** Actinolite in spinel • Bavenite in quartz • Diamond with mobile green diamond inclusion • Twinning in neodymium pentaphosphate • Needles in pallasitic peridot • 'Play-of-color' in sapphire • Staurolite in ruby • Triplite in beryl • Unknown inclusion in triphane. *Gems & Gemology*, **56**(1), 2020, 140–147, www.gia.edu/gg-issue-search?ggissueid=1495312555038&articlesubtype=microworld.*

Gem News International. 2020 Tucson gem shows • Burmese star peridot • Demantoid and emerald from Russia • Nephrite from various sources • Nigerian gems and jewellery • Large round freshwater pearl from USA • Sapphires from Montana (USA), Australia and Sri Lanka (Rakwana) • Trapiche gems • Carvings, fantasy cuts, and master recutting • Jadeite jewellery • Nordic gem materials and jewellery • Ethical Gem Fair • Bicolored synthetic sapphire • DNA barcoding of freshwater pearls • Sunstone feldspar from Ethiopia • Dyed chalcedony imitation of chrysocolla chalcedony • Jadeite and serpentine doublet • *Gems & Gemology*, **56**(1), 2020, 156–192, www.gia.edu/gg-issue-search?ggissueid=1495312555038&articlesubtype=gni.*

Lab Notes. Diamond with cavities showing radiation evidence • 'Matryoshka' diamond from Siberia, Russia • Graphitic cavities on diamond • Corundum inclusions in diamond • Solid carved dark gray diamond ring • Clarity-enhanced glass imitating emerald • Large grandidierite • Electronic device in a bead-cultured pearl • Fluorescence spectroscopy to detect pearl color treatments • Fossilized shell blister and blister pearl • Saltwater bead-cultured pearl with laminated nucleus • Bismuth glass-filled Burmese star ruby. *Gems & Gemology*, **56**(1), 2020, 126–139, www.gia.edu/gg-issue-search?ggissueid=1495312555038&articlesubtype=labnotes.*

CONFERENCE PROCEEDINGS

47th Rochester Mineralogical Symposium. Rochester, New York, USA, 25 April 2020, 32 pp., www.rasny.org/minsymp/47th%20RMS%20Program%20Notes.pdf.*

*Article freely available for download, as of press time

Buy Gem-A Instruments online!

OVER 100 PRODUCTS AVAILABLE

Gem-A INSTRUMENTS

View the full collection at:
shop.gem-a.com

GEM-A MEMBERS!

Login to the Gem-A Instruments website and gain instant access to discounted rates.

Username is the email address that you have provided to Gem-A Membership.

Password is your membership number.

You must login before adding products to your basket.

We recommend changing your password in the account settings.